KTH Architecture and
the Built Environment

Shear Strength of Unfilled and Rough Rock Joints in Sliding Stability Analyses of Concrete Dams

Fredrik Johansson

Doctoral Thesis

Division of Soil and Rock Mechanics
Department of Civil and Architectural Engineering
Royal Institute of Technology

Stockholm 2009

TRITA-JOB PHD 1013
ISSN 1650-9501

CONTENTS

ACKNOWLEDGEMENTS

First of all, I would like to express my gratitude to my supervisor Professor Håkan Stille; for his invaluable advices, patience and encouragement throughout this work.

Special thanks are also acknowledged to M. Sc. Karl Rytters who initiated the project. Without him, this project would not have been realized.

This project was financed by several participants. I would like to express my appreciation to Tomas Franzén together with Mikael Hellsten at SveBeFo. I am also most grateful to the other financiers, who are the Swedish power company's research and development organisation, ELFORSK, the Swedish construction industry's organisation for research and development, SBUF, the Swedish nuclear waste management, SKB, and the technical consultant firm SWECO Infrastructure AB.

During this project, the work has been followed by a reference group, consisting of persons competent in the subject. The group has assisted with valuable comments and discussions. A debt of gratitude is acknowledged to the persons who have participated in this group, which are:

- Tomas Franzén, SveBeFo
- Mikael Hellsten, SveBeFo
- Anders Gustafsson, SWECO Infrastructure AB
- Carl-Olof Söder, SWECO Infrastructure AB
- Catrin Edelbro, LTU
- Karin Hellstadius, Vattenfall Power Consultant AB
- Rolf Christiansson, SKB
- Tommy Flodin, FORTUM

Vattenfall AB, for financial support and permission of using Långbjörn hydropower station for shear testing of rock joints and discussion on different methods for sliding stability analyses.

Per Delin, Geometrik, who helped me with the test set-up and measurements during the *in situ* shear test.

Marie Westberg, Vattenfall Vattenkraft AB, for fruitful discussions regarding dam safety and reliability based design and for assistance with the program Comrel.

The staff at Complab, LTU, for assistance with the shear testing.

Kenneth Strand, Svensk Verktygsteknik, who performed the optical scanning of the joint surfaces.

Trotte and Peter, SBT, for their assistance with the *in situ* shear test.

And for all additional people not named here who has participated and helped me in my work.

I would also like to thank my colleagues and staff members at the department of soil and rock mechanics for their stimulating and interesting discussions and support.

Finally, to my son Filip and my dear Camilla, I would like to express my love and gratitude to their support during this period.

Fredrik Johansson

Stockholm, March 2009

SUMMARY

The horizontal water load combined with uplift forces implies that concrete dams are sensitive for sliding. At the same time, the safety of concrete dams against sliding in the rock foundation is associated with large uncertainties. One of the main uncertainties regards the shear strength of rock joints.

Several failure criteria exist to express the shear strength for unfilled and rough rock joints. However, these criteria do not in general consider a possible scale effect which means that the shear strength could be lower at larger scales. Some suggestions exist for how a possible scale effect could be considered, but these are mainly based on empiric grounds. This means that there exists a need of a more detailed and conceptual understanding on the scale effect of rock joints.

In an attempt to increase the understanding on the scale effect of unfilled and rough rock joints, a conceptual model was derived. The model is based on the assumptions that contact points occur at the steepest asperities facing the shear direction and that their total area could be expressed with adhesion theory. Fractal theory is used in order to idealize the surface roughness by superposition of asperities at different scales. Based on changes in the size and number of contact points, the conceptual model suggests that the scale effect does not occur for all types of rock joints. Perfectly mated joints are suggested to not exhibit any scale effect while a considerable scale effect could be expected for unmated joints.

The practical implications from this, for foundations with unfilled joints, is that unmated joints with large aperture are most critical for the sliding stability of concrete dams, since these joints probably are the ones with longest persistence and lowest shear strength.

In order to study the scale effect of rock joints further, eighteen shear tests at different scales were performed. All of the samples were taken from the rock foundation at Långbjörn hydropower station. Possible scale effects could be observed, but no firm conclusions could be made, mainly due to different surface characteristics of the tested joints. Three of the samples were also used to investigate the accuracy of the conceptual model. This investigation revealed that it may be necessary to distinguish between weathered and unweathered joints, since the distribution of contact points appears to become more randomly distributed for a weathered joint which in turn results in lower friction angles.

In Sweden, dam safety is governed by the Swedish power company’s guidelines for dam safety, RIDAS. When the Swedish guidelines were compared with guidelines and regulations in other countries, it was realized that there exists a need for a more balanced evaluation of the sliding stability for concrete dams founded on rock in Sweden. In a first step of development, it can be based on safety factors and an increased use of investigations. However, in a second step, a natural way of the development of RIDAS would be in a direction towards reliability based methods.

SYMBOLS AND NOTATIONS

Commonly used symbols and notations are presented below if not otherwise stated in the text. Others are defined as they first appear.

Roman Letters

A	area [m^2]
A_g	sample area at grain scale [m^2]
A_n	sample area at full size [m^2]
A_c	true contact area [m^2]
$A_{c,r}$	true contact area ratio [-]
$A_{c,av}$	average area of contact points
$A_{c,g}$	true contact area at grain size [m^2]
$A_{c,i}$	contact area of contact point i [m^2]
$A_{c,n}$	true contact area at full size [m^2]
$A_{c,p}$	potential contact area ratio [-]
A_o	maximum potential contact area ratio (Grasselli 2001)
a	amplitude constant based on asperity base length
C	roughness parameter (Grasselli 2001)
c	cohesion [MPa]
c_i	cohesion of intact rock [MPa]
COV	coefficient of variation defined as the ratio between standard deviation and mean value
$F_{n,0}$	initial normal force at contact prior to shearing [N]
FS	factor of safety
H	horizontal force [N] or Hurst exponent [-]
h_{asp}	asperity height [mm]
i	dilation angle, inclination angle of asperity [deg.]
i_m	maximal dilation angle [deg.]
i_n	dilation angle at full scale [deg.]
JRC	joint roughness coefficient (Barton and Choubey 1977)
JCS	joint wall compressive strength (Barton and Choubey 1977)
k	matedness constant [-]
L	length [m]
L_{asp}	asperity base length [mm]
$L_{asp,g}$	asperity base length at grain size [mm]
$L_{asp,max}$	maximum asperity base length for the sample [mm]
$L_{asp,n}$	asperity base lengths on the joint [mm]
L_g	length of sample at grain size [mm]
L_n	length of sample at full size [mm]
M	limit state function
N	normal force [N]
n	numbers [-]
n_g	number of contact points at grain size [-]
n_n	number of contact points on the full size joint [-]
P_i	resultant horizontal force acting on a vertical face of wedge i

P_{pas}	passive wedge resistance [N]
p	probability [-]
p_f	probability of failure [-]
q_u	yield stress of surface [N/m^2]
R	resistance [N] or Schmidt rebound number [-]
S	load [N]
s	adhesive strength [N/m^2]
T	shear force [N]
U	uplift force [N]
V	vertical force [N]
V'	effective vertical force [N]
W'	effective weight of passive wedge [N]
X^*	design value of variable X
X_k	characteristic value of variable X
Z_x	normalized form of variable X
Z_2	the root mean square of the first derivate of the sample [-]

Greek Letters

α_x	sensitivity factor of variable X
β	safety index
β_t	target safety index
Δx	sampling distance [mm]
γ	unit weight [kN/m^3]
γ_x	partial factor of variable X
$\delta_{asp,max}$	approximate relative shear displacement for maximal unmatedness
$\delta_{i,max}$	shear displacement at maximal dilation angle [mm]
$\delta_{s,p}$	shear displacement at peak shear strength [mm]
μ	coefficient of friction
μ_{all}	allowable coefficient of friction
μ_x	mean of variable X
θ^*_{max}	maximum measured dip angle (maximum apparent dip angle in Grasselli 2001)
θ^*	measured dip angle (apparent dip angle in Grasselli 2001)
σ_x	standard deviation of variable X
σ_{ci}	uniaxial compressive strength of intact rock or joint surface [MPa]
σ_n	normal stress [MPa]
σ'_n	effective normal stress [MPa]
σ_{ti}	tensile strength of intact rock [MPa]
τ	shear stress [MPa]
τ_f	shear stress at failure [MPa]
τ_p	peak shear strength [MPa]
ϕ	friction angle [deg.]
ϕ_b	basic friction angle [deg.]
$\phi_{b,av}$	average basic friction angle [deg.]
$\phi_{b,p}$	basic friction angle at peak shear strength [deg.]
ϕ_i	internal friction angle of intact rock [deg.]
ϕ_p	peak friction angle [deg.]

1 INTRODUCTION

1.1 Background

In Sweden there exist about 10 000 dams of varying size and age, 1 000 of them are related to hydropower. Of these, about 200 are high dams, i.e. with a height exceeding 15 m. Most of the hydro power dams were built during the 1950's, 60's and 70's (Cederström 1995). Several of them are concrete structures founded on rock. The horizontal water pressure, combined with acting uplift forces, makes these concrete gravity dams sensitive to sliding.

Figure 1.1 Spillway of the concrete dam at Pengfors hydroelectric power station, one of many in Sweden (Photo: SWECO VBB).

Sliding of a dam occurs along the plane with lowest shear resistance. The failure can occur either in the concrete dam, in the interface between dam and foundation or in the foundation. The shear resistance in the concrete dam is normally of no problem, since the mechanical properties of the concrete and the structural system of the dam is well known. In the interface between dam and foundation, the available shear strength is more uncertain, mainly depending on if cohesion is present or not. However, the largest uncertainties of the available shear strength concern the rock foundation.

International experiences show that failure in the foundation is a main source to the failure of concrete dams. A study performed by ICOLD (1995) showed that foundation problems due to internal erosion and insufficient shear strength of the

foundation were the most common causes of failure, each accounting for 21%. One example is the failure of the Malpasset arch dam in France 1959, where sliding failure occurred for a rock wedge in the foundation. The failure caused a 50 m high wave killing over 400 people (Bellier 1976).

During 1950's, 60's and 70's, the knowledge about rock mechanics was on a lower level than today. In the last decades, significant progresses have been made in the field of rock mechanics, and the knowledge of rock mass behavior has increased. Despite the improved knowledge of rock mass behaviour, there still exist significant difficulties to evaluate the safety against sliding in the foundation. For concrete gravity dams founded on a rock mass of good quality, which is common in Sweden, the main uncertainties originate from the shear strength and persistence of horizontal and sub-horizontal rock joints. This thesis focuses on the former, the shear strength of rock joints.

With the large amount of concrete dams of varying age that exist in Sweden, together with other types of large structures founded on rock, it is important for society to be able to evaluate the safety against failure in the foundation for these types of structures. Especially with respect to the possible consequences if failure occurs. Furthermore, if improved evaluations of the sliding stability can be performed; expensive measures such as post-tensioned anchors can be avoided.

1.2 Objectives

This thesis aims at:

- Describing the knowledge and current state of practice in sliding stability analyses of concrete gravity dams.

- Increasing the understanding about the conceptual behaviour for unfilled and rough joints, and how the shear strength for these joints is affected by scale.

- Compare and discuss different methods to express the calculated safety for sliding stability analyses of concrete gravity dams where persistent horizontal or sub-horizontal rock joints are present.

1.3 Disposition of the thesis

In order to get an overview of the thesis, a short description of the contents in each chapter is given.

The thesis starts with a general literature study about sliding stability analyses which is presented in chapter two. At first, some fundamental principles of stability analysis are looked upon. After that, different methods of sliding stability

analysis are reviewed. In the end of the study, laws, regulatory rules and guidelines in the subject are studied. Finally, a summary of the chapter is presented.

Chapter three concerns the estimation of shear strength for unfilled and rough joints, and how the shear strength for these joints is affected by scale. The chapter contains a literature survey of methods available to estimate the shear strength for laboratory samples and full sized joints in the rock mass.

In chapter four, the behavior of unfilled and rough joints is studied further. Based on a deeper literature study on the behavior of rock joints, together with analyses, a conceptual model is suggested. In the end of the chapter, verification analyses are performed.

Results from laboratory and *in situ* shear tests at Långbjörn hydropower station is presented in chapter five. These tests are performed at different scales in order to obtain information for estimating the shear strength of the horizontal joints present in the rock mass and to analyze if any scale effect could be observed. In addition to this, results from characterization of surface roughness from some of the samples are used to estimate the friction angle with the conceptual model proposed in chapter four. Calculated friction angles with the conceptual model are compared against observed friction angles and a discussion and interpretation of the results are performed.

Deterministic and reliability based sliding stability analyses are performed and compared in chapter six for a concrete monolith at Långbjörn hydropower station. At the end of the chapter, a discussion concerning some principal differences between the two methods are held and conclusions are presented.

Conclusions of the work are presented in chapter seven, while chapter eight contains suggestions for future work.

1.4 Extent and limitations

This thesis focuses on concrete gravity dams founded on rock. In other words a large massive structure considered as one unit founded on a rock foundation.

It mainly concerns a sliding failure mode in the foundation. Overturning or overstressing of the material capacity is not given any attention. Furthermore, failure modes in the overlying structure are not considered.

The study is focused on Swedish conditions. These conditions include a fractured rock mass with more or less horizontal joints in combination with vertical or sub vertical sets of discontinuities. The horizontal joints focused on for sliding stability are unfilled and rough joints. No attention has been given to seismic loading.

2 LITERATURE STUDY: SLIDING STABILITY ANALYSES

2.1 Introduction

The aim with this chapter is to describe the knowledge and current state of practice for sliding stability analyses of large structures founded on rock. The study is focused on the fundamental principles of stability analyses and the calculation methods together with guidelines and regulations used to assess the sliding stability.

However, stability analyses in general consist of more components than the ones mentioned above. In short, the process can be described according to Figure 2.1.

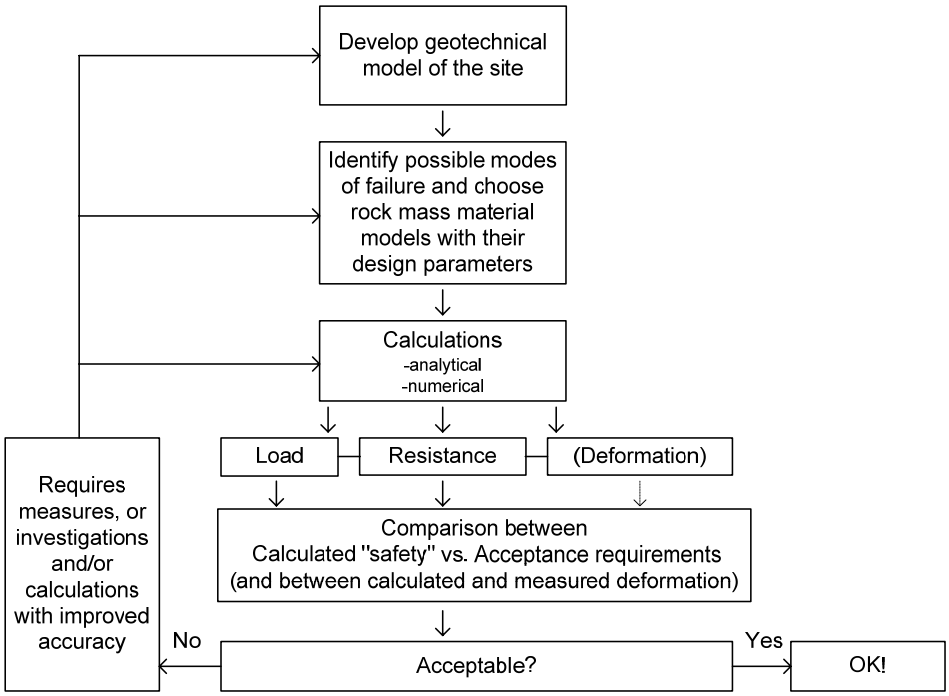

Figure 2.1 Main components in stability analyses for foundation on rock

The calculated or expressed safety is in general determined from knowledge about the load and the resistance. The process to estimate the resistance of the rock mass starts with the development of the geological model. This model is mainly developed from results of site investigations. However, which investigations that are necessary, or how they should be performed, will not be further studied.

Based on the information from the geological model, possible failure modes are identified. Different modes of failure can be possible, and it is necessary to analyze them all to find the weakest link. Material models representative for the rock mass behaviour are chosen to model it. For large structures such as concrete gravity dams, where rock masses with different characteristics may exists in the foundation, several types of models may be necessary for different parts of the foundation. Inputs to these models are a number of rock mechanical parameters, which can be determined through *in situ* or laboratory tests. Another common

technique in order to estimate the parameters representative for the rock mass is to use empirical correlations through rock mass classification systems and/or failure criteria, since laboratory and especially *in situ* test are expensive and time consuming.

The geometry of the structure and the geological model, together with assumed failure mode and chosen rock mass material model, are used to create a simplified model of the problem. Thereafter, the load together with resistance is calculated. Two main types of calculation methods exist, the analytical methods and the numerical methods. In addition to those, empirical methods can be used. However, this last method is primarily used for smaller foundations.

Design in rock masses is often associated with uncertainties. Therefore, it may be important to verify the expected behaviour with measurements, and take required measures if the measured behaviour deviates from the expected one. This concept of "active design" can be an important component of the analyses.

Usually, for the assessment of existing structures, stability is first calculated relatively roughly. An increased accuracy in the calculations is added if they indicate a low safety. If stability remains insufficient after this, measures have to be undertaken. For new structures, the principle is the same, with rough methods in the basic design and more refined calculations and investigations in the detail design.

For a more detailed description of all the components described above, see Johansson (2005).

This chapter contains a study that starts with a review of the principles for sliding stability analyses. Key questions are: (1) which fundamental assumptions are the analyses based upon; (2) how safety is expressed; and (3) what the acceptance requirements are based upon. Subsequently, different analytical methods are investigated. In addition to this, laws, regulatory rules, and guidelines on the subject, in Sweden and in other countries, are studied. Finally, a summary of the performed study is presented.

2.2 Principles of stability analyses

2.2.1 Basic principles

In general, stability analyses is based on the assumption that load and resistance is separated and independent of deformation. The principle is that the resistance or capacity, R, for the structural component considered should be equal to or greater than the applied load, S. The criterion is given by equation 2.1.

$$R \geq S \tag{2.1}$$

This assumption is only an approximation. In reality, the load to some extent can be related to the deformation. Under certain conditions, this dependence is more

pronounced. For example, it might occur when the stiffness of the rock foundation to a high degree is varying. At these occasions it is important to remember this limitation, and also to study the general behaviour of this dependence.

All stability analyses are associated with certain amounts of uncertainty. Regarding rock masses, the uncertainty is larger than for manufactured materials such as steel and concrete. They have been formed under millions of years and have a natural spatial variation of its properties. In addition to this, the information is always limited. It is hidden in the rock mass, revealing its properties costs time and money. Stability analyses are therefore to a large extent a question of finding the right balance between the load, the resistance, the uncertainties, and also the consequences of failure.

To find this balance, two components are generally used. The first is an expression for the calculated safety. The calculated safety can be expressed in several different ways. The most frequently used expressions are:

- A total factor of safety
- A probability of failure
- Limit states with partial factors of safety

The second component is the acceptance requirement. It determines which magnitude the calculated safety must have in order to obtain an acceptable risk.

2.2.2 Factor of safety

The most common way to express safety for foundations on rock is with the factor of safety. The factor of safety, *FS,* is obtained by dividing the resistance, *R*, with the acting load, *S*, according to equation 2.2.

$$FS = \frac{R}{S} \tag{2.2}$$

The values of *R* and *S* are expressed as deterministic values. However, one shortcoming with the factor of safety is that load and resistance depend on a number of parameters. In reality these parameters can exist in wide ranges, i.e. probability distributions. Examples of such distributions are shown in Figure 2.2. This means that for a given value of the resistance and the load, having the same factor of safety, different probabilities of failure can exist (Green 1989). Case *b* in Figure 2.2 illustrates a condition which is common for foundations on rock; good control of the load and poor control of the resistance. This illustrates the possibility to calculate an acceptable factor of safety but still have an unacceptable high risk of failure if these distributions are not considered.

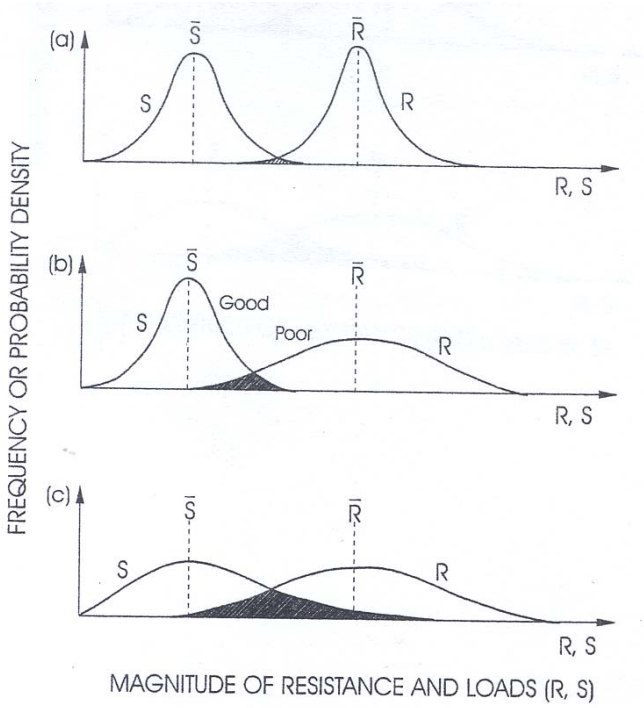

Figure 2.2 Possible load and resistance distributions (From Becker 1996 after Green 1989): (a) very good control of R and S; (b) mixed control of R and S; (c) poor control of R and S.

ICOLD (1993) describes with a striking example, see Figure 2.3, how different variations of the parameter and number of tests can change the probability of failure in a ratio of 100 000 with the same factor of safety.

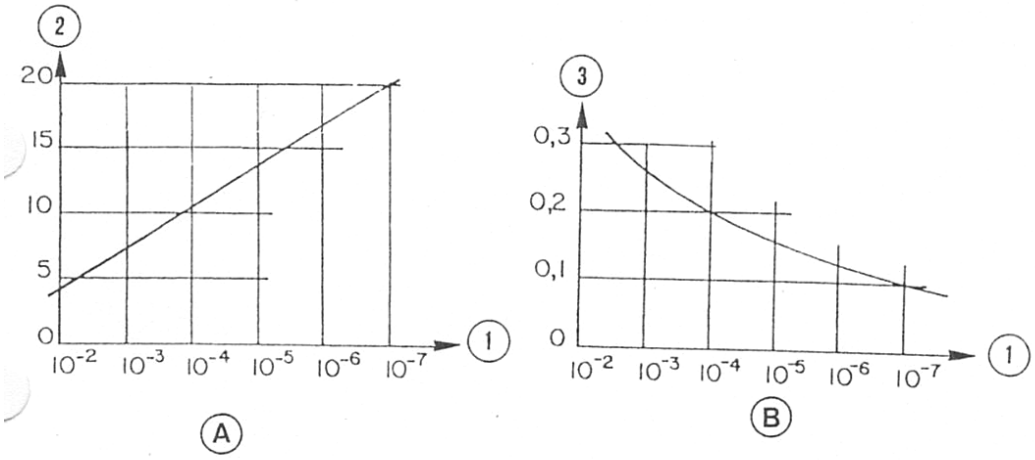

Figure 2.3 (A) Factor of safety FS=1.5 Scatter V=0.2; (B) Factor of safety FS=1.5 10 tests; (1) Probability of failure; (2) Number of tests; (3) Scatter V, defined as the standard deviation divided with the mean value (From ICOLD 1993).

Another shortcoming or disadvantage described by Becker (1996) is that the factor of safety does not distinguish between the sources of uncertainties, such as parameter uncertainty, model uncertainty or system uncertainty. Instead, all uncertainties are lumped into a single value. He is also of the opinion that it is not possible to exactly define safety with a single number due to the uncertainties.

The factor of safety and other ways of expressing safety are only relative and not absolute; the main task for them is to function as an aid or tool for managing safety.

However, its simplicity is also its strength. In the early era of stability analyses, it was an easy method to calculate safety. The lack of accuracy was compensated with experience. With time, empirical acceptance requirements were developed that successfully considered most of the uncertainties in the analyses. Today, the same method is still used even though the techniques to determine load and resistance have been refined. We still have uncertainties on the exact safety against failure, and continue to base our analyses on these partly empirical acceptance requirements.

2.2.3 Probability of failure

The spatial variation of rock mass properties and the awareness of the shortcomings with the factor of safety have lead to an increasing trend towards probabilistic or reliability based methods in rock engineering. With these methods, the probability of failure can be expressed as (Melchers 1999):

$$p_f = p[R - S \leq 0] \tag{2.3}$$

where, R and S are described by a known probability density function. It can also be expressed according to equation 2.4:

$$p_f = p[M \leq 0] \tag{2.4}$$

where, M is the "*limit state function*". It defines the limit between the "*safe*" and the "*unsafe*" region. The probability of limit state violation is equal to the probability of failure. In general, the problem can not be expressed with R and S as two basic variables. The problem is more complex than that, and a number of basic variables are needed. If the vector X represents all variables in the problem, the limit state function can be expressed as M(X). The probability of failure can then be expressed according to equation 2.5.

$$p_f = p[M(\mathrm{X}) \leq 0] = \int \ldots \int_{M(\mathrm{X}) \leq 0} f_x(x)dx \tag{2.5}$$

The integrand above can be solved with three different methods (Melchers 1999):

1. Direct integration which is possible only in some special cases.
2. Numerical integration, such as the Monte Carlo technique.
3. Obviating the integrand through a transformation into a multi-normal joint probability density function and instead solve it analytically.

For an account of these methods, see Melchers (1999) among others.

With failure probability it exist a theoretical possibility to express the probability of failure. The method has several potential advantages. Four of them were described by Becker (1996). He means that it has the potential advantages of being more realistic, rational, consistent and widely applicable. He is also of the opinion that the most important disadvantage of the method is that without proper information and data, these advantages can not be realized in practical design situations. Another disadvantage is pointed out in ICOLD (1993); it says that failure probability is too speculative to offer any practical solution to the engineer's problem. For example, it is a major difficulty to estimate uncertainty in numerical terms.

It should also be kept in mind that this technique normally assumes independence between the basic variables. Also, correlation structures in the rock mass may exist, which results in autocorrelation of the basic variables, i.e. a reduction of its variance. For geotechnical problems, Olsson (1986) means that neglecting the autocorrelation results in too strong structures without any direct apprehension of the magnitude of the underestimation of the soil's resistance. If autocorrelation exists in the rock mass, the same statement is valid for rock masses. Furthermore, the analyses are in general performed with the assumption that the mechanical system consist of one component. An incorrect assumption if autocorrelation exists. All of these factors have a significant effect on the probability of failure, and must be considered in a correct manner if the probability of failure should be determined accurately.

2.2.4 Limit states analyses with partial factors of safety

Limit states analyses with partial factors are usually referred to as a *level 1* method of reliability analyses (Melchers 1999). The reason for this is that the partial factors can be determined with higher orders of reliability methods, such as the first order second moment reliability method (FORM), described by Thoft-Christensen and Baker (1982). The method of partial coefficients implies that the calculated design value for the resistance, R^*, should not be smaller than the calculated design value for the load, S^*, according to equation 2.6:

$$R^* = \frac{R_k}{\gamma_R} = S_k \cdot \gamma_S \tag{2.6}$$

where R_k and S_k are characteristic values for the resistance and the load respectively and γ_R and γ_S are the corresponding partial coefficients. The theoretical relation for a variable X between its design value, X^*, the target safety index, β_t, the partial coefficient, γ_x, and the characteristic value, X_k, can be described according to equation 2.7, under the assumption that the variables in the problem are normal distributed and independent of each others.

$$X^* = \frac{X_k}{\gamma_X} = \mu_X + \alpha_X \cdot \beta_t \cdot \sigma_X \tag{2.7}$$

Where α_x is a sensitivity factor which describes the significance that the variable X has for the problem. μ_x is the mean value of the variable X and σ_x is its standard deviation. Studying the equation above, it can be seen that the quotient between the characteristic value and the partial coefficient should be a constant which depends on the required target safety index, the stochastic parameters of the variable and the sensitivity factor.

The target safety index, β_t, corresponds to a certain acceptable probability of failure. For example, the construction rules of the National Board of Housing, Building and Planning, BKR (Boverket 2003), states that the safety index should be; $\geq$3.7 for safety class 1; $\geq$4.3 for safety class 2; and $\geq$4.8 for safety class 3. These values correspond to a probability of failure of; 10^{-4} for safety class 1; 10^{-5} for safety class 2; and 10^{-6} for safety class 3.

Usually, two types of limit states are analysed in the design; the ultimate limit state (ULS); and the serviceability limit state (SLS). The ULS is related to failure or collapse of the structure. According to BKR (Boverket 2003), load bearing structures in the ULS should be designed so the safety against failure in the material, and against instability such as buckling and tilting etc., are adequately. It should be so during the construction of the structure, its lifetime, and in the event of fire. An advice in BKR is also to consider that deformations in the foundation can give rise to failure or instability. Furthermore, the structure should be designed with an adequate safety against overturning, uplift, and sliding. The structure should also be designed in such a way that the risk against progressive failure is insignificant. The SLS is related to normal use and function. BKR (Boverket 2003) states that the structure in SLS should be designed so that deformation, cracking and vibration do not have an injurious effect on its function or harm other parts of the structure. For stability analyses, only the ULS is normally considered.

The most important advantage with partial factors is that it leads to factors which reflect the uncertainty they embody (ICOLD 1993). However, even if limit state analyses with partial factors account for different sources of uncertainty, the use of them does not mean that the design automatically is acceptable. Limit state analyses with partial factors lack an objective quantitative assessment on the impact of the approximations inherent in the mechanical model, and also from human factors. These limitations can explain why the concept with a total factor of safety is still in use (ICOLD 1993). Also, which Mortensen (1983) points out, for less conventional constructions, full consideration must be given to the effect of the partial coefficient system in every single case, and to establish more or less fixed partial factors would appear to be an attempt to kill judgements.

For large structures, such as concrete gravity dams, each structure and foundation is unique. This means that partial factors would have to be calculated for each structure. It is therefore questionable as Mortensen discuss, if analyses with fixed partial factors are suitable for these types of structures.

2.2.5 Acceptance requirements

When the calculated safety has been determined, it must be decided whether it is acceptable or not. In order to provide an aid for this decision, acceptance requirements or acceptance criteria exist. They are associated with the acceptable risk of the structure. Risk is usually defined as the product of probability and consequence. In general, this means that three components are necessary to make a correct decision in stability analyses; an acceptable risk; the probability of failure; and the consequences if failure occurs.

Two methods are described by Melchers (1999), by which acceptance requirements can be founded on. The first method is to compare the calculated probability of failure with other risks in society, and by doing so infer acceptable risk for structures from these risks. In Figure 2.4, some risks associated with engineering projects in the society are presented.

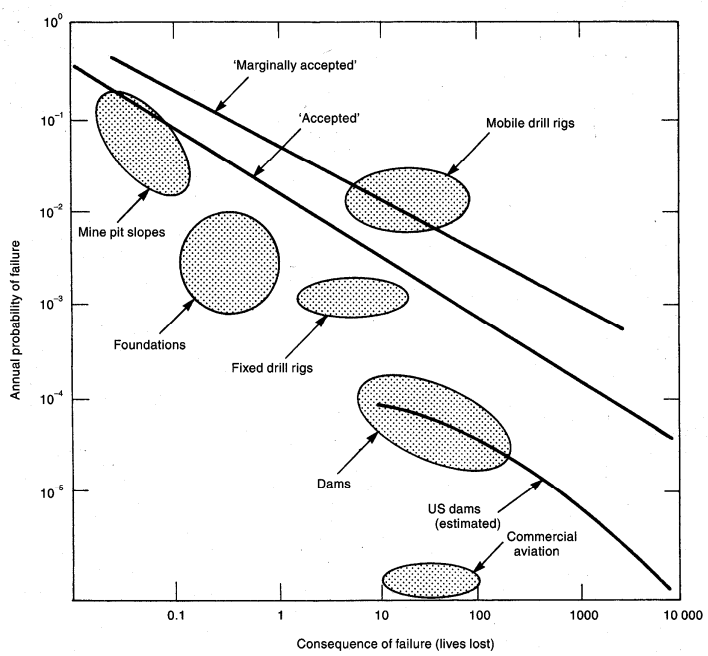

Figure 2.4 Risks associated with some engineering projects (From Wyllie 1999 after Whitman 1984).

The other is a socio-economic one, where a cost-benefit-risk analysis is used to assess the acceptable or most socio-economic probability of failure. This requirement is given by equation 2.8.

$$\max(B - C_T) = \max(B - C_I - C_{QA} - C_C - C_{INS} - C_M - p_f C_F) \qquad (2.8)$$

where B is the total benefit of the project, C_T is the total cost of the project, C_I is the initial cost of the project, C_{QA} is the cost of quality assurance measures, C_C is the cost of corrective actions in response to quality assurance measures, C_{INS} is the cost of insurance, C_M is the cost of maintenance, p_f is the probability of failure for the project, C_F is the cost associated with failure. The principle is illustrated in Figure 2.5.

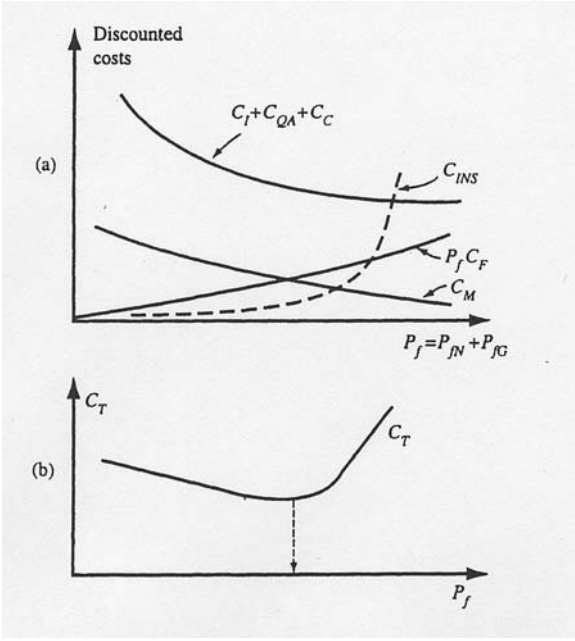

Figure 2.5 (a) Component costs and (b) total costs as a function of p_f (After Melchers 1999).

If a high safety is necessary due to severe consequences, the probability of failure must be small. Dams are an example of such types of structures, which falls into this category. This also means that the uncertainties in the stability analyses should be kept low. However, stability analyses of foundations on rock usually are associated with a substantial amount of uncertainty. The uncertainties in reliability assessment can be divided into the following components (Melchers 1999); phenomenological; decision; modelling; prediction; physical; statistical; and human factors. Many of these uncertainties are difficult to consider when the calculated safety is determined. Human factors such as gross error or intervention are hard to estimate. Also, in most of the cases, the statistical uncertainty is large due to a limited number of tests. Furthermore, if new types of construction techniques are used, the phenomenological uncertainty may be large. Several of these are omitted or only approximated. As a consequence, the calculated safety becomes a nominal one. The exact safety is probably not possible to determine in the stability analyses. Therefore, the acceptance requirements to a large extent are based on earlier experience and nominal safety of the same type of structures.

Mortensen (1983) means that factors of safety in geotechnical and foundation engineering to some extent are correction factors, and that the best way of determining acceptance requirements is by a combination of experience and back analysis of successful foundation constructions. An acceptance requirement based only on theoretical considerations implies a risk of losing extensive practical experience. He also means that, at least under Danish conditions, all foundation failures are a consequence of not considering the correct failure mode in the analysis. An increase in safety in these cases cannot be achieved by minor adjustment of the factors of safety, but must instead be achieved by more detailed geotechnical investigations, carrying out geotechnical calculations taking into account the critical factors, and by performing thorough control studies, measurements, and observations.

2.3 Methods of sliding stability analyses

Two different types of sliding failure in rock joints can be distinguished for foundations, plane sliding and wedge sliding. In this section, different analytical methods to assess plane sliding will be presented. The principle for wedge sliding are in many ways similar to plane sliding, with the exception that the geometry of the wedge makes it a three dimensional problem which is more complicated to solve analytically. For an account of the methods regarding wedge sliding, see for example John (1968), Londe et al. (1969) and Hoek and Bray (1981).

Before the 1900's, the only stability criterion for dams was that the resultant should fall in the middle third of the foundation cross-section in order to prevent overturning. At the end of the 1800's it was recognized that dam failures often occurred due to a downstream movement, without overturning. An awareness of sliding failure, and the significance of the uplift load, was developed. Stability analyses which accounted for those factors was started to be used at the beginning of the 1900's (Nicholson 1983). Thereafter, three different methods have been developed to assess the safety against plane sliding. These are *the sliding resistance method*, *the shear friction method* and *the limit equilibrium method*.

2.3.1 The sliding resistance method

The first criterion to assess the safety against sliding was the *sliding resistance method*, which calculated a coefficient of friction, μ. This coefficient was calculated by dividing the sum of the forces parallel the sliding plane, ΣH, by the sum of the effective vertical forces normal to the sliding plane, $\Sigma V'$. This calculated coefficient of friction, μ, should be smaller than an allowable coefficient of friction, μ_{all}, according to equation 2.9.

$$\mu = \frac{\sum H}{\sum V'} \leq \mu_{all} \tag{2.9}$$

In the USA, this method was used between the 1900's and the 1930's according to the US Army Corps of Engineers (1981). Furthermore, USACE writes that "*Experience of the early dam designers had shown that the shearing resistance of very competent foundation material needs not to be investigated if the ratio of horizontal forces to vertical forces (ΣH/ΣV) is such that a reasonable safety factor against sliding results*". In other words, this method was a control against sliding based on experience, both for the foundation material, and for the interface between the foundation and the concrete.

2.3.2 The shear friction method

The shear friction method was first published by Henna 1933 (Nicholson 1983). Henna introduced an equation to calculate the factor of safety against sliding for concrete dams based on the Coulomb equation, see equation 2.10.

$$FS = \frac{s1 + k \cdot (W - u)}{P} \tag{2.10}$$

In equation 2.10, *s1* was described as the shearing resistance without normal load, *k* as a factor for the increase of the shearing resistance, *W* was the dead weight of the structure, and *u* was the uplift load under the dam. *P* was the total load from water pressure perpendicular to the expected sliding direction. Today, the shear friction method usually has the form according to equation 2.11.

$$FS = \frac{c \cdot A + \sum V' \tan \phi}{\sum H} \tag{2.11}$$

Where c is the cohesion of the sliding plane, ϕ is its friction angle, and V' is the effective vertical load normal to the sliding plane. The simplest form of sliding failure for a dam on a rock foundation is with a horizontal joint in the rock mass which day-light downstream the dam. Analyzing it with the shear friction method, a 1 m wide strip of the foundation is usually assumed. This failure mode was described by Underwood and Dixon (1976), and is presented in Figure 2.6.

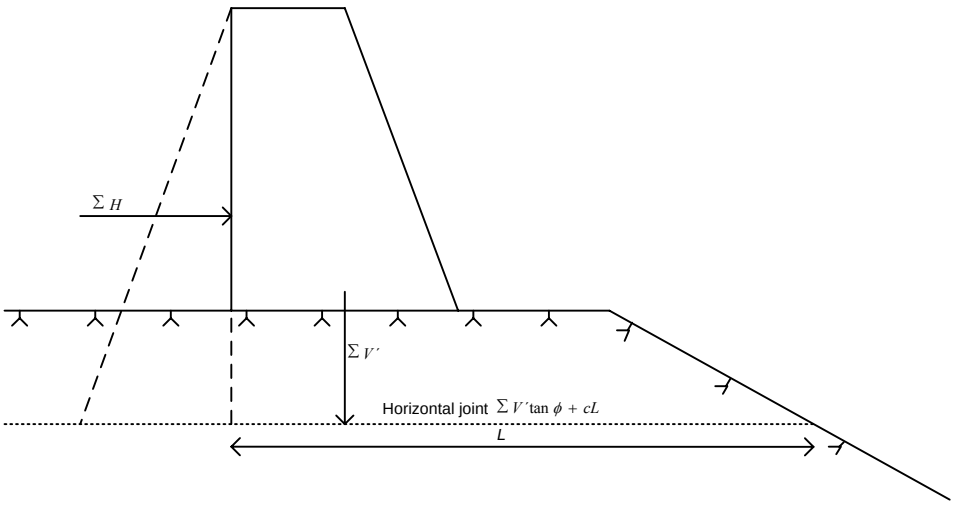

Figure 2.6 Plane sliding along a horizontal joint which day-light downstream the dam (After Underwood and Dixon 1976).

Since a one meter wide strip is assumed, equation 2.11 becomes:

$$FS = \frac{c \cdot L + \sum V' \tan \phi}{\sum H} \tag{2.12}$$

where L is the length of the considered sliding plane. Equation 2.11 and 2.12 are frequently used for assessing sliding stability, and originates from equation 2.10. According to Nicholson (1983), the basic assumptions necessary for this method are that the definition of the factor of safety is correct, that two-dimensional analysis is applicable, and that the analyzed mode of failure is kinematically possible. When equation 2.12 is used, Underwood and Dixon (1976) point out that if the calculation is done after deformations have occurred in the joint, the residual shear strength may has to be considered and the cohesion may be absent.

For low confining pressures, the apparent cohesion in joints is small. In addition to this, the uncertainties regarding it are large. It is therefore common to exclude the cohesion in the calculations. Excluding cohesion reduces equation 2.12 to:

$$FS = \frac{\sum V' \tan \phi}{\sum H} \tag{2.13}$$

However, equations 2.11 to 2.13 are only valid for plane joints which day-light downstream the dam, and these cases are rare for rock foundations. Underwood and Dixon (1976) also give another example where the horizontal joint ends in the rock mass according to Figure 2.7.

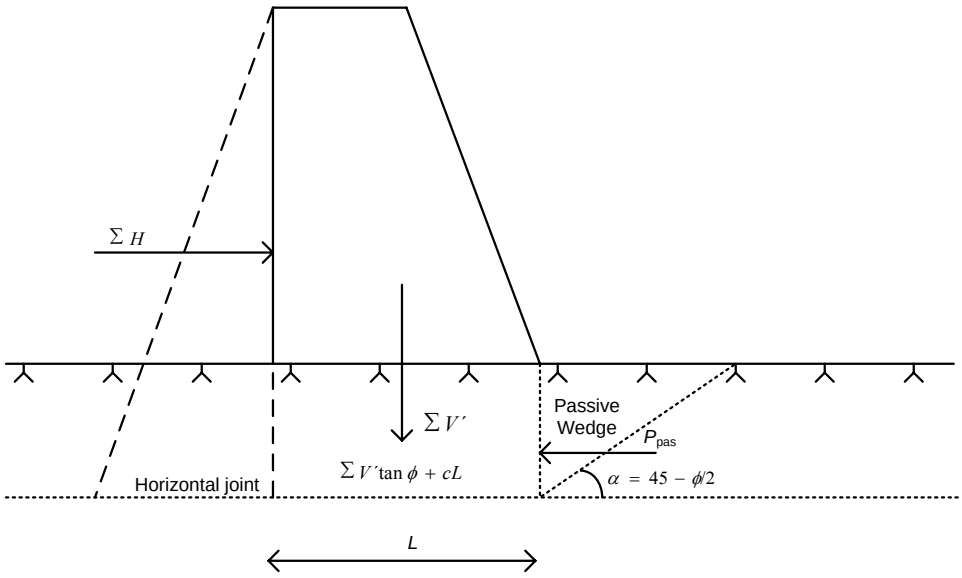

Figure 2.7 Plane sliding along a horizontal joint ending in the rock mass plus passive wedge resistance (After Underwood and Dixon 1976).

In this case, the failure plane will consist of sliding along the horizontal joint plus a passive wedge. The factor of safety calculated with the shear friction method in this case can be expressed as:

$$FS = \frac{\sum V' \cdot \tan \phi + c \cdot L + P_{\text{pas}}}{\sum H} \tag{2.14}$$

where P_{pas} is the passive rock wedge resistance. The same limitations that are valid for sliding along a joint day lighting downstream the dam are also valid here, i.e. cohesion may be absent after movement and friction angle may be residual. Furthermore, the vertical shear stress between the dam wedge and the passive wedge is neglected.

In addition to these limitations, there exists another limitation with this model. To develop full passive resistance in the passive wedge, a larger deformation in the rock mass is usually necessary than the deformation necessary to obtain peak shear strength in the joint under the dam. Therefore, according to Underwood and Dixon (1976), the passive resistance and the shear strength in the joint may not be additive.

In the examples above, the joints were horizontal. However, most joints in the rock mass are inclined. An inclined joint could be evaluated according to the same principles as shown above in equation 2.14. Nicholson (1983) described the following equations for an inclined sliding plane combined with a passive wedge. The failure mode is illustrated in Figure 2.8, and the definition of the factor of safety is presented in equation 2.15.

$$FS = \frac{R + P_{pas}}{\sum H} \tag{2.15}$$

Where R is the maximum horizontal force which can be resisted by the sliding plane beneath the dam wedge, P_{pas} is the maximum passive horizontal resistance by the rock wedge, and ΣH is the sum of the horizontal loads.

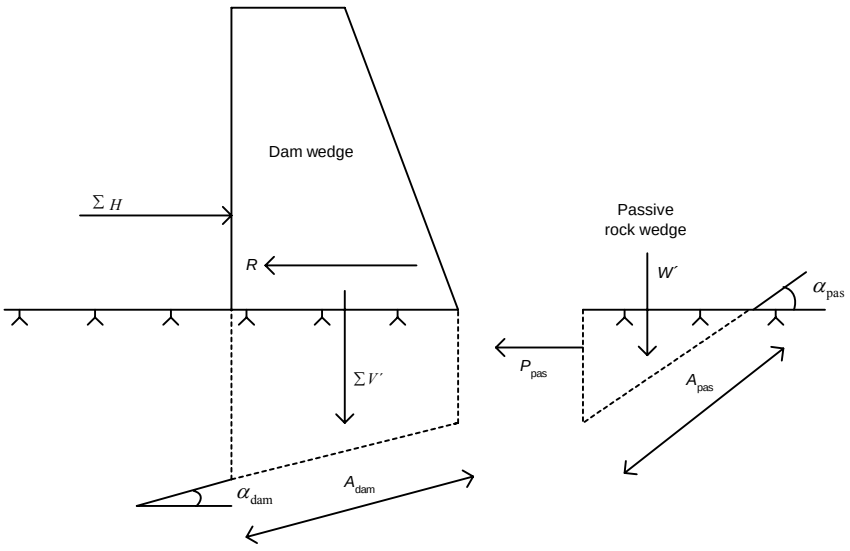

Figure 2.8 Forces acting on a hypothetical dam with inclined sliding plans according to the shear friction method (After Nicholson 1983).

For up-slope sliding, the following mathematical expressions were derived by Nicholson (1983) from static equilibrium:

$$R = \sum V' \cdot \tan(\phi + \alpha_{dam}) + \frac{c_{dam} \cdot A_{dam}}{\cos\alpha_{dam} \cdot (1 - \tan\phi \cdot \tan\alpha_{dam})} \quad (2.16)$$

And for down-slope sliding:

$$R = \sum V' \cdot \tan(\phi - \alpha_{dam}) + \frac{c_{dam} \cdot A_{dam}}{\cos\alpha_{dam} \cdot (1 + \tan\phi \cdot \tan\alpha_{dam})} \quad (2.17)$$

The passive resistance was expressed as:

$$P_{pas} = W' \cdot \tan(\phi + \alpha_{pas}) + \frac{c_{pas} \cdot A_{pas}}{\cos\alpha_{pas} \cdot (1 - \tan\phi \cdot \tan\alpha_{pas})} \quad (2.18)$$

In the three equations above, $\Sigma V'$ is the sum of vertical forces including the reduction from uplift forces, ϕ is the friction angle for the sliding plane, α is the angle for the inclined failure plane against the horizontal, c is the cohesion for the sliding plane, A is the area of the potential failure plane, and W' is the effective weight of the passive rock wedge, plus any superimposed loads. Subscripts *dam* and *pas* stands for dam wedge and passive wedge respectively.

In addition to the limitations described earlier, Nicholson (1983) described three more limitations associated with equation 2.16-2.18 and the shear friction method. The first limitations are due to the mathematics needed to solve R and P_{pas}. It can be seen that the factor of safety approaches infinity as the expression ($\phi \pm \alpha$) reaches 90°. The probability for this phenomenon is largest for the passive wedge, since the angle of inclination is more likely to be defined by relatively steeply dipping joints. The second limitation originates from the passive wedge force component. It is independent on the forces acting on the structure. Therefore, when the structure and the passive wedge are considered as a single block, it is not in static equilibrium except when the *FS* is unity. And finally, the application of the shear friction equations 2.15-2.18 is limited to failure modes along one or two planes only.

2.3.3 The limit equilibrium method

The third method to assess the safety against sliding is by *the limit equilibrium method*. The previous examples were based on the shear friction method, which means that the factor of safety is defined as resisting shear strength divided by the horizontal load. With the limit equilibrium method, the factor of safety against sliding is defined according to equation 2.19.

$$FS = \frac{\tau_f}{\tau} \quad (2.19)$$

In the equation above, τ_f is the available shear stress at failure and τ is the shear stress required for equilibrium. This way to define the factor of safety is also

referred to as the limit equilibrium method, and can be thought of as the degree of shear stress mobilized (Nicholson 1983).

According to Nicholson (1983), the basic assumptions required to develop the stability equations for the limit equilibrium method are as follows:

1. The factor of safety is defined according to equation 2.19.
2. Impending failure occurs according to the requirements imposed by perfectly-plastic failure theory.
3. The maximum shear strength that can be mobilized is adequately defined by the Mohr-Coulomb failure criteria.
4. Failure modes can be represented by two-dimensional, kinematically possible planes.
5. The factor of safety computed from the stability equations is the average factor of safety for the total potential failure surface.
6. The vertical forces between wedges are assumed to be negligible.
7. The structural wedge must be defined by one wedge.

The limit equilibrium method can be used when sliding occurs along a failure-plane of several joints, i.e. non-plane sliding, as well as for plane sliding. For non-plane sliding, the rock mass above the sliding plane is divided into several structural blocks. This method is often referred to as multiple wedge analyses. It is only two dimensional, and should not be mixed up with the three dimensional wedge stability.

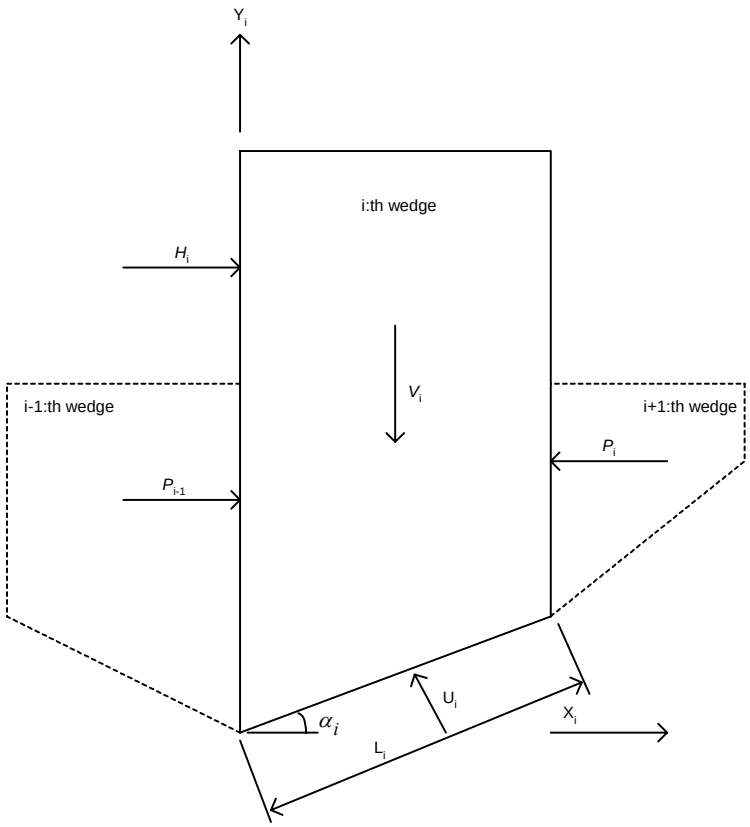

Figure 2.9 Geometry, forces, and coordinate system for an i:th wedge in a hypothetical wedge system (After Nicholson 1983).

When the factor of safety for a multiple system of *n* number of wedges with forces and angles according to Figure 2.9 is derived, it will result in *n+1* unknowns. The factor of safety should be equal for all wedges. This assumption produces *n* equations.

$$FS = FS_1 = FS_2 = ... = FS_n \tag{2.20}$$

The final equation for the solution comes from an additional equation which assumes horizontal equilibrium:

$$\sum_{i=1}^{i=n}\left(P_{i-1} - P_i\right) = 0 \tag{2.21}$$

where P_i is the resultant horizontal force acting on a vertical face of a typical wedge *i*. Based on the equations 2.20 and 2.21, the factor of safety can be calculated for the system of wedges according to equation 2.22 (Nicholson 1983).

$$FS = \frac{\sum_{i=1}^{i=n} \frac{c_i \cdot A_i \cdot \cos\alpha_i + (V_i - U_i \cdot \cos\alpha_i) \cdot \tan\phi_i}{n_{\alpha i}}}{\sum_{i=1}^{i=n} (H_i - V_i \cdot \tan\alpha_i)} \tag{2.22}$$

Where V_i is the total vertical force acting on the sliding surface for wedge *i*, *U* is the uplift force on the sliding surface for wedge *i*, and A_i is the area of the sliding surface for wedge *i*. α_i is the angle of the sliding surface for wedge *i* with respect to the horizontal, negative for down-slope sliding and positive for up-slope sliding. H_i is the total external horizontal force acting on the wedge. The factor $n_{\alpha i}$ can be determined with equation 2.23 below.

$$n_{\alpha i} = \frac{1 - \frac{\tan\phi_i \cdot \tan\alpha_i}{SF}}{1 + \tan^2\alpha_i} \tag{2.23}$$

This type of analyze was one among many other techniques that was used to assess the stability of the Three Gorges dam foundation (Liu et al. 2003). At the Three Gorges dam foundation there was one special problem. The joints along the expected sliding path were not persistent, i.e. there existed several “rock bridges” between the joints. To solve this problem, the friction angle and the cohesion were expressed as weighted values of the joints and the bridges of intact rock along the potential sliding surface of the wedges in the calculation.

Since the definition of the factor of safety is expressed differently in the shear friction method and the limit equilibrium method, it results, in most of the cases, in different factors of safety in the calculations. Nicholson (1983) performed a thorough comparison between the two methods. In the guidance given by the U.S. Army, the minimum acceptable factor of safety is 2.0 for the limit equilibrium method, while a factor of safety of 4.0 is the requirement for the shear friction method. Nicholson writes that:

”*This does not necessarily imply that the overall factor of safety has been reduced by 50 percent. As a general rule, for a given structure with an inclined potential failure surface the limit equilibrium method and shear friction methods will result in a different and unique factor of safety. The magnitude of the difference is dependent on the geometry of the problem, loading conditions, and resisting shear strength parameters”*.

This difference in factor of safety between the two methods clearly shows one of the difficulties in expressing the safety for a structure with a single factor of safety. The calculated safety is a nominal safety, and the assumptions that the calculations are based upon, including the definition of the safety factor, must be taken into consideration.

2.4 Laws, regulatory rules and guidelines

In Sweden, the law about technical property demands on constructional work, BVL, and the regulation about technical property demands on constructional work BVF, contain the statues regarding bearing capacity, stability, and durability. Design according to the construction rules of the National Board of Housing, Building, and Planning, BKR (Boverket 2003), makes sure that these laws and statues are obeyed. According to the plan and building law, PBL, it is the owner’s responsibility to see that these demands are fulfilled.

Chapter four in BKR contains construction rules for geotechnical structures, but those are primarily for earth structures. However, BKR are not valid for all types of structures. One example is that the National Road Administration has the right to announce regulations regarding roads and facilities that belongs to the road or street. For bridges, the National Road Administration has issued the Swedish bridge design code, Bro 2004 (Vägverket 2004). Another example is Swedish dams, which are not covered by the BKR. For dams, the owner has a strict responsibility in the event of failure or any other accident. As a consequence, the Swedish power companies, through the organisation Swedenergy, have issued the Swedish power companies guidelines for dam safety, RIDAS (Svensk Energi 2008).

In 2006, the transitional period started for the Eurocode regarding geotechnical structures, EN 1997-1. It will be going on until 2009, and after that replace BKR.

Since this study concerns concrete dams founded on rock, a study was performed based on the Swedish power company’s guidelines for dam safety, RIDAS. Furthermore, regulations and guidelines for concrete dams in Finland, Norway, Canada and USA, with conditions similar to Sweden, were studied. Since BKR will be replaced by Eurocode in 2009, it was also incorporated in the study.

2.4.1 The Swedish guidelines for dam safety, RIDAS

In Sweden, concrete gravity dams and buttress dams are designed according to RIDAS, the Swedish power companies' guidelines for dam safety (Svensk Energi 2008). They are based on normal practice in the design of dams, and are valid for both new and existing ones. No difference is made in the guidelines between ordinary concrete gravity dams or buttress dams. The guidelines are not valid for arch dams, since only a few of these structures exists in Sweden. Furthermore, their structural behaviour is different from conventional gravity or buttress dams.

According to the guidelines, it is recommended that the stability of concrete dams is assessed for several different load combinations. These are divided into normal, exceptional, and accidental load cases. For these load cases, the dam has to be checked against the following:

- Overturning.
- Sliding.
- Concrete or foundation strength not exceeded.

Regarding sliding, the Swedish guidelines recommend that the risk is assessed for the interface between the dam and the foundation, as well as for weakness planes within the foundation.

For dams founded on rock, RIDAS recommend the use of the sliding resistance method, see equation 2.9. For dams founded on rock of good quality, the values in Table 2.1 can be used as allowable coefficients of friction, where the failure value, $\tan\phi=1$, corresponds to a friction angle of 45^{o}.

Table 2.1 Recommended coefficients of friction according to RIDAS for dams founded on rock of good quality.

Foundation type	Normal load case	Exceptional load case	Accidental load case	Failure value for tan ϕ
Rock	0.75	0.90	0.95	1.0

If the dam is founded on rock, which can not be considered to be of good quality, the failure value of $\tan\phi$ should be determined with investigations of the rock mass. The failure value obtained from tests should thereafter be reduced with a factor of safety, *FS,* in order to obtain an allowable coefficient of friction. In RIDAS, the following values for the factor of safety are recommended.

Table 2.2 Factors of safety according to RIDAS for reduction of the failure value of tanϕ.

Foundation type	Normal load case	Exceptional load case	Accidental load case
Rock	1.35	1.10	1.05

The text in the guidelines does not say anything about the origin of the value for the failure coefficient of friction, or what its definition of a good rock mass is. In an attempt to answer these questions, common practice in Sweden, before the implementation of RIDAS, was studied.

The guidelines in RIDAS for concrete dams are in a great extent based upon a document issued by Vattenfall (1996). However, this document does not contain any supplementary information.

According to Reinius (1973), the coefficient of friction was usually given a maximum value of 0.75 for ordinary gravity dams, and a maximum value of 0.9 to 1.0 for buttress dams founded on a rock mass of good quality. Reinius also pointed out that for weak rock masses with horizontal seams etc., one must in every single case investigate which value of the coefficient of friction that can be allowed. He gave an example of the Possum Kingdom dam in USA. It was founded on clay slate with a horizontal stratification. After comprehensive tests, a value of $\tan\phi$=0.5 were chosen.

Vattenfall (1971) performed a literature study regarding allowable coefficient of frictions for concrete dams in Sweden and abroad. In this study, Vattenfall found that they were normally around 0.8. If small deformations could be expected, the allowable coefficient of friction could be 0.9.

Based on these references, it appears that the coefficient of friction in RIDAS probably is based on experience gained under decades of construction. The stability assessments were based on investigations of the rock mass. If no weakness planes were found, the allowable coefficient of friction, μ_{all}=0.75, were interpreted as a control against both sliding in the foundation and sliding in the interface between dam and foundation. If persistent weakness planes were found, the coefficient of friction for this plane was evaluated separately.

2.4.2 Guidelines used in other countries

In order to identify how sliding stability of concrete dams is assessed in other countries, guidelines and requirements regarding sliding have been studied in Norway, Finland, Canada, and USA. The basic stability requirements are similar to those in RIDAS. However, there exist differences between them. These are described shortly below.

In other countries such as USA, Canada, and Norway among others, the shear friction method with a factor of safety is the method that is recommended to assess the safety against sliding. In those guidelines, two lines in the selection of factors of safety can be distinguish, which mainly depends on if cohesion is accounted for or not.

According to the Federal Energy Regulatory Commission (FERC 2002) in the USA, the factors of safety in Table 2.3 are recommended for concrete gravity dams. In those guidelines, dams with high or low risks are separated.

Table 2.3 Minimum recommended factors of safety against sliding (FERC 2002).

Load case	Dams with high risk Factor of safety*)	Dams with low risk Factor of safety*)
Usual	3.0	2.0
Unusual	2.0	1.25
Post earthquake	1.3	>1.0

*) Factors of safety apply to the calculation of stress and the shear friction factor of safety within the structure, at the rock/concrete interface and in the foundation.

Furthermore, FERC (2002) recommend that if cohesion is not accounted for, the factors of safety in Table 2.4 can be used.

Table 2.4 Minimum recommended factors of safety if cohesion is not accounted for (FERC 2002).

Load case	Normal load case
Usual	1.5
Unusual	1.3
Post earthquake	1.3

According to the Canadian Dam Association, CDA (1999), the recommended factors of safety distinguish between if peak or residual strength is considered and also if investigations have been performed. Cohesion has also been limited to a maximum of 100 kPa. Factors of safety for gravity and buttress dams according to CDA guidelines are presented in Table 2.5.

Table 2.5 Sliding and strength factors for gravity and buttress dams (CDA 1999).

	Usual load case	Unusual load case (post- earthquake)	Earthquake	Flood
Peak Sliding Factor –No tests	3.0	2.0	1.3	2.0
Peak Sliding Factor –With tests*)	2.0	1.5	1.1	1.5
Residual Sliding Factor	1.5	1.1	1.0	1.3
Concrete strength factor	3.0	1.5	1.1	2.0

*) Adequate test data must be available through rigorous investigations carried out by qualified professionals.

The Norwegian "Retningslinje for betongdammer" (NVE 2002) enables the use of cohesion in the calculations, even though it is normally not included. The factors of safety presented in Table 2.6 are recommended.

Table 2.6 Factors of safety against sliding (NVE 2002).

	Normal load case	Accidental load case
With cohesion	3.0	2.0
Cohesion verified through tests	2.5	1.5
No cohesion	1.5	1.1

The Norwegian guidelines also say that a higher degree of safety should be used when sliding is assessed in the rock foundation. The factor of safety should be evaluated by a geologic engineer on the basis of local conditions and the extent of the chosen investigations.

The examples above show which factors that affect the recommended factors of safety. One important factor is the uncertainties regarding shear strength and how the parameters for it have been derived. Other factors are the consequences in case of a dam failure and the probability that a certain load case should occur.

2.4.3 Eurocode

The all-embracing document for structures is EN 1990 "Basis for structural Design". This standard, together with EN 1997-1 "Geotechnical design", are the ones that concerns large structures founded on rock. The Eurocode standard, EN 1990:2002, states that:

- Design for limit states shall be based on the use of structural and load models for relevant limit states.
- The safety requirements should be achieved by the partial factor method.
- As an alternative, a design directly based on probabilistic methods may be used.

According to Eurocode document EN 1997-1:2004, the limit states should be analyzed with any of the following methods:

- Use of calculations.
- Adoption of prescriptive measures.
- Experimental models and load tests.
- An observational method.

In EN 1997-1:2004, section 2.4.1 states that the design by calculation shall be in accordance with the fundamental requirements of EN 1990:2002. The calculation model may consist of any of the following:

- An analytical model.
- A semi empirical model.
- A numerical model.

Section 6.5 in EN 1997-1:2004 regards spread foundations in ultimate limit state. It addresses bearing resistance, sliding resistance, and structural failure due to foundation movement. To verify the sliding resistance, the criterion in equation 2.24 shall be satisfied.

$$H_d \leq R_d + R_{p;d} \tag{2.24}$$

Where H_d is the design value of the horizontal load, which shall include earth pressures acting above the foundation level. R_d is the design value of the sliding resistance and $R_{p;d}$ is the design value of the resisting force caused by passive earth pressure on the side of the foundation. Of special interest for foundation on rock is that the standard states that the values of R_d and $R_{p;d}$ should consider the relevance of post-peak behaviour.

2.5 Summary

The aim with this chapter was to describe the basic principles and current state of practice in sliding stability analyses. It focused on the fundamental principles of stability analyses and the analytical calculation methods, together with guidelines and regulations, used to assess the sliding stability. A summary of these sections are presented below.

All stability analyses are based on the criterion that the resistance, R, should be equal to, or larger than, the load, S. In general, it is assumed that R and S are deterministic values, which are independent of deformation. For foundations on rock, it is important to keep this assumption in mind since the resistance for rock masses is difficult to predict due to uncertainties. As a consequence, the resistance is better described with a probability distribution rather than a deterministic value. Furthermore, both the load and the resistance can vary significantly with deformation, depending on the stiffness of the foundation. It is important to keep this limitation in mind. In some cases, it could be better to relate R and S to deformation since it is easier to measure.

Stability analyses are to a large extent a question of finding the right balance between the load, the resistance, the uncertainties, and the consequences of a failure. To find this balance, an expression for the calculated safety together with an acceptance requirement is normally used. None of the methods for calculating safety can express the true or real safety. The calculated safety is nominal. As a consequence, acceptance requirements are usually determined by a combination of experience and back analysis. Even if the true safety probably can not be calculated exactly, it is preferable to use methods which reflect the uncertainties in the problem. It gives a better understanding of the problem and significant parameters can be identified. The probability of failure has the best potential to fulfil these demands.

In order to determine the calculated safety, analytical methods are generally used. In these methods, the rock mass is assumed to be perfectly plastic. The maximum shear strength that can be mobilized is usually defined by the Mohr-Coulomb failure criterion. Furthermore, the analytical methods assume that load and resistance is constant and independent of deformation. Also, with these methods the calculated factor of safety is the average factor of safety for the total potential failure plane.

To analyze the sliding stability, one of the following three methods is generally used; *the sliding resistance method*; *the shear friction method*; and *the limit equilibrium method*. The difference between them is how the factor of safety is defined. All of these methods results in different factors of safety, for the same problem, if both cohesion and friction exists. Normally, cohesion is not accounted for since the uncertainties regarding it are large. If large deformations are expected, the residual strength should be considered. When the resistance from a passive wedge is included in the total resistance, it may not be added to the resistance from the structural wedge, since the peak shear strength for the two wedges occur at different deformations.

In Sweden, the construction of dams is governed by the Swedish power company's guidelines for dam safety, RIDAS. If RIDAS is compared to guidelines and regulations in other countries, it can be seen that for sliding, the safety factors are somewhat low (1.35 instead of 1.5). On the other hand, the coefficient of friction at failure in RIDAS might be a bit conservative. In RIDAS, values on the coefficient of friction are based on experience. No consideration is taken for how the values of the parameters for shear strength are determined, through rigorous investigations or by experience. Furthermore, the coefficient of friction recommended in RIDAS is in general used as a control against sliding in both the interface between rock and concrete as well as for joints in the rock foundation. Different types of failure modes are not evaluated separately. Also, when the factor of safety is recommended in RIDAS, no consideration is taken to the difference between high hazard dams and low hazard dams.

Due to the limitations with the current guidelines, suggestions for new future guidelines were proposed by Gustafsson et al. (2008). These guidelines were also tested for the concrete dam at Laxede hydropower station in the northern part of Sweden (Gustafsson et al. 2009). The main difference to the current guidelines is that several potential failure modes must be analysed and that cohesion are allowed for low hazard dams.

Today, the safety against sliding failure for concrete dams founded on rock in general is verified with the factor of safety. However, in 2009 Eurocode will replace BKR. Therefore, the natural way for the development of RIDAS would be in a direction towards Eurocode, which means towards using limit states analyses with partial factors, or a design directly based on probabilistic methods. Regarding concrete dams, the latter is recommended before the former, mainly because each concrete dam and its foundation in many ways is a unique structure. In order to assign fixed partial factors, they would have to be large to cover all possible design situations. This may lead to a design which is too conservative.

3 LITERATURE STUDY: SHEAR STRENGTH OF UNFILLED AND ROUGH JOINTS

3.1 Introduction

When the safety against sliding failure is analysed for concrete dams founded on rock where horizontal joints are present; a key parameter is the shear strength of the joints. However, the shear strength is affected by several parameters, which makes it uncertain to predict. Parameters such as the normal stress, the uniaxial compressive strength of the joint surfaces, the surface roughness, weathering of the surfaces and possible infilling material affect the shear strength. However, the influence on the shear strength from these parameters is normally studied by performing small scale laboratory shear tests.

Unfortunately, the shear strength for rough unfilled joints could also be affected by scale; see for example Bandis (1980) and Yoshinaka et al. (1993). It is believed that the surface roughness, together with the compressive strength of the joint surface, may have an impact on the scale effect (Barton and Bandis 1982). This scale effect can not be studied in laboratory only. Instead, it must be studied by performing large scale tests *in situ*. Even these large scale tests have limitations since they are usually performed on blocks smaller than 1 by 1 m. For example, ISRM (1981) suggested that *in situ* shear test should have a dimension of 0.7 by 0.7 m.

Other parameters which may also affect the uncertainty of the shear strength are few samples and the variation in strength between different samples. However, this effect was not studied here.

To increase the understanding on how the peak shear strength for rough and unfilled joints can be predicted at laboratory and at full size scales, a literature study was performed. The study contains a review of available shear strength failure criteria for unfilled and rough joints, together with available expressions to account for scale.

3.2 Failure criteria

Before the 1960's, it was customary to describe the shear strength of joints with the linear Mohr-Coulomb failure criterion. The criterion is based on the work by Coulomb 1776 and Mohr 1882, and is described in most soil and rock mechanics textbooks. In its modern form the criterion can be expressed as:

$$\tau_f = c + \sigma'_n \cdot \tan\phi \qquad (3.1)$$

where τ_f is the shear stress at failure along the theoretical failure plane, c is the apparent cohesion of the plane, σ'_n is the effective normal stress acting on the failure plane and ϕ is the friction angle of the failure plane.

In the sixties it was recognized that the failure envelope was curved. One of the most important contributions was made by Patton (1966). He derived experimentally from "saw-tooth" specimens a bi-linear approximation of the curved failure envelope. Under low effective normal stresses the expression had the form:

$$\tau_f = \sigma'_n \cdot \tan(\phi_b + i) \tag{3.2}$$

where ϕ_b is the basic friction angle of a smooth but rough surface and i is the angle of the "saw-tooth" with respect to the direction of the applied shear stress. For the primary portion of the failure envelope, Patton observed that sliding occurred prior to shearing through the intact tooth. Over a certain level of normal stress, the effect of the asperities or "saw-tooth" disappeared due to failure through the asperities by shearing. When this happened, equation 3.2 was changed to:

$$\tau_f = c_x + \sigma'_n \cdot \tan(\phi_r) \tag{3.3}$$

where ϕ_r is the residual shearing resistance of an initially intact material and c_x is the cohesion when the teeth are sheared of at their base. The principle of the failure envelope is shown in Figure 3.1.

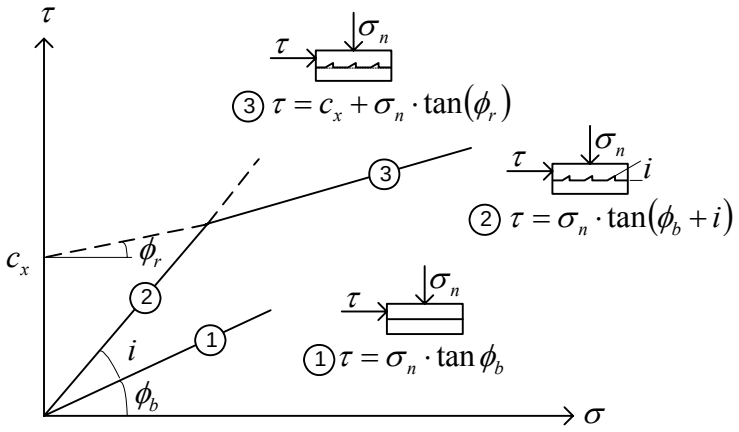

Figure 3.1 Bilinear failure envelope proposed by Patton (1966).

The region between the primary and secondary failure mode, Patton (1966) called the region of intermediate failure mode. In this region, the angle of the failure envelope changes from ϕ_b+i to ϕ_r. Patton (1966) described the discrepancy against the bilinear criterion in this region by saying that "*real failure envelopes for rock would not reflect simple change in the mode of failure but changes in the intensities of different modes of failures occurring simultaneously*".

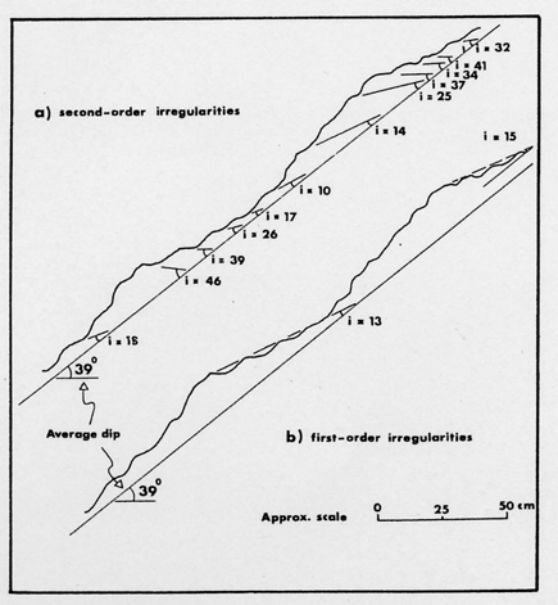

Figure 3.2 Inclination of asperities with respect to scale (From Barton 1973 after Patton 1966).

Patton also performed 247 field investigations of sandstone slopes and slopes of carbonate rocks. He classified the slopes into stable, unstable and failed slopes. In his field investigations, he gave particular attention to the inclination of the asperities for the joint on those slopes classified as unstable. However, he observed that the correction for the inclination of the asperities, *i*, was more difficult than anticipated. The inclination of *i* for small scale asperities, which he denoted second order irregularities (measured over a few centimetres), in some cases resulted in a friction angle for the joint which was negative. To account for this discrepancy he used another method, where he measured *i* for larger asperities, which he denoted first order irregularities (measured over a few decimetres). With this method he observed that measured *i* was usually considerably less than those obtained from the second order irregularities, se Figure 3.2. Based on the observation of instable slopes, Patton concluded that: "*for sandstone the effect of correcting for i was to lower the median 3^o, and for carbonate rocks the effect of correcting for i was to lower the median 5^o*". To verify that the correction for *i* was acceptable he compared the friction angle corrected for *i* from the slopes with laboratory shear test performed on macroscopically smooth but microscopically irregular wet surfaces. Values corrected for asperity inclination was 22^o to 31^o for sandstone and 25^o to 39^o for carbonate rock respectively. The results from laboratory shear test showed values for sandstone from 24.5^o to 33^o and for carbonate rock from 32.5^o to 36^o. Patton wrote that these changes in the median value were much less than anticipated when the study began.

A similar study was also performed by McMahon (1985), where the friction angle from eight rock slides was back-calculated. He concluded that the effective friction angle at failure could be estimated as the sum of the mean residual friction angle and the mean of the relatively large scale roughness angles. Best agreement with back-calculated friction angles were obtained if a dilation angle based on large scale asperities with a base length greater than 2% of the potential failure surface were used, together with measured residual friction angle from

laboratory tests. Measured large scale dilation angles varied in the different cases between one to nine degrees. The size of the rock slides ranged from 20 by 10 m up to 200 by 600 meters. Low dilation angles were mainly obtained in soft rock (σ_{ci}<20 MPa), while high dilation angles mainly were obtained in hard rocks (σ_{ci}>20 MPa).

According to Ladanyi and Archambault (1970), Pattons bilinear model is "*strictly valid for shearing along a regularly intended rock surface in which, at failure, the teeth have the same geometry and the degree of interlocking as at the beginning of loading in shear.*" They further stated that this rarely is the case in reality since a small displacement is necessary in order to mobilize friction along contact areas. Also, the stress distribution over the contact surfaces is non-uniform which results in that some of the teeth are usually partially broken before the maximum strength is reached. Furthermore, for irregular rock surfaces such as natural joints planes, both the average inclination angle, *i*, of the asperities at contact and the cohesion intercept are not easy to define.

In an attempt to solve these problems, Ladanyi and Archambault (1970) proposed a failure criterion where the total shear strength force, *S*, was expresses according to the following equation.

$$S = \left(S_1 + S_2 + S_3\right) \cdot \left(1 - a_s\right) + S_4 \cdot a_s \tag{3.4}$$

S_1 is a component due to external work done in dilation defined as:

$$S_1 = N \cdot \frac{\mathrm{dy}}{\mathrm{dx}} = N \cdot \dot{\upsilon} \tag{3.5}$$

In the equation above, *N* is the normal force on the surface, dy and dx is the increment in normal and shear displacement respectively, and $\dot{\upsilon}$ is the rate of dilation at failure.

S_2 is a component due to additional internal work in friction due to dilation, and is expressed as:

$$S_2 = S \cdot \dot{\upsilon} \cdot \tan \phi_{\mathrm{f}} \tag{3.6}$$

where $\dot{\upsilon}$ is the rate of dilation at failure. It should be observed that i=arctan ($\dot{\upsilon}$) represents a fictitious angle for irregular joint surfaces. For a regular saw toothed joint surface, *i* corresponds to the inclination of the teeth. ϕ_{f} were defined as the statistical average value of friction angle that is assessed when sliding occurs along the irregularities of different orientations.

S_3 is the component of friction for a flat, but rough, surface expressed according to the following equation.

$$S_3 = N \cdot \tan \phi_{\mathrm{u}} \tag{3.7}$$

Where ϕ_u were defined as the frictional resistance along the contact surfaces of the teeth. The shear area ratio for shearing through the asperities, a_s, was defined as:

$$a_s = \frac{A_s}{A} \tag{3.8}$$

where A_s is the portion of the asperities sheared off, and A is the total possible shear area. The contribution to the shear force from shearing through the asperities, S_4, was given by:

$$S_4 = A \cdot c_i + N \cdot \tan \phi_i \tag{3.9}$$

where c_i is the cohesion for the intact rock material and ϕ_i is the friction angle for the intact rock material. By substituting for S_1 to S_4 in equation 3.4, and accounting for the degree of interlocking, η, the shear strength was expressed as:

$$\tau = \frac{\sigma(1-a_s)(\dot{\upsilon} + \tan \phi_u) + a_s(\sigma \cdot \tan \phi_i + \eta \cdot c_i)}{1-(1-a_s)\cdot \dot{\upsilon} \cdot \tan \phi_f} \tag{3.10}$$

where the degree of interlocking, η, is defined as:

$$\eta = 1 - \frac{\Delta x}{\Delta L} \tag{3.11}$$

where Δx is the shear displacement and ΔL is the length of the asperities in the shear direction. How the interlocking is defined, together with results from the bilinear model and the proposed model, can be seen in Figure 3.3.

In equation 3.10, both $\dot{\upsilon}$ and a_s varies depending on the level of normal stress. Two extremes can occur. In the first case, when the normal stress is low, i.e. $\sigma \rightarrow 0$, the parameters $a_s \rightarrow 0$ and $\dot{\upsilon} \rightarrow \tan(i)$. In the other case, when the normal stress is high and approaches the transition pressure, $a_s \rightarrow 1$ and $\dot{\upsilon} \rightarrow 0$. However, determination of a_s and $\dot{\upsilon}$ are difficult to perform. A schematic presentation of basic assumptions, and how a_s and $\dot{\upsilon}$ were assumed to change with normal stress, can be seen in Figure 3.4.

Within the following interval of normal pressure, $0<\sigma_n<\sigma_T$, Ladanyi and Archambult proposed the following empirical expressions as a first approximation for the parameters a_s and $\dot{\upsilon}$.

$$a_s \approx 1 - \left(1 - \frac{\sigma_n}{\eta \sigma_T}\right)^{k1} \tag{3.12}$$

$$\dot{\upsilon} = \left(1 - \frac{\sigma_n}{\eta \sigma_T}\right)^{k2} \cdot \tan(i) \tag{3.13}$$

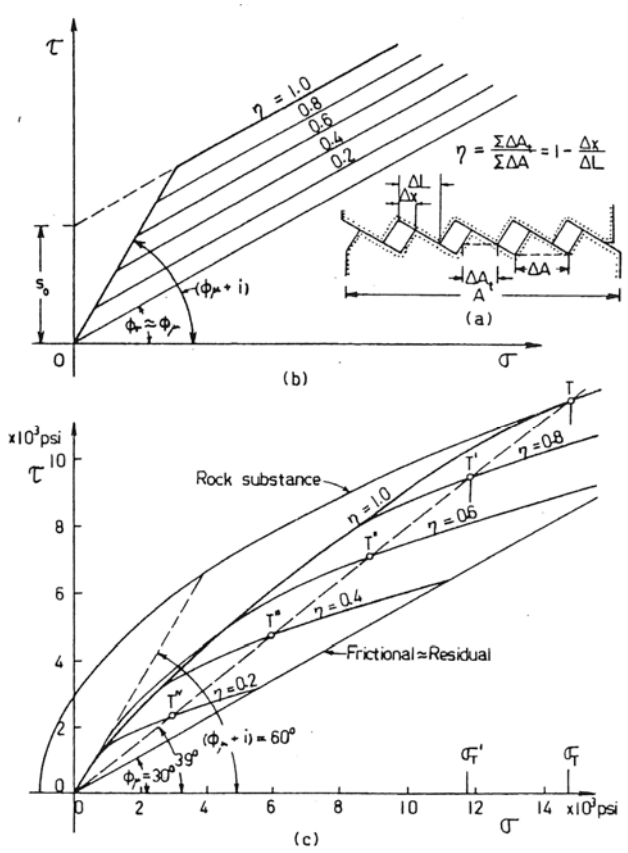

Figure 3.3 a) Definition of the degree of interlocking, η. b) Results according to the bilinear model. c) Results according to the proposed model (From Ladanyi and Archambault 1970).

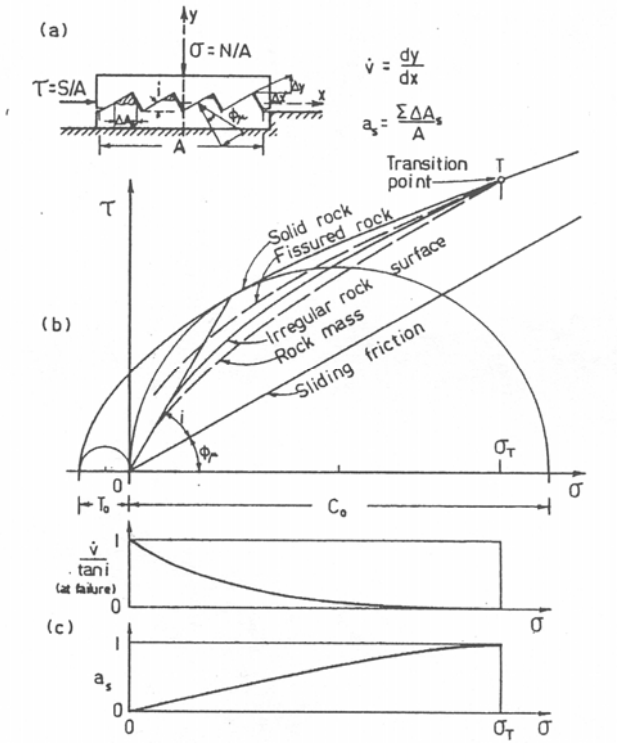

Figure 3.4 a) Definition of the dilation rate and the shear area ratio. b) Expected failure envelopes for irregular rock surfaces, and rock mass, respectively. c) Anticipated variation of dilation rate and shear area ratio with normal pressure. (From Ladanyi and Archambault 1970)

Where $k1$ and $k2$ are empirical constants, having values of about 3/2 and 4 respectively. However, Ladanyi and Archambault (1970) point out that these values were derived from a limited number of shear tests and are uncertain. In his work, no consideration to scale was taken.

A modified version of Ladanyi and Archambaults criterion (1970) was proposed by Saeb (1990). By studying the stress dilatancy theory of sand, two remarks were made on the original criterion. First, since no relocation of the rock particles occur he suggests that ϕ_u should be used instead of ϕ_f. Secondly, in the term S_2 he suggests that the total shear force, S, should be replaced by the total force required for sliding over the asperities, S_f. The result was a more simple form of the original criterion.

Barton (1973) and Barton and Choubey (1977) presented an empirical failure criterion with a curved failure envelope, which could be used to estimate the peak shear strength of joints. The criterion was based on extensive test results, and it included effects from the roughness of the joint and the compressive strength of the joint surface in relation to the applied effective normal stress. The criterion was expressed according to equation 3.14.

$$\tau_f = \sigma'_n \cdot \tan\left[JRC \log_{10}\left(\frac{JCS}{\sigma'_n}\right) + \phi_b \right] \qquad (3.14)$$

Where τ_f is the peak shear strength, σ'_n is the effective normal stress, *JRC* is the joint roughness coefficient, *JCS* is the joint wall compressive strength and ϕ_b is the basic friction angle measured from a saw-cut sample. If the joint was weathered or altered, Barton and Choubey (1977) suggested that the residual friction angle should be used instead of the basic friction angle.

According to Barton (1973), the *JCS* is equal to the unconfined compressive strength of the intact rock, σ_{ci}, if the discontinuity is unweathered. For weathered joint surfaces, the *JCS* should be reduced. The *JRC* represents a roughness scale which varies from 0 to 20, where 0 represents a completely smooth and plane surface, and 20 represents a very rough and undulating surface. In order to estimate the joint roughness coefficient, *JRC*, Barton and Choubey (1977) suggested two methods. The first method used predefined roughness profiles to determine *JRC*. However, the method is subjective and a correct profile can be difficult to predict from a three dimensional surface. Therefore, they suggested performing tilt test and back calculate the correct *JRC*.

A modification of Barton´s empirical *JRC-JCS* model was suggested by Zhao (1997 a, b) to account for degree of matedness. According to Zhao, the *JRC-JCS* model can overestimate the shear strength if the joint is unmated. He therefore suggests to incorporate a parameter denoted *JMC* (Joint Matching Coefficient), which ranged from zero to one representing the area of the joint surface in contact, i.e. zero for a maximal unmated joint and one for a perfectly mated joint.

Based on results from Pratt et al. (1972), which showed that the compressive strength of intact rock was scale dependent, Barton (1973) suggested that the *JCS* could be scale dependent.

The scale effect was further examined by Barton and Choubey (1977). In order to examine the scale effect they performed a tilt test on a 40 by 45 cm joint area. This block was thereafter sawn in 18 samples measuring 4.9 by 9.8 cm. These tests showed that measured difference between the large sample and the small samples could not be explained by a reduction of *JCS* alone. They therefore concluded that there must be a significant scale effect on *JRC*. They meant that the reason for the scale effect on *JCS* and *JRC* are related, at least qualitatively, since they appear to be in proportion to the joint length, up to some critical length. The explanation for this scale effect was that *"on a larger scale there are larger individual contact areas with correspondingly lower JCS values than those of the small steep asperities. The larger contact areas are themselves less steeply inclined in relation to the mean plane of the joint than the small steep asperities and therefore give correspondingly reduced JRC values"*.

Barton and Choubey (1977) also suggested that the scale effect might be reduced faster in a rock mass where the joint spacing and block size is small, since such a rock mass may not be stiff enough to mobilize the large scale asperities. As a consequence, they suggested performing tilt tests on blocks with sizes representative for the rock mass in order to account for a possible scale effect.

A systematic experimental study of scale effects for rough joints was also performed by Bandis et al. (1981), where they concluded that the peak shear strength is a strongly scale dependent property. They also observed that the shearing characteristics were altered significantly with increased scale. Peak shear strength could be taken equal to approximately 1% of the joint length and the behaviour changed from brittle to plastic with increased scale. Furthermore, they concluded that the average base length of critical asperities was about 4% of the joint length, and that maximum scale effects were associated with rough undulating joints, while minimum with almost smooth planar joints. They also performed tests on jointed models with different block sizes which indicated that block size may constitute a potential scale effect size limit. As a consequence, they recommend that estimates of *JRC* at larger scales should be performed on naturally occurring block sizes. If this is not possible, they proposed the following equation to estimate *JRC* at larger scales:

$$\frac{JRC_{naturalblock}}{JRC_{laboratory}} = \frac{\overline{a}^{o}_{naturalblock}}{\overline{a}^{o}_{laboratory}} \tag{3.15}$$

where $\overline{a}$ is the mean inclination angle for the asperities based on a 2% step-size of the specimen length.

Based on their previous data, Barton and Bandis (1982) developed the following equations to account for the scale effect:

$$JRC_{\mathrm{n}} = JRC_0\left(\frac{L_{\mathrm{n}}}{L_0}\right)^{-0.02JRC_0} \tag{3.16}$$

$$JCS_{\mathrm{n}} = JCS_0\left(\frac{L_{\mathrm{n}}}{L_0}\right)^{-0.03JRC_0} \tag{3.17}$$

where the subscripts (0) and (n) correspond to laboratory and *in situ* scale respectively. The length, L_{n}, is the length of the rock blocks along the joint being sheared, and L_0 is the length of the sample size.

The experimental results from Bandis et al. (1981), which showed that the block size affected the peak shear strength and mode of failure for jointed rock masses, was supported by Bhasin and Høeg (1997). They performed two dimensional numerical modelling of jointed rock masses with different block sizes with UDEC and obtained similar results as Bandis et al. (1981).

The argument of using the average block size as a definition of the *in situ* scale assumes that the blocks can rotate and arrange themselves in contact with the underlying joint surface. For a shallow joint under a concrete dam, this assumption is not obvious.

The blocks can to some degree be expected to be locked by the overlying structure. The rock mass between the dam and the shallow horizontal joint might therefore behave as a rigid body, which means that *in situ* scale becomes equal to the dimension of the overlying structure. In that case, *JRC* and *JCS* might be needed to be adjusted to the size of the overlying structure. However, the equations proposed by Barton and Bandis (1982) can not be used at these scales, especially for higher values of JRC_{o} .This limitation is illustrated in Figure 3.5, where it can be seen that the contribution to the friction angle from roughness decreases with rougher surfaces for large values on L_{n}.

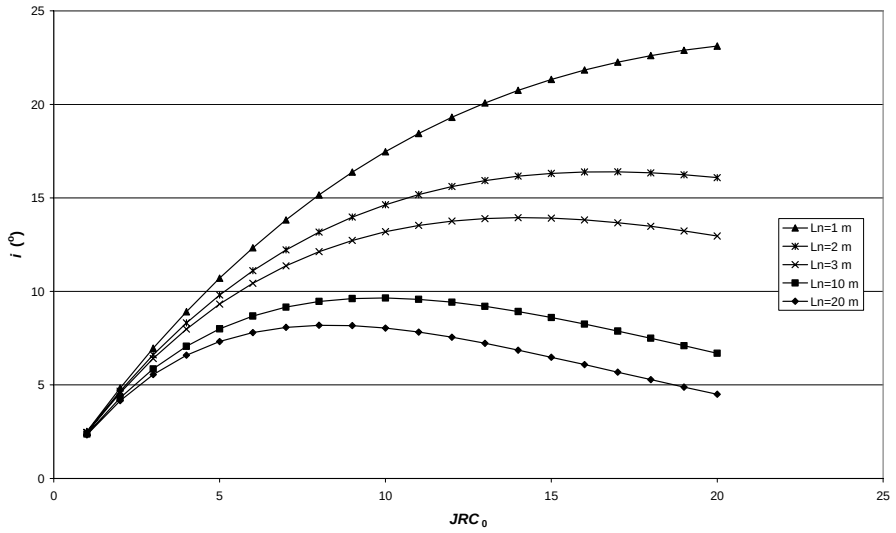

Figure 3.5 Estimated contributions to the friction angle from surface roughness with different JRC_o and at different scales using equations proposed by Barton and Bandis (1982).

It is also worth to comment that Bandis (1980) used casted joint replicas for his shear tests. In these replicas, he used a geometric scale factor to account for an increased scale. This means that material properties of the sample replicas were made weaker to scale them up from laboratory scale to *in situ* scale. An effect from this methodology, which also was pointed out by Bandis (1980), is that it may lead to an exaggerated surface geometry in relation to the length of the joint.

In order to investigate the scale effects found by Bandis et al. (1981), a testing program was performed and analysed by Hencher et al. (1993). It followed the same method as outlined by Bandis. The conclusions, among others, were that the basic friction angle had an extremely wide scatter and that the clearly defined scale effects observed by Bandis et al. (1981) were not confirmed. Furthermore, it was not confirmed that an asperity failure component is scale dependent. As a whole, they mean that "*The model material employed by Bandis and used in this study has severe limitations for accurately and consistently simulating shear behaviour of most rocks*".

Maksimovic (1992 and 1996) proposed a hyperbolic function to describe the angle of shearing resistance for rock joints. With the hyperbolic function, the peak shear strength was expressed as:

$$\tau_f = \sigma_n \tan\left(\phi_b + \Delta\phi / \left(1 + \sigma_n / p_n\right)\right) \tag{3.18}$$

where ϕ_b is the basic friction angle, $\Delta\phi$ is the joint roughness angle, or the angle of maximum dilatancy for an undamaged rugged surface, and p_n is the median angle pressure which is equal to the normal stress at which the contribution is equal to one half of $\Delta\phi$. Maksimovic (1996) meant that the proposed hyperbolic function is simple and can successively describe the non-linear failure envelope without involving logarithmic or power type expressions. The advantage is, according to Maksimovic (1996), that it gives a good approximation over all stress levels.

Papaliangas et al. (1995) proposed a criterion to estimate the peak shear strength for unfilled and rough joints. The criterion consisted of one friction component and one dilation component according to the equation below.

$$\tau_f = \sigma_n \cdot \tan(\phi_m + \psi) \tag{3.19}$$

The friction component, ϕ_m, was suggested by Papaliangas et al. (1995) to be an inherent property of the intact rock material and independent of normal stress. The values of ϕ_m therefore, according to Papaliangas et al. (1995), vary between different types of rock and are independent of scale.

The criterion was built on the assumption that deformation in the contact points occur at high pressures usually referred to as "*cataclastic flow*". In order to derive values of ϕ_m, the authors used the state of stress where a transition occurs from brittle to ductile behaviour for intact rock material. A stress state which is usually called the "*brittle ductile transition stress*", denoted σ_T. Using Fairhurst (1964)

parabolic criterion for intact rock, the shear stress, τ, for a normal stress, σ, was given by:

$$\tau = C_o \frac{\left(\sqrt{1+n}-1\right)}{n}\sqrt{\left(1+n\frac{\sigma_n}{C_o}\right)} \qquad (3.20)$$

where C_o is the uniaxial compressive strength and n is the ratio between compressive and tensile strength. By taking the transition pressure equal to the uniaxial compressive strength, the coefficient of friction became:

$$\mu_m = \frac{\sqrt{1+n}-1}{n}\sqrt{1+n} \qquad (3.21)$$

where n is the ratio between the uniaxial compressive strength, σ_{ci}, and the tensile strength, σ_{ti}, for the intact rock. The principle is shown in Figure 3.6.

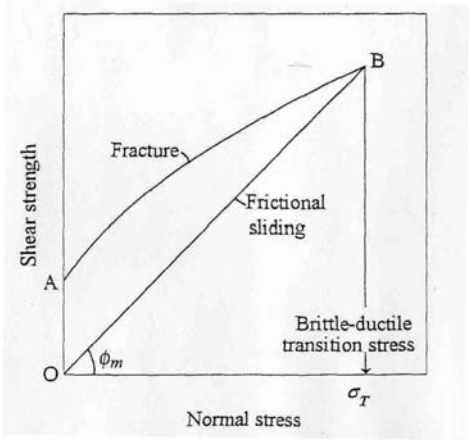

Figure 3.6: Determination of friction angle for intact rock material, ϕ_m (From Papaliangas et. al 1995).

However, the assumption that the transition stress is equal to the uniaxial compressive strength is only an approximation according to the authors. Strong rocks, such as granite, may have values five times higher than the uniaxial compressive strength. Examples of typical values for ϕ_m and σ_T for some types of soft and hard rocks are presented in Table 3.1.

Table 3.1: Typical values for friction angle, ϕ_m, and transition stress, σ_T, (From CEATI 1998 based on Papaliangas 1996).

Type of rock	Estimated ϕ_m (°)	Transition stress σ_T (MPa)	Ratio σ_T/σ_{ci}
Dolomite	41,5	234	1,3
Limestone	41,6	138	1,4
Marble	42,9	64	0,8
Granite	32,0	1243	5,2
Sandstone	34,2	186	3,1

The dilation component, ψ, consists of a maximal dilation angle at low normal stresses, ψ_0. With increasing normal stresses the dilation component, ψ, reduces logarithmically. This continues up to a certain state of normal stress at which dilation becomes negligible, σ_{nT}. Based on the principles of contact theory they proposed the following expression for the estimation of the dilation angle:

$$\psi = \psi_0 \frac{\log\left(\frac{\sigma_{nT}}{\sigma_n}\right)}{\log\left(\frac{\sigma_{nT}}{\sigma_{n0}}\right)} \tag{3.22}$$

where σ_{n0} is a lower limit for normal stresses, usually assumed to be 1 kPa.

In the expression above, it should be emphasized that σ_{nT} is different than σ_T, since the true contact area affects at which normal stress dilation becomes negligible. Based on his testing, Papaliangas obtained results which suggested that σ_{nT} occurred when the contact area was about 10% of the nominal area of the sample. As a result, he proposed the following equation to estimate sigma σ_{nT}.

$$\sigma_{nT} = \frac{\sigma_{ci}}{10} \tag{3.23}$$

According to Papaliangas, the above expression was only a rough estimation, but on the other hand, possible errors were of minor importance due to the logarithmic nature of equation 3.22.

Regarding the shear strength at *in situ* scale Papaliangas (1996) was of the opinion that any variation in the peak shear strength was due to dilation caused by roughness. Therefore, any variation in peak shear strength at different scales was due to variations in dilation. Using extrapolation of measured dilation at different scales, he proposed that a critical length, L_{cr}, existed where the dilation became zero, see Figure 3.7. Therefore, he concluded that for *in situ* scale dilation was negligible and the shear strength was purely due to the frictional component, ϕ_m.

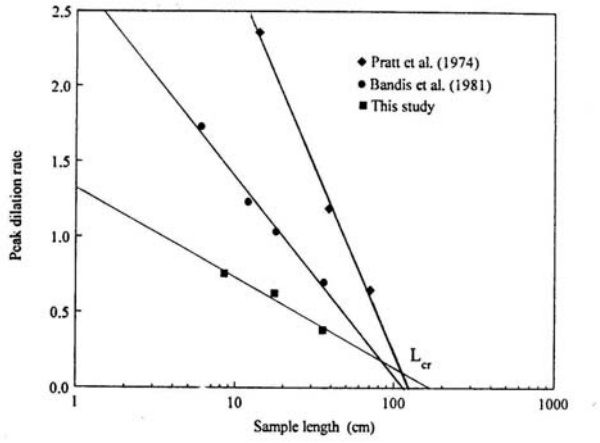

Figure 3.7 Scale free block size according to Papaliangas (1996) from three different experimental data sets.

From fractal theory, Kulatilake (1995) proposed a new shear strength criterion for unfilled and rough joints on the form:

$$\tau = \sigma\left(\phi + \mathrm{a}\left(SRP\right)^{\mathrm{c}}\left(\log_{10}\left(\frac{\sigma_{\mathrm{j}}}{\sigma}\right)\right)^{\mathrm{d}} + I\right) \tag{3.24}$$

where ϕ represents the basic friction angle and I considers the non-stationary part of the roughness approximated as the average inclination of the roughness. σ_{j} is the compressive strength of the joint surface. a, c and d are empirical constants which according to Kulatilake et al. (1995) should be determined by regression analysis of data from shear tests. *SRP* denotes the stationary roughness parameter and is based on two fractal parameters for quantification of surface roughness. Different techniques were proposed to describe *SRP* which resulted in four different forms of *SRP* in the criterion presented in equation 3.24. By determination of fractal parameters in different direction, Kulatilake et al. (1995) estimated the shear strength in different directions for their samples. They also concluded that some of the parameters are scale dependent and could be used to model the scale effect.

The criterion by Kulatilake et al. (1995) was later modified by Kulatilake et al. (1999) to account for the effect from shearing through the asperities. The modification was done since "*at very low effective normal stresses, the effect of shearing through the asperities plays a negligible role compared with the dilation on peak shear strength. However, with increasing normal stress, in addition to dilation, shearing through the asperities may contribute to the peak shear strength.*" Furthermore, effect from a non-stationary roughness was modelled in more detail.

Fractal theory were also used by Borri-Brunetto et al. (1999 and 2004) to suggest possible explanations for changes in peak shear strength due to changes in normal stress and scale.

Based on extensive experimental results Grasselli (2001) proposed a failure criterion for rough unfilled joints that considers the anisotropy of the shear strength. It was based on detailed surface measurements of the joints, using a optical measurement system called ATS (Advanced Topometric System). The result from the measurements was a point cloud which was used to reconstruct the joints surface by triangulation. He suggested that it is only the triangles of the reconstructed surface facing the shear direction that provide shear resistance. By calculating the sum of the areas of these triangles the result is a total potential contact area ratio, denoted A_{c}. The contribution from each triangle projection was described by a parameter called apparent dip angle, denoted θ^{*} and described in Figure 3.8.

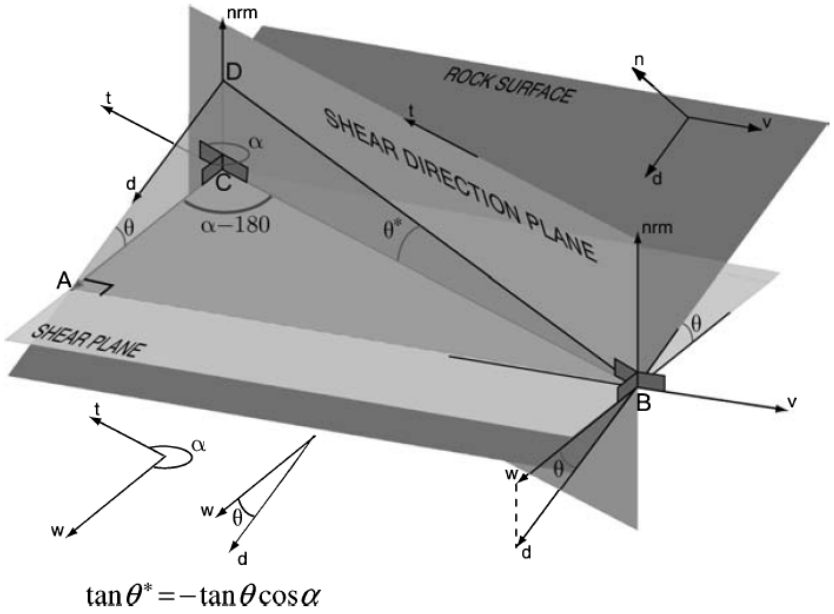

Figure 3.8 Geometrical identification of the apparent dip angle θ^*, as a function of shear direction (From Grasselli 2006).

He suggested that the shearing mechanism could be simplified by assuming that only the zones of the surfaces facing the shear direction, and steeper than a threshold inclination, θ^*_{cr}, were involved in the shearing. Zones inclined exactly θ^*_{cr} will be just in contact, while zones inclined more than θ^*_{cr} will be deformed, sheared or crushed depending on the applied normal load.

Based on curve fitting and regression analysis he proposed an empirical equation to describe the relation between these two parameters.

$$A_c = A_o \cdot \left(\frac{\theta^*_{\max} - \theta^*}{\theta^*_{\max}} \right)^C \tag{3.25}$$

Where A_c is the sum of the total potential contact area ratio, and A_o is the maximum possible contact area ratio which, according to Grasselli, usually is around 50% of the total potential area for fresh mated discontinuities. θ^*_{max} is the maximum apparent dip angle and θ^* is the apparent dip angle as described in Figure 3.8, and C is a "roughness" parameter.

Based on his experimental results, Grasselli (2001) proposed the following empirical expression to predict the peak shear strength.

$$\tau_p = \sigma_n \cdot \tan(\phi'_r) \cdot (1 + g) \tag{3.26}$$

Where σ_n is the applied average normal stress, ϕ'_r is the residual friction angle, and g is a term which account for the contribution to the peak shear strength from surface morphology given by:

$$g = e^{\frac{-\theta^*_{\max}}{9 \cdot A_o \cdot C} \cdot \frac{\sigma_n}{\sigma_t}} \tag{3.27}$$

In equation 3.27, $\theta^*_{\max}$ is the maximum apparent dip angle with respect to the shearing direction, A_o is the maximum potential contact area, C is the roughness parameter, and σ_t is the tensile strength of the intact rock material.

The residual friction angle, ϕ'_r, could be expressed as (Grasselli 2001):

$$\phi'_r = \phi_b + \beta \tag{3.28}$$

where β is the contribution from roughness to the residual friction angle and is calculated with the following equation.

$$\beta = \left(C \cdot A_o^{1.5} \cdot \theta^*_{\max} \cdot \left(1 - A_o^{\frac{1}{C}} \right) \right)^{\cos\alpha} \tag{3.29}$$

The parameter α is the angle of schistosity planes in the rock with respect to the normal of the joint. If no schistosity planes are present α is set to zero.

In his work, no attempt was made to investigate the influence of scale. Furthermore, Grasselli pointed out that the criterion only has validity in the range of the samples tested in the laboratory, i.e. $\sigma_n/\ \sigma_c$=0.01-0.4 and $\sigma_c/\ \sigma_t$=5-46, and that further studies are needed to investigate its applicability to *in situ* conditions.

Seidel and Haberfield (2002) developed a model for joints in soft rock (i.e. uniaxial compressive strength of about 3.5 MPa) based on several analytical models which accounted for asperity sliding, shearing through asperities and elastic distribution of stresses. The analytical models were incorporated in a computer program and shear stress at different shear displacements was predicted. Good agreement was obtained against observed behaviour in shear tests of two dimensional roughness profiles.

3.3 Summary

A number of failure criteria for rough unfilled joints have been proposed by different authors. In their construction they are fundamentally built on the same principle. The total friction angle is assumed to consist of two parts; one part which is constant and only depend of rock type, and another part which depends on surface roughness and is dependent of parameters such as normal stress, strength of the joint surfaces and most likely scale. However, these criteria are mainly derived based on tests in laboratory scale.

Barton and Bandis (1982) suggested that reductions of the friction angle from laboratory scale to *in situ* scale should be performed based on the average block size in the rock mass. But this assumption imply that the rock mass has a

sufficiently low stiffness to mobilize the active asperities at block scale. This is an assumption which is not obvious for a shallow horizontal joint under a concrete dam. If the rock mass is sufficiently stiff, the rock mass between the dam and the joint might work as a single block, and *in situ* scale thereby means the dimensions of the overlying structure. Another suggested method is to use a fixed percentage of the sample length to find the asperity which governs the dilatation angle (Bandis et al. 1981, Patton 1966, MacMahon 1985). A third proposed alternative is to not account from the effect of roughness since it is suggested that it becomes negligible at a sample length of one to one and a half meter (Papaliangas 1996).

The major drawback with these suggested methods are that they are mainly based on empirical grounds. Which alternative is correct, and under which conditions they can be used, are not clear. Fractal theory, as suggested by for example Kulatilake et al. (1995 and 1999) and Borri-Brunetto et al. (1999 and 2004), may be used to find possible explanations for the scale effect. This means that there exists a need for a method based on a conceptual and more detailed understanding of the mechanisms that governs the shear strength at different scales.

4 A CONCEPTUAL MODEL FOR PEAK SHEAR STRENGTH OF UNFILLED AND ROUGH JOINTS

4.1 Introduction

As shown in the previous chapter, it is clear that several parameters affect the shear strength of unfilled and rough joints in a rock mass. Parameters such as normal stress, uniaxial compressive strength of the joint wall surface, roughness of the wall and scale influence the peak shear strength. However, different shear strength criterion uses different explanations for some of the mechanisms of the shearing process, and proposes different methods to describe it mathematically, when the peak shear strength should be estimated.

In order to reduce some of the uncertainties regarding peak shear strength for full sized joints, an attempt is made in this chapter to develop a conceptual model which describes the basic mechanisms behind the peak shear strength for an unfilled rough joint of different scales.

At the end of the chapter, the conceptual model is used in a verification analysis. Based on the results from this analysis, conclusions about the peak shear strength for full sized joints are presented.

4.2 Fundamental mechanics of friction

The sliding resistance between two contacting bodies at their interfaces is a subject that has been extensively studied during the latest decades. The following section in the subject is mainly based on the review in the subject performed by Lambe and Whitman (1969) and the literature study by Papaliangas (1996).

Two basic laws are used to describe frictional behaviour. These laws were first stated by Leonardo da Vinci in the 1400s. They were largely forgotten until they were rediscovered by the French engineer Amontons (1699). They are often called Amontons laws and states that:

- The shear resistance between two bodies is proportional to the normal force between the bodies.

- The shear resistance between two bodies is independent of the dimensions of the two bodies.

The generally accepted theory for the friction process is called the adhesion theory and was first stated by Terzaghi (1925). Bowden and Tabor (1950 and 1964) showed that it could explain the frictional behaviour for a wide range of materials.

The adhesion theory of friction states that on a microscopic level, all surfaces, even smooth ones, are rough. Contact points will only be developed where the asperities from the two opposing surfaces touch each other. The true area of contact will only be a small part of the total nominal contacting area of the two surfaces. As a consequence, the normal stresses at these contact points can be so high that the local plastic yield strength of the rock material at the asperity scale is reached. The true contact area, A_c, can be defined as:

$$A_c = \frac{N}{q_u} \tag{4.1}$$

where N is the normal load and q_u is the stress required to obtain plastic flow at the contact points. Since q_u is constant, the true contact area will increase proportional to the normal stress. At these contact points, the two opposing surfaces will be welded together at "junctions", creating adhesive bonds. The shear resistance, T, is provided by the adhesive strength of these junctions, s_i, and can therefore be expressed as:

$$T = \Sigma s_i \cdot A_{c,i} = s \cdot A_c \tag{4.2}$$

where $A_{c,i}$ is the contact area for contact point i, see Figure 4.1.

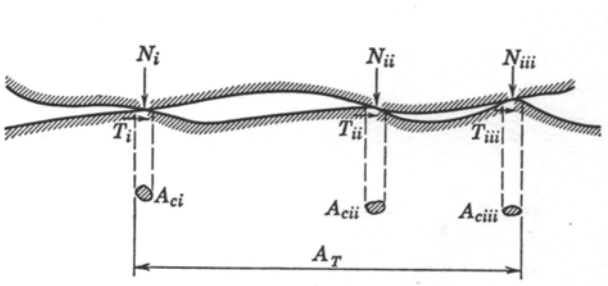

Figure 4.1 Microscopic view of two bodies in contact (From Lambe and Whitman 1969).

Combining equations 4.1 and 4.2 leads to the following expression:

$$T = N \cdot \frac{s}{q_u} \tag{4.3}$$

The quotient s/q_u is often called the familiar term coefficient of friction, μ, or from a geometrical interpretation of the relation between normal and tangential (shear) force components of the system, the tangent of a friction angle, ϕ.

$$\frac{s}{q_u} = \mu = \tan\phi \tag{4.4}$$

When s and q_u are constant, the shear strength will be proportional only to the normal load.

When the yield strength, q_u, is not reached at the contact points, the asperities forming these contact points will deform elastically. Archard (1957 and 1974) shows that for a surface with asperities of a uniform distribution, A_c increases as $N^{2/3}$. On the other hand, for a surface with asperities of different sizes following a Gaussian distribution, A_c increases as $N^{44/45}$.

Therefore, in both plastic and complex elastic deformation cases of the asperities at contact, the true contact area will be proportional to the normal load (Papaliangas 1996).

Another approach has been suggested by Greenwood and Williamson (1966). They developed an analytical model for contact mechanics of one nominally planar rough surface with its asperity height following a Gaussian distribution and one smooth surface. The model was based on the assumptions that the summits of the asperities are spherical and have the same radius and are sufficiently apart from each other to deform independently. Using their model they showed that exact proportionality between contact area and normal load will exist independently of mode of deformation (elastic or plastic). Instead, the model showed that the proportionality between contact area and load lies in the statistical distribution of the asperity heights of the surface roughness.

A further development of this model was presented by Greenwood and Tripp (1971). In this paper, an analytical model for the contact of two nominally flat rough surfaces was derived. They showed that results from previous models, i.e. Greenwood and Williamson (1966), were unaffected.

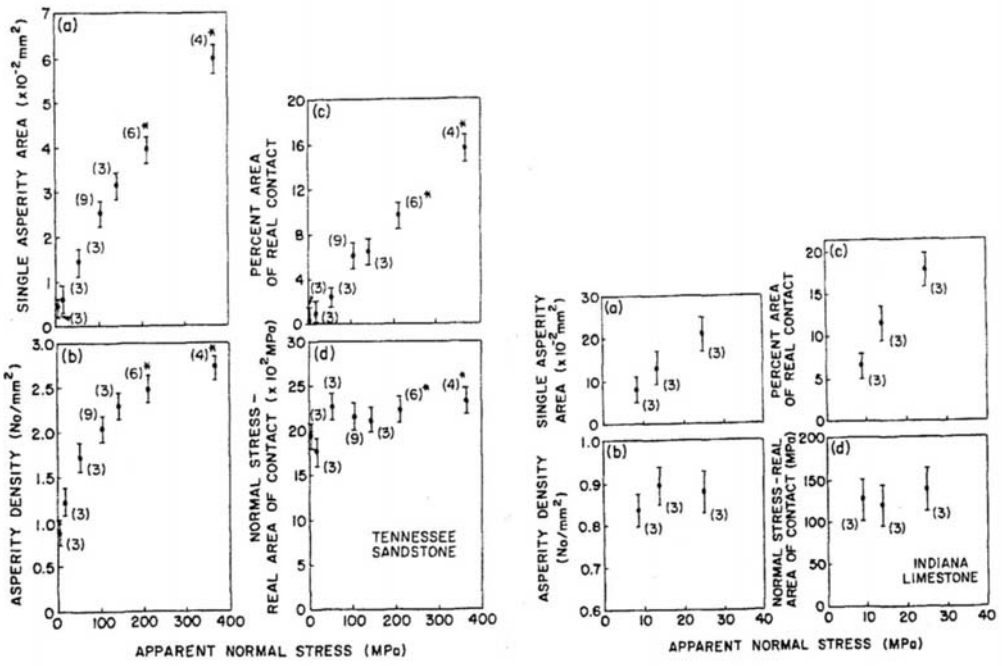

Figure 4.2 Variation of contact area with normal stress (From Logan and Teufel 1986).

The concept of adhesion were developed with observations of mainly engineered planar metal surfaces whose roughness is both stationary and regular compared with rough surfaces of rock joints. However, the model by Greenwood and Tripp (1971) has been used with success to estimate different joints properties, see for example in Swahn (1983) and Swahn and Zongqi (1985).

If the contact stress is sufficiently high to induce plastic flow of asperities under shearing of rock joints, the proportionality can be estimated by comparing measured contact area of the tested sample surfaces against the applied normal stress. Logan and Teufel (1986) measured the contact areas at different normal stresses during shearing for sandstone and limestone surfaces, see Figure 4.2. Calculated normal stresses at the contact points were around 125 MPa for limestone and 2200 MPa for the sandstone. These values are close to the uniaxial compressive strength for calcite and quartz, both minerals that form a part of limestone respectively sandstone. It can also be observed that the contact area increases linearly with increasing normal stress and that the contact stress is approximately constant, which is in line with the adhesion theory.

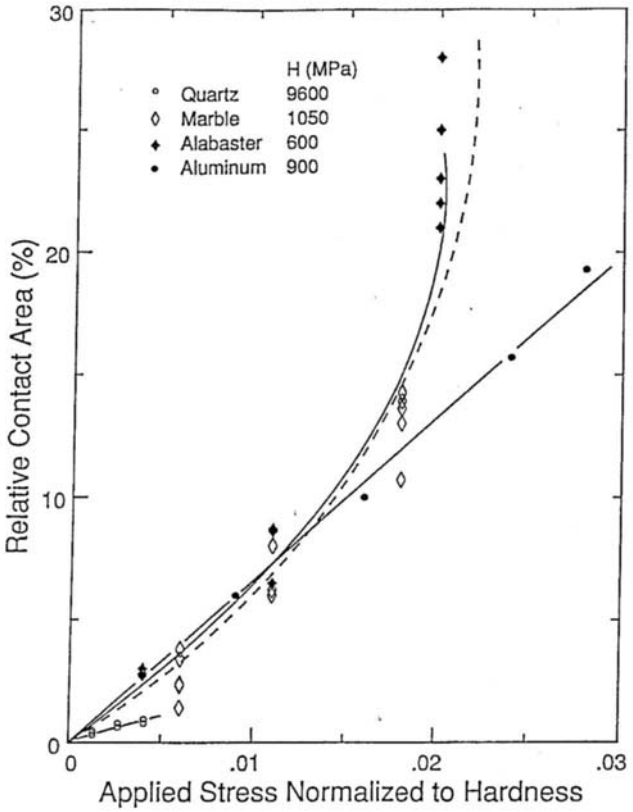

Figure 4.3 The variation of relative contact area with stress normalized to indentation hardness, H (From Stesky and Hannan 1987).

A similar type of experiment was also performed by Stesky and Hannan (1987) who measured the contact areas under different normal loadings for marble, alabaster, and quartzite surfaces, see Figure 4.3. They also observed increasing contact areas with increasing normal stress. They concluded that surface asperities in marble and alabaster were weakened by cataclastic flow, which lead to the increase of contact areas with stress. Even the quartzite undergoes some

cataclastic deformation and a significant growth of contact area with stress. The fact that the increase of contact area became non-linear at stresses around 1-2% of the indentation hardness for marble and alabaster is not significant according to the authors due to the uncertainties in the hardness values and the appropriateness of using hardness as a measure of relative asperity strength.

In summary, the experimental evidence points to the fact that plastic flow do occur at the contact points of the asperities, and that this gives rise to adhesive bonds in the contact points as proposed by Terzaghi 1925. It therefore seems likely that the contact area can be reasonably approximated as the load acting over the surface divided by the yield strength of the material.

It is most likely that the adhesion theory can explain the constant part of the friction angle in all failure criteria, often denoted the basic friction angle, ϕ_b. The fact that adhesion is responsible for friction is something that could feel like a paradox. However, it can explain Amontons laws and the theory is realistic. Based on the origin of the friction force, it could also be discussed whether or not it is appropriate to express it with a friction angle since it mainly is material constants that are responsible to it. Probably, the use of a friction angle dates from the days of Leonardo da Vinci, when the friction force was determined with inclined planes.

It has been observed by both Johnson et al. (1971) and Fuller and Tabor (1975), who investigated the adhesion at the contact points, that adhesion diminishes with increasing microscopic roughness. This should be kept in mind when the basic friction angle should be determined. Barton and Choubey (1977) suggest that the basic friction angle should be determined by shearing two saw cut surfaces against each other. It is possible that the sawing creates macroscopically planar surfaces and thereby alters the basic friction angle. Tests performed by Hencher and Richards (1989), and Hencher et al. (1993) showed practical difficulties in the determination of the basic friction angle. Their results exhibited a large variation between 12^o and 32^o. Influencing factors were thought to be the roughness of the surfaces, the properties of the saw blade, powder from the rock and other materials that have been gathered on the surfaces.

Based on the previous text, the following statements can be made regarding the fundamental frictional behaviour:

- The contact area is proportional to the normal load.
- The true contact area can be approximated as the load acting over the surface divided by the yield strength of the material.
- The basic friction angle originates from the adhesion theory of a microscopic rough but macroscopic smooth surface.

4.3 Description of surface roughness

Surface roughness has been described by a number of different approaches and parameters. The most commonly used parameter in engineering practice is the joint roughness coefficient, *JRC*, defined by Barton (1973) and Barton & Choubey (1977). Other methods which have been proposed to measure roughness, especially at larger scales, are for example a compass clinometer with variable sizes of base plates; see ISRM suggested methods (1981) and remote-controlled laser scanning (Feng et al. 2001).

Another approach which has been used to quantify surface roughness is by using statistical parameters from analysis of two dimensional profiles. To measure the magnitude of roughness, the root mean square (*RMS*) and the centre line average (*CLA*) is commonly used, see for example (Thomas 1982). By using the *RMS* as the basic parameter, Myers (1962) proposed for 2D profiles three additional parameters to describe surface roughness, the root mean square of the first derivate of the profile (Z_2), the root mean square of the second derivate of the profile (Z_3), and (Z_4) defined as the percentage excess of distance measured along the profile where the slope is positive over the distance where the slope is negative. Other examples of statistical parameters used to quantify surface roughness are auto-correlation function, spectral density function, structure function (*SF*), roughness profile index (R_p), and micro average angle (A_t) (Papaliangas 1996).

Tse and Cruden (1979) investigated the correlation between *JRC* values given by Barton and Choubey (1977) in their predefined profiles with different statistical parameters. They found good correlation between *JRC* and the parameters Z_2. The parameter Z_2, which is a measure of the average inclination over a certain sampling distance Δx, is defined as:

$$Z_2 = \frac{1}{(n-1)(\Delta x)} \sum_{i=1}^{n} \left[\left(z_{i+1} - z_i \right)^2 \right]^{1/2} \tag{4.5}$$

where n is the number of discrete measurements of the asperity height, z_i and z_{i+1} are the asperity height of two adjacent sampling points separated by the sampling distance Δx.

Based on their work, Tse and Cruden (1979) concludes that there exist physical reasons for expecting Z_2 to characterize the frictional behaviour of rock surfaces since arctan(Z_2) should be proportional to an i angle of an appropriate order according to Patton´s (1966) definition. It should be noted that Tse and Cruden used a constant sampling distance of 1.27 mm in their analyses. The meaning of the parameter Z_2 and the length of the sampling distance, Δx, will be discussed further in Chapter 4.5, where the relevance of asperity slope angle with respect to dilational behaviour are discussed.

The awareness of scale effects, and the fact that natural rock joints are rough at all scales, led to the idea that surface roughness can be described with fractal models. The fractal dimension, D, can in general be defined with the following relation (Mandelbrot 1967).

$$N = \frac{1}{r^D} \tag{4.6}$$

Where N is the number of square boxes of linear size r needed to cover the profile. Using equation 4.6, the fractal dimension, D, is:

$$D = \frac{\log(N)}{\log(1/r)} \tag{4.7}$$

In other words, the fractal dimension D describes how the total size of the set depends on the sampling size. For a line, the fractal dimension is 1.0, and for a plane it is 2.0, equal to their respective Euclidean dimension. However, for a profile of a rough surface, the fractal dimension varies between the Euclidean dimension of a line and a plane, see Figure 4.4.

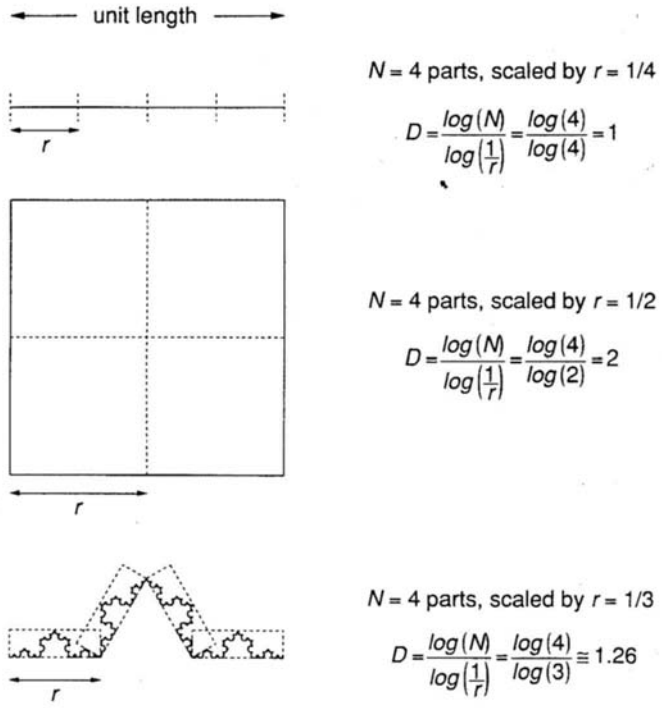

Figure 4.4 A unit segment can be divided into four equal parts, each scaled by a factor r=1/4 which gives D=1, a unit square can be subdivided into four equal parts, scaled by a factor r=1/2 which gives D=2. Four equal parts of a von Koch curve are scaled by a factor r=1/3 which gives a fractal dimension of D=1,26 that is intermediate between the dimension of a line and the dimension of a square (From Maliverno 1995).

Two different ways to represent the surface roughness has been proposed, self similar and self-affine fractal models. In short, the difference between them is that for self-similar fractal models the geometric statistical moments remain constant to all scales, while a self-affine fractal models only remains the same statistically

if they are scaled differently in different directions (Mandelbrot 1983). In general, self-affine fractal models are considered to be more applicable to describe surface roughness of joints compared to self-similar models, see for example Mandelbrot (1983); Brown and Scholz (1985); Kulatilake et al. (1995) and (1997); Lanaro (2001); and Fardin (2003).

However, it should be noticed that a fracture surface probably could not be considered fractal at all scales. For example, Brown and Scholz (1985) concluded that surfaces may be considered fractal only over limited scale ranges above the grain size. The size of the grains varies depending on type of rock and can range from a few hundreds to thousand of a millimetre (very fined grained) up to a few centimetres (very coarse grained), see for example in the book Engineering Geology and Rock Engineering (NBG 2000). For larger scales, measurements by Fardin (2003) indicate that the self-affine fractal model might only be applicable up to about 3 m, where a stationary threshold is reached for the roughness.

For a self-affine fractal, there exists a power law relation between the standard deviation of the asperity height, $S(w)$ and the spanning length of the profile, w (Maliverno 1990):

$$S(w) = Aw^H \tag{4.8}$$

where H is the Hurst exponent and A is the amplitude parameter. When w=1, $S(w)$=A and is a measure on the roughness amplitude. The Hurst exponent, H, describes how roughness changes with scale. H and the fractal dimension D is related by a relation H=E-D, where E is the Euclidean dimension (3 for a surface and 2 for a profile).

The fact that surface roughness can be correlated for self-affine fractal models points to the fact that there exists a scaling relation between the asperity height, h_{asp}, and the base length of different sized asperities, L_{asp}, which can be expressed with a power function on the form:

$$h_{asp} = a \cdot L_{asp}^H \tag{4.9}$$

where a is an amplitude constant based on the asperity base length and therefore is related to the amplitude parameter, A. H is the Hurst exponent. If H=1, then the height of the asperity increases proportional to the length of the asperities. However, natural rock surfaces usually have a value of H lower than one; see for example Lanaro (2001). This means that the increase of the asperity height is lower than the increase of asperity length. In other words, the inclination of the asperities decreases exponentially with asperity base length, since the dilation angle for a geometric idealized asperity could be defined as:

$$i = \arctan\left(\frac{2h_{asp}}{L_{asp}}\right) \tag{4.10}$$

This effect can be seen in the paper by Sfondrini and Sterlacchini (1996). They determined the statistical parameter Z_2 (mean inclination angle of asperity) at different sampling sizes, see Figure 4.5.

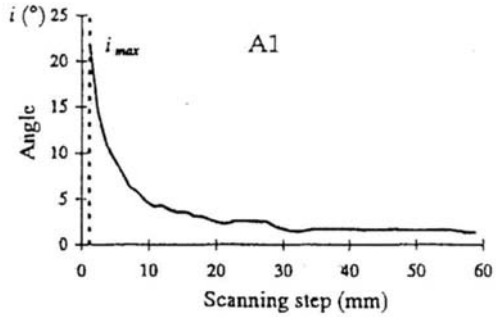

Figure 4.5 Measured positive inclination angles based on the parameter Z_2 at different scanning steps (From Sfondrini and Sterlacchini 1996).

This also means that different scales of asperities exist, with different heights, on the same sample. By superposition in the order of the measurement scales, it may be possible to idealize the surface roughness. The basic principle is shown in Figure 4.6.

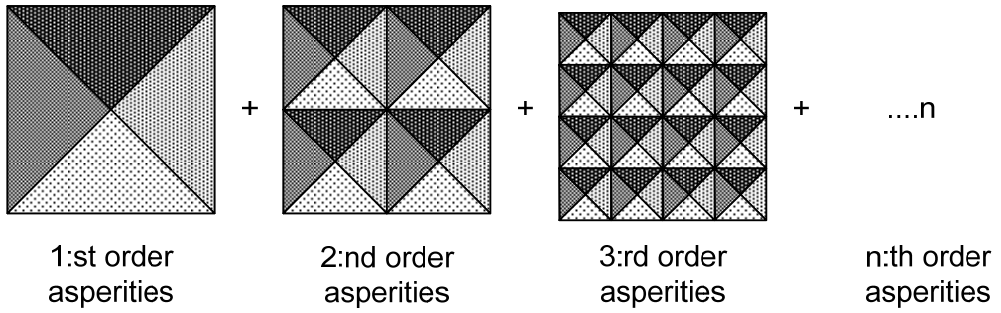

Figure 4.6 Idealized description of surface roughness.

In Figure 4.6, it has been assumed that the theoretical maximum asperity base length that could exist on the sample is equal to the sample length. In reality, they could be smaller as observed by for example Lanaro (2001). However, for the purpose of this discussion, the assumption that a maximum base length of the asperity that could exist on a sample is equal to the sample length is sufficient. It could therefore be assumed that:

- The change of height for surface asperities, h_{asp}, with respect to asperity base length, L_{asp}, for natural rock joints can be expressed with a power function based on a self-affine fractal model.

- Therefore, surface roughness could be idealized by superposition of a large number of asperities at different scales.

- The grain size could be assumed to constitute a lower limit of the fractal scale.

- At larger scales, an upper limit of the fractal scale might exist due to a stationary threshold of the roughness.

4.4 Contact area during shear

For a smooth planar surface, the adhesion theory states that the contact area is proportional to the applied normal stress and that the contact area can be defined as the load acting over the surface divided by the yield strength of the material. It could be anticipated that the same mechanism is valid for a very rough surface, i.e. a macroscopic rough surface. The difference is that during shear, the contact points will be located on the sides of the asperities facing the shear direction.

It has been observed that the contact areas for a macroscopic rough surface for fresh and mated joints are located in the steepest zones facing the shear direction (Grasselli and Egger 2000; Kimura and Esaki 1995), as previously described in Chapter 3. Based on regression analyses of scanning data from joint surfaces, Grasselli (2001) proposed the following empirical relation to express the contact area ratio at different asperity inclinations for a mated joint. Grasselli called this parameter the potential contact area ratio, in this work denoted $A_{c,p}$.

$$A_{c,p} = A_o \left[\frac{\theta^*_{max} - \theta^*}{\theta^*_{max}} \right]^C \tag{4.11}$$

Where A_o is the maximum possible contact area ratio, which usually is around 50% of the total sample area for fresh and mated joints. θ^*_{max} is the maximum apparent dip angle and θ^* is the apparent dip angle. The apparent dip angle is defined as the inclination of the asperity against the shear direction. From now on in this work, θ^* is called the measured dip angle against the shear direction. C is a "roughness" parameter which governs the concavity of the curve. An example from one of Grasselli´s samples which shows how the potential contact area changes with the measured dip angle is presented in Figure 4.7.

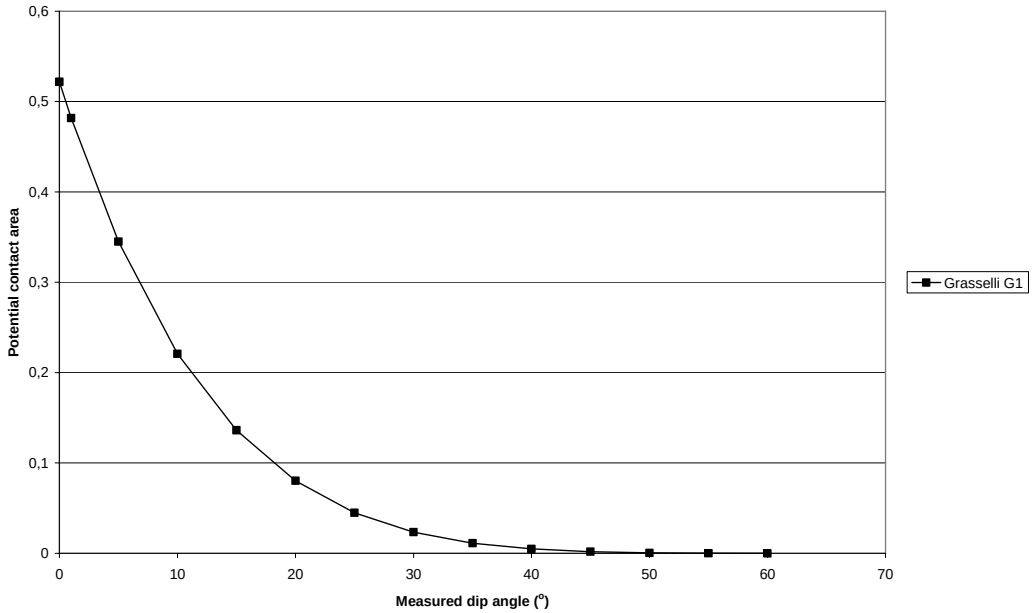

Figure 4.7 Example of potential contact area for different measured dip angles (Grasselli 2001).

Based on the potential contact area ratio, $A_{c,p}$, the potential contact area is given by the product of the potential contact area ratio and the area of the sample.

The potential contact area, $A_{c,p}$, is determined by dividing the sample into a large number of triangles or squares at a predefined resolution. Thereafter, the cumulative sum of all areas with different inclinations is calculated. The calculation starts with the sum of the potential contact area for the maximum apparent dip angle. Next, areas with lower inclinations are successively added until all areas in the sample facing the shear direction are included.

This technique, where the potential contact area ratio is determined based on scanning data has one significant limitation. As previously shown in Figure 4.6, the surface roughness consists of asperities at multiple scales. This multiple scale behaviour is not captured by using a fixed resolution of the scanned joint surface.

However, it could be assumed, as suggested by Brown and Sholz (1985), that the grain size of the intact rock constitutes a lower limit of the fractal scale. If a scanning resolution was chosen at grain size scale, it could be considered to represent this lower limit of the fractal scale. Under these assumptions, it would be possible to use the adhesion theory, combined with the concept of a potential contact area ratio, in order to estimate the dilation angle for perfectly mated joints.

Still, this does not explain the mechanism behind the scale effect. In order to study this effect, it must be further discussed how the contact points change with scale.

First of all, the adhesion theory states that the contact area increases proportionally to the sample size for a given normal stress. At the same time, it will remain the same independently to the sample size. This can be shown with the following equations:

$$A_c = \frac{N}{q_u} = \frac{A \cdot \sigma'_n}{q_u} \tag{4.12}$$

where A is the nominal area of the sample and σ'_n is the effective normal stress. The effective normal stress is defined as:

$$\sigma'_n = \sigma_n - u \tag{4.13}$$

where σ_n is the total normal stress and u is the pore pressure. If equation 4.12 is rearranged it becomes:

$$\frac{A_c}{A} = \frac{\sigma'_n}{q_u} \tag{4.14}$$

Since the ratio between the true contact area and the sample area is dependent only on effective normal stress and the yield stress of the material, but independent of scale, the following expression is valid:

$$\frac{A_{c,n}}{A_n} = \frac{A_{c,g}}{A_g} \tag{4.15}$$

where subscript (n) and (g) stands for full joint size and grain size respectively. The true contact area could also be expressed as:

$$A_c = n \cdot A_{c,av} = n \cdot L_{asp}^2 \tag{4.16}$$

where n is the number of contact points and $A_{c,av}$ is the average area of the contact points. L_{asp} is the average length of the contacting asperities if they are assumed to be shaped quadratic on the joint wall surface. Combining equation 4.15 and 4.16 gives:

$$\frac{n_n \cdot L_{asp,n}^2}{L_n^2} = \frac{n_g \cdot L_{asp,g}^2}{L_g^2} \tag{4.17}$$

where L is the length of the sample. Equation 4.17 indicates that the change in the number of contact points will govern how the length or area of the contacting asperities change with increased scale under a constant normal stress. This is in line with the conclusions in Yoshinaka et al. (1993). They concluded that the scale effect occurs as a result of changes of the contact points.

How the contact area and the number of contact points change with sample size was studied by Bandis (1980). He concluded that an increased scale resulted in larger number of contact points, which is in line with the assumption above. In his observations, the size of the contact points did not increase proportionally to the increase of the sample size. Instead a mixture of increased number of contact points and an increased length or area of contacting asperities was observed with increased scale. His results also indicate that the increase of the number of contact points and the length or area of the contacting asperities could be dependent of roughness. These results indicate that the asperity base length or area at contact for full sized joints, $L_{asp,n}$, could be expressed as:

$$L_{asp,n} = L_{asp,g} \cdot \left(\frac{L_n}{L_g} \right)^k \tag{4.18}$$

where k is an empirical constant. If the results by Bandis (1980) are analysed, values on k with respect to the *JRC* according to Figure 4.8 were obtained. The results indicate that the value of k increases with an increased roughness.

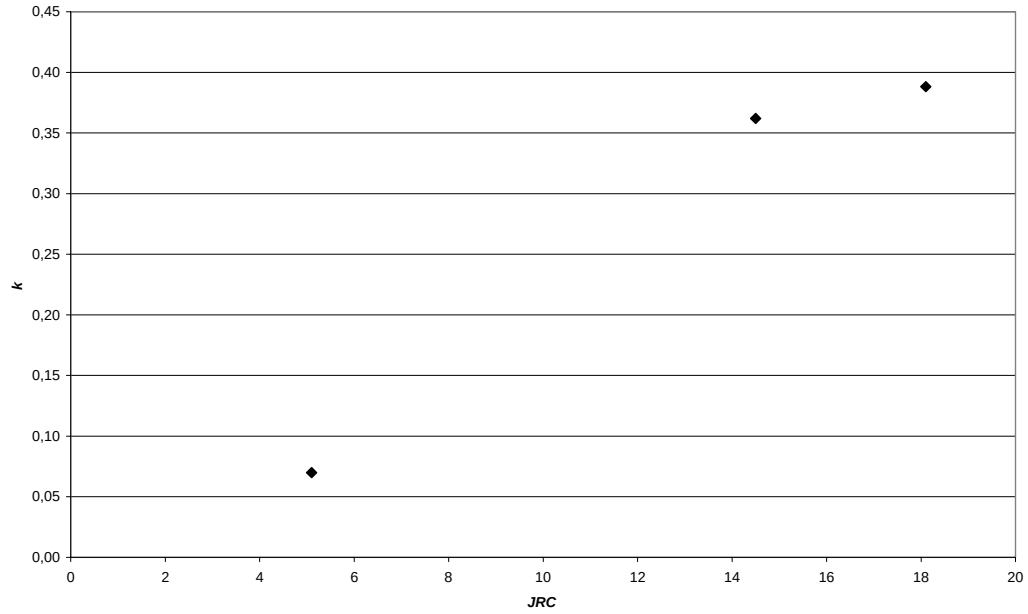

Figure 4.8 Values on k with respect to the JRC based on results from Bandis (1980).

It could be further discussed which mechanisms that control the value of *k*. In Figure 4.9, an example of potential contact areas for different apparent dip angles are presented. In this figure, it can be seen that potential contact areas with higher inclinations always are located in the same area of the sample as the potential contact areas with lower inclinations. This is most likely an effect from different orders of asperities that superimpose each other.

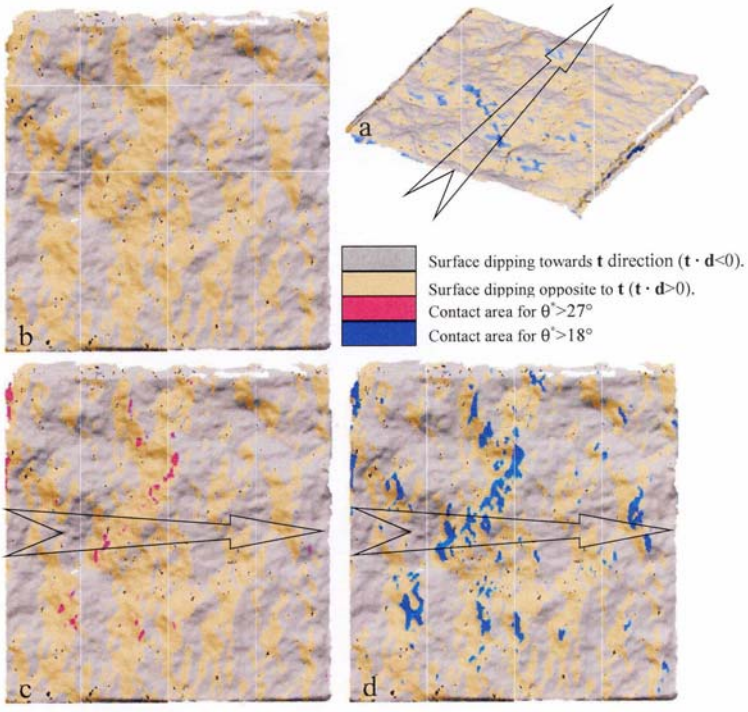

Figure 4.9 Figure showing potential contact area (b) Surface dipping against shear direction (c) Contact area with θ>27^o (d) Contact area with θ*>18^o (From Grasselli 2001).*

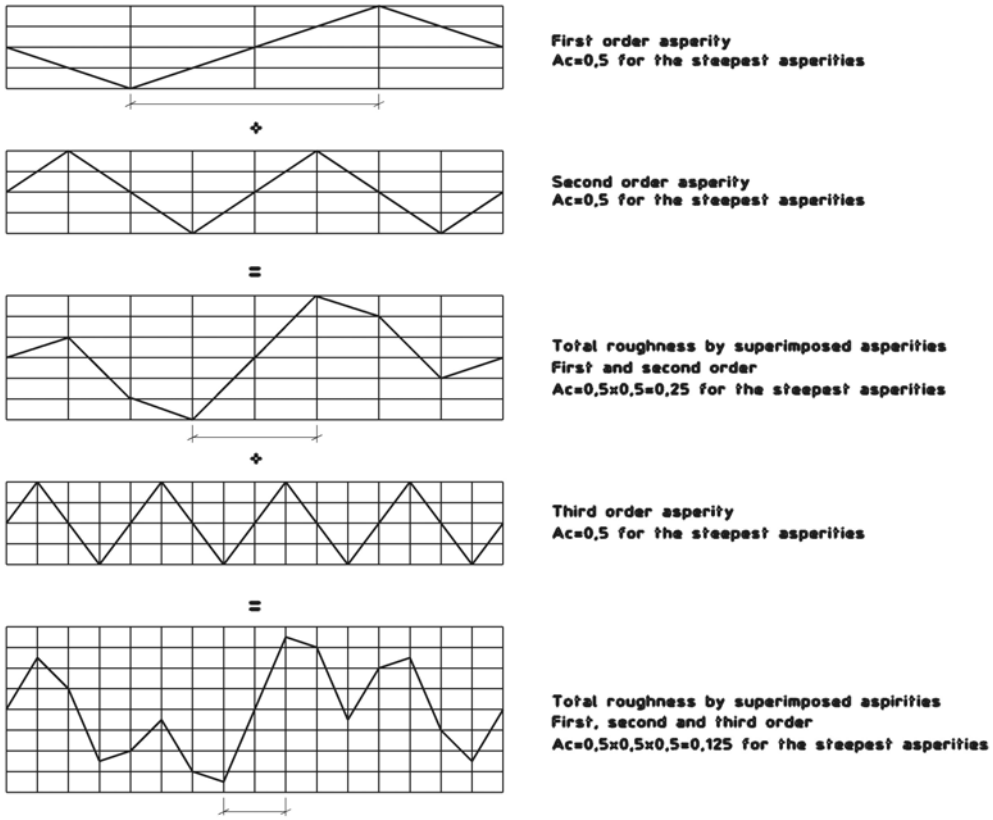

Figure 4.10 Basic mechanisms behind the change of the potential contact area with superimposed order of asperities. Notice how the potential contact area decreases while the inclination of the steepest asperities increases.

When scale is increased, the potential contact area ratio is affected in two ways by additional orders of asperities that are included into the sample: (1) it reduces the potential contact area ratio for that order of asperities and (2) it increases the inclination angle of the asperities for that order. The basic mechanism for changes in the potential contact area ratio with superimposed asperities has been illustrated in Figure 4.10.

It is unclear how this affects the potential contact area. Measurements by Fardin (2003) indicated that the potential contact area decreased with an increased scale. However, this observation has not been verified by the author. Instead, according to the author's experience, the curve which describes the potential contact area appears to remain almost unchanged with an increased scale if the resolution is fixed. The exception is that the tail of the curve that represents the steepest asperities becomes shorter with an increased scale. This would imply that joints mated down to grain size scale, under a constant normal stress, would have a dilation angle that is independent of scale. In other words, the number of contact points increases proportionally to the area of the sample. This suggests that the factor k=0 for perfectly mated joints. How the curve which describes the potential contact area changes with scale is further analysed in Chapter 5.

This further suggests that observations from mated joints down to grain size scale could not explain the scale effect observed by for example Bandis et al. (1981) and Yoshinaka et al. (1993). If a full reduction of the asperity inclination should

occur according to the scaling relation that exist between asperity length and asperity height, then it must lead to k=1. This only takes place when the number of contact points remains unchanged with scale. This requirement is fulfilled when the contact points are associated with the maximum asperities that could exist on the sample. In this work, for the sake of simplicity, the maximum asperity base length was assumed to be equal to the sample length.

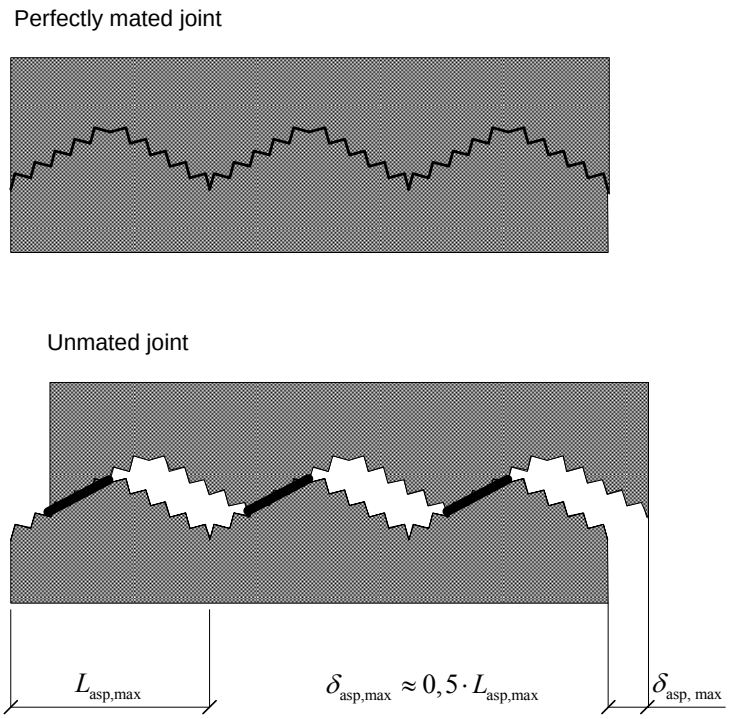

Figure 4.11 Illustration of the reduction of the number of contact points between a perfectly mated joint and an unmated joint.

During shearing, the number of contact points could become associated with the maximum number of asperities that could exist on the sample in two ways. In the first case, the normal stress is so high that all other asperities that are smaller than the largest ones are crushed. In this case, the dilation originates from the inclination of the remaining maximal sized asperities. For the other case, when the normal stress is low, dilation could originate from the largest asperities in active contact areas if the upper part of the sample undergoes a relative displacement equal to about half of the length of the maximum asperity base length. The principle is illustrated in Figure 4.11.

This suggests that the full scale effect occurs indirectly as a result of a maximal unmatedness between the upper and lower part of the sample. When this happens, k=1 and the number of contact points remains constant with scale.

Combining equation 4.17 and 4.18, the quotient between the numbers of contact points could be expressed as:

$$\frac{n_{\mathrm{n}}}{n_{\mathrm{g}}} = \left(\frac{L_{\mathrm{n}}}{L_{\mathrm{g}}} \right)^{2-2k} \tag{4.19}$$

In equation 4.19, L_{g} are assumed to represent the grain size scale and L_{n} the full sized joint scale. Figures 4.12 and 4.13 show how the number of contact points and the contacting asperity length changes with scale when k=0 (no scale effect) and when k=1 (full scale effect).

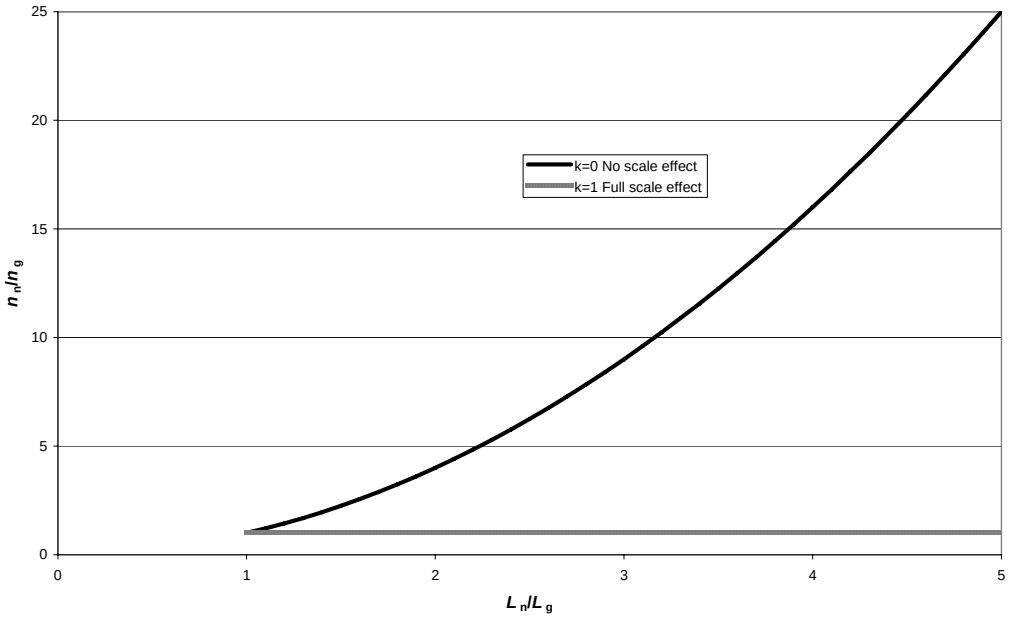

Figure 4.12 Changes in the number of contact points with scale when k=0 and k=1.

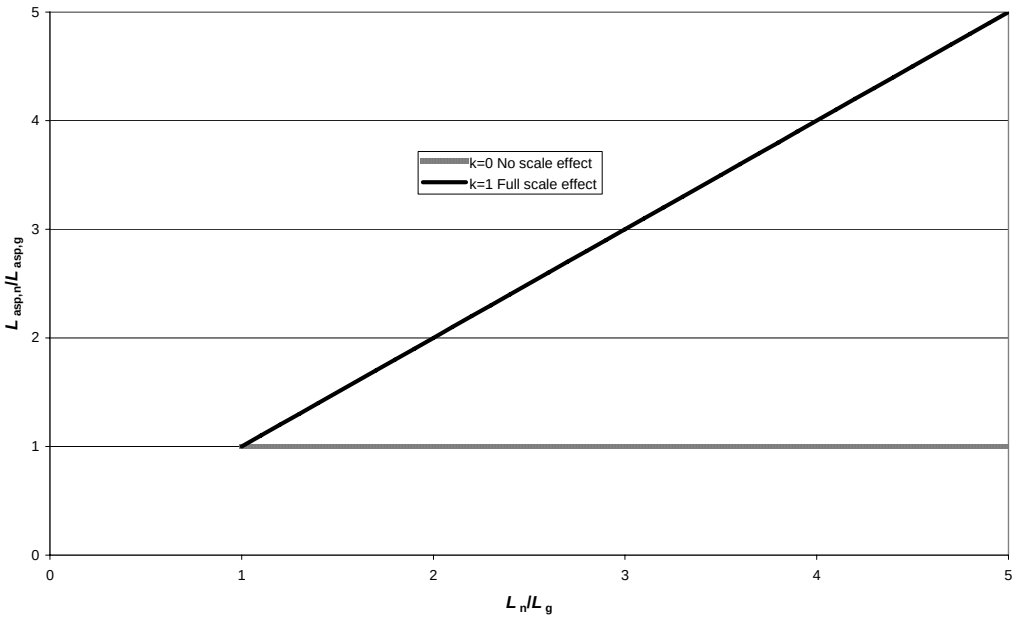

Figure 4.13 Changes in length of the contacting asperities with scale when k=0 and k=1.

Based on the analysis performed above the following assumptions can be made:

- For a macroscopic rough mated surface, the shear deformation leads to a concentration of the contact area to the steepest zones facing the shear direction.

- If the normal stress is constant, the contact area is independent of the sample size. Therefore, any changes in the dilation angle occur due to changes of the number and size of the contact points.

- The number of contact points for perfectly mated joints increase proportionally to the area of the sample (k=0).

- For a maximal unmated joint, the number of contact points are constant at an increased scale (k=1).

4.5 Frictional component due to surface roughness

In the previous section about the fundamental mechanics of friction, friction for a microscopic rough but macroscopic smooth surface was discussed. However, for a macroscopic rough surface an additional contribution to the friction angle is added. Patton (1966) introduced the concept of a dilation component, i, and suggested that the total friction angle could be expressed as:

$$\phi_p = \phi_b + i \tag{4.20}$$

where ϕ_p is the total friction angle at peak shear strength and ϕ_b is the basic friction angle.

Ladanyi and Archambult (1970), Barton (1973), and Bandis et al. (1981) added a third component called asperity failure component, sometimes denoted s_n.

It is the dilational component and the asperity failure component that originates from roughness. The magnitude of i and s_n depends on several factors, such as the normal stress, strength of the joint wall surface, the degree of roughness, and also scale. However, what all these factors have in common is that they together govern how, and at which order of the asperities, that the asperities will fail. The failure mode of the asperities is a key factor to understand the conceptual mechanism of the peak shear strength.

How asperities fail, and in turn affect the shear strength, concern a complex process with several different types of failures. For example, Patton (1966) observed that in the primary portion of the failure envelope, sliding occurred prior to shearing through the intact rock, while the secondary portion of the envelope were obtained from tests where the teeth were sheared off at their base without sliding. Furthermore, he observed anomalous reductions in shear strength in some specimens at low normal loads. He wrote that "*This was most common in*

specimens that failed by internal shearing preceding sliding, especially on specimens with teeth which were rectangular or inclined at an angle of 55^o. The reductions in shear strength appeared to be the result of either the introduction of tensile stresses in the teeth due to a possible eccentricity of loading or to a change in the failure mode that varied according to the normal load in the intact material. Either explanation indicated that a change in the mode of failure was related to a change in the slope of the failure envelope."

Results published by Fishman (1990) also suggest that asperities could fail through tensile failure rather than compressive failure. In the same manner, Grasselli (2001) found indications that individual asperities broke by tensile failure instead of compressive failure, since the failure planes tended to be rough and intact fragments sheared from the surface were observed.

This means that failure of asperities can occur by any of the following types: sliding failure, shear or crushing failure, and tensile failure. However, it seems more likely that tensile failure of the asperities would occur at steeper angles of the asperity inclination *i*, while sliding mainly occur at smaller angles of the asperity inclination, *i*.

Between the different failure modes, it is important to distinguish between the mechanical behaviour behind them. Sliding over inclined asperities requires a displacement increment along the contact interface between asperities at contact in order to shear off the adhesive bonds that exist at the contact points. On the other hand, prior to the shear or tensile failure of interlocked asperities, the displacement increment along the contact interface between asperities in contact decreases. This means that no sliding occurs along the side of the asperities simultaneously as interlocking. Therefore, it appears unreasonably to add an asperity failure component, s_n, to a dilation angle, *i*, simultaneously, at least for the same asperity.

In order to investigate how a single asperity can fail at different angles of the asperity inclination, *i*, a calculation of a two dimensional idealized asperity was performed. The idealized asperity is shown in Figure 4.14.

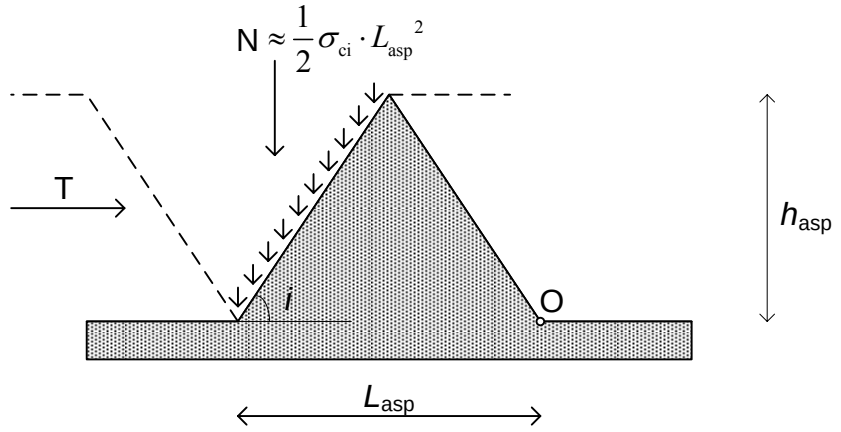

Figure 4.14 Figure of a two dimensional idealized asperity used in the calculation with a base area equal to L_{asp}^2, height, h, and inclination, i.

In the calculations it is first assumed that the normal pressure on the contact points is near the uniaxial compressive strength of the intact rock, i.e. the contact area is equal to the ratio between the normal stress and the uniaxial compressive strength of the joint wall surface such as stated by the adhesion theory. Secondly, when the shear load starts to be applied, it is assumed that only the side of the asperity facing the shear direction is loaded. The width of the asperity is assumed fixed, while the angle of i varies between 0 to 90°.

The resistance for sliding failure, T, along the side of the asperity facing the shear direction is calculated using the primary portion of Patton's criteria.

$$T = N \cdot \tan(\phi_b + i) \tag{4.21}$$

where N is the normal load. It is based on the adhesion theory and equals:

$$N = L_{asp}^2 \cdot \sigma_{ci} \cdot \frac{1}{2} \tag{4.22}$$

since it only is the side of the asperity facing the shear direction that will be in contact. For a shear failure through the intact rock at the base of the idealized asperity, the shear resistance, T, is calculated with Mohr-Coulombs failure criterion.

$$T = c_i \cdot L_{asp}^2 + N \cdot \tan(\phi_i) \tag{4.23}$$

For a tensile failure to occur in the intact rock at the base of the asperity, it is assumed that the average tensile stress at the asperity base needs to exceed the tensile strength of the intact rock. Moment equilibrium at point O in Figure 4.14 gives:

$$T \cdot \frac{h_{asp}}{2} - N \cdot \frac{3}{4} \cdot L_{asp} = \sigma_{ti} \cdot L_{asp}^2 \cdot \frac{L_{asp}}{2} \tag{4.24}$$

where:

$$h_{asp} = \frac{L_{asp}}{2} \cdot \tan(i) \tag{4.25}$$

Combining equation 2.24 and 2.25 gives:

$$T = \frac{(3 \cdot \sigma_{ci} + 4 \cdot \sigma_{ti}) L_{asp}^2}{2 \cdot \tan(i)} \tag{4.26}$$

In the calculations, typical values for intact granite were assumed. The uniaxial compressive strength, σ_{ci}, is assumed to be 150 MPa, the tensile strength, σ_{ti}, to be 10 MPa, cohesion, c_i, to be 20 MPa, and friction angle, ϕ_i, to be 60°. Furthermore,

a basic friction angle, ϕ_b, of 30° has been used, and the base width, L_{asp}, has been set to ten millimetres. The results from this calculation can be seen in Figure 4.15.

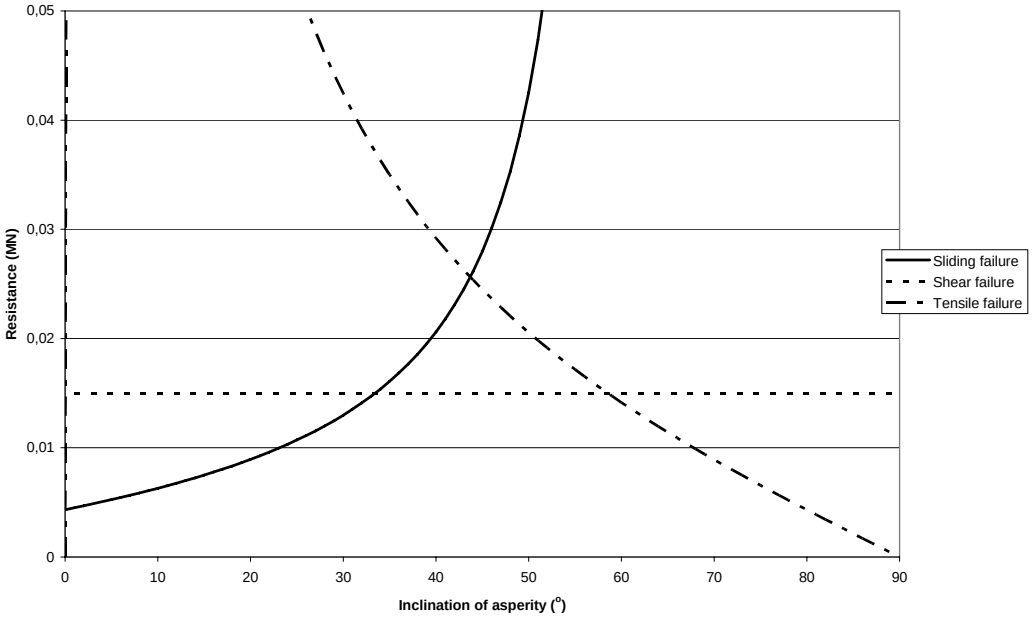

Figure 4.15 Resistances for different failure modes for an idealized asperity where the inclination angle of the asperity varies (sliding failure, equation 4.21; shear failure, equation 4.23; and tensile failure equation 4.26).

The results from the calculations agree with the observations made by Patton (1966). For low values of the asperity inclination, it is sliding failure that probably governs the shear strength. However, around inclination angles above 30°, shearing through, or crushing, of the asperities starts to take place. As the inclination angle further increases, tensile stresses start to appear at the base of the asperity. In the figures above, tensile failure occurs at an inclination angle slightly above 70°.

A limitation with the used model is that the base width is fixed, while the angle i increase. This means that the height, h_{asp}, becomes infinite when the inclination angle, i, approaches 90°. An effect from this can be seen in the results in Figure 4.15, where the strength for tensile failure appears to become zero for values of i close to 90°. However, this is only a hypothetical state and will not occur in a real discontinuity since these high asperities will fail quickly and the state of failure will pass over to shearing of or sliding over the asperities.

Based on the results in Figure 4.15, a total friction angle for different values of i can be calculated for the idealized asperity. The results are shown in Figure 4.16. It should be observed that the limits between different modes of failure shown in Figure 4.16 are most likely not fixed values. At which inclination angles different modes of failure occur depends to a great extent on the geometry and strength of the intact rock for every single asperity.

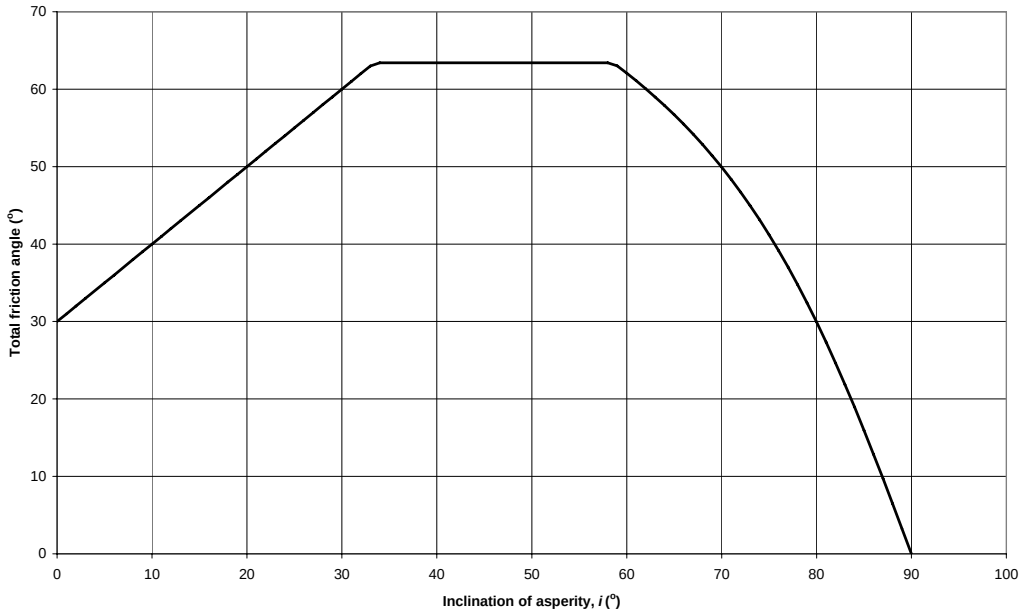

Figure 4.16 Total friction angle for an idealized asperity with a varying angle of inclination i.

This means for example that the horizontal line in Figure 4.16 that represents shear failure of the asperity can both decrease or increase depending on the strength of individual asperities.

Based on the analysis performed above the following assumptions can be made:

- For shearing under a constant normal load, tensile failure and shearing through the asperities mainly occur for samples at small scales.
- For lower inclinations of the asperities, sliding on the asperities is the dominating failure mode.
- This transition between the different failure modes appears to occur around inclinations of the asperities around 35^o for hard rocks. However, this transition angle depends on the cohesion and internal friction angle of the intact material.
- For joints of full size, the peak friction angle can be expressed with the equation proposed by Patton (1966). In other words $\phi_p=\phi_b+i$

4.6 Conceptual model

Based on the literature study and the analyses performed in this chapter, a number of statements and assumptions were made regarding the frictional behaviour and some of the parameters that affect the peak shear strength. From these, it is possible to set up a conceptual model for the peak shear strength at different scales.

The peak friction angle for a rough surface can be divided into two parts; one part which originate from a smooth but microscopic rough surface defined as the basic friction angle, ϕ_b; and one part which originate from the macroscopic roughness defined as the dilation angle, i.

For the smooth but microscopic rough surface, contact points will develop where asperities touch each other. At these contact points, the stress may become so high that the material yields plastically. Therefore, the true area of contact could be expressed as the quotient between the normal load and the yielding stress of the material. At these contact points, the surfaces are welded together at junctions creating adhesive bonds. The shear resistance is provided by the adhesive strength of these junctions. It implies that the friction could be expressed as the quotient between the sum of the adhesive strength for these junctions and the yield stress of the surface. This mechanism explains the constant part of the friction angle in all failure criteria, ϕ_b.

The other part of the friction angle that originates from a macroscopic rough surface is more complex. It has been shown that roughness of joint surfaces can be described using self-affine fractal models in the relevant range of scales. This implies that there exists a scaling relation between asperity heights and asperity lengths of different orders, where the increase of the asperity heights is lower than the asperity lengths. Furthermore, it implies that it may be possible to idealize the surface roughness as a large number of superimposed asperities at different scales. The range of scale for this fractal self-affine model could be assumed to start at the grain size of the intact rock up to a possible stationary threshold of the roughness.

How these asperities fail during shear will govern the contribution from roughness to the peak friction angle. In principle, three different failure modes are possible for the asperities: (1) sliding over the asperities, (2) shearing or crushing of the asperities, and (3) tensile failure. However, shearing through and tensile failure mainly occur for high inclinations of the asperities. For lower inclinations of the asperities, sliding appears to be the dominating failure mode. For hard rocks, the transition between these two modes of failure is approximately around 35^o. This means that an asperity failure component, if present, only exists for small scale samples under low normal stresses. For full sized joints, sliding over the asperities will be the dominating failure mode and the average angle of the contacting asperities will be equal to the dilation angle, i. As a consequence, the peak friction angle for a full sized joint could be expressed as the sum of the basic friction angle and the dilation angle.

The mechanism behind the dilation angle could be explained as follows. When shearing is initiated for a perfectly mated, unfilled and rough joint, subjected to a constant normal load, the asperities will first be deformed elastically. At the same time, the load at the initial contact points starts to increase and quickly reaches the yield strength of the material. At this point, the smallest asperities facing the shear direction will be crushed since the potential contact area for these asperities are too small to carry the total load. This process will successively continue until a critical number of asperities are reached when the potential contact area becomes

equal to the true contact area. At this state, the measured dip angle of the contacting asperities becomes equal to the dilation angle of the joint surface.

Changes in the dilation angle for joint of different sizes are due to changes in the size of the contact points. The adhesion theory states that for a constant normal stress, under the assumption that the plastic yield stress of the asperities remains constant; the ratio between contact area and sample area should remain constant for joints of different sizes. At the same time, when a scale effect is observed, it can also be seen that the size of the contact points increases with an increased scale, see for example Bandis (1980). For a perfectly mated joint, the number of contact points under low normal stresses could be expected to increase proportionally to the increase of the area of the sample. When this occurs, no scale effect is observed. On the other hand, if the joint is maximally unmated, the number of contact points could be expected to remain constant at an increased scale. For these types of joints, a full scale effect could be observed.

From the conceptual understandings presented above, five basic mechanisms can be identified to derive a failure criterion for the peak shear strength for full sized joints. These five mechanisms are shortly described below and presented in equations 4.27 to 4.31.

For a full sized joint, the peak shear strength, τ_p, for a rough and unfilled joint can be described with the following equation:

$$\tau_p = \sigma'_n \cdot \tan(\phi_b + i_n) \tag{4.27}$$

where ϕ_b is the basic friction angle and i_n is the dilation angle for a full sized joint. σ'_n is the effective normal stress.

The adhesion theory states that the true contact area ratio, $A_{c,r}$, can be expressed as the quotient between effective normal stress, σ'_n, and yielding stress of the joint surface, σ_{ci}:

$$A_{c,r} = \frac{\sigma'_n}{\sigma_{ci}} \tag{4.28}$$

The potential contact area ratio, $A_{c,p}$, for rough joint surfaces could be expressed by an empirical formulation as suggested by Grasselli (2001):

$$A_{c,p} = A_o \left[\frac{\theta^*_{max} - \theta^*}{\theta^*_{max}} \right]^C \tag{4.29}$$

where A_o is the maximum possible contact area ratio against the shear direction. θ^*_{max} is the maximum measured dip angle measured on the sample and θ^* is the measured dip angle defined as the inclination of the asperities against the shear direction. C is a roughness parameter which governs the concavity of the curve.

Surface roughness for joints can be described using self-affine fractal models. Therefore, the relation between asperity heights, h_{asp}, and base lengths of different asperity orders, L_{asp}, can be expressed with a power function on the form:

$$h_{asp} = a \cdot L_{asp}{}^{H} \tag{4.30}$$

where a is the amplitude constant and H is the Hurst exponent, both based on the base lengths of different asperity orders.

Under a constant normal stress, since the true area of contact is constant, the change in the number of contact points with an increased size of the joints will govern how the area of the average contacting asperities will change. If the contact points are assumed to be shaped quadratic on the joint wall surface, this change could be expressed as:

$$L_{asp,n} = L_{asp,g} \cdot \left(\frac{L_n}{L_g} \right)^k \tag{4.31}$$

where L is the length of the sample and L_{asp} is the base length of the asperity. The subscript (g) corresponds to grain size and (n) to full sized joints. k is an empirical constant which range between zero and one, depending on the degree of matedness.

Using the five equations above, an equation has been derived to show how the dilation angle changes with roughness, the strength of the surface, the normal stress and increased scale.

When equilibrium is reached with the potential contact area equal to the true contact area, the measured dip angle, θ^*, becomes equal to the inclination of the asperities where sliding occurs, i. In other words, the apparent dip angle, θ^*, becomes equal to the dilation angle, i. Combining equation 4.28 and 4.29, the dilation angle, i, for a perfectly mated joint could be expressed as:

$$i = \theta^*_{\max} - 10^{\frac{\log\frac{\sigma'_n}{\sigma_{ci}} - \log A_o}{C}} \cdot \theta^*_{\max} \tag{4.32}$$

The dilation angle is by geometry calculated as:

$$i = \arctan\left(\frac{h_{asp}}{0{,}5 \cdot L_{asp}} \right) \tag{4.33}$$

By using the scaling relation expressed in equation 4.30, together with equation 4.32 and 4.33, the length of the contacting asperities at grain size could also be expressed as:

$$L_{asp,g} = \left[0,5a^{-1} \left[\tan\left(\theta^*_{\max} - 10^{\frac{\log\frac{\sigma'_n}{\sigma_{ci}} - \log A_o}{C}} \cdot \theta^*_{\max} \right) \right] \right]^{\frac{1}{H-1}} \quad (4.34)$$

Combining equation 4.30, 4.31, 4.33 and 4.34, the equation which express the dilation angle for full sized joints becomes:

$$i_n = \arctan\left(2a \cdot \left(\left[0,5a^{-1} \left[\tan\left(\theta^*_{\max} - 10^{\frac{\log\frac{\sigma'_n}{\sigma_{ci}} - \log A_o}{C}} \cdot \theta^*_{\max} \right) \right] \right]^{\frac{1}{H-1}} \cdot \left(\frac{L_n}{L_g} \right)^{`k} \right)^{H-1} \right) \quad (4.35)$$

Equation 4.35 could be simplified into:

$$i_n = \left(\theta^*_{\max} - 10^{\frac{\log\frac{\sigma'_n}{\sigma_{ci}} - \log A_o}{C}} \cdot \theta^*_{\max} \right) \cdot \left(\frac{L_n}{L_g} \right)^{kH-k} \quad (4.36)$$

The equation above suggests that the conceptual behaviour of the dilation angle could be summarized according to Figure 4.17.

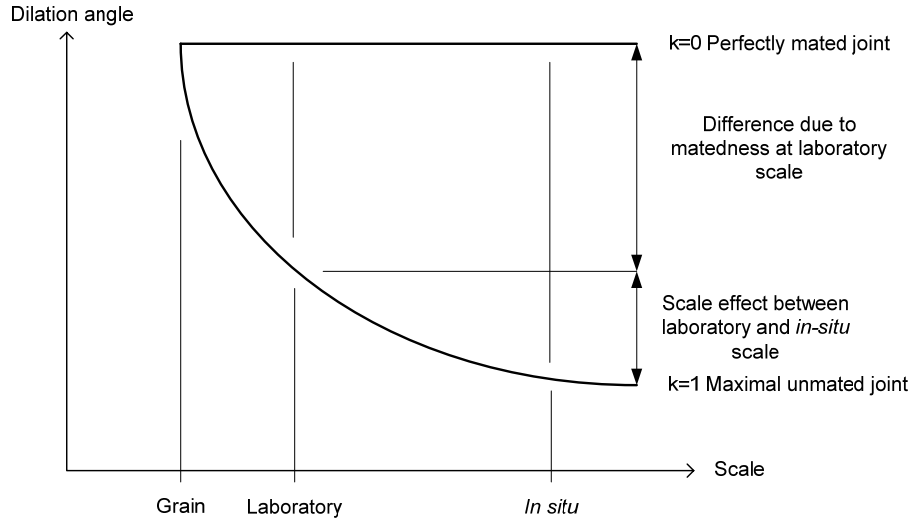

Figure 4.17 Conceptual behaviour of the dilation angle at different scales and matedness.

An example on the behaviour of the dilation angle for an unfilled rough joint was analysed by using equation 4.36. In this example, the dilation angle for a perfectly mated joint was assumed to be 35^o under a constant normal stress and the grain size was assumed to be 1 mm. The Hurst exponent, *H*, was assumed to be 0.8. The example shows how the dilation angle changes at different scales and different degrees of matedness. The results are presented in Figure 4.18 and 4.19.

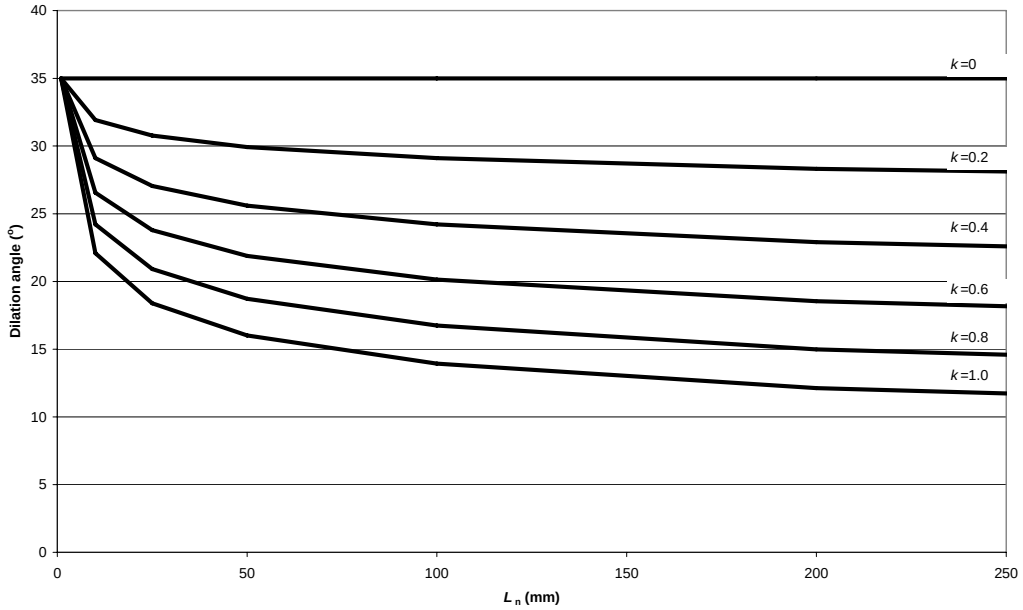

Figure 4.18 Example of changes in the dilation angle at different degrees of matedness up to a scale of 250 mm.

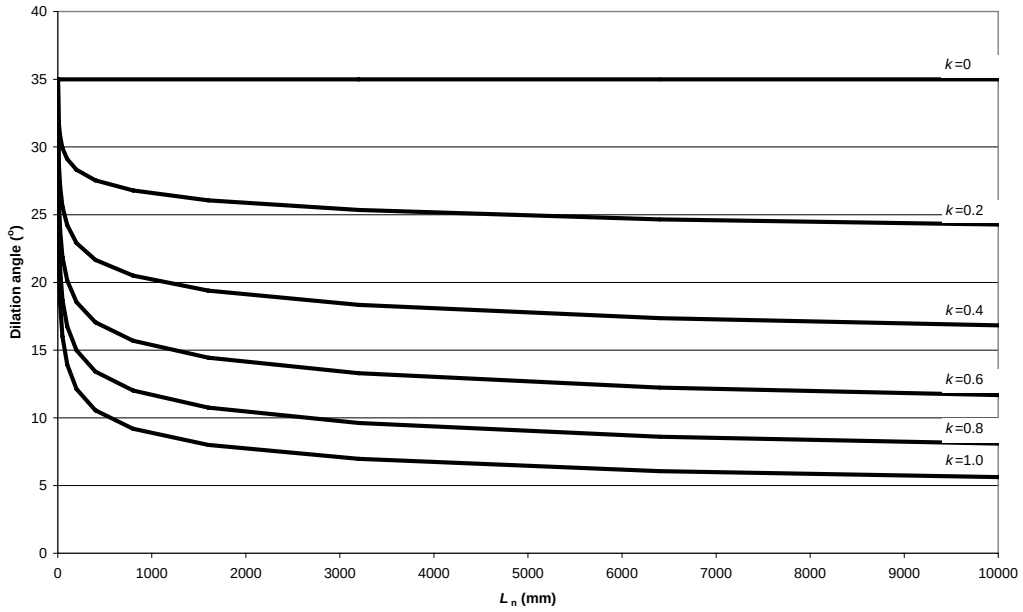

Figure 4.19 Example of changes in the dilation angle at different degrees of matedness up to a scale of 10 000 mm (No stationary threshold for the roughness has been considered).

This conceptual model is based on several statements and assumptions, which are simplified descriptions of the reality. One limitation is that no scale dependence is used for the yielding strength of the joint surface. It could be expected that active asperities at laboratory scale, only at millimetres scale, probably has yield strength higher than the uniaxial compressive strength of the intact material.

It should also be emphasized that the conceptual model is developed under the assumption that the normal stress is monotonically increasing. Changes in the dilation angle due to cyclic stress changes are not considered.

It should also be observed that the calculated length in equation 4.34 is derived from a regression curve based on the average inclination of all asperities present on the sample at different sampling sizes. However, only a small percentage of the sample is involved in the shearing. If the average inclination of all asperities over the whole sample is used to determine the constants, the amplitude constant, a, of contacting asperities will be underestimated. This is of no importance if the purpose is only to estimate i_n, since a does not effect it. However, if it is of interest to calculate the true length of the contacting asperities, it is necessary to base the regression analysis with the constants a and H derived from the asperities in contact. This could be achieved if the area under the tail of the Gaussian distribution curve are used which corresponds to the true contact area according to the adhesion theory.

4.7 Verification analysis

In order to determine if the conceptual model realistically captures the fundamental principles of the shearing mechanism at peak shear strength, calculations were performed to investigate it. These calculations consist of two parts. The first part investigates if the adhesion theory combined with measurements of surface roughness at grain scale can be used to calculate the dilation angle for a perfectly mated joint. The other part investigates if the Hurst exponent, H, together with the constant of matedness, k, could be used to describe changes in the dilation angle for joint planes of different sizes.

4.7.1 Grain size scale

Grasselli (2001) performed a large number of shear tests on fresh tensile induced joints in the scale 140 by 140 mm. The fact that they were fresh and tensile induced means that the constant of matedness was assumed to be 0. Furthermore, Grasselli (2001) determined the parameters for the potential contact area ratio with a resolution equal to 0.3 mm. It was in these calculations assumed that this resolution represent a grain scale for the intact rock of the joint surface. By using equation 4.32 was the dilation angle calculated and compared with measured dilation angles from the shear tests. Data from Grasselli (2001), together with calculated dilation angles are presented in Table 4.1 and 4.2. The results from the comparison between calculated and measured dilations angles are presented in Figure 4.20.

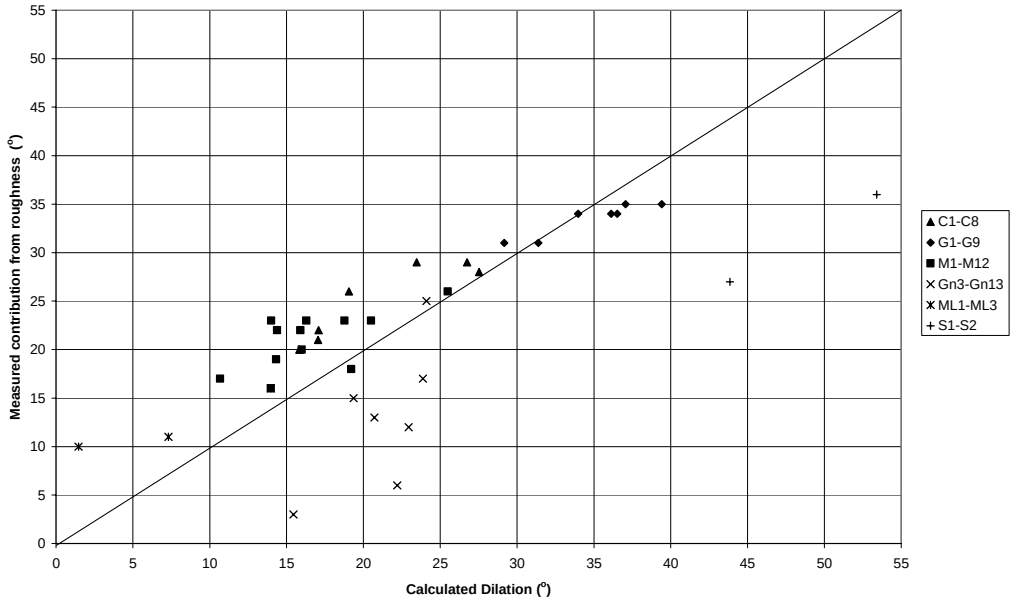

Figure 4.20 Calculated dilation with the conceptual model at laboratory scale compared to measured contribution to the friction angle from roughness in Grasselli´s (2001) samples.

If the results in Figure 4.20 are studied, three things can be observed. First, it can be seen that the calculated dilation agree reasonably well with measured contribution from roughness. Sliding over the asperities appears to be the dominating failure mechanisms for asperities with an inclination up to 35°. At higher calculated values for the dilation, they appear to deviate from the measured contribution from roughness. This is in line with expected behaviour from the calculations presented in Figure 4.16, where sliding over the asperities occurs up to inclinations of about 35°. However, only a few of Grasselli´s (2001) tests have a calculated dilation angle which exceeds 35° and no firm conclusions can be drawn.

Secondly, it can be seen that the Gneiss samples clearly deviate from the expected behaviour. The cause for this deviation might be due to an anisotropic uniaxial compressive strength for the gneiss due to foliation. For example, Grasselli (2001) introduced the parameter α is his criterion, which was the angle of schistosity planes in the rock with respect to the normal of the joint.

The third thing that can be observed in Figure 4.20 is that the calculated dilation angle usually is a little smaller than observed contribution from roughness, especially for the samples with a lower uniaxial compressive strength. The reason for this could be due to a low estimated basic friction angle, ϕ_b.

Another possible explanation is that the strength of the asperities in reality is higher than the uniaxial compressive strength. The samples that Grasselli tested were 140 by 140 mm. The size of the contact points are small compared to the samples for testing the uniaxial compressive strength. It is also well known that the uniaxial compressive strength is scale dependent; see for example the empirical correlations proposed by Hoek and Brown (1980), Barton (1987) and Wagner (1987). It therefore seems realistic that the strength of individual contact points at this sample size is higher than the uniaxial compressive strength.

Table 4.1 Mechanical properties of rocks used in shear test by Grasselli (2001)

Rock type	Sample Name	σ_{ci} (MPa)	ϕ_b (^{o})
Magny Limestone	C	25	36
Tarn Granite	G	173	34
Gneiss	Gn	184*	36
Carrara Marble	M	87	37
Sandstone	ML	10	37
Serpentite	S	74	39

*) 160 MPa for sample Gn6

Tabell 4.2 Data from Grasselli (2001) of surface roughness characterization and shear test results of different samples together with calculated dilation.

	Surface roughness characterization			Results shear tests			Performed calculation	
Sample	A_o	C	Θ^*_{max} (^{o})	ϕ_p (^{o})	σ_n (MPa)	i (^{o})	$A_{c,th}$	i (^{o})
C1	0.491	7.03	80	65	1.07	29	0.043	23
C2	0.462	5.64	80	64	1.07	28	0.043	28
C3	0.507	6.18	88	56	3.72	20	0.149	16
C4	0.508	4.74	65	62	2.45	26	0.098	19
C5	0.495	5.26	74	58	3.11	22	0.124	17
C6	0.546	5.19	68	65	1.02	29	0.041	27
C8	0.555	5.71	74	57	3.11	21	0.124	17
G1	0.522	5.75	72	68	2.30	34	0.013	34
G2	0.553	6.63	84	68	2.30	34	0.013	36
G4	0.484	6.12	65	65	2.19	31	0.013	29
G5	0.460	5.33	57	65	1.12	31	0.007	31
G6	0.477	7.39	84	69	1.12	35	0.007	37
G7	0.470	7.15	81	68	1.12	34	0.007	37
G9	0.508	5.85	75	69	1.12	35	0.007	39
Gn3	0.496	8.47	65	42	2.65	6	0.014	22
Gn6	0.462	8.52	69	61	1.90	25	0.012	24
Gn9	0.488	8.12	63	49	3.52	13	0.019	21
Gn10	0.500	8.18	70	48	3.57	12	0.019	23
Gn11	0.432	10.28	74	51	3.52	15	0.019	19
Gn12	0.413	8.87	66	39	4.08	3	0.022	15
Gn13	0.503	9.17	74	53	2.60	7	0.014	24
M1	0.513	9.64	76	63	0.87	26	0.010	25
M2	0.399	9.36	51	53	1.73	16	0.020	14
M3	0.509	14.93	83	55	0.87	18	0.010	19
M4	0.501	10.51	77	57	3.78	20	0.043	16
M5	0.533	8.92	59	60	2.60	23	0.030	16
M6	0.450	10.18	68	59	2.60	22	0.030	16
M7	0.529	10.75	69	56	3.78	19	0.043	14
M8	0.459	10.52	72	59	3.83	22	0.044	14
M9	0.494	10.36	59	60	2.60	23	0.030	14
M10	0.515	10.79	67	60	0.87	23	0.010	21
M11	0.533	9.89	68	54	8.57	17	0.099	11
M12	0.429	7.28	55	60	1.79	23	0.021	19
ML1	0.573	7.25	66	53	1.02	16	0.102	14
ML2	0.481	5.66	55	47	4.13	10	0.413	1
ML3	0.523	7.81	66	48	2.09	11	0.209	7
S1	0.497	4.99	83	66	1.94	27	0.012	44
S2	0.497	4.58	86	75	0.97	36	0.006	53

The yield strength might be somewhere between the transition stress and the uniaxial compressive strength. If this is the case, a smaller contact area could be expected which in turn would imply that a higher dilation angle will be calculated.

A third explanation could also be that the resolution used by Grasselli (2001) does not represent the grain size of the intact rock. He used a resolution of 0.3 by 0.3 mm. If a higher resolution had been used, the calculated dilation angle would increase.

For the rock samples with low uniaxial normal stress, i.e. soft rock, shearing through the base of the might occur at a low dilation angle. This might explain the poor fit for the sandstone samples (ML1-ML3).

In summary, the performed calculations, with the exception of the Gneiss samples, support the results which suggest that the developed model could be used to estimate the dilation angle under different normal loads for a perfectly mated full sized joint. Furthermore, sliding over the asperities is the major failure mechanism, at least for hard rocks. This implies that the peak friction angle could be expressed as the sum of the basic friction angle and the dilation angle.

4.7.2 Full size scale

In order to investigate if the conceptual model describes changes in the dilation angle due to changes in scale correctly, it is necessary to have data from performed shear tests in different sizes. Furthermore, the Hurst exponent must have been determined together with parameters for the potential contact area ratio and the constant which describes the degree of matedness. Cases do not exist in the literature where all these parameters and test results were derived. Therefore, it was not possible to perform an accurate verification.

To be able to perform some form of comparison, five shear tests performed by Lanaro (2001) were used. The results from these tests were compared to results obtained with Barton and Bandis (1982) empirical equations for scale corrections. The shear strength of the samples tested by Lanaro (2001) was performed with direct shear test carried out according to the recommendations by ISRM (1981). The tests were performed on drill core samples with a diameter of 61 mm. The orientation of the joint was perpendicular to the core axis for all samples. All results from the shear tests were not published by Lanaro, but were obtained through personal communication.

Lanaro (2001) measured the surface topography of the joint surfaces with a 3D laser scanner having an accuracy of ±50 μm. The statistics of the average slope were expressed by Lanaro using a power law for the standard deviation of the mean slope, σ_{slope}, calculated for sub-samples of different sampling sizes, Δx.

$$\sigma_{slope} = \sqrt{G_{ah}} \cdot \Delta x^{H-1} \tag{4.37}$$

Where G_{ah} is a dimensional proportionality constant related to the amplitude or asperity height and H is the Hurst exponent, see Lanaro (2001) for a more thorough description of the different parameters. The sampling size, Δx, varied between 2 to 20 mm. No stationary threshold for the standard deviation of the asperity height was observed in this sampling size interval.

The samples consisted of Äspö Diorite with inconclusive band of fine grained granite. The uniaxial compressive strength was estimated to 195 MPa. Data from the surface characterization for these five samples are presented in Table 4.3 below.

Table 4.3 Data for surface characterization of five samples from Lanaro (2001).

Sample	$G_{ah}^{0,5}$	H
KA3579G-9.43	0.256	0.738
KA3579G-10.73	0.164	0.799
KA3579G-11,25	0.187	0.686
KA3579G-14.86	0.153	0.676
KA3579G-19.45	0.117	0.615

Each sample was tested under normal stresses equal to 0.5 MPa, 5 MPa and 10 MPa. The exceptions were KA3579G-9.43 and KA3579G-10.73 which were tested at 1 MPa instead of 0.5 MPa. In this analysis, the results from the tests with the lowest normal stress were used, since they were performed with an undamaged joint surface.

In order to estimate the basic friction angle it was assumed that the residual shear strength from the tests with a normal stress of 10 MPa corresponds to the basic friction angle. This methodology was used since normal and shear deformation during the tests were logged at long time intervals (10 sec), which resulted in an insufficient resolution for the dilation angle. Therefore, reliable basic friction angles could not be derived from measured normal and shear deformations. With this methodology, a basic friction angle of 34.4^o was derived. The standard deviation of the five samples for the basic friction angle were 2.56^o, giving a coefficient of variation of 0.07.

In the table below, normal stress, σ_n, measured peak shear strength, ϕ_p, shear displacement at peak shear strength, $\delta_{s,p}$, and estimated contribution from roughness, ϕ_p-ϕ_b, together with back calculated values on *JRC* are presented based on the shear tests performed by Lanaro.

Table 4.4 Measured normal stress, σ_n, peak shear strength, ϕ_p, shear displacement at peak shear strength, $\delta_{s,p}$, and estimated contribution from roughness, ϕ_p-ϕ_b, together with back calculated JRC values based on shear test by Lanaro.

Sample	σ_n (MPa)	ϕ_p (^{o})	$\delta_{s,p}$ (mm)	ϕ_p-ϕ_b (^{o})	*JRC*
KA3579G-9.43	1.08	51.1	0.97	16.7	7.4
KA3579G-10.73	1.10	66.5	0.33	32.1	14.3
KA3579G-11,25	0.63	59.0	0.51	24.6	9.9
KA3579G-14.86	0.60	50.2	0.44	15.8	6.3
KA3579G-19.45	0.56	63.8	0.23	29.4	11.6

However, no determination of the parameters for the potential contact area ratio and no estimation of the degree of matedness were performed. This means that it only is possible to perform an indirect comparison between the conceptual model and the Barton and Bandis (1982) model.

The comparison performed here was done with the following methodology. The dilation angle, i_n, was based on the results from the shear test performed by Lanaro and the constant of matedness, k, was varied. The ratio L_n/L_g was based on the sample scale 61 mm. Values on the Hurst exponent was chosen according to Table 4.3. As previously mentioned, this is no direct verification. Also, to base the estimation on the sample scale 61 mm instead on the grain scale means that the dilation angles will not be estimated in the same way. This effect decreases for larger scales and are mainly of importance for scales under a few decimetres. Since no other data is available, this methodology was used as a rough indication to see if the reduction obtained with the equation proposed by Barton and Bandis (1982) agree with those proposed with the conceptual model.

Based on this methodology, the contribution from roughness at 0.1 m, 0.3 m, 0.5 m, 1 m, 5 m, and 10 m was calculated for the five samples using equation 4.36. The results are presented in Figure 4.21 and 4.22.

As the results in Figure 4.21 and 4.22 shows, the conceptual model predicts changes in the dilation angle which agree with the results using the Barton and Bandis (1982) model for a k=0.8. The close correlation between the curves suggests that the conceptual model probably captures the basic mechanism behind the scale effect; namely how the inclination of the asperities at the contact points changes. However, it should be observed that the methodology where the sample scale is used as a reference scale gives values on k which probably are slightly higher than they would have been if the grain scale was used. Supplementary calculations not shown here indicate that a more correct value on k might be around 0.6 if a grain scale was used. This value also corresponds better to the results presented in Figure 4.8.

It is interesting to notice that Barton and Bandis uses scale correction on both the *JRC* and the *JCS* component, while the conceptual model uses only changes in inclination of active asperities and degree of matedness. It is possible that the effect from an unmated joint, i.e. k<1, has been interpreted by Barton and Bandis (1982) as a possible scale dependent *JCS* component. If it really exists, a contribution to the scale effect from changes in the uniaxial compressive strength, and how large this contribution might be, can not be concluded with this analysis.

Furthermore, for sample KA3579G-10.73, the predicted values with Barton and Bandis (1982) model appears to be underestimated at larger scales. This agrees with the discussion in the previous chapter, see Figure 3.5, where it was seen that high *JRC* values at laboratory scale, in combination with larger scales, resulted in a contribution from roughness that probably are too low. On the other hand, it should be kept in mind when these results are analysed that Barton and Bandis (1982) model were not derived for scales which exceeds the block size, i.e. a few meters.

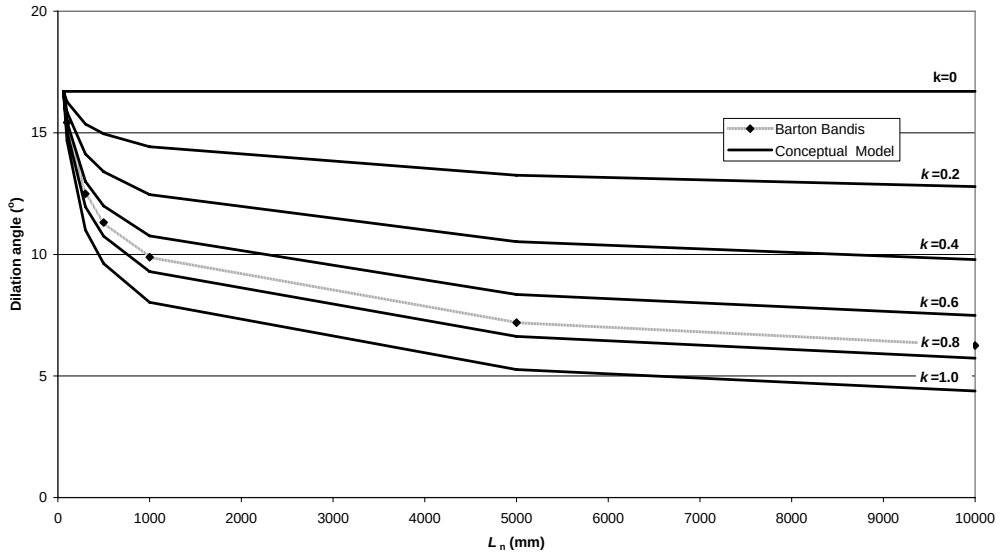

Figure 4.21 Comparison between predicted contribution from surface roughness according to Barton Bandis and predicted dilation angle from conceptual model for sample KA3579G-9,43 at a normal stress of 1,08 MPa.

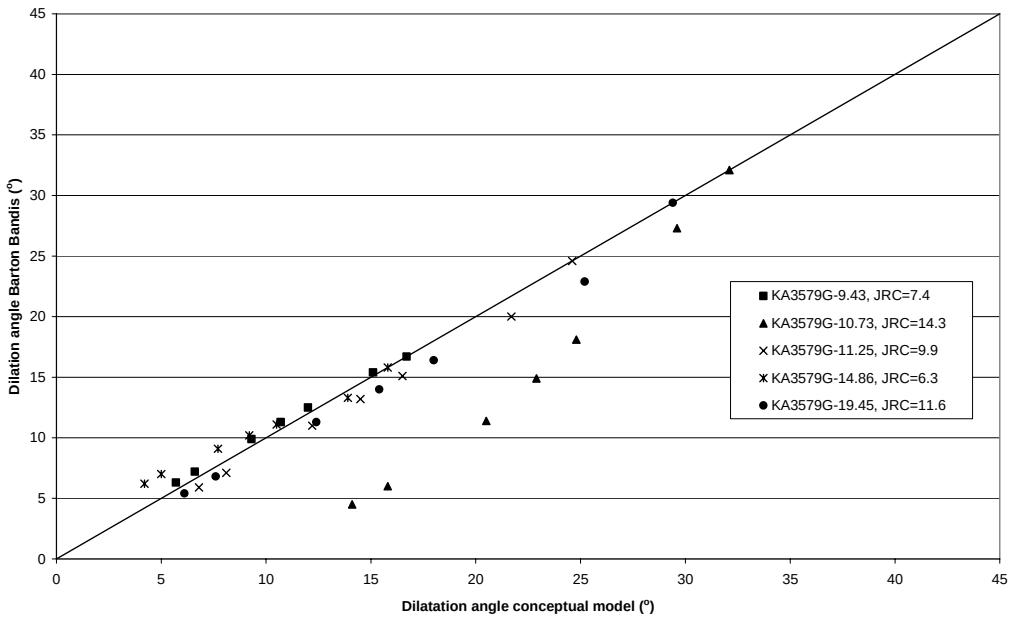

Figure 4.22 Predicted dilation angle at the scales 0.061 m, 0.1 m, 0.3 m, 0.5 m, 1 m, 5 m, and 10 m from conceptual model compared against values predicted with Barton Bandis criteria using samples from Lanaro (2001).

4.8 Conclusions

In order to obtain better and more detailed understandings of the mechanisms that affect the peak shear strength of full sized joints at different scales, a conceptual model for unfilled rough joints was developed based on adhesion theory, measurements of surface roughness and assumption regarding the change in size of contact points.

This model was partly verified for samples under different normal loads in laboratory scale and partially by comparing results for different scales with the empirical equations for scale correction proposed by Barton and Bandis (1982).

However, more shear tests have to be performed at different scales, where all the parameters necessary to calculate the dilation angle with the conceptual model have been determined, before the model could be used with confidence.

Based on the results from these analyses it can be concluded that the conceptual mode in the main questions can: (1) propose an explanation for the measured dilation angle for laboratory samples of perfectly mated unfilled rough joints and, (2) suggest an explanation for changes in the dilation angle due to an increased scale and different degrees of matedness.

5 LABORATORY AND *IN SITU* SHEAR TESTS AT LÅNGBJÖRN HYDROPOWER STATION

5.1 Introduction

Långbjörn hydropower station is located at the river Ångermanälven in the county of Jämtland and was put into operation 1960. The concrete dam is about 30 m in height. The central part of the dam consists of two power intakes and a spillway section of buttress type with three spillway openings. The dam is divided into monoliths with a width between 8 to 18 m. On the left side there are two abutment monoliths of buttress type, and on the right side there are three of buttress type, see Figure 5.1.

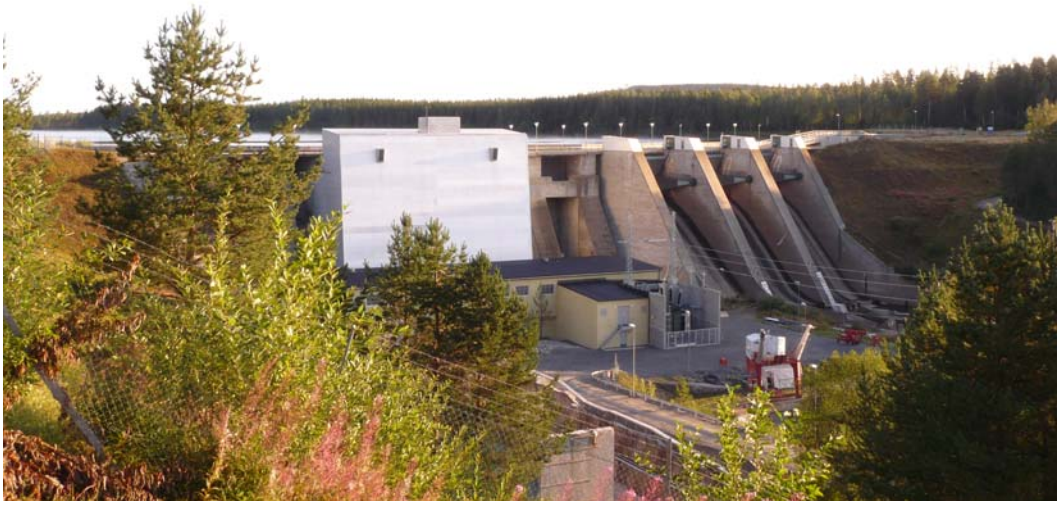

Figure 5.1 Overview of Långbjörn hydropower station.

The geology at the site was investigated by core drilling and surveys of outcrops (VBB Anläggning 2000a). The intact rock consists of grey coarse grained granite with some small intrusions of pegmatite. Two almost vertical joint sets exist with strikes perpendicular and parallel to the dam axis respectively. In addition, a joint set with varying strike and an almost horizontal dip exist in the rock mass. Some of these joints are thought to be relaxation joints with a high persistence, see Figure 5.2. These joints are slightly weathered and have an aperture between 0-5 mm. The joints are, in general, unfilled, but some infilling materials consisting of weathered materials and silt particles were found in some joints at shallow depth under the spillway section.

In 1994, by commission of the dam owner Vattenfall, a SEED (Safety Evaluation of Existing Dams) evaluation of the structure was performed (VBB Anläggning 1994). In this evaluation, questions regarding the stability of the dam emerged.

One of the questions was the safety against sliding along horizontal joints in the rock mass. As a consequence, the shear strength of these joints was investigated based on laboratory shear tests on drilled cores performed at the Department of Soil and Rock Mechanics, Royal Institute of Technology (KTH), in the year 2000 (VBB Anläggning 2000b). The results from these tests are described in a separate subchapter below.

Based on the estimated shear strength from the laboratory testing of the horizontal joints, a new stability analysis of the concrete dam was performed (SWECO VBB VIAK 2002). In this analysis, it was concluded that the dam did not meet the acceptance requirements for sliding stability. Therefore, in 2006, the dam was reinforced with pre-stressed anchor cables. However, there still exist uncertainties regarding the shear strength of the joints since it mainly was estimated on results from small scale laboratory testing. In order to reduce these uncertainties, and at the same time investigate possible scale effects for the shear strength of unfilled and rough joints, a shear testing programme at different scales in both laboratory and *in situ* was undertaken.

Figure 5.2 Photo of persistent relaxation joints in the tailrace channel.

The main objective for the shear tests performed and described in this chapter is to obtain information for estimating the shear strength of the horizontal joints present in the rock mass under the dam. An additional objective is to study possible scale effects on the peak shear strength of the joints.

In this chapter, the results from previously performed laboratory shear tests at KTH are first presented, followed by laboratory shear tests performed at SP (Technical Research Institute of Sweden) and LTU (Luleå Technical University). Thereafter, the *in situ* shear test is described and the results are presented. Based on this series of tests of joint samples of different sizes, the peak shear strength and possible scale effects on the friction angle are investigated and discussed. Finally, a summary and an interpretation of the results are performed. At the end, conclusions are presented.

5.2 Previously performed laboratory shear tests

In 2000, by commission of VBB Anläggning, the Department of Soil and Rock Mechanics at KTH performed several shear tests on joint samples from cores drilled under the dam (VBB Anläggning 2000b). The shear tests were performed according to the methods suggested by ISRM (ISRM 1981). All of the samples consisted of coarse grained granite. Four samples were sheared, each under four different normal stresses, resulting in sixteen shear test cases. The diameter of the samples was 42 mm for two samples and 62 mm for the other two.

Surface roughness was characterized by estimating the parameter *JRC* of the samples. This was done by visually comparing the roughness of the joint surfaces against predefined profiles by Barton and Choubey (1977).

The results from the shear tests, together with estimated and back calculated *JRC* values, are presented in Table 5.1 below. For the back calculation of the *JRC* parameter, a basic friction angle of 35° was used. The joint wall compressive strength, *JCS*, was estimated to be 100 MPa.

Table 5.1 Results from shear tests showing normal stress, σ_n, peak shear strength, τ_p, shear displacement at peak strength, $\delta_{s,p}$, and peak friction angle, ϕ_p, together with estimated and back calculated JRC values (VBB Anläggning 2000b).

Sample	σ_n (MPa)	τ_p (MPa)	$\delta_{s,p}$ (mm)	ϕ_p (°)	$JRC_{estimated}$	$JRC_{back\ calculated}$
D4 ϕ=42 mm	0.89	1.71	2.5	62.5	10	13.4
	1.76	2.52	0.7	55.1		11.5
	2.64	3.32	1.1	51.5		10.5
	3.52	4.57	1.3	52.4		12.0
D10 ϕ=42 mm	0.79	1.22	1.0	57.1	9	10.5
	1.44	2.04	1.5	53.7		10.2
	2.88	3.39	1.5	49.7		9.5
	4.05	4.56	1.9	48.4		9.6
A1 ϕ=62 mm	0.60	2.03	2.2	73.5	6	17.3
	1.11	2.83	1.6	61.3		13.5
	2.21	4.18	1.5	62.1		16.4
	3.31	5.57	2.0	59.3		16.4
B3 ϕ=62 mm	0.71	1.41	1.0	63.3	5	13.2
	1.42	2.01	1.3	54.8		10.7
	2.13	3.21	1.7	56.4		10.0
	2.98	3.88	2.3	52.5		11.5

As the results in Table 5.1 shows, the peak friction angle varied between 48.4 and 73.5 degrees. For the samples tested under the lowest normal stress, the mean peak friction angle was 64.1° with a standard deviation of 8.6°. The peak friction angle occurred at shear displacements between 1.0 and 2.5 mm.

Studying the estimated and back calculated values on *JRC*, it can be seen that there exist a discrepancy between them. One reason for this is that there exists a subjective uncertainty in choosing correct *JRC* values from predefined profiles. It can also be seen that there exist variations in the back calculated *JRC* for different normal stresses. As a general trend, *JRC* becomes lower with increasing normal

stresses. This is mainly an effect from a successive degradation of the surface roughness with increasing normal stress for each shear test case.

Based on the results from these shear tests, an attempt was made to analyse if the peak friction angle at laboratory scale could be expressed as the sum of the basic friction angle and the dilation angle, ϕ_b+i, as suggested in Chapter 4. However, when the files containing the results from the shear tests were analysed, it became clear that the sampling interval was too long and that the shear rate was not entirely constant. It was therefore not possible to calculate an accurate dilation angle with a sufficiently small increment of shear and normal displacements.

5.3 Laboratory shear test performed at SP

5.3.1 Introduction

In order to further analyse the peak shear strength at laboratory scale, three additional direct shear tests on drilled cores containing a joint were carried out by commission of the author. The testing was carried out by the Technical Research Institute of Sweden (SP). The main objective, in addition to measure the peak shear strength, was to investigate if the peak shear strength could be expressed as the sum of a basic friction angle and a dilation angle.

5.3.2 Test samples

When joints are tested, and results are compared against each other, it is important that the shear tests are carried out on similar types of joints, preferably on the same joint if possible, since the surface characteristics of the joints might be different from one joint to another. For the joints tested in this chapter, it is samples representative for the persistent joints that are of interest. The surfaces of these joints are usually slightly weathered and not perfectly mated, contrary to the other joints in the rock mass which could be expected to be unweathered and better mated. In this case, the author was not able to retrieve samples from the same joint. Instead, joints with similar surface characteristics were retrieved from drilled cores stored under the dam with the following methodology.

The matedness of the joints was first visually inspected when the cores were lying in their boxes. Those joints which were horizontal and not perfectly mated were identified. The surfaces of these joints were further inspected in order to judge if the surface could be considered to originate from more persistent joints. Example of reduced matedness due to weathering for one of the samples can be seen in Figure 5.3 below. On the basis of this visual inspection, three samples were chosen, B1, B5, and D24. They were then sent to SP for direct shear testing. However, it should be observed that this methodology does not necessarily mean that the samples were taken from the intended relaxation joints, since it is difficult to judge the persistence of a specific joint from drilled cores.

The rock type for all the samples is gray, coarse grained granite. Since the orientations of the joints with respect to the axis of the drilled cores were not exactly perpendicular, the shapes of the samples were not exactly circular. In Table 5.2, the length and width, together with the total area of the joint surfaces, are presented. Pictures of the joint surfaces in profile can be seen in Figure 5.4.

Table 5.2 Length, width, and total area of the joint surfaces.

Sample	Width (mm)	Length (mm)	Area (cm^2)
B1	61.6	63.1	30.5
B5	61.8	63.1	30.6
D24	61.7	63.1	31.1

Before the joints were sheared, the drilled cores were cut and placed in circular steel moulds which were used to keep the samples in place during the shear testing. The upper and lower surface was centred in the moulds in such a way that the joint surfaces became mated. The samples were thereafter fixed in the moulds with rapid-hardening cement.

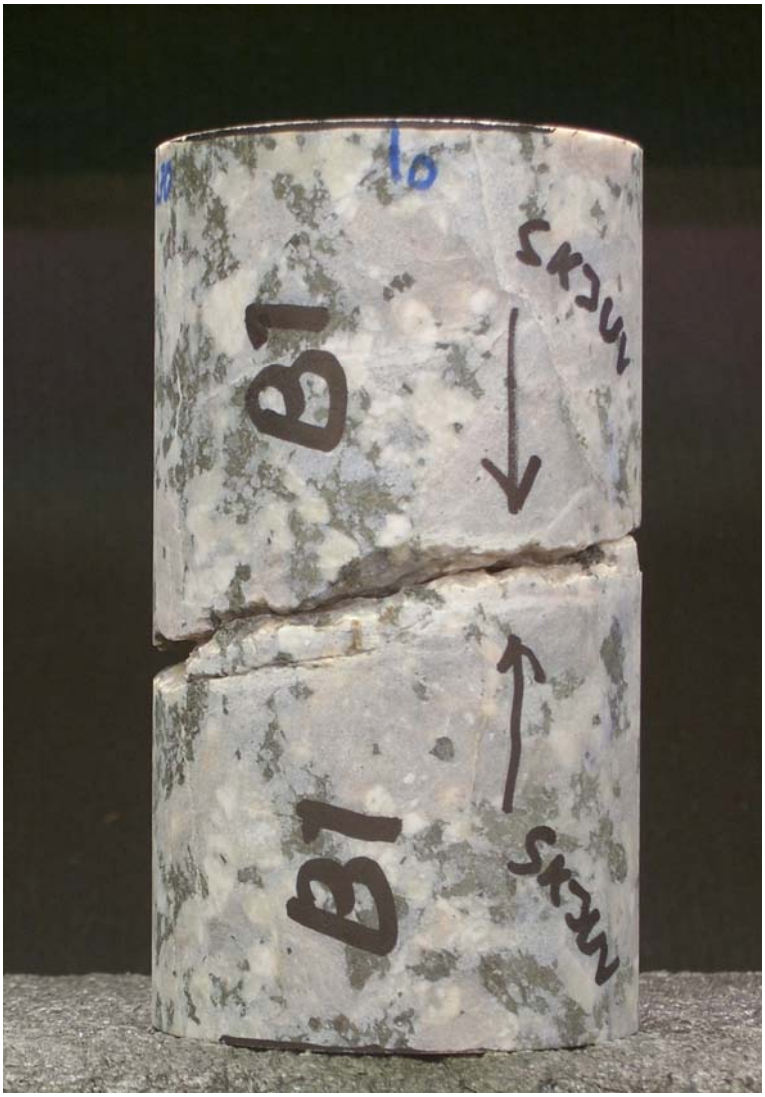

Figure 5.3 Photo of sample B1 showing reduced matedness due to weathering.

Figure 5.4 Photos of the samples B1, B5 and D24 before shearing.

5.3.3 Test set up and procedure for shear tests

Before the shear testing was performed, the joint surfaces were moistened with water which was allowed to sink in a few minutes. This was done since it has been observed that water reduce the friction angle, see for example Barton and Choubey (1977). After that, the upper and lower part of the sample was placed in the shear box. A constant normal load corresponding to a normal stress of 0.8 MPa was applied on the samples. This value corresponds to the maximal effective normal stress under the dam. Shearing was performed approximately 5 mm for each sample at a constant shear rate of 0.5 mm/min. Data was registered during the test at an interval of 0.5 sec which correspond to a shear rate of 0.008 mm/s.

Normal and shear load were measured during the test with electronic load-cells, while normal and shear displacements were measured with LVDT´s (Linear Variable Differential Transformers). In the normal direction, the displacements were measured with four LVDT´s, one in each corner of the sample. The mean value of the measured data was used as a measure of the average normal displacement. In the shear direction, one LVDT was used to measure the shear displacement.

5.3.4 Results

In Table 5.3 below, the results from the shear test are presented. The table shows normal stress, σ_n, peak shear stress, τ_p, shear displacement at peak, $\delta_{s,p}$, peak friction angle, ϕ_p, dilation angle at peak, i_p, and basic friction angle at peak, $\phi_{b,p}$. The dilation angle has been calculated with equation 5.1 below.

$$i = \arctan\left(\frac{dn}{ds}\right) \tag{5.1}$$

Where dn is the increment of normal displacement for a given increment of shear displacement, ds. This increment of shear displacement was chosen to be 0.08 mm. A reduction of the contact area between the upper and lower joint surfaces due to shear displacement was performed and normal stress was adjusted. The basic friction angle at peak was calculated as the peak friction angle minus the dilation angle at peak. The average basic friction angle, $\phi_{b,av}$, was also calculated, based on the average value for a shear displacement interval of 1 to 5 mm. In addition to this, the maximal dilation angle, i_{max}, and the shear displacement when maximal dilation angle occurs, $\delta_{i,max}$, was also calculated. The results are presented in Table 5.3. Figures showing the shear test results are presented in Figure 5.5 to 5.7. In Figure 5.8, photos after the shear tests are shown.

Table 5.3 Results from direct shear tests of samples B1, B5 and D24.

Sample	σ_n (MPa)	τ_p (MPa)	$\delta_{s,p}$ (mm)	ϕ_p (^{o})	i_p (^{o})	$\phi_{b,p}$ (^{o})	$\phi_{b,av}$ (^{o})	i_{max} (^{o})	$\delta_{i,max}$ (mm)
B1	0.80	1.82	0.26	66.2	33.5	32.7	34.1	36.3	0.09
B5	0.80	1.33	0.27	59.0	29.6	29.4	31.0	30.3	0.30
D24	0.80	2.69	0.14	73.4	31.2	42.2	37.3	36.2	0.25

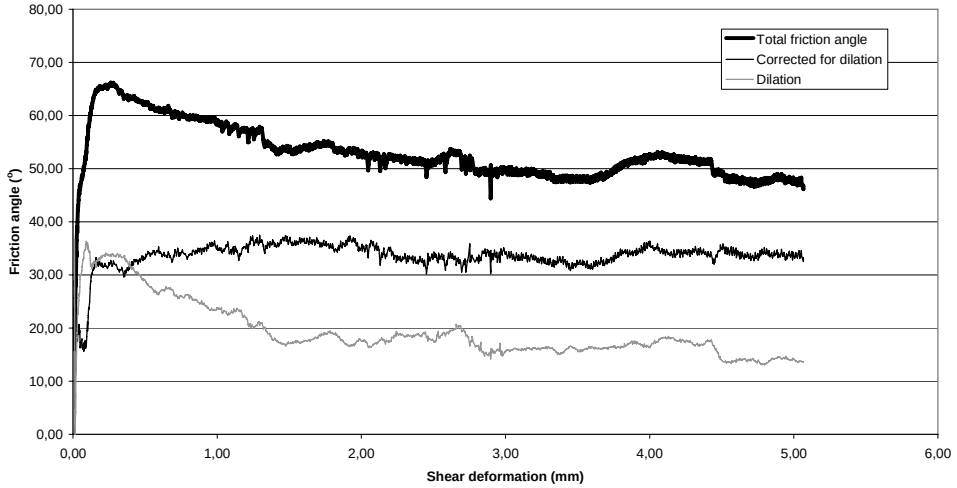

Figure 5.5 Stress ratio (friction angle) – shear displacement diagram for sample B1.

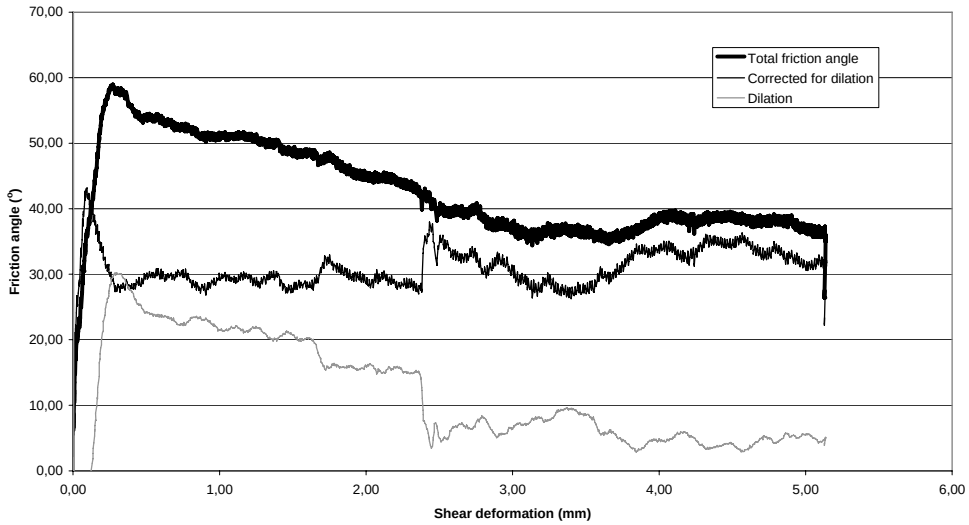

Figure 5.6 Stress ratio (friction angle) – shear displacement diagram for sample B5.

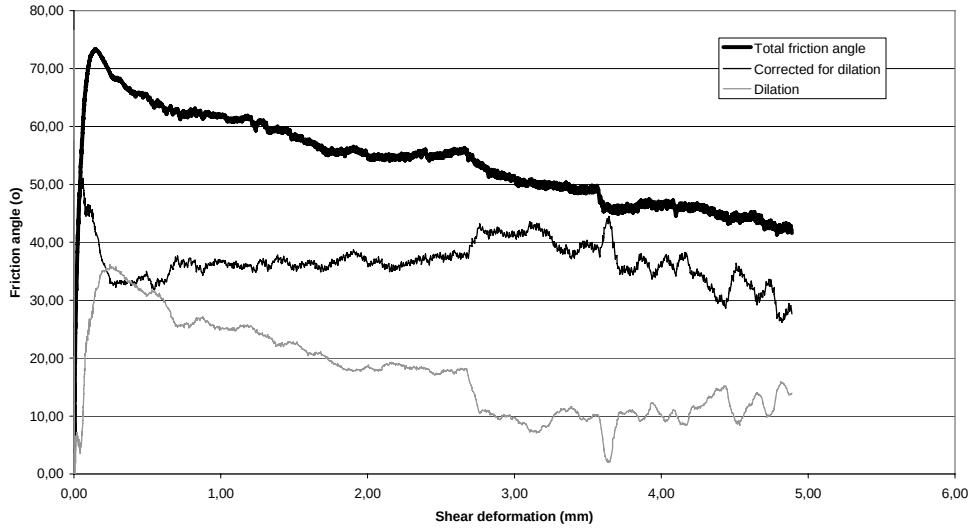

Figure 5.7 Stress ratio (friction angle) – shear displacement diagram for sample D24.

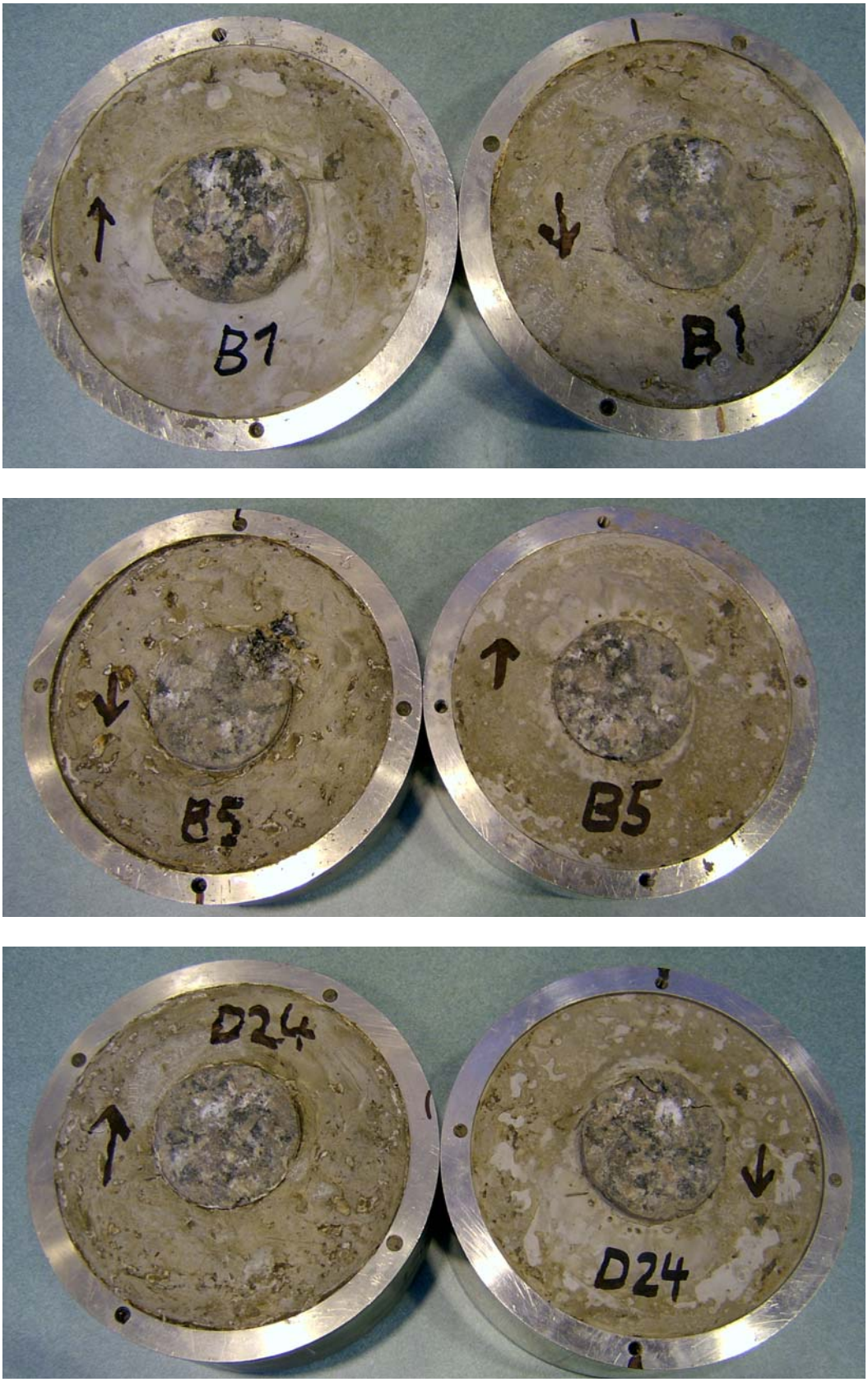

Figure 5.8 Photos of samples after shear tests.

5.3.5 Summary and interpretation of results

The results from the shear test yielded peak friction angles of 66.2, 59.0 and 73.4 degrees for samples B1, B5 and D24 respectively. These results are in line with the results from the previous shear testing performed on drilled cores taken from the rock foundation under the dam. The dilation angles at peak shear strength were observed to be 33.5, 29.6 and 31.2 degrees for samples B1, B5 and D24 respectively. Furthermore, peak shear strength occurred at small shear displacements between 0.15 to 0.30 mm.

According to the adhesion theory, as previously described in Chapter 4, the contact points are welded together at "junctions". The shear force required to break these bonds under a certain normal load express the basic friction angle between two planar but microscopic rough surfaces. In Chapter 4, it was further concluded that the total friction angle could be expressed as the sum of the basic friction angle and the dilation angle. However, it was further shown by conceptual calculations that an asperity component may be present for small samples. By studying the results, it is possible to analyse if this might be the case.

If the results in Figure 5.5 to 5.7 are studied, it can be seen that for sample B1, a correction for dilation on the total friction angle gave an almost linear horizontal term. This indicates that no contribution from any asperity failure component was present for this sample. If the diagram for sample B5 is studied, signs of interlocking can be seen at approximately 2.5 mm. At a shear displacement of 2.5 mm, the dilation suddenly drops which results in an increase of the basic friction angle. This indicates that interlocking might occur at this shear displacement, which means that the rate of shear displacement between the upper and the lower surfaces might have decreased locally. When this happens, the mechanism for the basic friction angle may be disturbed. A similar behaviour can also be seen for sample D24 at a shear displacement of 2.7 mm. It is also interesting to notice that sample B5 and D24 has crushed edges, which could be seen in Figure 5.8. It is possible that interlocking occurred at these asperities, which lead to the cracking of the sample at these locations. It is also possible that the granular material which resulted from this cracking affects the frictional process necessary to develop the basic friction angle. It might also be possible that the crushing of the edges resulted in a stress concentration at the remaining part of the sample which affected the dilation angle.

The results from these three samples point towards the fact that interlocking may affect the shearing for small samples under low normal stresses. It may therefore not be suitable to estimate the basic friction angle from samples with this relatively small dimension under low normal stresses.

Even if interlocking might affect the basic friction angle, it could be seen in Table 5.1 that the basic friction angle appears to be around 35^{o} for these samples. However, it is possible that the mineral composition of the granite for each sample lead to a variance of the basic friction angle. This may be possible since different minerals probably have different adhesive strengths. Furthermore, the relative spatial variation of the minerals is larger for a small sample than for a

larger sample. It could therefore also be expected that the variance of the basic friction angle, up to a representative elementary area (REA), would decrease for larger samples. How large this REA might be is unknown.

No estimation of surface roughness was performed for these samples. Estimation of the *JRC* from predefined profiles was not performed, since analysis of the previous performed shear tests showed that this methodology gave unreliable results. To carry out tilt, push or pull-tests in order to estimate the *JRC* is difficult on the drill cores and was therefore not performed. Back calculated values on *JRC*, with an assumed basic friction angle of 35^{o} and an assumed *JCS* of 100 MPa, gave *JRC* equal to 16.0, 14.1 and 14.9 for sample B1, B5 and D24 respectively. These back calculated values are in line with values back calculated based on the previously performed shear tests on the drill cores.

5.4 Laboratory shear tests performed at LTU

5.4.1 Introduction

Due to the uncertainties regarding the peak shear strength from previously described shear tests at drilled core scales, it was determined to perform additional laboratory shear tests at larger scales. The main objective with these tests was to investigate a possible scale effect and variations of the peak shear strength. These tests were performed with a shear box at Luleå University of Technology. The shear box has the capacity to perform shear tests of dimensions up to 280 by 280 mm according to the methods suggested by ISRM (ISRM 1981).

Back-calculated values for the previously performed shear tests gave a mean *JRC* value of 14.2. For samples with dimensions of 125 by 125 mm and 240 by 240 mm, under the assumption of a basic friction angle of 35^{o} and a *JCS* equal to 100 MPa, the contribution due to roughness was estimated by using Barton and Bandis (1982) equations for scale corrections. The contribution due to roughness became 22.6^{o} for the small samples and a contribution of 17.4^{o} for the larger samples. It was therefore decided to use these dimensions in the test program. Seven samples were chosen for each dimension in order to investigate the variation of the peak shear strength, the basic friction angle and the dilation angle in terms of sample sizes.

5.4.2 Obtaining the samples

Adjacent to the concrete dam at Långbjörn there exist several blasted rock walls where persistent relaxation joints are visible. Their location implies a benefit compared to drilled cores, since it is possible to choose a joint based on visual inspection and thereafter drill out the samples.

The samples were obtained by over-drilling the chosen joint with the desired dimension, i.e. with diameters equal to 125 mm and 240 mm. Since the rock wall

was blasted, it was important that the drilling continued into the rock before the samples were taken in order to reduce possible blast damages. On the other hand, with an increased length it also became harder to keep the joints centred in the core. It was therefore necessary to drill a number of trial holes in order to analyse the orientation of the joint before the samples were drilled. In general, the samples were taken a few decimetres from the rock wall surface. The persistent joint together with the holes drilled for the samples can be seen in Figure 5.9.

Figure 5.9 Photo over the blasted rock wall where the samples were taken.

Samples sent to LTU for shear testing are shown in Figure 5.10 and 5.11. In the two figures, it can be observed that the joints are not well mated. The joint undulate and sometimes splits into two parallel joints with lenses of intact rock in between. As far as possible, the sections of the samples where lenses of intact rock were present were omitted when the samples for shear testing were prepared.

Figure 5.10 Samples sent to LTU for shear testing.

Figure 5.11 Samples sent to LTU for shear testing.

5.4.3 Preparation of samples

Initially, those parts of the drilled cores appropriate for shearing was sorted out. This meant that those parts of the drilled cores where the upper and lower joint surfaces were separated by one or several lenses of intact rock were omitted.

After that, the samples were cut into its desired dimensions; i.e. 125 mm by 125 mm and 240 mm by 240 mm.

Thereafter, the samples were fixated into stiff steel moulds. Rapid hardening concrete was casted in the moulds, which created samples of equal shape and dimension ready for the shear box. Totally, seven small samples and seven large samples were prepared. The shape and outer-dimensions of the prepared samples can be seen in Figure 5.12.

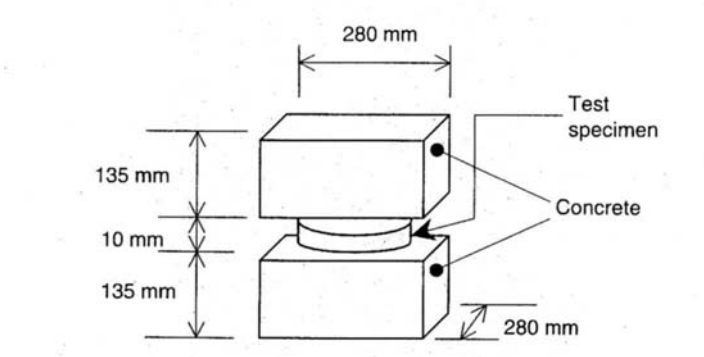

Figure 5.12 Shape and dimensions of direct shear test sample (From Saiang et al. 2005).

5.4.4 Test set up and procedure for shear testing

The servo controlled shear test machine has a capacity of 500 kN for both normal and shear forces and can be seen in Figure 5.13. The principal components of the shear machine are presented in Figure 5.14.

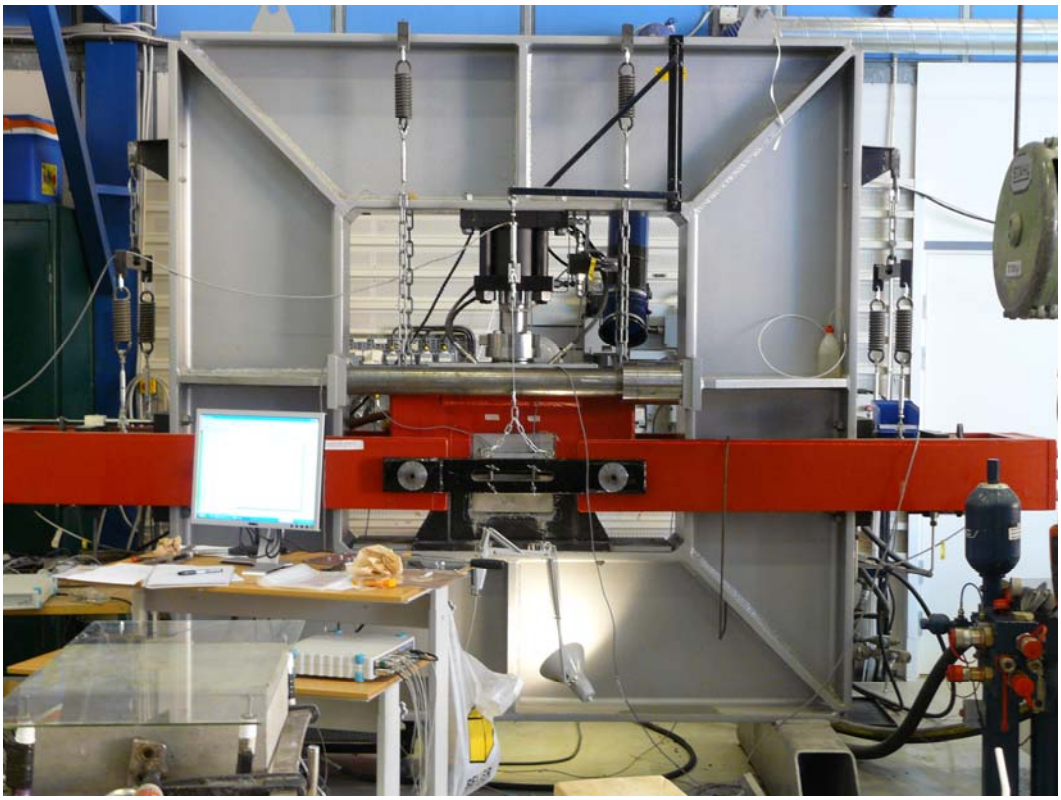

Figure 5.13 Photo of the direct shear machine at Luleå Technical University.

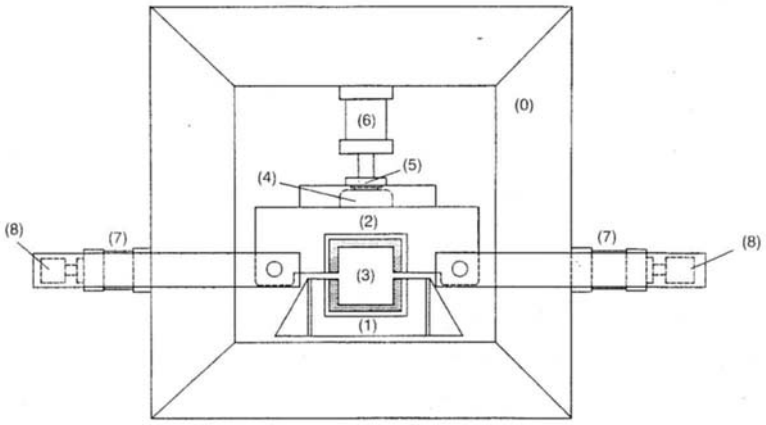

Figure 5.14 Principal components of the shear machine, (0) stiff steel frame, (1) lower box, (2) upper box, (3) specimen holder, (4) hydrostatic bearing, (5) spherical bearing, (6) & (7) hydraulic actuators, (8) bucker up (From Saiang et al. 2005).

After a sample was placed in the shear box, four LVDTs were glued on the sample according to Figure 5.15 below in order to measure the normal displacement of the sample.

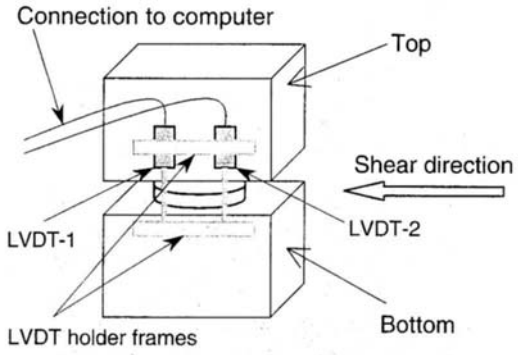

Figure 5.15 Location and set up for the LVDTs. Two additional LVDTs are placed on the back of the sample (From Saiang et al. 2005).

All shear tests were performed with a shear rate of 0.1 mm/min. This shear rate was chosen in order to avoid uncontrolled displacements and failures. A normal stress of approximately 0.8 MPa was used for all fourteen samples. The shear and normal displacement increment for calculation of the dilation angle according to equation 5.1 was chosen to be 0.1 mm. One shear test was performed for each sample, with a maximum shear displacement of 5 mm. The reason to only perform one shear test for each sample was due to the successive degradation of the surface roughness that would occur if multiple tests were performed on the same sample. This would lead to results which are not representative for the *in situ* joint. Also, multiple shear tests make it difficult to investigate the contact areas of the joint surfaces after testing.

5.4.5 Correction of test data

After the samples were placed in the direct shear machine, the upper part of the shear box was successively lowered until the upper and lower surface of the sample were just in contact.

The upper part of the shear box is suspended with a number of springs which can be seen in Figure 5.13. This means that the total force applied by the vertical actuator becomes equal to the force taken by these springs and the force applied on the sample. As a consequence, it is necessary to subtract the force taken by the springs from the total force in order to obtain the force applied on the sample.

The force in the springs can be determined by repeatedly apply normal displacements without any sample in the machine and at the same time measure the normal force. The result is shown as a curve describing the spring stiffness, see Figure 5.16. Studying the curve in Figure 5.16, it can be seen that the curve creates a hysteresis during loading and unloading paths. This means that energy is lost in the spring due to friction and heat. The maximal vertical difference between the upper and lower part of the curve is approximately 4 kN. This is

important to take into consideration, especially for small samples under low normal stresses. The hysteresis of the springs clearly reveals that small samples with low normal stresses are associated with relatively high uncertainties. For the samples in this test series, a normal load of 0.8 MPa gives a total normal load equal to 12.5 kN for the small samples and 50 kN for the large samples, which should be compared to the maximal vertical difference in the curve equal to approximately 4 kN.

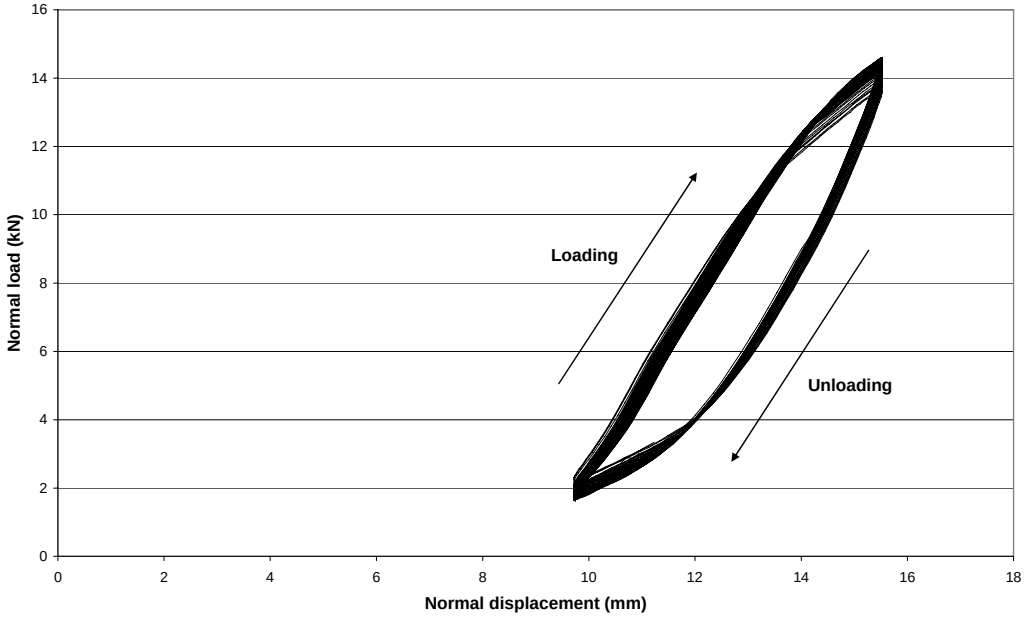

Figure 5.16 Normal displacements versus normal load for the shear machine without any sample in the shear box.

When the upper part of the sample is successively lowered in order to reach contact between the surfaces, normal force is first applied in the springs and thereafter, when contact is made, in both the springs and on the sample. This means that it is mainly the upper part of the curve in Figure 5.16 that is followed during the test. Therefore, a fourth degree polynomial for the spring stiffness was derived based on regression analysis of the upper part of the curve in order to describe it, see Figure 5.17.

With this methodology, initial normal forces at contact prior to shearing, $F_{n,0}$, according to Table 5.4 was obtained.

Table 5.4 Initial normal forces at contact prior to shearing.

Sample	$F_{n,o}$ (kN)	Sample	$F_{n,o}$ (kN)
S1	1.8	L3	3.5
S2	3.0	L4	2.5
S3	-1.3	L6	2.9
S4	4.1	L7	2.8
S5	1.0	L8	6.0
S6	-2.4	L9	3.6
S8	3.1	L10	3.5

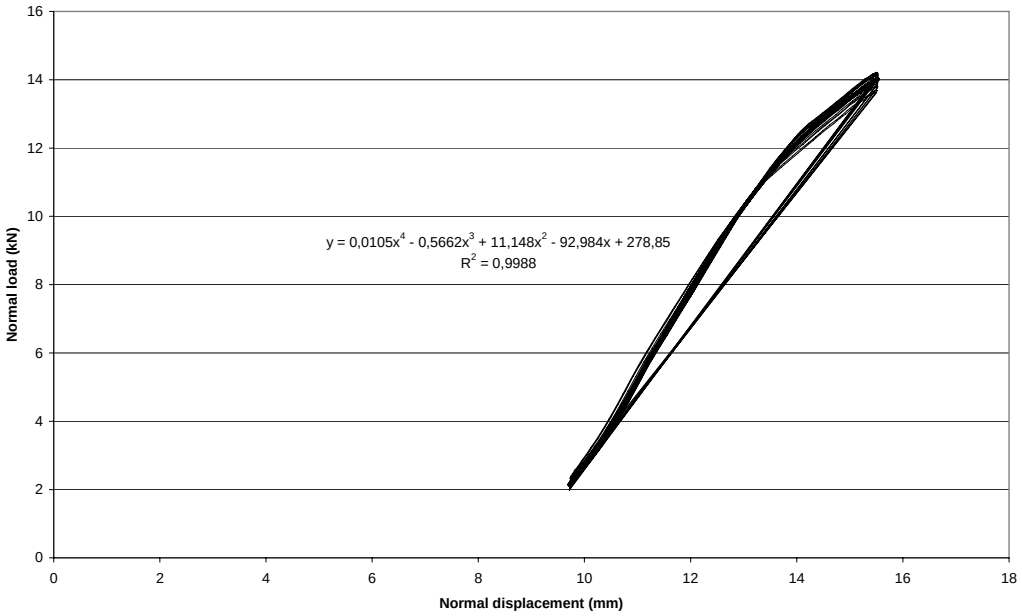

Figure 5.17 Upper part of the curve for spring stiffness with fourth degree polynomial.

Studying the values in Table 5.4, it can be seen that $F_{n,0}$ is about a few kN for most of the samples, which appears to be reasonable. To obtain forces equal to zero is difficult, since it is necessary to apply some load in order to verify that true contact has been established between the upper and the lower part of the sample.

However, for sample S3 and S6, $F_{n,0}$ is negative which is not realistic. The reason for the negative values can be found in the process when the upper part of the sample was successively lowered. For these two samples, a high normal load was applied on the samples due to mistakes in the steering process when the upper part of the sample was lowered. As a consequence, S3 and S6 was exposed for a force of 46 and 69 kN equal to a normal stress of 2.3 and 4.5 MPa respectively. Therefore, it was necessary to unload these samples before shearing could take place.

This also means that the upper part of the curve in Figure 5.16 can not be used for these samples. Therefore, $F_{n,0}$ was determined with the lower part of the curve instead, which gave initial normal forces equal to 2.2 kN for S3 and 1.1 kN for S6 respectively.

5.4.6 Results

The results from the direct shear tests are presented in Table 5.5 and 5.6. Figure 5.18 presents the results from sample S1. Figures showing the results for all of the samples can be found in Appendix A, while photos of the samples after shear testing are presented in Appendix B.

Table 5.5 Results from shear tests of samples with dimensions 125 by 125 mm..

Sample	σ_n (MPa)	τ_p (MPa)	$\delta_{s,p}$ (mm)	ϕ_p (^{o})	i_p (^{o})	$\phi_{b,p}$ (^{o})	$\phi_{b,av}$ (^{o})	i_{max} (^{o})	$\delta_{i,max}$ (mm)
S1	0.98	0.76	3.16	37.8	3.5	34.3	33.5	6.2	3.90
S2	0.94	0.83	7.08	41.5	8.9	32.6	32.7	8.6	6.83
S3	1.06	1.10	1.94	46.0	11.9	34.2	32.4	13.4	1.34
S4	1.03	0.83	0.96	38.7	7.1	31.6	27.2	11.0	4.74
S5	0.83	0.60	3.40	35.8	0.6	35.2	33.8	2.5	2.07
S6	0.85	0.82	3.22	44.6	7.3	37.3	35.6	8.3	3.10
S8	0.98	0.90	6.05	42.7	8.7	34.1	29.6	12.6	6.08

Table 5.6 Results from shear tests of samples with dimensions 240 by 240 mm.

Sample	σ_n (MPa)	τ_p (MPa)	$\delta_{s,p}$ (mm)	ϕ_p (^{o})	i_p (^{o})	$\phi_{b,p}$ (^{o})	$\phi_{b,av}$ (^{o})	i_{max} (^{o})	$\delta_{i,max}$ (mm)
L3	0.86	0.77	2.41	41.9	6.5	35.4	34.7	8.6	1.40
L4	0.79	0.68	2.70	40.5	5.7	34.8	33.9	7.3	6.30
L6	0.78	0.82	2.82	46.5	8.9	37.6	35.8	13.2	3.18
L7	0.90	0.82	2.20	42.4	7.6	34.8	34.2	9.4	1.39
L8	0.83	0.80	2.42	43.9	2.7	41.2	38.3	6.3	7.03
L9	0.81	0.69	2.66	40.2	6.5	33.7	32.6	7.3	2.73
L10	0.80	0.79	1.71	44.9	7.1	37.8	37.3	8.1	1.80

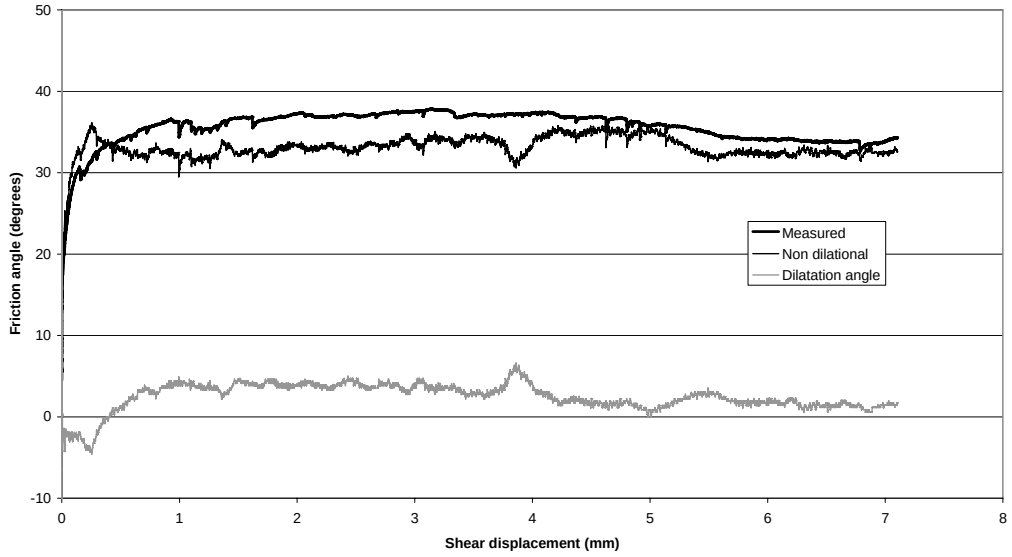

Figure 5.18 Measured friction angle and dilation angle, together with basic friction angle for sample S1.

5.4.7 Estimation of JCS from Schmidt rebound tests

The use of the adhesion theory implies that the strength of the joint wall surface is important for the shear strength, since it can be used to estimate the true contact area for a given normal stress. However, the relaxation joints at Långbjörn are slightly weathered, which is known to affect the strength of the intact rock adjacent to the joint surface. It is therefore not possible to perform uniaxial compressive tests on drilled cores of intact rock in order to estimate the compressive strength of the granite, since they will overestimate the strength.

Therefore, Schmidt rebound hammer index tests were performed in order to estimate joint wall compressive strength, *JCS*, as suggested by Barton and Choubey (1977), see equation 5.2.

$$\log_{10}\left(\sigma_{ci}\right) = 0.00088 \cdot R \cdot \gamma_{\mathrm{m}} + 1.01 \qquad (5.2)$$

Where σ_{ci} is the unconfined compressive strength of the joint wall, i.e. *JCS*. *R* is the Schmidt rebound number and γ_{m} is the rock density (kN/m^3). Since it is important that the impulse from the Schmidt rebound hammer do not move the rock sample being tested, it was judged appropriate to perform the rebound measures on the large samples.

Ten tests were performed on the large samples with the hammer directed vertically downward. Of these ten tests, the five lowest were omitted and an average of the five highest were calculated according to the recommendation by Barton and Choubey (1977). A density of the granite equal to 27 kN/m^3 was assumed. Results from the tests and the estimation of the *JCS* using equation 5.2 are presented in Table 5.7.

Table 5.7 Results from Schmidt rebound hammer tests together with estimation of JCS.

Sample	*R*	R_{mean} (five highest)	γ (kN/m^3)	σ_{ci} (MPa)
L3	43			
L3	43			
L6	31			
L6	27			
L7	40	48.4	27	140
L7	53			
L8	48			
L8	41			
L9	51			
L9	47			

5.4.8 Estimation of JRC from pull tests

In order to estimate the surface roughness of the samples, the joint roughness coefficient, *JRC*, was determined based on performed pull tests. In these tests, the upper part of the sample was pulled over the lower part of the sample; a sort of simple shear tests carried out under a normal load equal to the weight of the upper

part of the sample. When the upper half of the sample was pulled, a load-cell registered the force, *T*, required to move it. Based on the measured force, *T*, in the load-cell, together with the weight of the upper part of the sample and estimated values on *JCS* and the basic friction angle, it was possible to back-calculate *JRC*. Results from this back calculation are presented in Table 5.8.

Table 5.8 Results from direct shear tests of samples with dimensions 240 by 240 mm.

Sample	Test No.	Weight (N)	T (N)	ϕ_p (^{o})	$\phi_p - \phi_b$ (^{o})	σ_n (MPa)	$JRC_{back\text{-}calculated}$	$JRC_{average}$
S1	1	221	283	55.8	20.8	0.014	5.2	4.7
	2		275	53.8	18.8		4.7	
	3		299	52.0	17.0		4.3	
S3	1	222	373	59.2	24.2	0.014	6.6	6.2
	2		363	58.6	23.6		6.4	
	3		331	56.2	21.2		5.7	
S4	1	232	531	66.4	31.4	0.015	8.5	8.0
	2		462	63.3	28.3		7.7	
	3		457	63.1	28.1		7.6	
S5	1	229	233	45.5	10.5	0.015	2.9	2.7
	2		224	44.4	9.4		2.5	
S6	1	228	504	65.7	30.7	0.015	8.3	7.0
	2		338	56.0	21.0		5.7	
	3		409	60.9	25.9		7.0	
S8	1	224	287	52.0	17.0	0.014	4.6	3.8
	2		252	48.4	13.4		3.6	
	3		237	46.6	11.6		3.1	
L3	1	255	439	59.8	24.8	0.004	5.9	4.6
	2		316	51.1	16.1		3.8	
	3		321	51.5	16.5		3.9	
L4	1	245	306	51.3	16.3	0.004	3.9	3.9
	2		297	50.5	15.5		3.7	
	3		323	52.8	17.8		4.2	
L6	1	248	413	59.0	24.0	0.004	5.7	5.2
	2		358	55.3	20.3		4.8	
	3		370	56.2	21.2		5.0	
L7	1	246	295	50.2	15.2	0.004	3.6	3.4
	2		287	49.4	13.4		3.2	
	3		291	49.8	14.8		3.5	
L8	1	254	410	58.2	23.2	0.004	5.5	5.3
	2		416	58.6	23.6		5.6	
	3		364	55.1	20.1		4.8	
L9	1	266	372	54.4	19.4	0.005	4.6	4.1
	2		312	49.6	14.6		3.5	
	3		347	52.5	17.5		4.2	
L10	1	260	339	52.5	17.5	0.005	4.2	3.6
	2		300	49.1	14.1		3.4	
	3		290	48.1	13.1		3.1	

As shown in Table 5.8, the values on *JRC* are considerable lower than those first estimated in the beginning of Chapter 5.4. Average values on *JRC* range from 3.4 to 8.0. By using Barton´s (1973) criterion, together with average *JRC* values in Table 5.8, the calculated contribution from roughness was 7.5 to 17.0^o. This is in line with observed dilation angles in Table 5.5 and 5.6, even though 17.0^o are somewhat high.

5.4.9 Measurement of surface roughness with optical scanning

In the conceptual model in Chapter 4 it was concluded that the dilation angle originates from surface asperities at contact, which could be idealized as superimposed asperities at different scales. It was further concluded that during shearing, the shear displacement leads to a concentration of the contact area to the steepest asperities at contact facing the shear direction. This contact area could, for a perfectly mated and unfilled joint, be described with the potential contact area ratio, $A_{c,p}$, as suggested by Grasselli (2001). In addition, it was assumed that the change of heights for surface asperities, h_{asp}, with respect to asperity base lengths of different sizes, L_{asp}, could be expressed with a power function by defining two constants related to the amplitude parameter and the Hurst exponent.

In order to make it possible to analyse these parameters described above, the joint surfaces for two of the samples, S6 and L7, were measured with optical scanning technique. The scanning was performed by the company Svensk Verktygsteknik in Luleå with the system ATOS III, see Figure 5.19. During the scanning, different fringe patterns was projected on the object to be measured, which was recorded by two cameras. In order to scan the joint surface completely, it was necessary to perform several individual measurements, where each single measurement generates up to 4 million data points. Circular markers were placed on the object, which made it possible to arrange all data points in a global coordinate system. The density of the point cloud made it possible to obtain an accuracy of ±50 μm of the measured object.

Figure 5.19 The measurement system ATOS III (Picture from Svensk Verktygsteknik).

The scanning was first performed for the upper and lower surfaces of sample S6 and L7 before the direct shear tests were performed. After that, the upper and lower part was put together and scanned one more time. This methodology makes it possible to analyse the degree of contact and aperture between the upper and lower part of the sample prior to shearing. After the direct shear tests were performed, the procedure described above was repeated. By doing so, it was also possible to analyse the degree of damage on the surfaces due to shearing.

The data from the laser scanning were used to regenerate the surfaces with a resolution of 0.5 by 0.5 mm. It was assumed that this sampling distance approximates the grain size scale, i.e. an asperity base length at grain size of 1 mm. The regeneration of the surfaces and other analyses of the data were made with the program MATLAB (MathWorks 2007). Based on the regenerated surfaces, parameters for the potential contact area ratio were derived together with constants for the scale relation between the asperity heights and the asperity base lengths of different sizes. The results from these analyses are presented below. However, aperture and surface damage was not investigated in this section. Their influence on the peak shear strength for these samples will be discussed in the end of this chapter.

Parameters that describe the potential contact areas between the upper and lower surfaces of sample S6 and L7 were calculated with the following methodology. First, normal vectors for each element, $\mathbf{n}_i$, in the 0.5 by 0.5 mm grid were generated. Thereafter, the shear direction were defined as a vector, $\mathbf{t}$. Using equation 5.3, the contribution for each element inclination to the measured dip angle, θ_i, was calculated.

$$\cos\left(90-\theta_i\right)=\frac{\left|\mathrm{n}_i\cdot\mathrm{t}\right|}{\left|\mathrm{n}_i\right|\cdot\left|\mathrm{t}\right|} \tag{5.3}$$

Once they were calculated, they were sorted in descending order and arranged into a vector which was plotted on the x-axis. A vector that described the cumulative area of the surface based on the 0.5 by 0.5 mm grid was plotted on the y-axis. The data from this curve were used for regression analysis in order to obtain the following parameters; A_o, maximum potential contact area ratio; θ_{max}, maximum measured dip angle; and C which described the concavity of the curve. A high value of C corresponds to a high degree of concavity, which in turn correspond to a low degree of roughness. Results from the analyses are presented in Table 5.9.

Table 5.9 Parameters describing the potential contact area in the shear direction. Direction defined as 0^o in the positive x-axis direction with 90^o in the positive y-axis direction.

Sample	Direction (^{o})	A_o	C	θ_{max} (^{o})	r^2	θ_{max}/C
S6 lower	0	0.778	8.76	57.0	0.977	6.5
S6 upper	180	0.703	4.92	39.5	0.988	8.0
L7 lower	180	0.321	7.41	65.9	0.813	8.9
L7 upper	0	0.330	5.23	47.5	0.865	9.1

As the data in Table 5.9 show, the maximum potential contact area ratio deviates from the anticipated value 0.5. This was mainly due to an inclination of the samples, i.e. they were not completely horizontal. According to the analyses, sample S6 had an average inclination of 2.8° against the shear direction while sample L7 had an average inclination of 2.2° away from the shear direction. Total difference between the two samples is about 5°. Another possible source of error is the regression analyses. In table 5.9, it can be seen that r^2 indicates a considerably poorer fit for sample L7 than that for sample S6.

Measured dip angle with respect to the shear direction was plotted in Figure 5.20 and 5.21. In these figures, the difference in average inclination between samples S6 and L7 can be observed. Sample S6 has a larger area where the measured dip angle is negative, i.e. a dip against the shear direction. On the other hand, sample L7 has a larger area with a positive measured dip angle, i.e. a dip away from the shear direction.

The scale relation between asperity heights, h_{asp}, and asperity base lengths, L_{asp}, was determined by calculating the root mean square, Z_2, at different sampling distances, Δx, over the sample in the shear direction. The sampling distance ranged from 0.5 mm up to a length of 10 mm for sample S6 and 20 mm for sample L7. The results from the calculations are shown in Table 5.10 and 5.11.

Table 5.10 Measured average asperity heights, h_{asp}, at different asperity base lengths, L_{asp}, for sample S6.

	Lower part of sample S6				Upper part of sample S6			
Δx (mm)	**L_{asp} (mm)**	**Z_2**	**Average dip angle (°)**	**h_{asp} (mm)**	**L_{asp} (mm)**	**Z_2**	**Average dip angle (°)**	**h_{asp} (mm)**
0.5	1	0.1549	8.81	0.077	1	0.1644	9.34	0.082
1.0	2	0.1450	8.25	0.145	2	0.1542	8.77	0.154
2.0	4	0.1308	7.45	0.262	4	0.1384	7.88	0.277
5.0	10	0.1090	6.22	0.545	10	0.1130	6.45	0.565
10.0	20	0.0924	5.28	0.924	20	0.0969	5.53	0.969

Table 5.11 Measured average asperity heights, h_{asp}, at different asperity base lengths, L_{asp}, for sample L7.

	Lower part of sample L7				Upper part of sample L7			
Δx (mm)	**L_{asp} (mm)**	**Z_2**	**Average dip angle (°)**	**h_{asp} (mm)**	**L_{asp} (mm)**	**Z_2**	**Average dip angle (°)**	**h_{asp} (mm)**
0.5	1	0.1935	10.95	0.097	1	0.1936	10.95	0.097
1.0	2	0.1799	10.20	0.180	2	0.1826	10.35	0.183
2.0	4	0.1612	9.16	0.322	4	0.1649	9.36	0.330
5.0	10	0.1308	7.45	0.654	10	0.1375	7.83	0.688
10.0	20	0.1085	6.19	1.085	20	0.1146	6.53	1.146
20.0	40	0.0903	5.16	1.806	40	0.0926	5.29	1.852

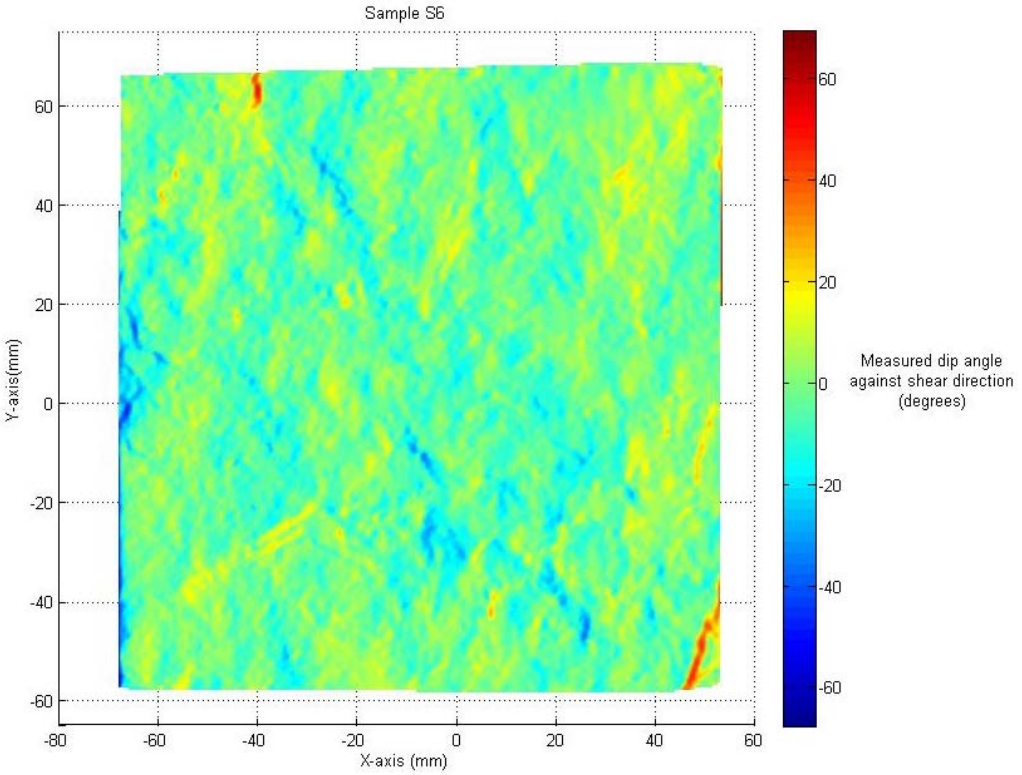

Figure 5.20 Measured dip angle against the shear direction for the lower part of sample S6 (Negative dip angles against shear direction).

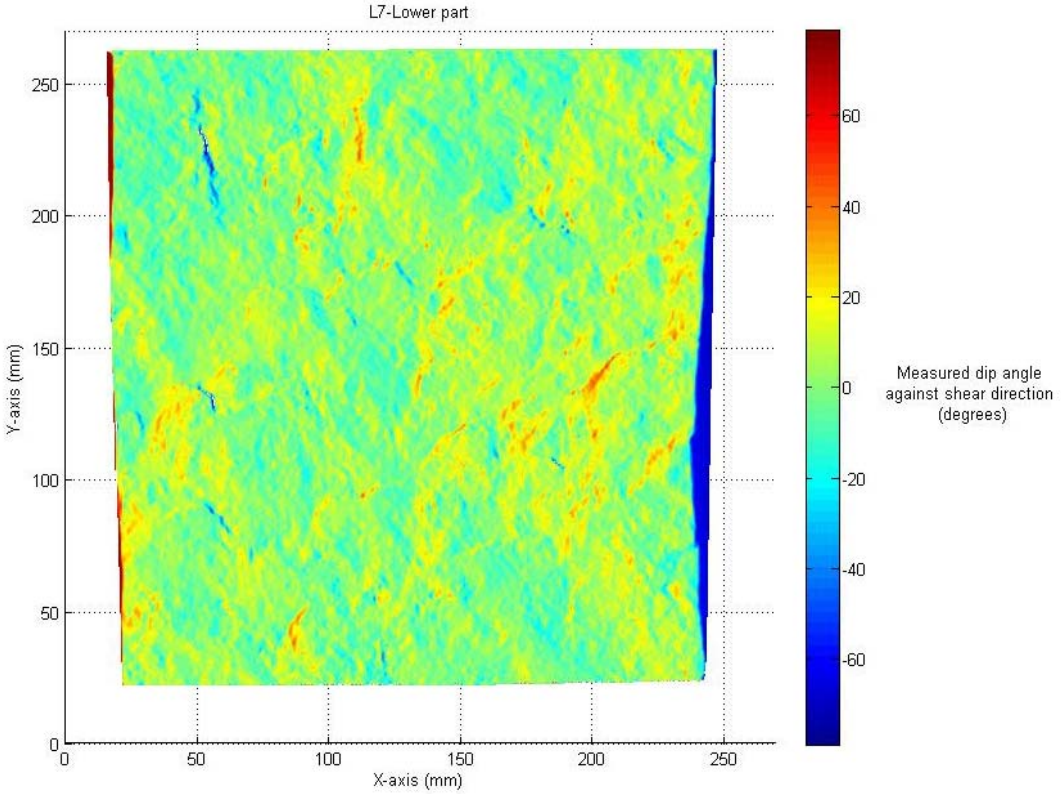

Figure 5.21 Measured dip angle against the shear direction for the lower part of sample L7 (Negative dip angles against shear direction).

In order to determine the constants *a* and *H*, which describes the scale relation between asperity heights and asperity base lengths, regression analyses on the data in the Table 5.9 and 5.10 were performed. The results from these analyses are presented in Table 5.12 and Figure 5.22 and 5.23.

Table 5.12 Constants based on regression analyses describing the scale relation between asperity base lengths and asperity heights.

		a	***H***	$\mathbf{r}^2$
S6	Lower part	0.080	0.826	0.999
	Upper part	0.086	0.819	0.999
L7	Lower part	0.103	0.789	0.999
	Upper part	0.103	0.800	0.998

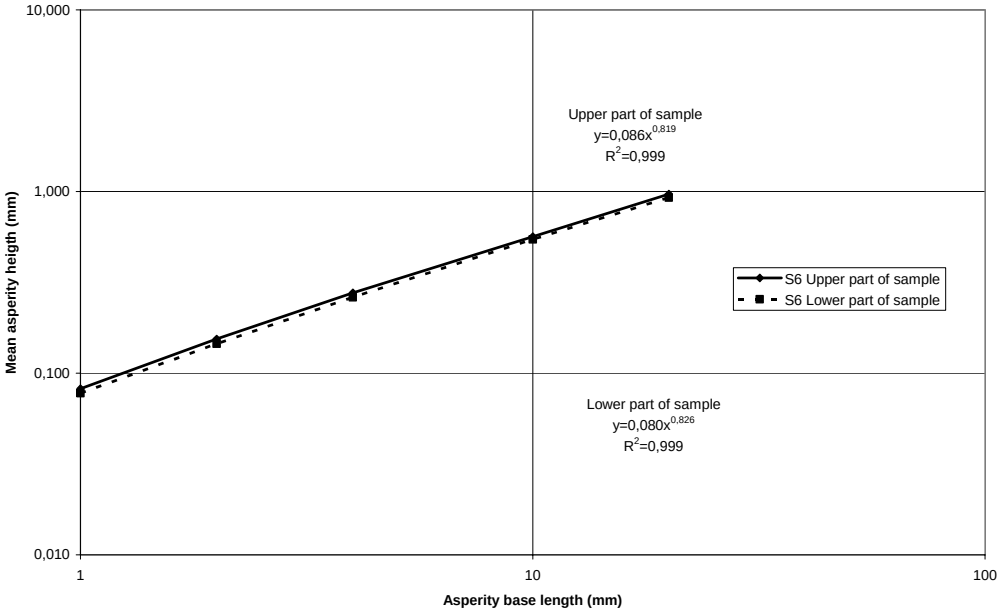

Figure 5.22 Mean asperity heights at different asperity base lengths for sample S6.

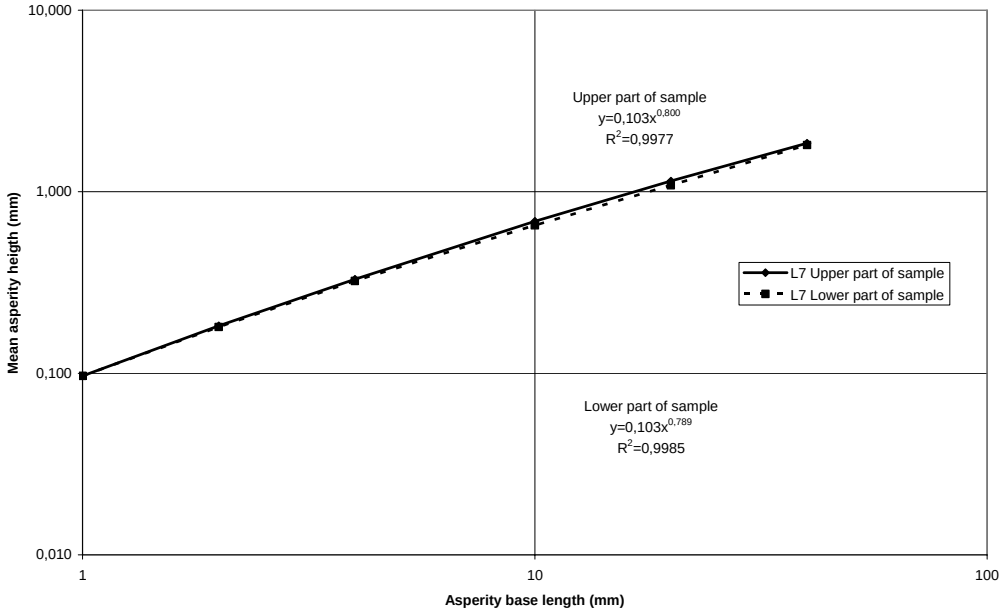

Figure 5.23 Mean asperity heights at different asperity base lengths for sample L7.

5.4.10 Summary and interpretation of results

Due to the uncertainty in the observed peak shear strength in laboratory shear tests compared to the peak shear strength for joints in field scale, additional laboratory shear tests of larger scales were performed. Totally, fourteen samples were prepared and tested, seven with a size of 125 mm by 125 mm and seven with a size of 240 mm by 240 mm. The main objective with these new tests was to investigate if a scale effect could be seen in the results between these two scales for the peak shear strength. In addition, the objective was also to investigate the variation on the peak shear strength at these two scales.

In the beginning of this subchapter it was described that an anticipated dilation angle of 22.6° and 17.4° were expected for the small and large samples respectively. This prediction was based on an average *JRC* value of 14.2 for the drilled core samples combined with Barton-Bandis (1982) empirical equations for scale corrections. Prediction on *JRC* values based on visual inspection of the joint surfaces for the 125 by 125 mm samples and the 240 by 240 mm samples indicated that the surface was rough and undulated. *JRC* values in the range of 8 to 14 could be anticipated. However, pull tests performed prior to shear tests gave low *JRC* values indicating that a dilation angle between 7 to 17°. These low dilation angles were also verified in the shear tests. However, the cause for this relatively low dilation angle despite the high roughness is unclear and is discussed further in Chapter 5.8 "Discussion and interpretation of results". A summary of the results from the shear test performed at LTU are presented in Table 5.13.

Table 5.13 Summary from shear tests at LTU.

Sample	125 by 125 mm			240 by 240 mm			All samples		
	ϕ_p (°)	i_p (°)	$\phi_{b,p}$ (°)	ϕ_p (°)	i_p (°)	$\phi_{b,p}$ (°)	ϕ_p (°)	i_p (°)	$\phi_{b,p}$ (°)
Average	41.0	6.9	34.2	42.9	6.4	36.5	42.0	6.6	35.3
Std.	3.7	3.7	1.8	2.3	1.9	2.6	3.1	2.9	2.5
COV	0.09	0.54	0.05	0.05	0.30	0.07	0.07	0.43	0.07

An average peak friction angle of 41.0° were obtained for the 125 by 125 mm samples, while an average peak friction angle of 42.9° were obtained for the 240 by 240 mm samples. The average dilation angle for both of the test series were about 7°, with a lower variation for the larger samples. The values in the table above shows that no scale effect can be seen for the dilation angle between the two series of samples. The average basic friction angle for all tests is 35°, with a coefficient of variation of 0.07. As expected, no scale effect could be observed for the basic friction angle.

An important aspect when the results should be interpreted is also that they contain uncertainties. When the shear tests were analysed it was observed that small samples combined with low normal load could result in uncertain values on the normal load acting on the sample. In addition to this, optical scanning of the surfaces revealed that it was difficult to cast the samples in the steel mould completely horizontal. For example, the difference in average inclination between sample S6 and L7 was measured to be 5°. All in all this means that care should be taken before any conclusions are made.

5.5 *In situ* shear test

5.5.1 Introduction

Even though the laboratory shear test provided consistent values on the basic friction angle, the dilation angle at field scale are uncertain. Therefore, an *in situ* shear test was planned and carried out adjacent to the concrete dam. After the shear test was performed, the surfaces of the joint were measured with optical scanning in order to determine the thickness of infilling materials and the roughness.

The advantages with the *in situ* shear test, in addition to minimize possible scale effects, are that the joint can be tested in undisturbed conditions. By doing so, the effect on the peak friction angle from infilling materials such as silt and loose pieces of weathered rock are considered.

It should be emphasized that the joint tested in this *in situ* test contained some infilling material, even though it was the author's intention to study unfilled joints. However, the presence of infilling material was detected after the test block was created and it was decided to carry out the testing despite this undesired condition.

5.5.2 Creation of test block

Before the *in situ* shear test could be performed it was necessary to find a suitable joint to be tested. After a survey of visible outcrops adjacent to the dam, a part of it was judged to have been formed by a persistent joint, see Figure 5.24.

Figure 5.24 Location of the in situ test site. The test is performed in the white tent to the right, with the outcrop formed by the chosen joint to the left.

It was assumed that this joint surface, which had formed the outcrop, continued into the rock mass. In order to investigate if this was the case, the rock surface for

an area a few meters away was uncovered from overlying soil. Once this was done, several vertical cores were drilled by the company SBT, see Figure 5.25. The drilling confirmed that a shallow persistent joint existed under the rock surface.

Figure 5.25 Drilling of vertical cores in order to investigate the extent and inclination of the assumed location of the persistent joint.

After the location and inclination of the joint was verified, the test block was created by sawing. The dimensions of the block were 700 by 700 mm in accordance with the suggestions by ISRM (1981). Before the sawing took place, the rock surface was carefully inspected in order to locate possible joints or other weaknesses in the intact rock. In addition to the creation of the test block, additional rock was removed to create space for the jack that should apply the shear force. Also, slits with a width of about 10 centimeters were created around the block. A picture of the created test block is shown in Figure 5.26.

Figure 5.26 Photo of the created test block.

5.5.3 Test set up and procedure for shear test

Before the shear test could be performed, it was necessary to prepare the test site. This included the construction of support for the normal and shear loading from the jacks. Also, the upper side of the block and the side facing the shear jack had to be prepared for the application of forces from the jacks. In addition to this, steel plates and pieces of plexiglass had to be fixed for the LVDT´s which measured the displacements of the block during the test. A photo over the test site during the test can be seen in Figure 5.27.

Figure 5.27 Photo of the test site during the shear test.

The support for the normal load from the jack was constructed by first grouting three GWS struts with a diameter of 32 mm and a length of two meters into the rock. Between the two struts a steel beam was mounted, which consisted of two UPE 270 steel profiles which had been welded together. In order to prevent tilting of the beam due to eccentric loading, an additional beam was mounted under and perpendicular to the one described above, see Figure 5.27.

The support for providing the shear load from the jack was of specific concern. The joint continued into the rock but it was uncertain at what shear load the joint would slide. To prevent the rock above the joint from sliding, six GWS struts with a diameter of 32 mm was grouted one meter into the rock below the joint. After that, a concrete support was casted on the rock surface. Finally, each strut was pre-stressed to 150 kN. By doing so, shear strength was mobilized in the joint which prevented it from sliding. Shear resistance was also mobilized in the interface between concrete and rock.

On the upper side of the block, for the application of the normal load, a surface aligned with the inclination of the joint was first casted with concrete. On this concrete surface, a truncated pyramid of concrete was casted. This was done in order to spread the normal load on the block.

For the application of the shear load, a concrete heel was casted against the side of the block. The side of the concrete heel was aligned in such an angle that the line of action from the shear force from the jack went through the middle of the joint. Two layers of 10 mm Styrofoam were placed under the concrete heel to avoid additional sliding resistance from it.

At the corners of the block, rapid hardening concrete was used to build surfaces aligned parallel with the joint surface. On these surfaces, pieces of plexiglass were glued. The low friction surface of the plexiglass was used as a sliding surface for the steel points of the LVDT´s, which were used to measure the displacements of the block. For the same purpose, four pieces of plexiglass was glued at the sides of the block. The fixation of the LVDT´s was arranged by using attachments of magnets. Several steel plates were therefore fixated with rapid hardening concrete on the rock surface surrounding the test block.

The principal components for the test set up and their locations can be seen in Figure 5.28 below.

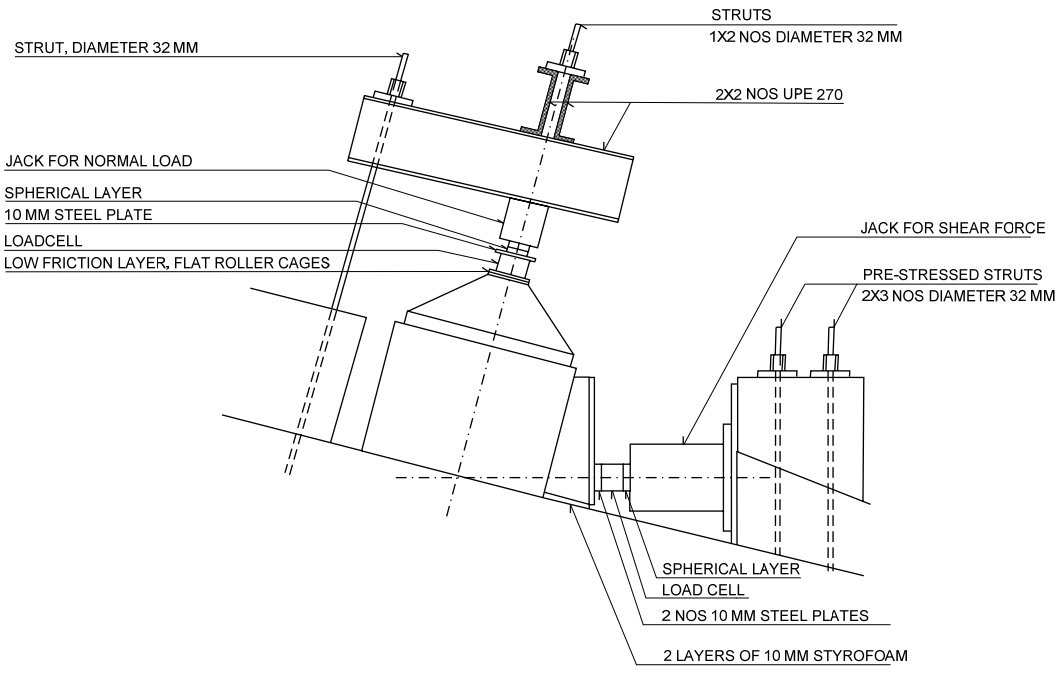

Figure 5.28 Principal components for the in-situ shear test.

The jack for the normal load had a capacity of 500 kN. Attached to the hydraulic system for the jack, in order to keep the normal pressure constant, a compressor combined with an air-pressure regulator was used.

The jack for application of the shear load was constructed in order to apply a constant shear rate. The capacity of the jack was 500 kN. Load cells with a capacity of 500 kN were used to measure the applied normal and shear loads.

During the shearing of the block, friction between the block and the jack for the normal load was minimized by a sliding layer. The sliding layer was constructed by five flat roller cages with a dimension of 30 by 150 mm. The rollers in the cages had a diameter of 4 mm. The dynamic and static load capacity for each roller cage was 107 and 380 kN respectively. Two hardened steel plates with a dimension of 200 by 200 mm and a thickness of 10 mm were used as sliding plates. The hardened steel plates had a Rockwell hardness of 60 HRC. To keep the cages aligned in the shear direction during the test, a frame was welded and fixed to the lower steel plate. A photo of the sliding layer can be seen in Figure 5.29 below.

Figure 5.29 Sliding layer constructed by five flat roller cages and two 10 mm hardened steel plates.

For measurements of displacements of the block during the shear test, eight LVDT´s were used. The LVDT´s were placed in accordance with the suggestions by ISRM (1981). Four were placed at the corners on the upper side of the block for measurements of the normal displacement. Two were placed on the side of the block in the shear direction and two were placed on the side of the block perpendicular to the shear direction for measurement of lateral displacements. In addition to these, deformations for the support of the jack for the shear load were also measured. The location and numbering of the LVDT´s can be seen in Figure 5.30. The readings of the displacements were averaged to obtain the mean shear and normal displacements. The lateral displacements were mainly recorded in order to evaluate the behaviour of the test block during the shear test.

For interpretation of the test results, it was necessary to account for the inclination of the joint with respect to the applied shear load. Shear and normal stresses, τ and σ_n, were computed as follows:

$$\tau = \frac{T \cdot \cos\alpha}{A} \tag{5.4}$$

$$\sigma_n = \frac{N + T \cdot \sin\alpha}{A} \tag{5.5}$$

where T is the total applied shear force and N is the total normal force. α is the inclination angle of the applied shear force to the shear plane and was measured to be 12.2^o. A is the area of the joint surface for the test block.

A normal load corresponding to a normal stress of 0.5 MPa was initially chosen for the test. Together with the additional normal stress component from the jack for the shear load, a total normal stress of 0.8 MPa could be anticipated. This corresponds to the maximal normal stress under the dam, and it was also a normal stress value that was used for the previous performed shear tests at SP and LTU. During the test, a constant shearing rate of 0.2 mm/min was used. The dilation was calculated with equation 5.1 based on a shear displacement increment equal to 0.4 mm.

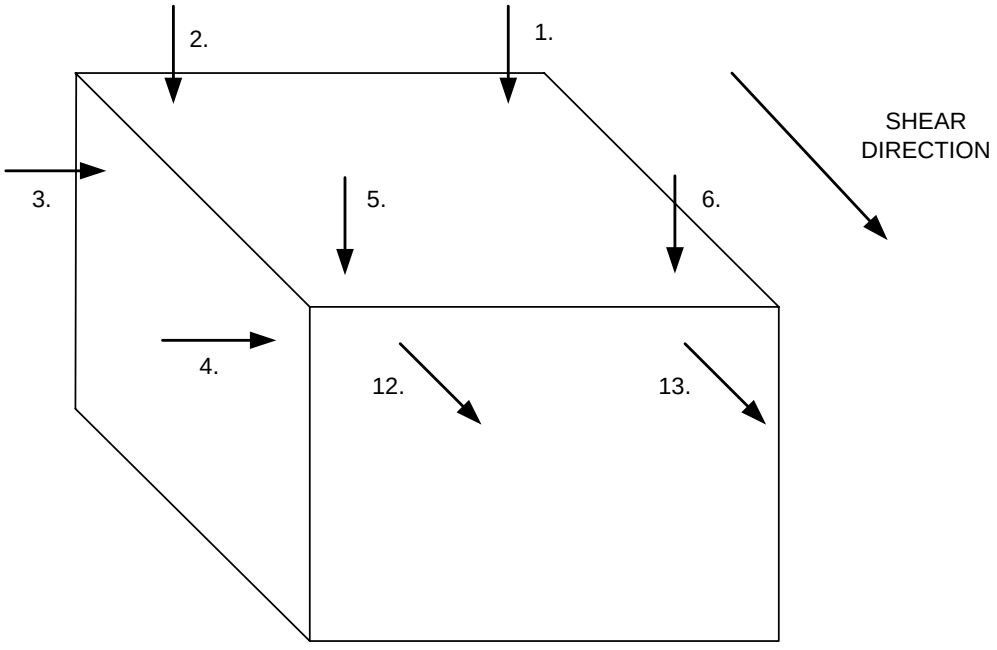

Figure 5.30 Location and identification of the LVDT's for measurements of the normal, shear and lateral displacements of the block. (Measured deformation positive in the direction of the arrows).

5.5.4 Results

How the measured normal and shear loads changed during the test can be seen in Figure 5.31.

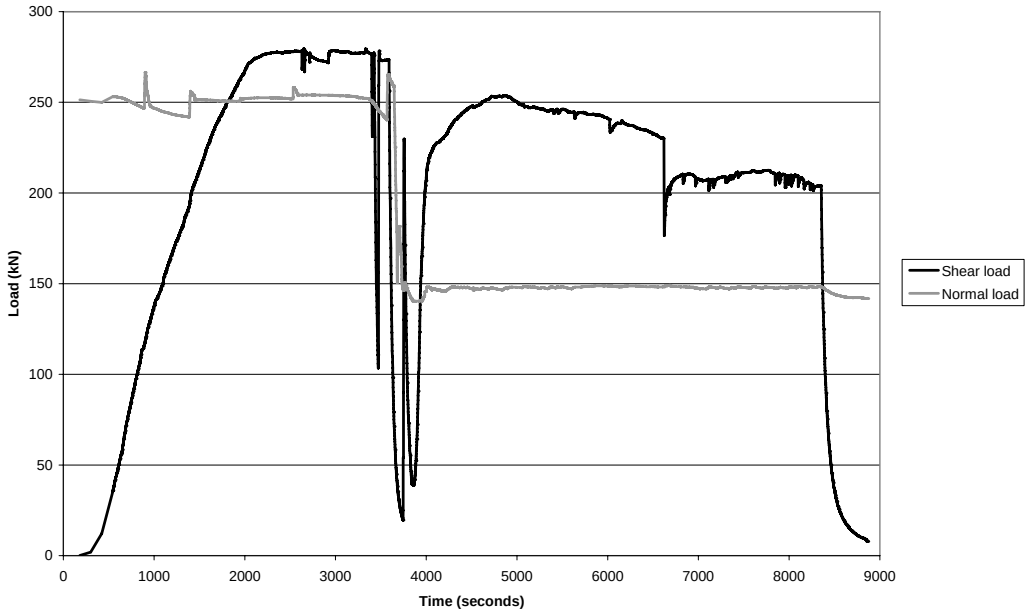

Figure 5.31 Measured normal and horizontal shear load during the test (Not corrected for the inclination of the block).

Initially, a normal load of 250 kN was planned to be used. However, during the test it was observed that the jack for the shear load only had a maximum working pressure of 60 bar instead of the expected 100 bar due to a mistake by the manufacturer of the jack. This implied that the capacity of the jack was reduced from 450 kN down to 270 kN. As a consequence, the normal load had to be reduced from 250 kN down to 150 kN in the middle of the test.

In Figure 5.31, it can be seen that the shear load decreased three times, when the normal load was decreased to 150 kN. The first time it decreased, the jack was stopped, which resulted in a decreased pressure. Thereafter, shear loading was re-activated and resulted in an increased load. At the second decrease, the jack was stopped. However, when the steering mode was switched from automatic to manual, a rapid increase of the load occurred. This also resulted in an uncontrolled displacement of the block with about 0.8 mm. After that, the load was successively decreased in the jack and the shear test could continue with the new normal load.

Throughout the shear test, the displacements of the abutment were continuously measured. The results from this measurement can be seen in Figure 5.32. As the figure shows, a maximum displacement of about 0.5 mm was observed.

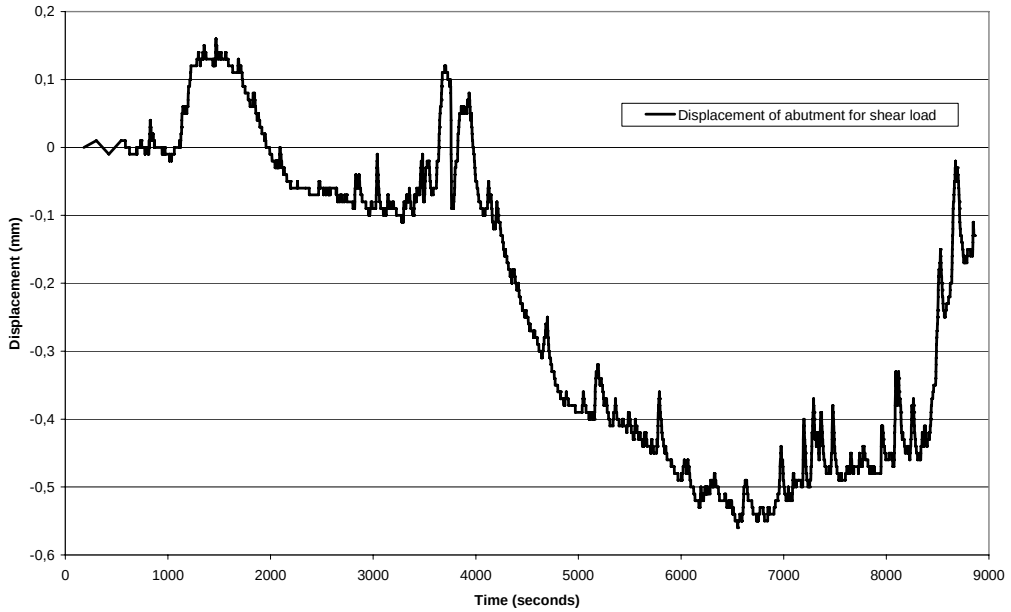

Figure 5.32 Displacement of the abutment for the shear load (Positive displacement in the shear direction).

The total friction angle against shear displacements can be seen in Figure 5.33. The total friction angle was defined as the secant between the shear and normal forces calculated with equations 5.4 and 5.5. Total friction angle together with dilation angle and basic friction angle are presented in Figure 5.34.

Diagram showing the normal displacements can be seen in Figure 5.35, while lateral and shear displacements are presented in Figure 5.36. It should be observed that LVDT 2 showed stick slip behaviour. Most likely, the point of the gauge did not slide properly on the plexiglass. As a consequence, it was excluded in the calculation of the dilation angle in Figure 5.34. Instead, LVDT 6 was used in its place since it had a similar normal displacement curve. This should be kept in mind when the results are interpreted. In addition, an unexplained scatter was registered in LVDT 13 during the first three millimetres of shear displacement. However, after the reduction of the normal load, this ceased to appear. Due to the unexplained scatter in LVDT 13, the first three millimetres of the calculated dilation angle in Figure 5.34 was not possible to interpret. A possible source to this unexplained scatter might be caused by an incompatible normal load relative the stiffness of the supporting frame that might not be high enough.

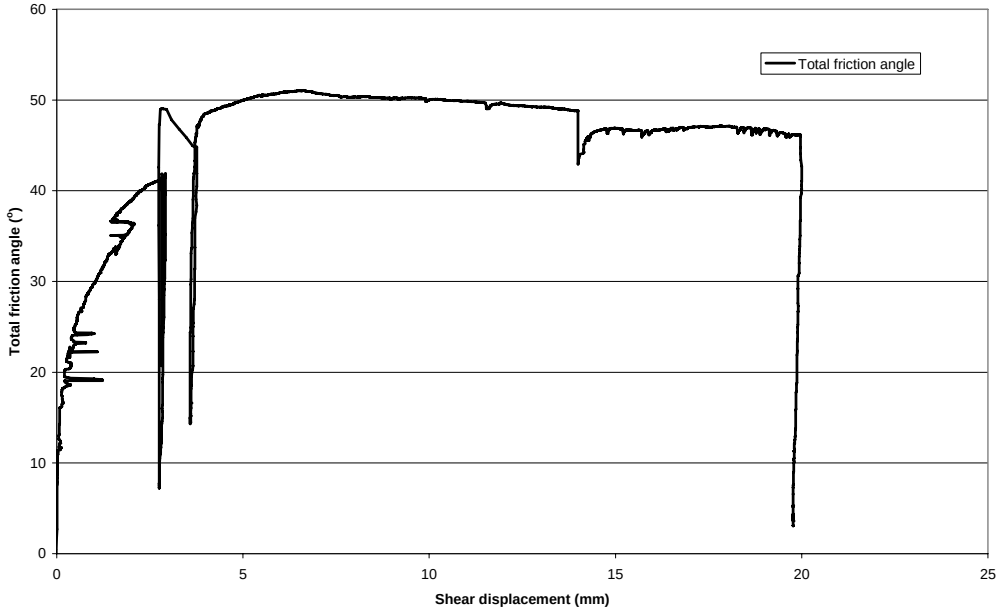

Figure 5.33 Total friction angle –shear displacement diagram.

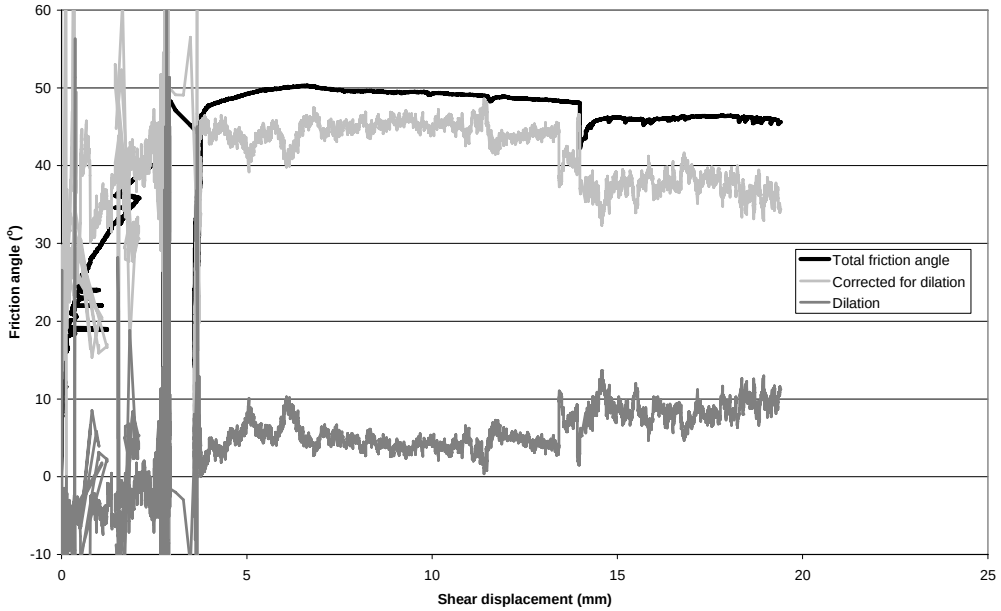

Figure 5.34 Friction angle (stress ratio) – shear displacement diagram.

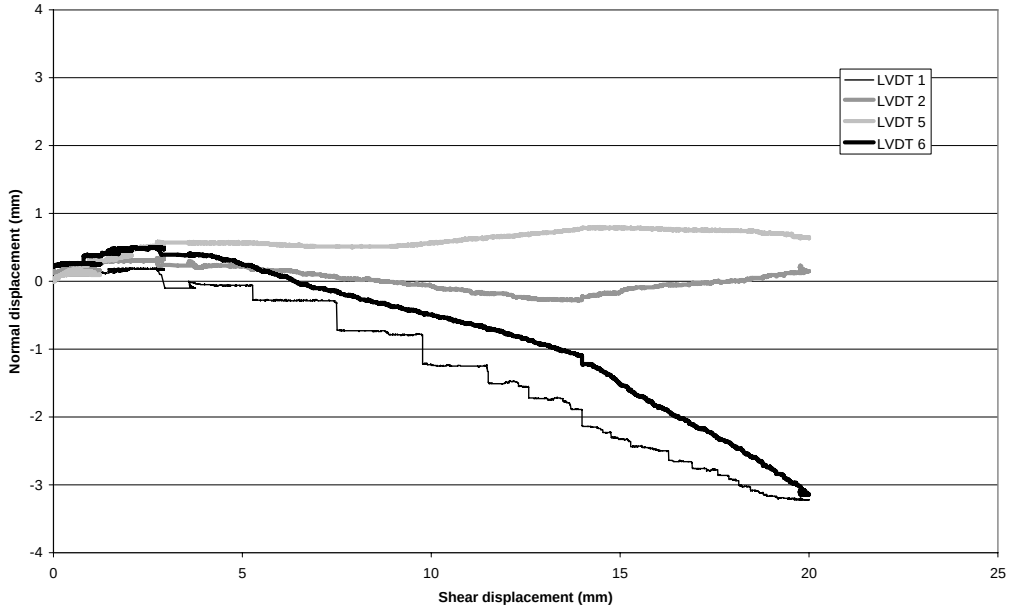

Figure 5.35 Measured normal displacements – shear displacement diagram.

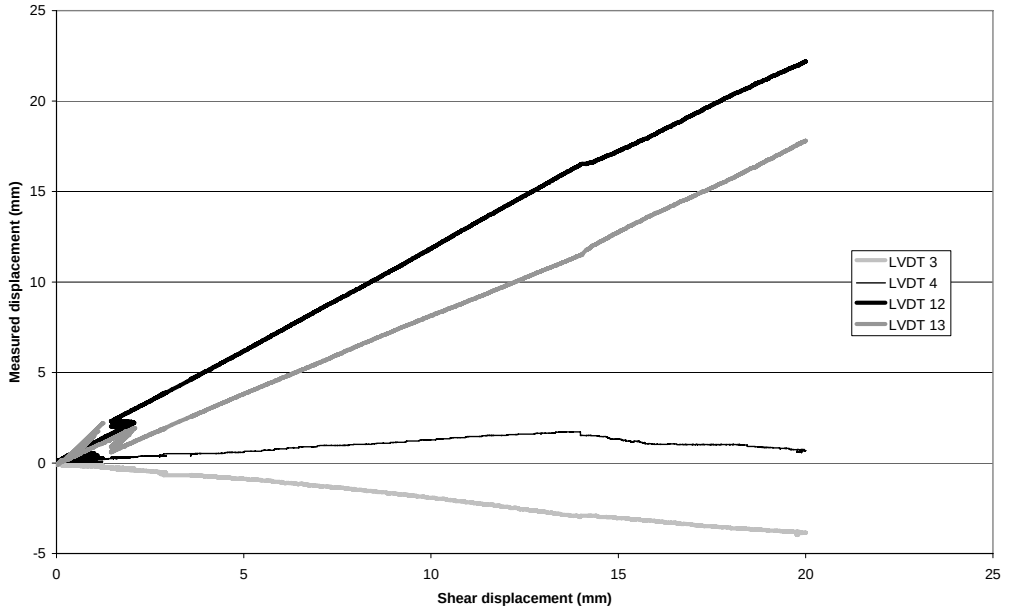

Figure 5.36 Measured shear and lateral displacements - shear displacement diagram.

5.5.5 Measurement of surface roughness with optical scanning

After the shear test had been performed, the block was tilted on its side in order to investigate the surface roughness and the infilling of the joint. The roughness and the thickness of the infilling was measured with optical scanning as previously described in Chapter 5.4.9, see Figure 5.37. In order to measure the thickness of the infilling, the surface was first measured untouched. After that, the surface was cleaned from infilling material and the surface was scanned one more time. Both the upper and the lower parts of the surface were scanned.

Figure 5.37 Measurement of surface roughness with optical scanning.

A photo which shows the surface of the joint after the block was tilted can be seen in Figure 5.38. The photo shows that the joint surface was covered with infilling materials, which consisted of soil and weathered rock particles. The white spots in the picture are contact points with rock to rock contact. These contact points were mainly located to a ridge which passes in the middle of the block perpendicular to the shear direction.

The thickness of the infilling is presented in Figure 5.39. The thickness was in general only a few millimetres, but was locally up to 30 mm. In the upper side of the picture it can be seen that the infilling increased up to 90 mm. This originated from a wedge of intact rock. The wedge was formed by two joints, since the joint in this area was divided into two parallel joints. Based on visual observations, the lower joint under the wedge appeared to be more rough and fresh compared to the joint above the wedge, whose roughness coincided better with the main joint.

Figure 5.38 Lower part of the untouched joint surface after the upper block has been tilted.

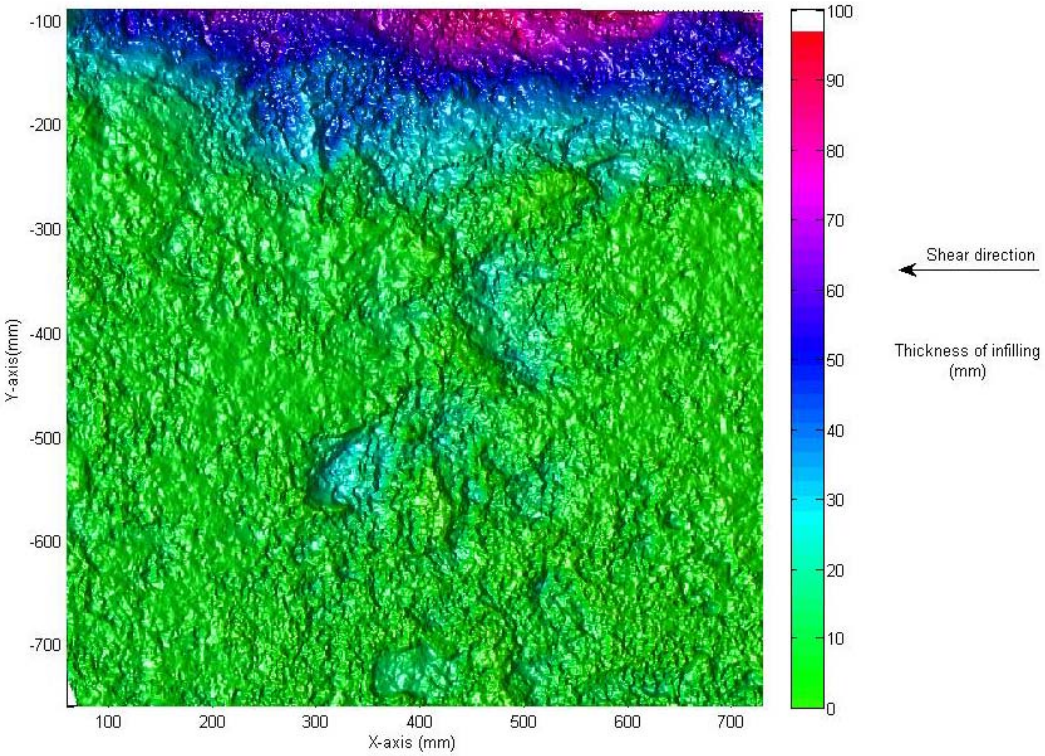

Figure 5.39 Thickness of infilling material.

Values for the parameters describing the potential contact area ratio are presented in Table 5.14. Due to the inclination of the joint, a best fit plane of the joint was first determined by regression analysis. After that, the parameters were calculated according to the technique described in Chapter 5.4.9. Measured dip angles against the shear direction are plotted in Figure 5.40.

Table 5.14 Parameters describing the potential contact area ratio. Direction defined as 0^o in the positive x-axis direction.

Sample	Direction (^{o})	A_o	C	θ_{max} (^{o})	r^2	θ_{max}/C
In-situ upper	0	0.457	7.76	71.9	0.991	9.3
In-situ lower	180	0.452	8.23	81.7	0.953	10.7

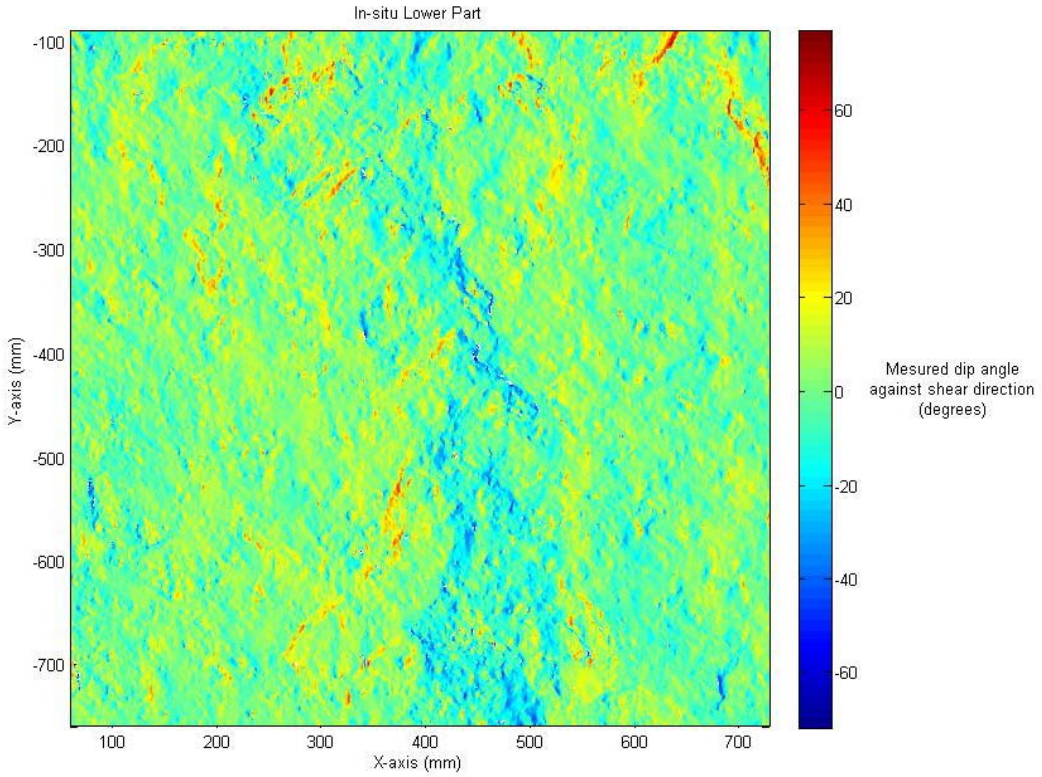

Figure 5.40 Measured dip angles against the shear direction for the lower part of the joint surface (Negative values indicate potential contact points, shear direction to the left).

The scale relation between asperity heights and asperity base lengths was determined by calculating the root mean square, Z_2, at different sampling distances over the sample in the shear direction. The sampling distances ranged from 0.5 mm up to a length of 67 mm for the lower joint surface. For the upper part of the joint surface, a maximal sampling distance of 63 mm was used. The sampling distance of 0.5 mm, which corresponds to an asperity base length of 1 mm, was assumed to represent the grain size. The results from the calculation are presented in Table 5.15.

Table 5.15 Measured average asperity height, h_{asp}, at different asperity base lengths, L_{asp}, for the in situ joint.

	Lower part of *in situ* joint				Upper part of *in situ* joint			
Δx (mm)	**L_{asp} (mm)**	**Z_2**	**Average dip angle (^{o})**	**h_{asp} (mm)**	**L_{asp} (mm)**	**Z_2**	**Average dip angle (^{o})**	**h_{asp} (mm)**
0.5	1	0.2129	12.02	0.106	1	0.2721	15.22	0.136
1.0	2	0.2066	11.67	0.207	2	0.2545	14.28	0.255
2.0	4	0.1951	11.04	0.390	4	0.2339	13.16	0.468
5.0	10	0.1682	9.55	0.841	10	0.1933	10.94	0.967
10.0	20	0.1409	8.02	1.409	20	0.1584	9.00	1.584
67/63	134	0.0822	4.70	5.507	126	0.0913	5.22	5.752

In order to determine the constants *a* and *H* describing the scale relation between asperity heights and asperity base lengths, regression analyses on the data in Table 5.15 were used. The results from these analyses are presented in Table 5.16.

Table 5.16 Constants based on regression analyses describing the scale relation between asperity length and asperity height.

		a	***H***	***r^2***
In-situ	Lower part	0.120	0.803	0.996
	Upper part	0.150	0.771	0.997

Diagram showing the mean asperity height at different asperity base lengths are presented in figure 5.41.

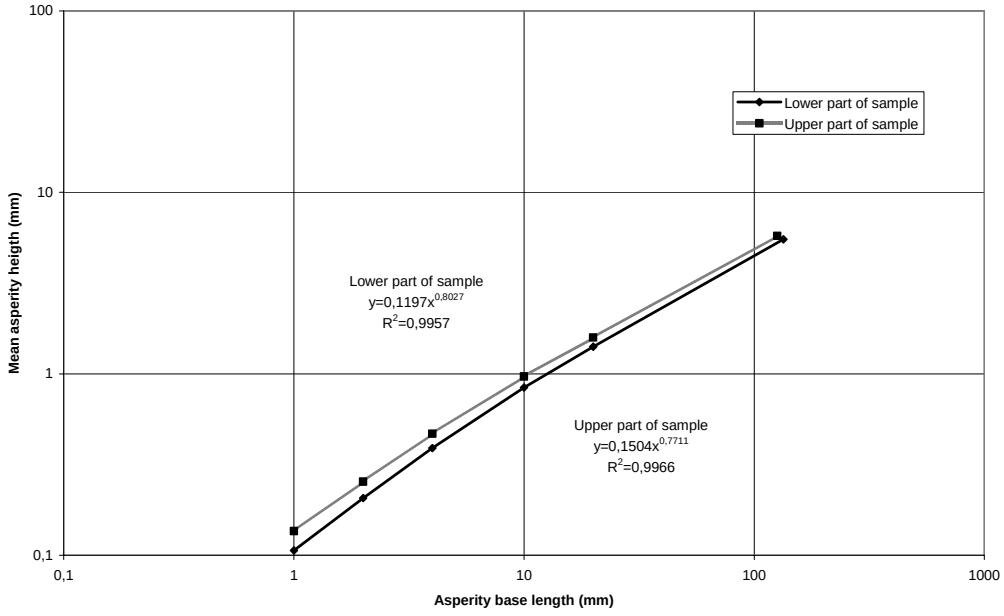

Figure 5.41 Measured mean asperity heights at different asperity base lengths.

5.5.6 Summary and interpretation of results

An *in situ* shear test was carried out at the concrete dam site at Långbjörn hydropower station. The advantages with these types of tests are that they reduce possible scale effects and that the joint could be tested under *in situ* conditions.

Initially, the shear test was intended to be performed at a normal stress around 0.8 MPa. However, during the test it was observed that the capacity of the jack that applied the shear load unintentionally had been reduced from 450 kN to 270 kN by the manufacturer. As a consequence, the normal load was reduced after a shear displacement of about 3 mm. The new load that was used throughout the rest of the test corresponded to a normal stress of 0.42 MPa.

A peak friction angle of 50.3^{o} was obtained from the test. Unfortunately, a completely correct dilation angle was not possible to be calculated since LVDT 2 exhibited stick slip behaviour. To overcome this problem, LVDT 2 was excluded in the calculations of the dilation angle. Instead, LVDT 6 was used in its place since it had normal displacements similar to LVDT 2. The results from the calculation of the dilation angle showed that the test could be divided into three parts. In the first part, which occurred up to a shear displacement of 4 mm, the high normal load was used. In the second part, which occurred for a shear displacement between 4 mm to 14 mm, the normal load was reduced. The peak shear stress occurred at a shear displacement of 6.6 mm. The dilation angle at peak shear strength was calculated to be 4.8^{o}. This means that the basic friction angle became 45.5^{o}. This value was unexpectedly high. At a shear displacement of about 14 mm, a sudden drop of the shear load was registered. This initiated the third part of the test, occurring for a shear displacement from 14 mm to 19 mm. In this part of the test, the average calculated dilation angle was 8.6^{o}. The average basic friction angle became 37.4^{o}, a value that is in line with previously performed laboratory shear tests in this chapter.

Regarding the high value on the basic friction angle, it could be discussed if it was correct to use a mean value of the normal displacements, which is the current practice in shear tests, in order to calculate the dilation angle. In the test, the right side of the block showed no negative normal displacement while the left side show a clear negative normal displacement. It is possible that the parallel joints on the right side reduced the normal displacements on this side. Using a mean value on the normal displacements, the dilation angle for the left side will be increased by 50% and the dilation angle for the right side will be decreased by 50%. At the same time, the dilation angle for the left side may constitute a sliding resistance for the total block. On the other hand, if this methodology was used, the basic friction angle would be about 8.6^{o} lower than 37.4^{o} obtained in the third part of the test.

A possible reason for the drop in the shear load at a shear displacement of 14 mm could be found if the shear and lateral displacements were studied. It can be seen that the block rotated counter clockwise up to a shear displacement of 14 mm. After the drop in the shear load, this rotation stopped and only a displacement in the shear direction occurred. The stopped rotation might have indicated crushing

of an asperity under the left side of the block. Before the crushing of the asperity interlocking may have been present and this effect disappeared after the crushing of the asperity.

After the shear test was performed, the block was tilted and the surface was measured with optical scanning. The scanning was performed two times, before and after the infilling material was removed. With this methodology, it was possible to measure the thickness of the infilling material.

In general, the infilling material, which consisted of soil and pieces of weathered rock, had a thickness of a few millimetres. At some locations the thickness of the infilling was up to 30 mm. This infilling also resulted in fewer rock to rock contact points. The contact points were mainly concentrated to the ridge present in the middle of the sample coinciding with the steepest measured dip angles against the shear direction. The area of the contact points ranged from approximately 20 mm^2 up to about 2000 mm^2.

Measurements of the average asperity heights with respect to the asperity base lengths showed that the roughness at larger scales could not be characterized as completely self-affine. With increased sampling distance, the inclination in the log-log diagram decreased. It might be an effect of a non-stationary roughness due to the ridge present in the middle of the sample. It could also indicate the existence of a stationary threshold for the roughness at larger scale. If a stationary threshold exists at a certain scale, it would imply that the scale dependence cease to exist at this scale.

5.6 Summary and interpretation of results for all shear tests

5.6.1 Introduction

Several laboratory and one *in situ* shear test were performed on samples of rock joints from the rock foundation under and adjacent to the concrete dam at Långbjörn hydropower station. The tests were performed at different scales ranging from 42 to 700 mm. The main objective with these tests was to obtain information for estimating the peak shear strength of the persistent horizontal relaxation joints which exist in the rock mass under the concrete dam. A second objective was to study if a scale effect could be observed on the peak shear strength for joints of different sizes. In addition, optical scanning was performed on three samples in order to characterize surface roughness.

5.6.2 Summary

A summary of all tests with their peak friction angle at different scales are presented in Figure 5.42. If the results in Figure 5.42 are studied, it can be seen that results from the drilled cores exhibit a higher peak friction angle than the

other tests. On the other hand, total friction angle for the shear test at 125 and 240 mm scale were lower than that from the *in situ* shear test.

As previously discussed, the peak shear strength could be divided into a basic friction angle and a dilation angle. In Figure 5.43 and 5.44, the basic friction angle and the dilation angle respectively were plotted at different scales. In these two figures, samples D4, D10, A1 and B3 were excluded since it was not possible to correctly calculate the dilation angle. For the *in situ* test, the dilation angle and the basic friction angle were determined and showed in Figure 5.43 and 5.44 at two different shear displacements, i.e. at the peak friction angle and at the residual friction angle.

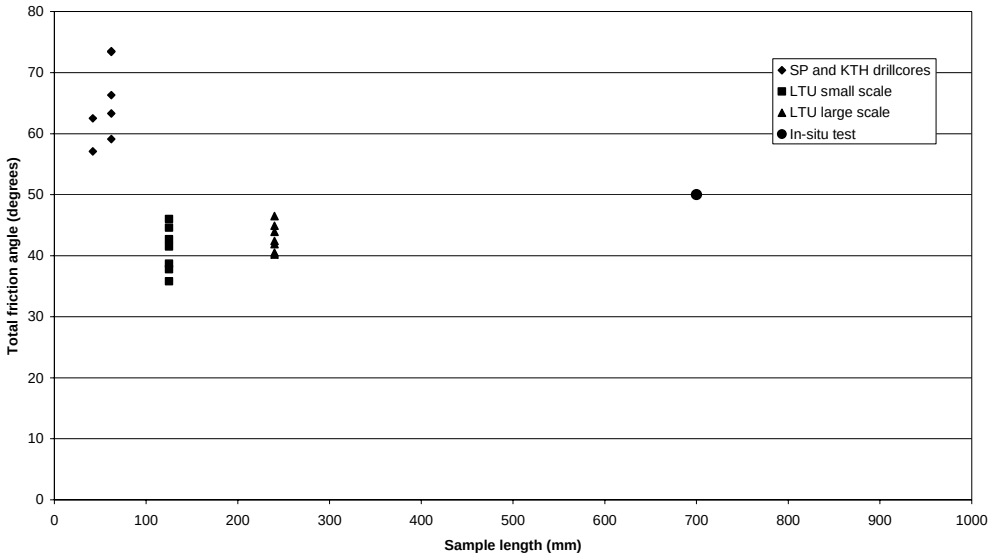

Figure 5.42 Peak friction angle for the shear tests at different sample scale.

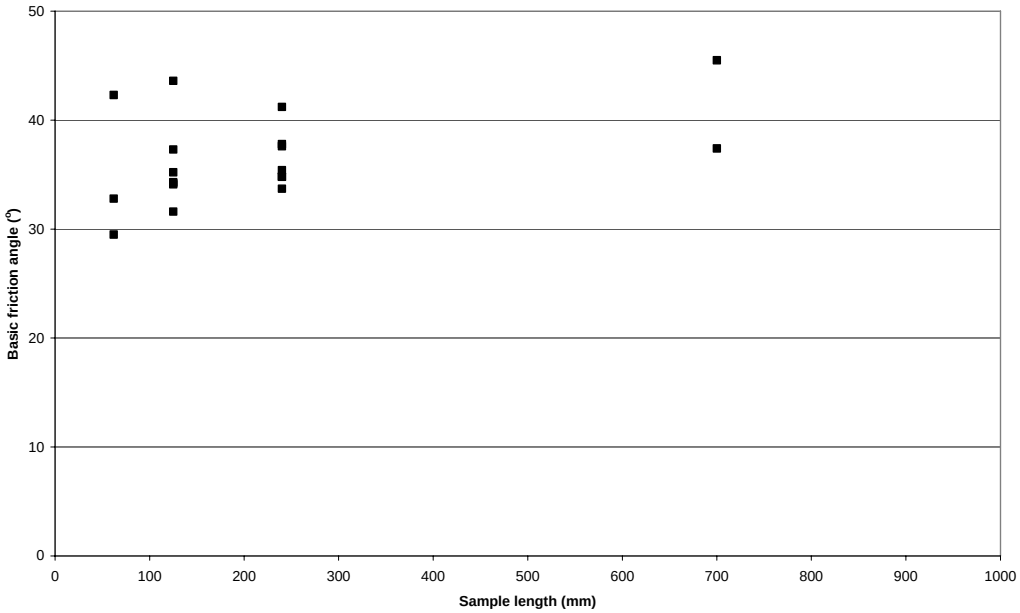

Figure 5.43 Measured basic friction angles at peak shear strength for different sample lengths.

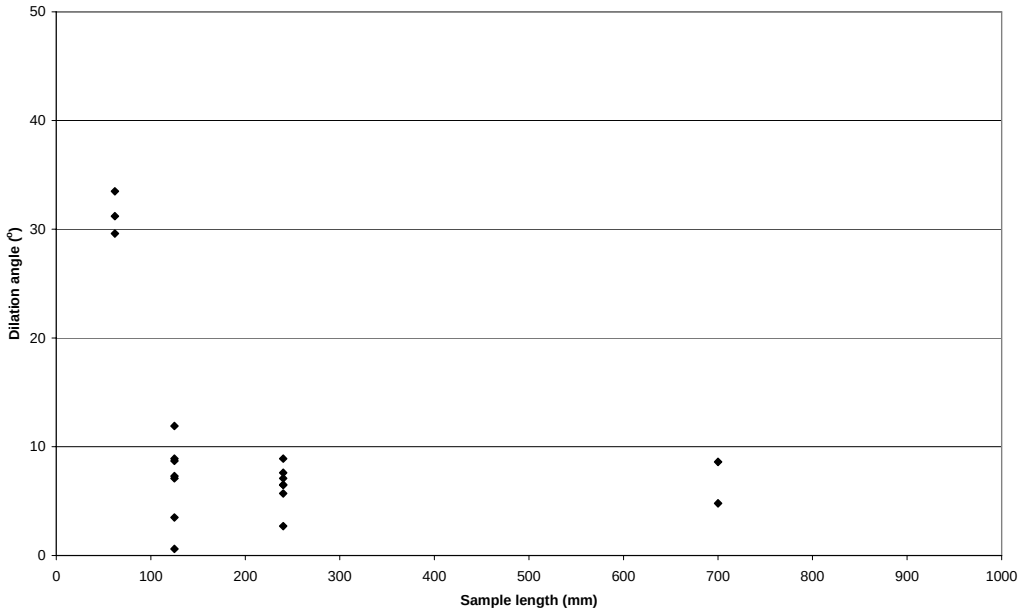

Figure 5.44 Measured dilation angles at different sample lengths.

The results in Figure 5.43 point out that the basic friction angle could be considered constant and not scale dependent. From Figure 5.44 it can be seen that variations in the peak shear strength mainly appears to originate from changes in the dilation angle. In Table 5.17 and 5.18, average values, standard deviations and coefficient of variations are presented for the tests at different scales.

Table 5.17 Average value, standard deviation and coefficient of variation for the basic friction angle for the different test series.

	Drillcores	**LTU 125 by 125 mm**	**LTU 240 by 240 mm**	***In situ***	**Total**
n	3	7	7	1	18
Average	34.9	35.8	36.5	45.5	36.4
Stdev.	6.6	3.8	2.6	-	4.3
COV	0.19	0.11	0.07	-	0.12

Table 5.18 Average value, standard deviation and coefficient of variation for the dilation angle for the different test series.

	Drillcores	**LTU 125 by 125 mm**	**LTU 240 by 240 mm**	***In situ***
n	3	7	7	1
Average	31.4	6.9	6.4	4.8
Stdev.	2.0	3.7	1.9	-
COV	0.06	0.54	0.30	-

As the values in Table 5.17 shows, the mean value of the basic friction angle is around 36^{o}. The coefficient of variation is about 0.1 for this parameter.

The dilation angle was more difficult to interpret. At drilled core scale, the coefficient of variation is only 0.06. However, only three tests were performed at this scale. If the other four tests performed by KTH were included, and a basic friction angle of 36.4^{o} was assumed, the coefficient of variation increased to 0.18

and the standard deviation increased to 5.4. With these new values for the drilled cores, together with the test performed at LTU, a trend against a decreasing standard deviation with increasing scale was seen for the dilation angle. This could be interpreted as a result from an averaging process for the contacting asperities with increased scale. On the other hand, it should be observed that if the dilation angle decreases, the coefficient of variation will increase. It is therefore important to consider the magnitude of the dilation angle in combination with the coefficient of variation.

The differences in surface damage and infilling materials for the joint samples tested in this chapter makes any statement regarding a possible scale effect uncertain. However, it can be concluded that shear tests at the drilled core scale resulted in total friction angles considerably higher than the other larger samples. It can also be concluded that changes in the total friction angle mainly originate from changes in the dilation angle and that the basic friction angle appears to be constant and independent of scale.

5.6.3 Implementation of conceptual model

For three of the samples, S6, L7 and the *in situ* sample, optical scanning of the joints was performed for characterization of surface roughness. Based on data from the optical scanning, parameters were derived which made it possible to apply the conceptual model for these three samples.

Input data for these calculations are presented in Table 5.19 and are based on the results from the shear test described previously in the chapter. The parameters used in the calculations that describe the roughness were taken from the lower part of the sample. The matedness constant, k, was varied.

Table 5.19 Input data for calculations of total friction angle with conceptual model.

Sample	**S6**	**L7**	***In situ***
ϕ_b [^{o}]	36.4	36.4	36.4
σ_n [MPa]	0.98	0.90	0.42
σ_{ci} [MPa]	140	140	140
L_g [mm]	1	1	1
A_o	0.778	0.321	0.457
C	8.76	7.41	7.76
θ_{max}	57.0	65.9	71.9
H	0.826	0.789	0.803

Total friction angle was calculated with equation 4.27 and dilation angle was calculated using equation 4.36. The results are presented in Figure 5.45 to 5.47.

The results show that the observed total friction angle for sample S6 and L7 are smaller than what could be anticipated for a maximal unmated joint, i.e. k>1. For the *in situ* joint, the observed total friction angle corresponds to a k=0.7. It can also be observed that at the drilled core scale, i.e. 40 to 60 mm, the conceptual model predicts total friction angles in the range of 50 to 70^o. These values agree well with the observed total friction angle from tests performed on drilled cores.

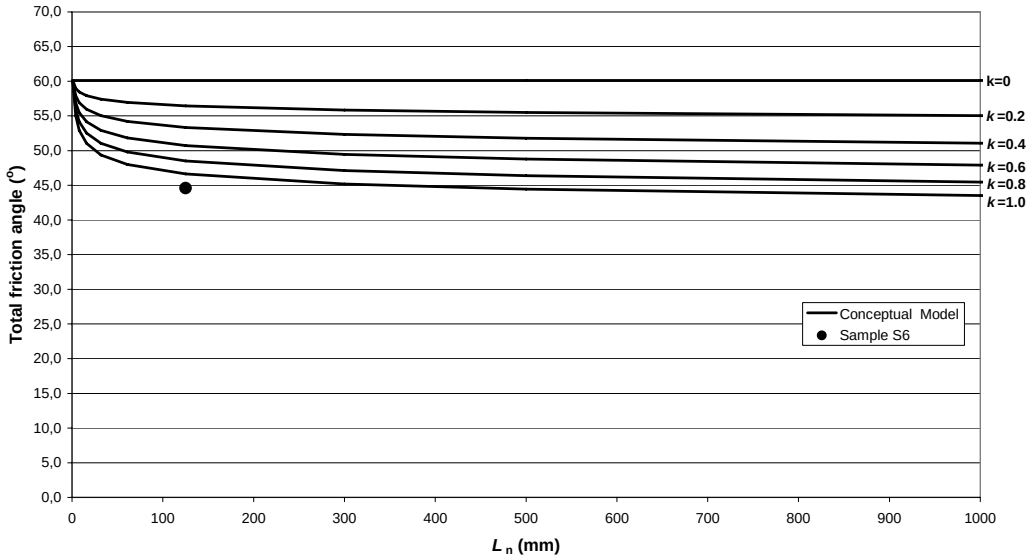

Figure 5.45 Calculated total friction angles for sample S6 for different values of k compared with measured value from shear test.

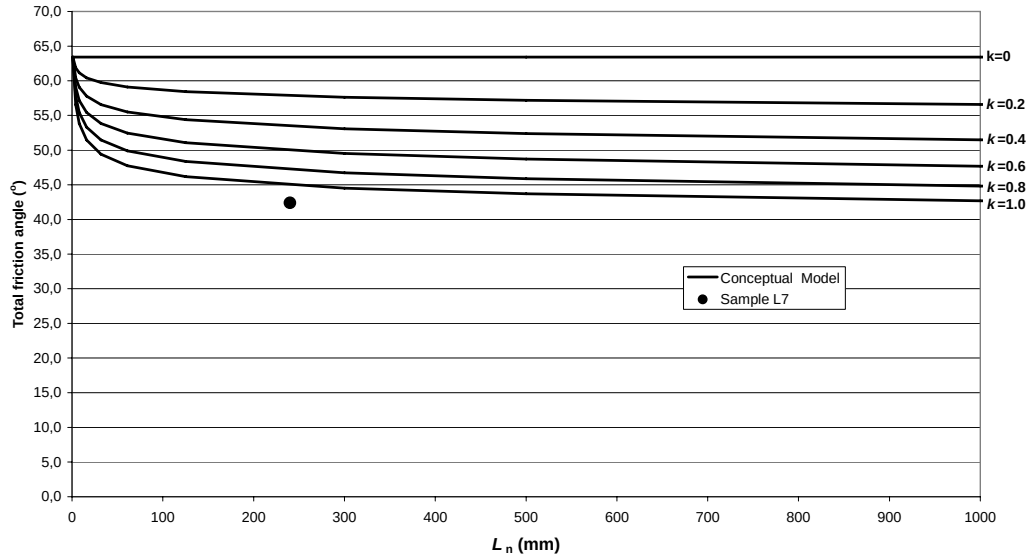

Figure 5.46 Calculated total friction angles for sample L7 for different values of k compared with measured value from shear test.

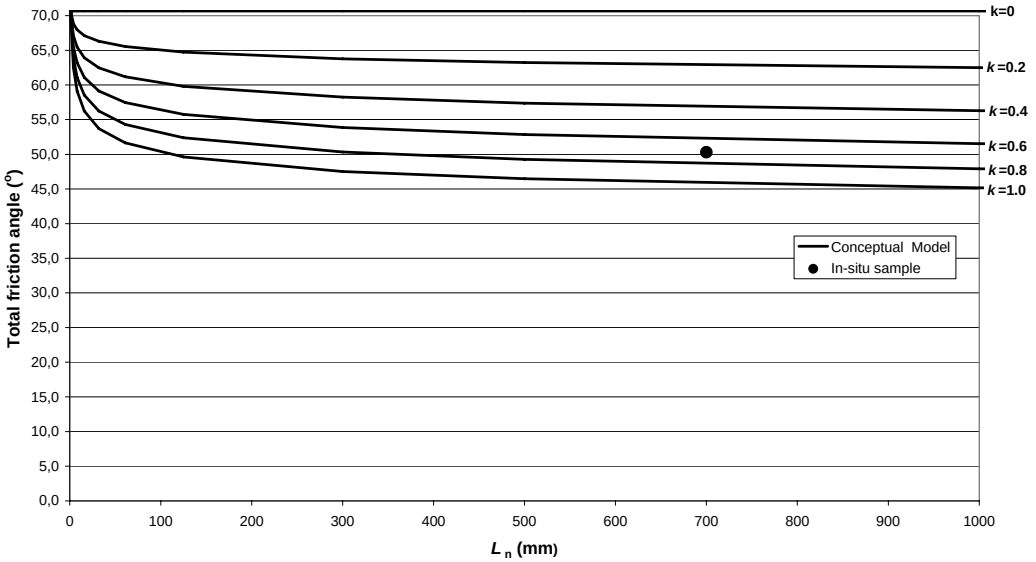

Figure 5.47 Calculated total friction angles for in situ sample for different values of k compared with measured value from shear test.

5.6.4 Analyses on the distribution of contact points for sample S6 and L7

As shown in the previous Figures 5.45 to 5.47, the measured dilation angles for the shear tests performed at LTU were unexpectedly low. The values were lower than the conceptual model predicted for a maximal unmated joint. In order to investigate the cause for these unexpectedly low values; the data from the optical scanning of sample S6 and L7 were used to study aperture at rest and surface damage after the shear test were performed.

First, the aperture at rest was determined based on the data from the optical scanning, i.e. before the shear test. The results are presented in Figure 5.48 and 5.49. As the results in the figures shows, the aperture varies from 0 up to about 3.5 mm for sample S6 and from 0 up to about 5 mm for sample L7. In the figures, red spots are areas close to contact under normal load equal to the dead weight of the sample. These figures indicate a poor initial matedness of the samples.

After that, differences in surface height before and after the shear test were calculated for the upper and lower parts of the samples. The total differences with changes larger than 0.1 mm were added together for the lower and the upper parts of the sample and plotted. The results are shown in Figure 5.50 and 5.52. The measured dip angles against the shear direction larger than 7^o were plotted in Figure 5.51 and 5.53. If the locations of the damaged zones are compared with the zones for the potential contact areas, it can be observed that a perfect correlation does not exist between actual damages areas and predicted contact areas. This implies that the dilation angle did not originate from the steepest inclined asperities as it was assumed in the conceptual model. Instead, the contact points appeared to be more randomly distributed depending on the initial points of contact at rest. As a consequence, the dilation angles become smaller than those that would originate from the steepest inclined asperities on the sample. This indicates that it might be necessary to distinguish between undamaged and damaged joints, since the mechanism that governs the distribution and density of the contact points could be different.

The results from the *in situ* test might further support this idea. Even though the joint has some infilling materials, results indicates that the joint is more undamaged than sample S6 and L7. Contact points shown as white spots in Figure 5.38 are located on the steepest asperities facing the shear direction in Figure 5.40. This might explain why the total friction angle calculated with the conceptual model agrees better for the *in situ* shear test than for sample S6 and L7.

Whether the steepest asperities facing the shear direction come into contact, or if a more random distribution of the asperities at contact occur, is important in order to understand the origin of the dilation angle. The three test cases analysed here indicate that both of these distributions could be possible depending on initial surface damage. Further studies are required to analyse the effect from surface damage on the distribution of the contact points before this could be verified.

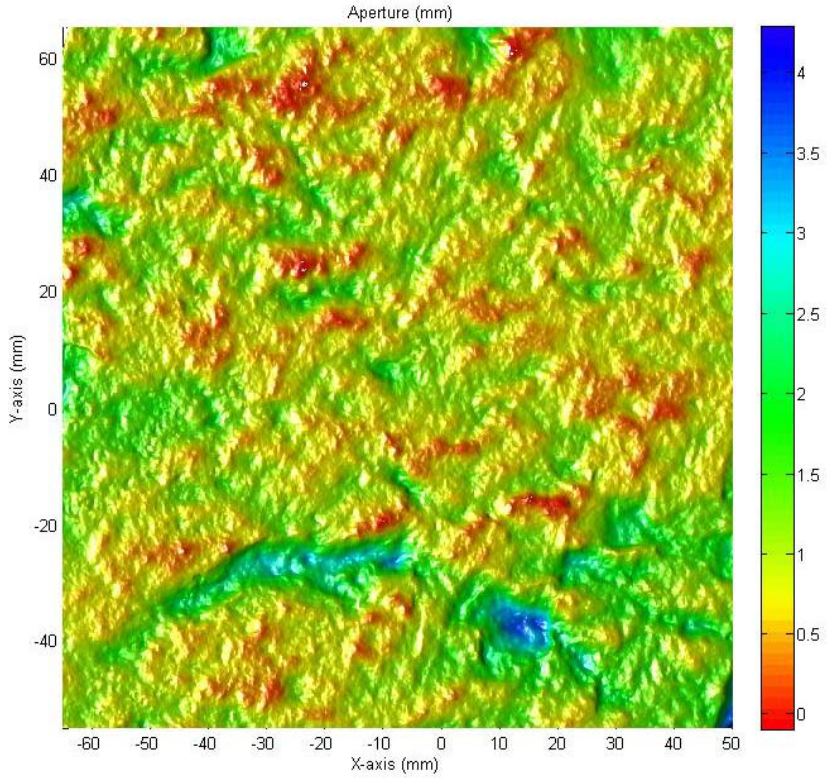

Figure 5.48 Aperture at rest for sample S6 before direct shear testing.

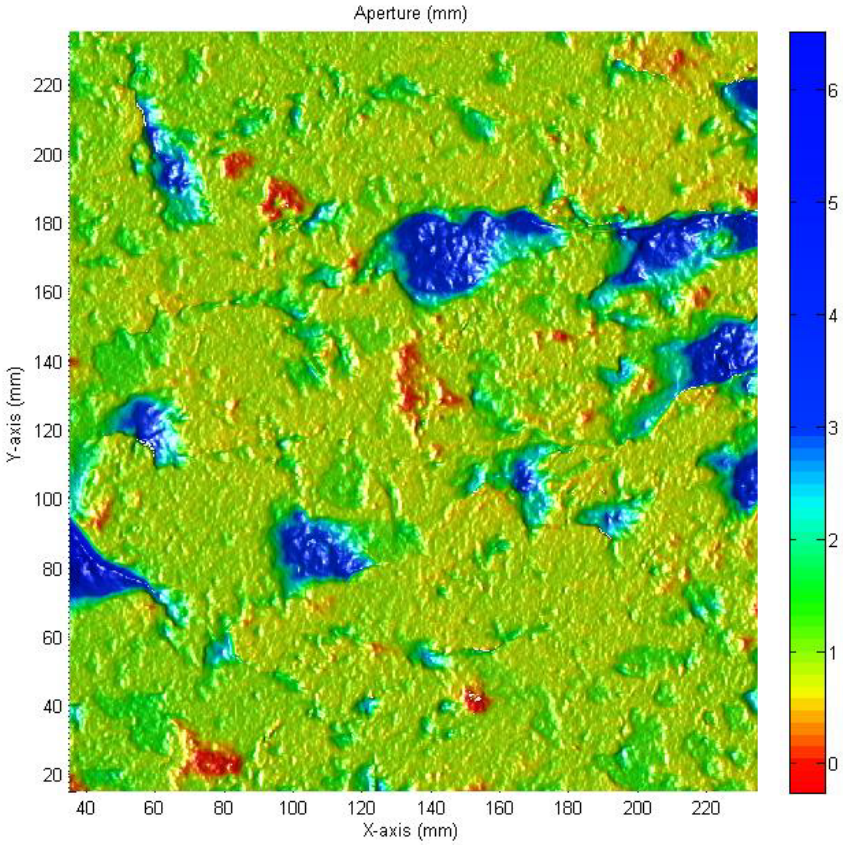

Figure 5.49 Aperture at rest for sample L7 before direct shear testing.

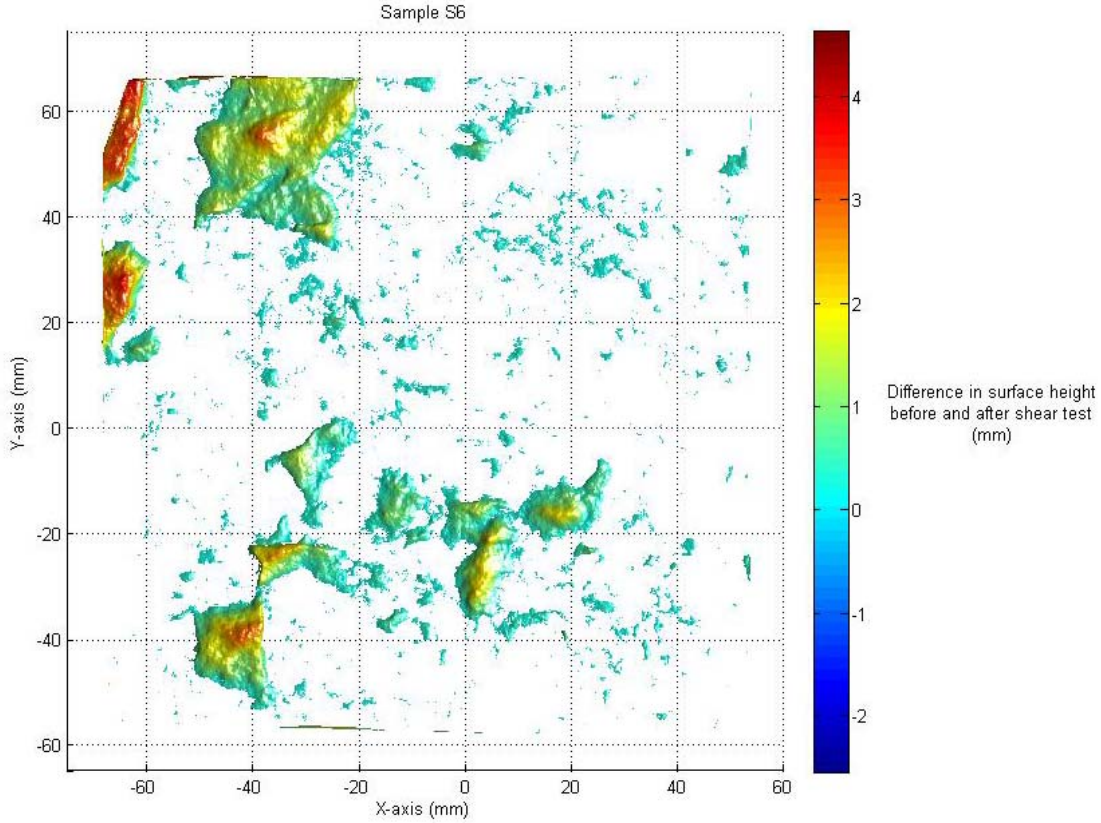

Fig 5.50 Differences in surface height for sample S6 before and after the shear test.

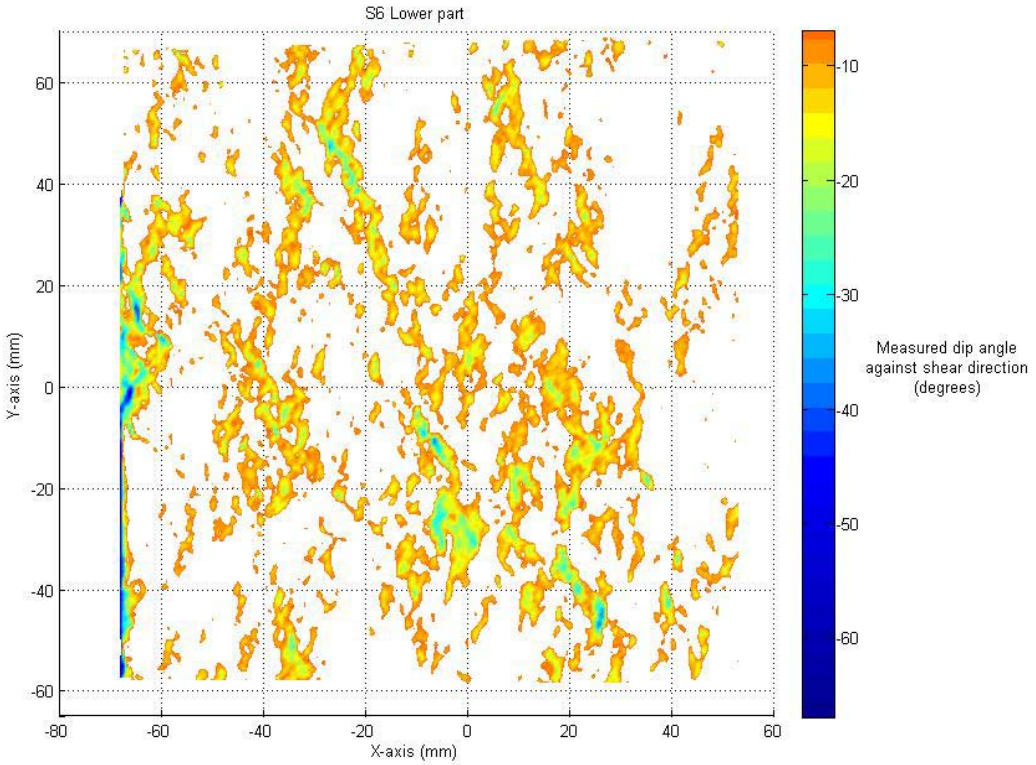

Fig 5.51 Potential contact areas with measured dip angles larger than 7^{o} for sample S6.

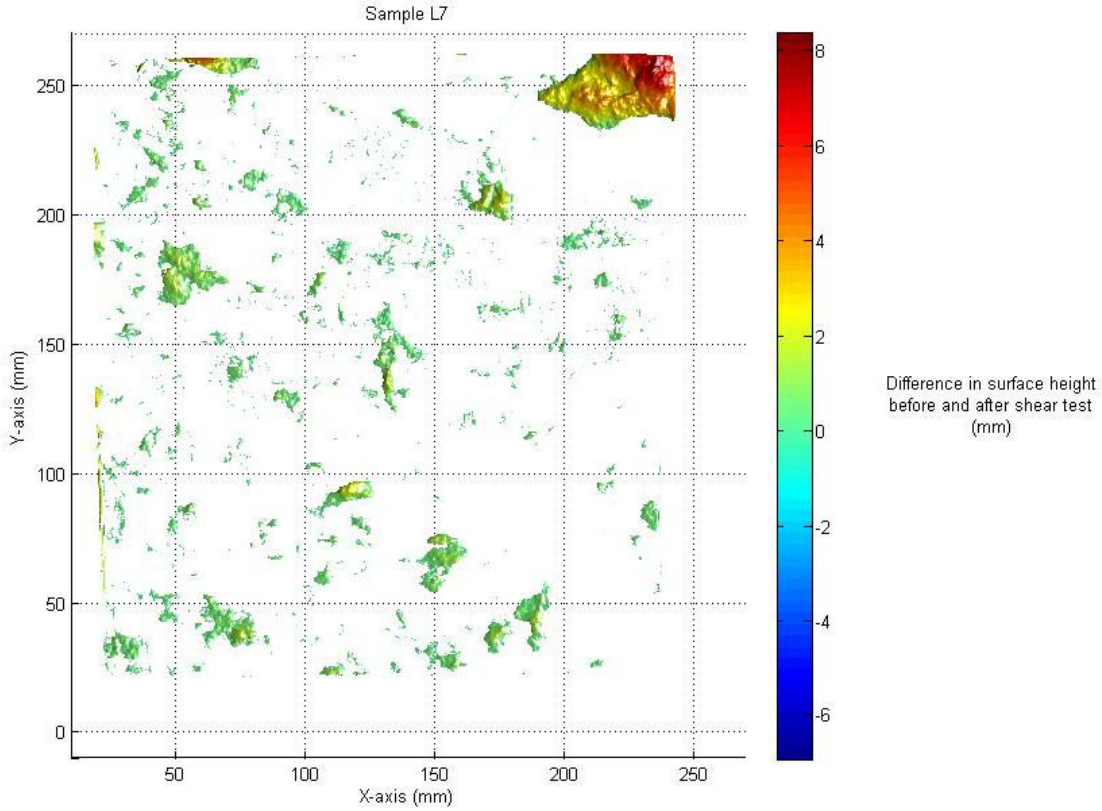

Fig 5.52 Differences in surface height for sample L7 before and after the shear test.

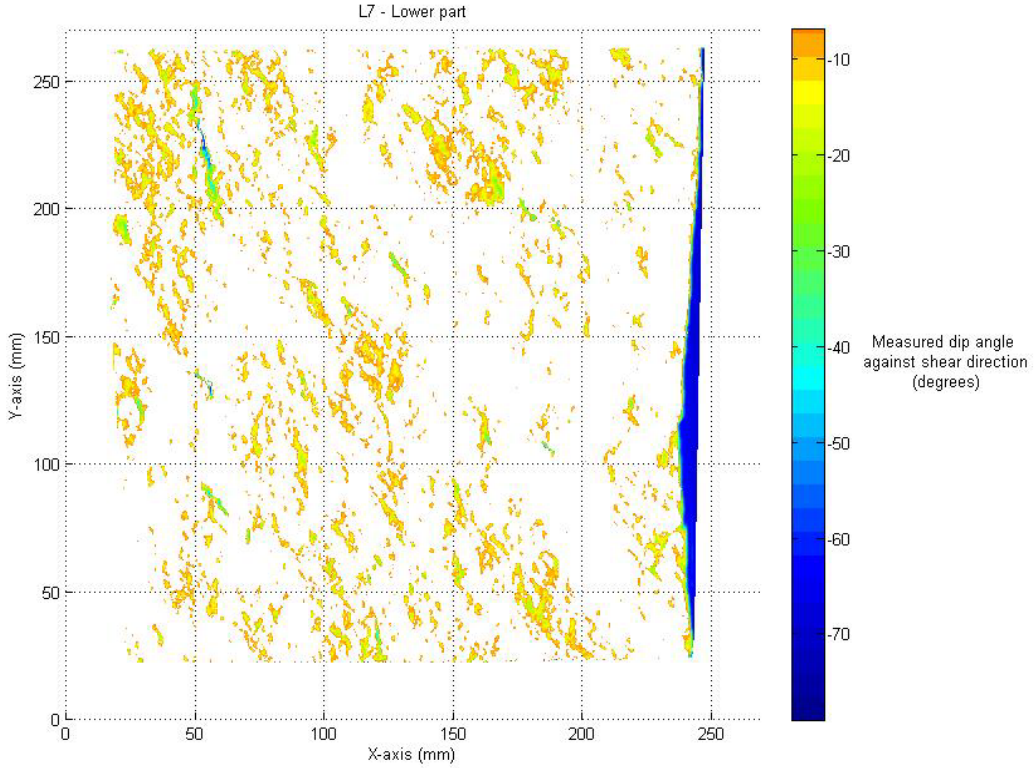

Fig 5.53 Predicted contact areas with measured dip angles larger than 7^{o} for sample L7.

5.6.5 Discussion on the potential contact area ratio for different sampling distances

In Chapter 4, a discussion was presented on how the potential contact area ratio changes with increasing scale for a constant sampling distance. According to the assumptions made in the conceptual model, the potential contact area ratio should, in principle, remain unchanged. To study if this is the case, the potential contact area ratio was determined for the lower surface of the *in situ* sample at four different scales. The results are presented in Figure 5.54.

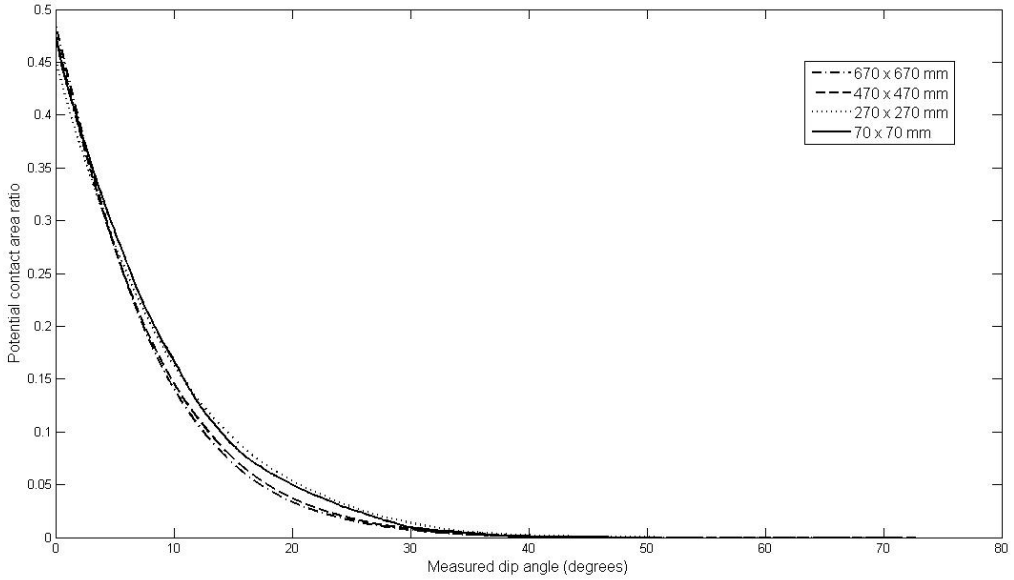

Figure 5.54 Potential contact area ratios for the lower surface of the in situ sample at four different scales, sampling distance was held constant at 0.5 mm.

As shown by the results, the potential contact area ratio are in principle constant for different sizes of the joint surface if the sampling distance is constant. These results support the assumption made in Chapter 4.

5.6.6 Discussion on the matedness constant

In the previous calculations, the value on the constant k was varied. However, no discussion was held regarding how it could be estimated.

According to the conceptual model in Chapter 4, k is a constant that describes the degree of matedness for a joint. In Figure 4.11, the difference between a perfectly mated joint and an unmated joint is described as an effect from a relative shear displacement between the upper and the lower joint surface. Following the assumption from Chapter 4, the shear displacement could be assumed to range from half of the grain size scale to half of the sample length for a perfectly mated and a maximal unmated joint respectively. Under these assumptions, and by using equation 4.31, the relation between k and the shear displacement at peak shear strength, $\delta_{s,p}$, could be expressed as:

$$k = \frac{\log \delta_{s,p} - \log \delta_{s,min}}{\log \delta_{s,max} - \log \delta_{s,min}} \quad (5.6)$$

Based on the assumption illustrated in Figure 4.11, which illustrates that shear displacements are associated with asperity base lengths, it can be assumed that $\delta_{s,min}$ for a perfectly mated joint is equal to $L_g/2$ and $\delta_{s,max}$ for a maximal unmated joint is equal to $L_n/2$.

With equation 5.6 and the assumptions that $\delta_{s,min} = L_g/2$ and $\delta_{s,max} = L_n/2$, values on k for different shear displacements at peak shear strength, $\delta_{s,p}$, were calculated according to Figure 5.55.

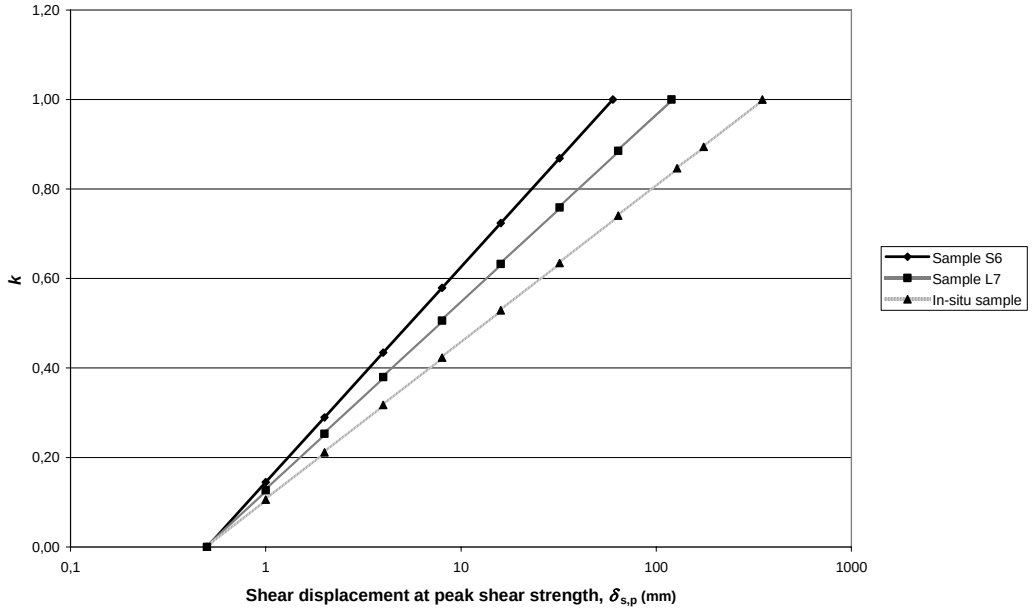

Figure 5.55 Calculated values on k for different peak shear displacements, $\delta_{s,p}$.

The relation between k and $\delta_{s,p}$ shown in the figure illustrates that k is sensitive to small changes of relative shear displacement with respect to the grain scale. However, if this relation is used and compared against results from shear tests, it should be emphasized that observed $\delta_{s,p}$ in shear test is not necessarily equal to the true shear displacement of the joint. Any displacements that occurred prior to the start of the shear test are not included. It is therefore possible to underestimate the value of k if observed $\delta_{s,p}$ from shear test are used in equation 5.6.

Other sources of uncertainty are also the assumptions that the maximal asperity length of the joint, $L_{asp,max}$ equals the sample length or that the grain size, L_g, equals 1 mm. It is possible that the maximal asperity base length is smaller than the sample length. If so, the value on k increases for a specific shear displacement at peak shear strength.

Observed shear displacements at peak shear strength for sample S6, L7 and the *in situ* sample was used to estimate values on k with equation 5.6. Total friction

angles were calculated with the data in Table 5.19, together with calculated values on *k* by using equation 5.6. The results are presented in Table 5.20.

Table 5.20 Calculated values on k based on shear displacement at peak shear strength, $\delta_{s,p}$ together with total friction angles calculated with conceptual model and from shear tests.

Sample	**S6**	**L7**	***In situ***
$\delta_{s,p}$ [mm]	3.2	2.2	6.6
k (Eq. 5.6)	0.39	0.27	0.39
ϕ_p (Eq. 4.27+4.36)	53.5	56.2	57.1
ϕ_p (From shear tests)	44.6	42.4	50.3

As shown by the results in Table 5.20, the conceptual model predicted total friction angles higher than observed for sample S6 and L7. This might partly be an effect of too low values on *k*, and it might partly be an effect of that asperity inclinations at contact were not associated with the steepest ones facing the shear direction on the samples S6 and L7. Furthermore, the infilling material present in the joint for the *in situ* sample might have reduced the total friction angle in the shear test.

Even if equation 5.6 underestimate the value on *k* for samples S6, L7 and the *in situ* sample, it is showing an important conceptual mechanism, that is the rapid decrease of the matedness constant for small relative shear displacements.

5.7 Conclusions

Laboratory and an *in situ* shear test were performed on samples taken from the rock foundation of Långbjörn concrete dam. All in all, 22 shear tests of different scales were analysed, seven in drill core scale (40 and 60 mm), seven in 125 by 125 mm scale, seven in 240 by 240 mm scale, and one *in situ* shear test at 700 by 700 mm scale.

The results show that: (1) the peak friction angle could be expressed as the sum of a basic friction angle and a dilation angle as initially proposed by Patton (1966). (2) The basic friction angle appears to be independent of scale which is in line with results by, for example, Barton and Choubey (1977). (3) Changes in the total friction angle for different joint sizes in hard rocks mainly originate from changes in the dilation angle as suggested by Papaliangas (1996). (4) A possible scale effect on the dilation angle could be observed since shear tests in the smallest scale gave considerably higher values than the other larger samples. However, the magnitude of this effect is uncertain due to differences in joint surface characteristics. (5) Before the conceptual model could be used in design, further studies are required. In particular, it is recommended that these studies focus on the distribution of contact points for damaged and undamaged surfaces, i.e. weathered and unweathered surfaces, with respect to the inclination of the asperities.

6 DISCUSSION ON DETERMINISTIC AND RELIABILITY BASED METHODS IN SLIDING STABILITY ANALYSES

6.1 Introduction

During the past few years, there has been a discussion in Sweden about the implementation of reliability based methods in geotechnical and dam design, especially after the implementation of Eurocode. However, the use of probabilistic concepts is not new in these areas. For example, Höeg and Murarka (1974) presented an example where they designed a retaining wall with both deterministic and probabilistic methods in order to encourage the use of probabilistic methods in geotechnical engineering. Studies of the application for reliability based analyses with respect to sliding stability have been performed on Swedish concrete dams by Jeppsson (2003) and Westberg (2007). Their results showed that the shear strength of the interface between concrete and rock were the most important variable for the reliability of the dams.

In this chapter, deterministic and reliability based analyses are carried out for a concrete monolith at Långbjörn hydropower station. Based on the results from sliding stability analyses, the two methods are compared and discussed. At the end of the chapter, conclusions are presented. It should be emphasized that this chapter primarily intends to bring focus on some key questions regarding reliability based design and sliding stability analyses in rock foundations. By doing so, areas for further studies in the subject are identified. Furthermore, it should be observed that the calculated safety of the monolith in this chapter does not necessarily reflect the actual safety of the dam.

The analyses performed here are similar to those performed by Jeppsson (2003) and Westberg (2007). However, the analyses performed in this chapter focus on the sliding stability in a shallow persistent joint assumed to exists in the rock mass. The friction angle for this joint is based on the results from the conceptual model presented in Chapter four and the performed shear tests described in Chapter five.

6.2 The analysed monolith

The study was performed on a monolith in the spillway section of the concrete dam at Långbjörn hydropower station. The monolith for column three, which was analysed in this chapter, can be seen in Figure 6.1.

A normal load case was analysed with closed gates and ice load. A horizontal persistent joint was assumed to exist three meters below the rock surface, together with a vertical tension crack in the rock mass at the upstream face of the dam. No consideration was taken to a possible passive rock wedge at the downstream side of the dam.

Figure 6.1 Photo of the spillway at Långbjörn concrete dam. The monolith for column 3, analysed in this chapter, is the second one from the right side in the picture.

In 2006, several of the monoliths at the concrete dam were reinforced with pre-stressed anchor cables. Each cable were pre-stressed with 2 160 kN and inclined 70^{o} upstream with respect to the horizontal plane. The monolith for column three was reinforced with ten pre-stressed anchor cables adding a total vertical load of 18 706 kN and a horizontal load of 10 800 kN directed upstream.

6.3 Estimation of shear strength

6.3.1 Basic friction angle

According to the results from the shear tests, the basic friction angle varied between 29.5 to 45.5^{o}. Mean value of all eighteen tests was 36.4^{o}. The highest value originated from the *in situ* shear test. If the *in situ* shear test was excluded, the mean value became 35.9^{o}, with a minimum value of 29.5^{o} and a maximum value of 43.5^{o}. In these analyses, a mean value of 36^{o} was used together with two different coefficients of variations equal to 0.07 and 0.10.

Normal distributions were assumed for the basic friction angle. Figures showing the assumed distributions for the basic friction angle can be seen in Appendix C.

6.3.2 Dilation angle

The dilation angle was estimated with the conceptual model in Chapter four, together with data from the optical scanning of the three samples previously described.

Normal stress in the calculations was set to 0.8 MPa, which was the calculated maximal stress under the dam (SWECO VBB VIAK 2002). The dilation angle at

grain size scale was calculated with equation 4.32. Input data and results are presented in Table 6.1.

Table 6.1 Input data and calculated dilation angle at grain size scale.

Sample	**S6**	**L7**	**In-situ**
σ_n [MPa]	0.8	0.8	0.8
σ_{ci} [MPa]	140	140	140
A_o	0.778	0.321	0.457
C	8.76	7.41	7.76
Θ^*_{max}	57.0	65.9	71.9
Calculated i_g [^{o}]	25	28	31

The results in Table 6.1 show that i_g vary between 25 and 31^o. Furthermore, results in the previous chapter indicated that k could be assumed to vary between 0.5 and 1.0, and the Hurst exponent could be assumed to vary between 0.77 to 0.83. By using equation 4.36, with L_g=1 mm and L_n=30 000 mm, different values on the dilation angle, i_n, at a size of 30 m were calculated. The results are presented in Table 6.2.

Table 6.2 Calculated values on the dilation angle.

k	i_g [^{o}]	H	i_n [^{o}]
0.5	25	0.77	8
		0.80	9
		0.83	10
	28	0.77	9
		0.80	10
		0.83	12
	31	0.77	9
		0.80	11
		0.83	13
0.7	25	0.77	5
		0.80	6
		0.83	7
	28	0.77	5
		0.80	7
		0.83	8
	31	0.77	6
		0.80	7
		0.83	9
1.0	25	0.77	2
		0.80	3
		0.83	4
	28	0.77	3
		0.80	4
		0.83	5
	31	0.77	3
		0.80	4
		0.83	5

The results in Table 6.2 show that the dilation angle might range from 2 up to 13^o. These results indicate a possible mean value equal to about 7^o. However, it could be assumed that the joints under the dam are less weathered than the LTU samples and have less infilling than the *in situ* sample. Therefore, a slightly higher mean value on the dilation angle equal to 9^o was assumed together with two different coefficients of variations equal to 0.15 and 0.30.

Normal distributions were assumed for the dilation angle. Figures showing the assumed distributions for the dilation angle can be seen in Appendix D.

6.4 Input data

An illustration showing the layout of the monolith and the forces with their notations are presented in Figure 6.2.

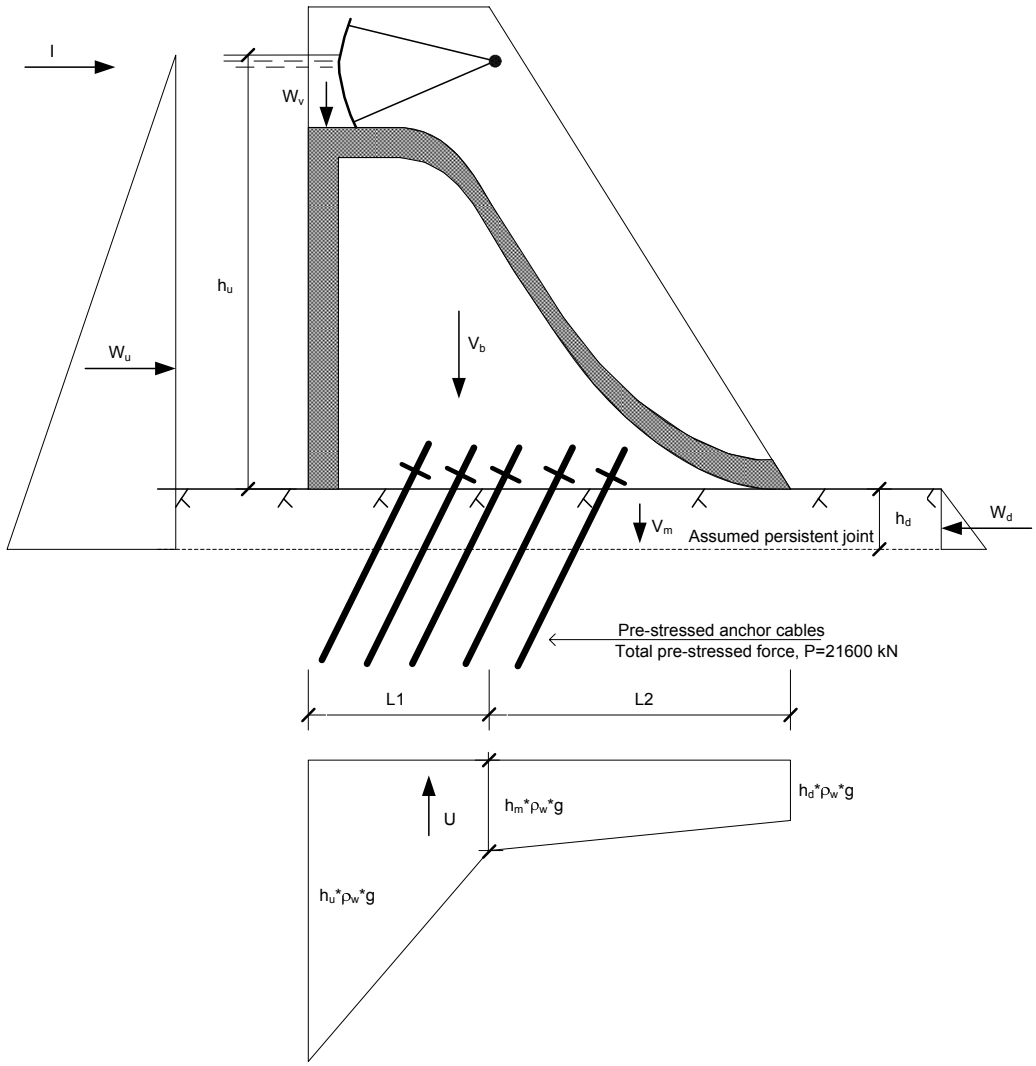

Figure 6.2 Illustration of the monolith with major forces and their notations.

In addition to the basic friction angle and the dilation angle, three additional variables were chosen to be non-deterministic. These were the measured pore pressure ten meters downstream the upstream face, the unit weight of the concrete and the unit weight of the rock mass. These variables were assumed to be normal distributed.

Under the spillway, pore pressures were measured three to five meters under the rock surface at five locations ten meters downstream the upstream face. Measurements were performed from June 2006. This means that only a limited period of measurements is available. Since the target safety index is expressed in terms of a reference period of one year, maximum measured pore pressure for each year should be used to obtain the mean and standard deviation of it. Due to the short period of measurements, the maximum measured value under the monolith was used as a mean value. A COV=0.15 was assumed in the reliability analysis. The uplift pressure was assumed to vary according to Figure 6.2 and can be considered to be conservative.

The coefficient of variation for the unit weight of the concrete and the rock mass was assumed to be 0.04.

Input data for all parameters are presented in Table 6.3.

Table 6.3 Input data for the calculations.

Description	**Denotation**	***μ***	***COV***	***σ***
Unit weight of water	γ_w [kN/m^3]	9.81	-	-
Unit weight concrete	γ_c [kN/m^3]	23.54	0.04	0.94
Volume concrete	V_c [m^3]	4316	-	-
Unit weight rock mass	γ_m [kN/m^3]	26.00	0.04	1.04
Volume rock mass	V_m [m^3]	1802	-	-
Total horizontal water load	W_h [kN]	96413	-	-
Total vertical water load	W_v [kN]	8858	-	-
Iceload	I [kN]	3640	-	-
Pre-stressed anchor cables	P [kN]	21600	-	-
Upstream water height	h_u [m]	33.0		
Measured pressure head	h_m [m]	6.2	0.15	0.93
Downstream water height	h_d [m]	3.0		
Length u.s. face to pressure measurement	$L1$ [m]	10.0		
Length d.s. face to pressure measurement	$L2$ [m]	23.0		
Width of block	L_{width} [m]	18.2		
Basic friction angle	ϕ_b [°]	36	0.07/ 0.10	2.52/ 3.60
Dilation angle	i [°]	9	0.15/ 0.30	1.35/ 2.70

6.5 Deterministic analyses

According to the present Swedish guidelines (RIDAS 2008), the safety against sliding should be evaluated by calculating the coefficient of friction, μ, defined as:

$$\mu = \frac{\sum H}{\sum V'} \leq \mu_{all} \qquad (6.1)$$

where ΣH is the sum of the loads parallel to the sliding plane and $\Sigma V'$ is the sum of the loads vertical to the sliding plane. According to RIDAS (2008), the coefficient of friction should be lower than 0.75 for a normal load case.

The factor of safety, *SF*, was calculated according to equation 6.2:

$$FS = \frac{\sum V' \cdot \tan\left(\phi_b + i\right)}{\sum H} \tag{6.2}$$

According to RIDAS, the factor of safety should be at least 1.35 for a normal load case.

A summary of all vertical and horizontal loads is given in Table 6.4. The values in the table are based on the mean values of the variables.

Table 6.4 Summary of vertical and horizontal loads.

Description	Denotation		*V* (kN)	*H* (kN)
Self weight concrete	Vb		101602	
Self weight rock mass	Vm		47748	
Vertical water load	Wv		8858	
Horizontal water load	Wh			96413
Ice load	I			3640
Uplift pressure	U		-53883	
		Σ:	**104325**	**100053**
Pre-stressed anchor cables	L		18706	-10800
		Σ:	**123031**	**89253**

Coefficients of friction and factors of safety for the case with and without pre-stressed anchor cables were calculated using equation 6.1 and 6.2. The results are presented in Table 6.5.

Table 6.5 Calculated coefficients of friction and factors of safety.

	μ	*FS*
Without pre-stressed anchor cables	0.96	1.04
With pre-stressed anchor cables	0.72	1.38

6.6 Theory of reliability based design

The method used in this chapter to calculate the probability of failure is FORM, First Order Reliability Method. A brief description of the theory behind this type of calculations is presented below. The theory behind the method can be found in literature such as Melchers (1999) among others.

As described previously in Chapter 2, the probability of failure can be expressed as:

$$p_f = p\left[R - S \le 0\right] \tag{6.3}$$

where, R and S are described by a known probability density function. It can also be expressed according to equation 6.4. The safety margin M=R-S can be used to express the probability of failure as:

$$p_f = p[M \le 0] \tag{6.4}$$

If the capacity, R, and the load, S, is normal distributed and independent variables, M will also be normal distributed since M is a linear function of R and S. Therefore, the mean value of M can be expressed as:

$$\mu_{\mathrm{M}} = \mu_{\mathrm{R}} - \mu_{\mathrm{S}} \tag{6.5}$$

where μ_{M}, μ_{R} and μ_{S} is the mean value of the safety margin, the resistance and the load respectively. The standard deviation of M will be:

$$\sigma_{\mathrm{M}} = \sqrt{\sigma_{\mathrm{R}}^2 + \sigma_{\mathrm{S}}^2} \tag{6.6}$$

With this information the probability of failure can be expressed as:

$$p_{\mathrm{f}} = \Phi\left(\frac{0 - \mu_{\mathrm{M}}}{\sigma_{\mathrm{M}}}\right) \tag{6.7}$$

where Φ is the standard normal distribution.

The probability of a structure can be expressed with the safety index, β. The safety index expresses how many standard deviations that μ_{M} exceeds zero. In other words, the safety index, β, can be defined as:

$$\beta = \frac{\mu_{\mathrm{M}}}{\sigma_{\mathrm{M}}} \tag{6.8}$$

From equation 6.7 and 6.8, the probability of failure can be written as:

$$p_{\mathrm{f}} = \Phi(-\beta) \tag{6.9}$$

Hence, the safety index can be expressed as the inverse of the standard normal distribution for a given probability of failure.

The calculation of the safety index for a structure can be performed with the method presented by Hasofer and Lind (1974), i.e. FORM. In this method, each variable, X_i, is first normalized with a mean, $\mu_{\mathrm{X}i}$, and standard deviation, $\sigma_{\mathrm{X}i}$. By doing so, the normalized variables, Z_{i}, can be expressed as:

$$Z_i = \frac{X_i - \mu_{\mathrm{X}i}}{\sigma_{\mathrm{X}i}} \tag{6.10}$$

It should be observed that with this definition, μ_{Xi}=0 and σ_{Xi} =1. The new set of normalized variables can be used to express the performance function as:

$$f\left(Z_1, Z_2, ..., Z_n\right) = 0 \tag{6.11}$$

The function above results in a failure surface in the z-coordinate system. The shortest distance from origo, *O*, to the performance function is to a point called the design point, *D*. In mathematical terms, the shortest distance is expressed as:

$$\beta = \min\left(\sum_{i=1}^{n} Z_i^2\right)^{\frac{1}{2}} \tag{6.12}$$

The unit vector of $\overline{OD}$ can be expressed in terms of the sensitivity coefficients α_i as $\beta\overline{\alpha}$. The sensitivity factors are calculated according to equation 6.13:

$$\alpha_i = \frac{-\frac{\partial f}{\partial Z_i}\left(\beta\overline{\alpha}\right)}{\left[\sum_{k=1}^{n}\left(\frac{\partial f}{\partial Z_k}\left(\beta\overline{\alpha}\right)^2\right)\right]^{\frac{1}{2}}} \tag{6.13}$$

where $\beta\alpha_i, \ldots, \beta\alpha_n$ are the coordinates of the design point, D.

The sensitivity factors calculated according to equation 6.13 can be used to calculate partial coefficients for each variable according to equation 2.7.

The strength with the method described above is that all variables do not have to be normal distributed. Instead, any arbitrary distribution function can be transformed into an equivalent normal distribution. With many basic variables in the problem, analytical calculations tend to be quite tedious. As a consequence, the program COMREL (RCP 2008) was used for the calculations presented in this study.

6.7 Reliability requirements

Swedish dams are designed according to the concept of a coefficient of friction or a safety factor. In addition to this, the dam owner also has a strict responsibility for the dam according to the plan and building law, PBL. As a consequence, no target safety index has been recommended for Swedish dams.

However, as pointed out by Jeppsson (2003), reference is made in RIDAS (2008) to BBK 94 (Boverket 1995) and it would therefore seem logical to relate the safety system to BKR (Boverket 2003). The Swedish design guidelines, BKR (Boverket 2003) relate different types of structures to different safety classes. The highest safety class, 3, is used when collapse involve a high risk of personal injury, or when the properties of the structure are such that failure would cause

immediate collapse. In Table 6.6, target safety index from BKR (Boverket 2003) at different safety classes are presented.

Table 6.6 Target safety index from BKR (Boverket 2003).

Safety Class	β_t (one year reference period)
1	3.7
2	4.3
3	4.8

The recommendations in RIDAS (2008) suggest that all dams should be classified into a consequence class, depending on the consequences if failure occurs. Lower hazard dams are classified into class 2 and 3, while higher hazard dams are classified into class 1A and 1B. Roughly, the values in Table 6.6 could be assumed to correspond with reasonable demands for Swedish dams in the different consequence classes. Where consequence class 2 respectively 1B would correspond with a target safety index of 3.6 and 4.3 respectively. Dams in the highest consequence class, 1A, could in other words be assumed to have a target safety index around 4.8. The concrete dam at Långbjörn is classified as a class 1A dam. The corresponding target safety index would therefore be 4.8.

However, it should also be observed that the consequence classes used by RIDAS are not correlated with the safety classes in BKR (2003). For a more comprehensive description of recommended target safety index in different structural codes, see for example Westberg (2007).

6.8 Reliability analyses

The limit state function for sliding of column three could be expressed as:

$$\sum V' \cdot \tan\left(\phi_b + i\right) + L \cdot \sin 30 - \sum H = 0 \tag{6.14}$$

where

$$\sum H = W_{\mathrm{h}} + I \tag{6.15}$$

$$\sum V' = V_{\mathrm{c}} \cdot \gamma_{\mathrm{m}} + V_{\mathrm{m}} \cdot \gamma_{\mathrm{m}} + W_{\mathrm{v}} - U + L \cdot \cos 30 \tag{6.16}$$

and

$$U = \left(0.5 \cdot L1 \cdot \left(h_{\mathrm{u}} + h_{\mathrm{m}}\right) + 0.5 \cdot L2 \cdot \left(h_{\mathrm{m}} + h_{\mathrm{d}}\right)\right) \cdot L_{\mathrm{width}} \cdot \gamma_{\mathrm{w}} \tag{6.17}$$

Description and input data for the variables are given in Table 6.3.

Results from the calculations with normal distributed variables are given in Table 6.7-6.12.

Table 6.7 Calculated β-index for the case without pre-stressed anchor cables. Basic friction angle and dilation angle assumed independent and normal distributed.

Without pre-stressed anchor cables						
Basic friction angle ϕ_b (°)			Dilation angle i (°)			Calculated β
μ	COV	σ	μ	COV	σ	
36	0.07	2.52	9	0.15	1.35	0.13
	0.07	2.52		0.30	2.70	0.11
	0.10	3.60		0.15	1.35	0.10
	0.10	3.60		0.30	2.70	0.09

Table 6.8 Sensitivity factors for the case without pre-stressed anchor cables. Basic friction angle and dilation angle assumed independent and normal distributed.

Without pre-stressed anchor cables										
Basic friction angle ϕ_b (°)			Dilation angle i (°)			$\alpha_{\rho b}$	$\alpha_{\rho m}$	α_{hm}	α_{ϕ}	α_i
μ	COV	σ	μ	COV	σ					
36	0.07	2.52	9	0.15	1.35	-0.35	-0.17	0.24	-0.78	-0.42
	0.07	2.52		0.30	2.70	-0.28	-0.13	0.19	-0.63	-0.68
	0.10	3.60		0.15	1.35	-0.27	-0.13	0.19	-0.87	-0.33
	0.10	3.60		0.30	2.70	-0.24	-0.11	0.16	-0.76	-0.57

Table 6.9 Partial factors for the case without pre-stressed anchor cables. Basic friction angle and dilation angle assumed independent and normal distributed.

Without pre-stressed anchor cables										
Basic friction angle ϕ_b (°)			Dilation angle i (°)			$\gamma_{\rho b}$	$\gamma_{\rho m}$	γ_{hm}	γ_{ϕ}	γ_i
μ	COV	σ	μ	COV	σ					
36	0.07	2.52	9	0.15	1.35	1.07	1.03	0.85	1.36	1.16
	0.07	2.52		0.30	2.70	1.06	1.03	0.88	1.27	1.30
	0.10	3.60		0.15	1.35	1.05	1.03	0.88	1.72	1.19
	0.10	3.60		0.30	2.70	1.05	1.02	0.90	1.57	1.38

Table 6.10 Calculated β-index for the case with pre-stressed anchor cables. Basic friction angle and dilation angle assumed independent and normal distributed.

With pre-stressed anchor cables						
Basic friction angle ϕ_b (°)			Dilation angle i (°)			Calculated β
μ	COV	σ	μ	COV	σ	
36	0.07	2.52	9	0.15	1.35	2.71
	0.07	2.52		0.30	2.70	2.17
	0.10	3.60		0.15	1.35	2.09
	0.10	3.60		0.30	2.70	1.81

Table 6.11 Sensitivity factors for the case without pre-stressed anchor cables. Basic friction angle and dilation angle assumed independent and normal distributed.

With pre-stressed anchor cables										
Basic friction angle ϕ_b (°)			Dilation angle i (°)			$\alpha_{\rho b}$	$\alpha_{\rho m}$	α_{hm}	α_{ϕ}	α_i
μ	COV	σ	μ	COV	σ					
36	0.07	2.52	9	0.15	1.35	-0.31	-0.15	0.21	-0.81	-0.43
	0.07	2.52		0.30	2.70	-0.24	-0.11	0.17	-0.65	-0.69
	0.10	3.60		0.15	1.35	-0.23	-0.11	0.16	-0.89	-0.33
	0.10	3.60		0.30	2.70	-0.20	-0.09	0.14	-0.77	-0.58

Table 6.12 Partial factors for the case without pre-stressed anchor cables. Basic friction angle and dilation angle assumed independent and normal distributed.

With pre-stressed anchor cables										
Basic friction angle ϕ_b (°)			**Dilation angle i (°)**			$\gamma_{\rho b}$	$\gamma_{\rho m}$	γ_{hm}	γ_{ϕ}	γ_i
μ	COV	σ	μ	COV	σ					
36	0.07	2.52	9	0.15	1.35	1.06	1.03	0.87	1.37	1.17
	0.07	2.52		0.30	2.70	1.05	1.02	0.89	1.28	1.30
	0.10	3.60		0.15	1.35	1.05	1.02	0.90	1.75	1.19
	0.10	3.60		0.30	2.70	1.04	1.02	0.91	1.59	1.39

In order to illustrate the results more clearly the COV for the total friction angle, i.e. the sum of the basic friction angle and the dilation angle, has been approximated. The approximation of the COV for the total friction angle has been performed as follows. The mean and variance for the sum of the basic friction angle and the dilation angle can, under the assumption that they are independent and normal distributed, be expressed as:

$$\mu_{\phi,\text{tot}} = \mu_{\phi_b} + \mu_{i_n} \tag{6.18}$$

$$\sigma_{\phi_{\text{tot}}} = \sqrt{\sigma_{\phi_b}^2 + \sigma_i^2} \tag{6.19}$$

Since the density function of $\tan(\phi_b+i)$ is unknown, a first order approximation of the mean and variance can be performed to estimate it, see for example (Ang & Tang 1975). By doing so, the mean and variance of the total friction angle, ϕ_{tot}, can be approximated as:

$$\sigma_{\phi,\text{tot}} = \sqrt{\left(\sigma_{\phi_b}^2 + \sigma_{i_n}^2\right)\cdot\left(\frac{1}{\cos^2 \mu_{\phi_{\text{tot}}}}\right)^2} \tag{6.20}$$

$$\mu_{\phi,\text{tot}} = \tan\left(\mu_{\phi_b} + \mu_{i_n}\right) \tag{6.21}$$

The coefficient of variation for the total friction angle can thereby be expressed as:

$$COV\left(\phi_{\text{tot}}\right) = \frac{\sqrt{\left(\sigma_{\phi_b}^2 + \sigma_{i_n}^2\right)\cdot\left(\frac{1}{\cos^2 \mu_{\phi_{\text{tot}}}}\right)^2}}{\tan\left(\mu_{\phi_b} + \mu_{i_n}\right)} \tag{6.22}$$

Based on this approximation, calculated safety indexes and the product of the partial coefficients for the basic friction angle and the dilation angle have been plotted against the COV for the total friction angle, see Figure 6.3 and 6.4.

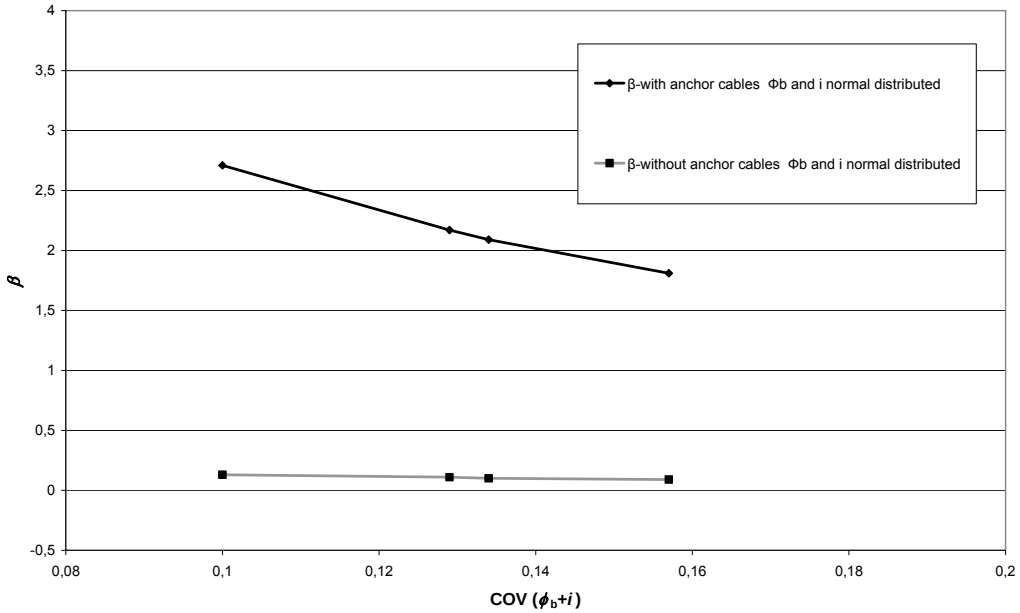

Figure 6.3 Calculated safety indexes against the coefficient of variation for the total friction angle.

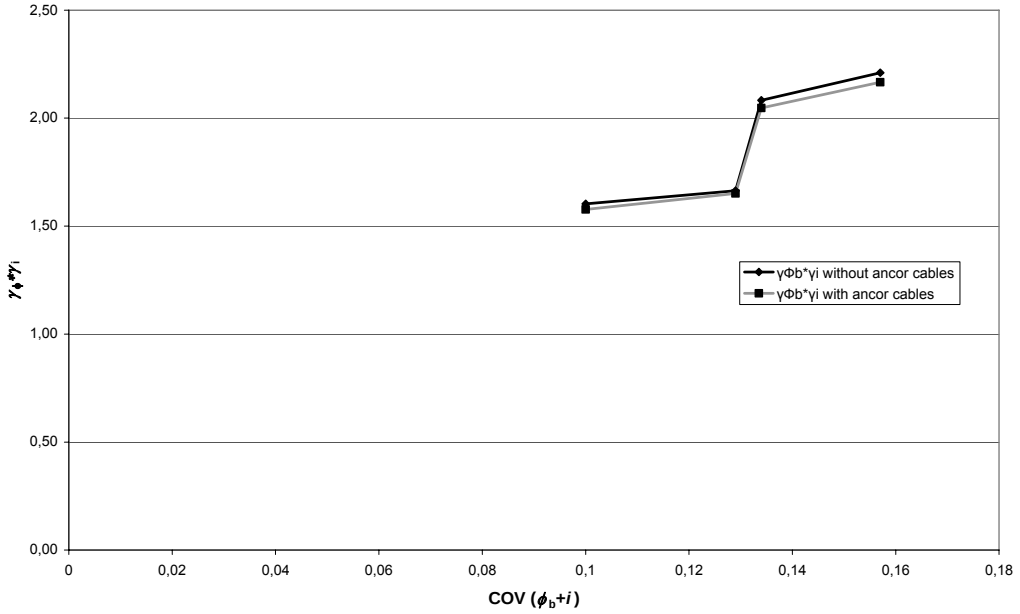

Figure 6.4 Product of partial coefficients for basic friction angle and dilation angle against the coefficient of variation for the total friction angle.

6.9 Summary and discussion

In this chapter, the sliding stability for a monolith in the spillway section of Långbjörn concrete dam under a normal load case was studied. The safety against sliding was calculated both with deterministic methods, i.e. in terms of a coefficient of friction and a safety factor, and with a reliability based method, FORM. In the reliability based calculations, the impact of a varying uncertainty regarding the basic friction angle and the dilation angle was studied.

First of all, to use a fixed value on the allowable coefficient of friction, as suggested in RIDAS (2008), in principle implies that all foundations at the Swedish dams should have the same shear strength. Of course, this is not the case; the shear strength varies for each foundation depending on the characteristics of the rock mass and the concrete rock interface. Still, according to the author's knowledge, no large dams founded on rock have failed in Sweden. This indicates that the applied method has fulfilled its purpose but might also be conservative.

Under the assumption that a horizontal persistent joint existed in the rock mass under the concrete monolith, performed calculations of the factors of safety and the safety indexes showed that acceptance requirements were not fulfilled for the deterministic nor for the reliability based calculations. The installation of pre-stressed anchors cables increased safety, but not enough reach the target safety index. In these calculations, it is interesting to observe that the concept with a factor of safety does not have the capability to reflect the uncertainty associated with a specific variable. Since it does not have this ability, it also means that a uniform level of safety is not obtained when this method is used.

Figure 6.5 compares the calculated factors of safety against calculated safety indexes. The figure illustrates how variations in the distribution of the total friction angle affect the safety index while the factor of safety remains unchanged.

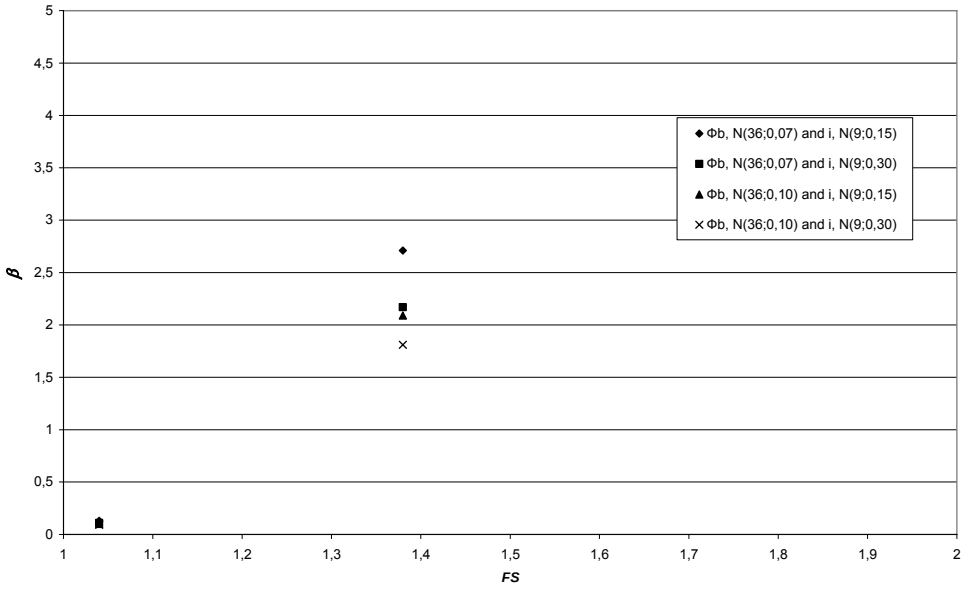

Figure 6.5 Safety factor against calculated safety index.

In addition to this benefit, reliability based methods can incorporate additional information on return periods for different load cases, the number of concrete monoliths included in the dam etc. As a tool for decision-making, the reliability based methods are preferable in front of the factor of safety.

However, both the calculated factor of safety and the reliability based method ended in the same decision. For example, at least in this case, it was not the type of calculation method that decided if the dam should be reinforced. Instead, it was the values on the parameters for the shear strength of the rock joint, together with engineering judgement. Values on the sensitivity factors in Table 6.8 and 6.11, together with the partial factors in Table 6.9 and 6.12, shows clearly that the parameters describing the shear strength are most important for the sliding stability. This also justifies the attempt in the previous chapters to describe the total friction angle for rock joints.

Despite the work done in this thesis substantial uncertainties remain regarding the shear strength of a potential sliding plane in the rock mass. These uncertainties are not only related to the shear strength of the joints, but also to the persistence and orientation of them. In the calculations in this chapter, a persistent horizontal joint was assumed to exist three meters into the rock mass. In reality, this is a conservative assumption. If a distribution of the joint length and their orientations existed, it would be possible to estimate the probability that the case assumed in these calculations actually exists.

The probability of failure for sliding along a persistent joint in the foundation, $p(B)$, could be approximated as the probability of failure for this failure mode multiplied with the probability that there exist a joint in the foundation that is persistent, $p(L_{dis} \geq L_{dam})$. This could be expressed as follows:

$$p\left(B \cap L_{dis} \geq L_{dam}\right) = p\left(B \middle| L_{dis} \geq L_{dam}\right) \cdot p\left(L_{dis} \geq L_{dam}\right) \tag{6.23}$$

If it is assumed that B and $L_{dis} \geq L_{dam}$ are statistically independent events, then the multiplication rule gives:

$$p\left(B \cap L_{dis} \geq L_{dam}\right) = p\left(B\right) \cdot p\left(L_{dis} \geq L_{dam}\right) \tag{6.24}$$

where L_{dis} is the length of the horizontal joint and L_{dam} is the length of the dam. This also means that if we can approximate the distribution for the length of the joints, it is possible to estimate the probability that the length of the joint exceeds a certain length. Equation 6.24 indicates that calculated probabilities of failure in this chapter might be overestimated and that the factors of safety might be underestimated, i.e. the assumption of a persistent joint could be conservative.

With additional information of the joint system and on the shear strength of the joints, it might be possible to improve the calculation model. To some extent, additional information can be achieved with more investigations. However, quite large uncertainties will remain regarding the shear strength of the foundation. This means that the calculated safety is nominal and that many questions remains before the true probability of failure can be expressed.

The safety indexes given in BKR (Boverket 2003) are mainly intended for materials such as steel and concrete where the material properties and the mechanical systems are well known. For rock masses and rock joints, their material properties are not well known and neither is the mechanical system. Therefore, it will probably not be possible to describe the probability of failure with the same level of detail as for structures made of steel and concrete.

As a consequence, for the future development of sliding stability analyses of concrete dams in Sweden, different possible alternatives exist. A first step could be towards a more nuanced methodology based on safety factors where possible modes of failure are analyzed and where investigations are used in a larger extent to determine the shear strength and the persistence of the joints as proposed by Gustafsson et al. (2008), instead of a single allowable coefficient of friction. A further development of the methods could incorporate the use reliability based methods. Through extended investigations of the rock mass and research within the area of rock mechanics, it might be possible to come closer to the true probability of failure. However, an exact description of it is hard to attain. If reliability based methods should be used, it might also be necessary to accept some uncertainties in the calculation model and establish target safety index partly based on back calculation of existing Swedish dams.

6.10 Conclusions

In this chapter, a concrete column in the spillway of Långbjörn was analysed against sliding for a normal load case. The sliding stability was analysed under the assumption that a horizontal persistent joint existed three meters under the monolith. From these analyses, it can be concluded that:

- The concept with an allowable coefficient of friction, or a factor of safety, does not result in a uniform level of safety.
- Reliability based methods are preferable compared to the factor of safety.
- It is suggested that future developments of sliding stability of concrete dams in Sweden should be performed in two steps. In the first step, a methodology based on safety factors and an increased use of investigations is recommended. In a second step, the use of reliability based methods is recommended where target safety indexes might be partly based on back calculated values from existing Swedish dams.

7 CONCLUSIONS

This thesis started since difficulties in expressing the safety against sliding failure had been encountered in safety evaluations of existing Swedish dams. A main problem was how to estimate the shear strength of weakness planes in the rock mass under the dam.

When Swedish guidelines for dam safety were compared with guidelines and regulations in other countries several critical conclusion could be drawn. (1) It was found that allowable safety factors for normal load cases are somewhat low, i.e. 1.35 instead of 1.5. On the other hand, the proposed allowable coefficient of friction at failure might be low. (2) This allowable coefficient of friction mainly originates from experience. No consideration is taken for how the values of the parameters for shear strength are determined, through rigorous investigations or by experience. (3) The coefficient of friction recommended in RIDAS is used as a control against sliding in both the interface between rock and concrete as well as for joints in the rock foundation, despite the fact that these potential sliding planes can have different shear strength. (4) No consideration is taken between high hazard dams and low hazard dams in the acceptance requirements.

The limitations with the current guidelines in RIDAS (2008) led to new proposed guidelines presented by Gustafsson et al. (2008). The main difference compared to the present guidelines in RIDAS (2008) is that several potential failure modes must be analysed and that cohesion can be used for low hazard dams.

In the past few years, there has been a discussion in Sweden about the implementation of reliability based methods in geotechnical and dam design. With the implementation of Eurocode, this discussion has been intensified. A natural way for the development of RIDAS would be in a direction towards Eurocode and reliability based methods. Two slightly different approaches are possible, limit states analyses with partial factors or a design directly based on reliability based methods. Since each concrete dam and its foundation in many aspects is unique, the latter is recommended. There might be a risk when fixed partial factors are used that they have to be large in order to cover all design situations. This can result in a design which is too conservative.

Regarding the peak shear strength of unfilled and rough joints, the performed literature study showed that several failure criteria have been proposed to express the shear strength. However, most of them are only valid in laboratory scale. The suggestions that exist in the literature for how the *in situ* friction angle at a full field size should be estimated are not uniform. To neglect the dilation angle as proposed by Papaliangas (1996) seems to be too conservative with respect to the results from back analysed failures of rock slopes (Patton 1966 and McMahon 1986). On the other hand, to use the average block size of the rock mass, as suggested by Barton and Bandis (1982), imply that individual blocks can rotate and arrange themselves in contact with the underlying surface. This assumption is not obvious under a concrete dam.

The major drawback with these methods is that they mainly are based on empirical grounds. Under which conditions they could be used are not clear since a detailed understanding of the mechanisms behind the scale effect is missing. It was therefore concluded that there exists a need for a more detailed understanding in this question.

In an attempt to increase the understanding of the scale effect and the mechanisms that govern the peak shear strength of rock joints, a conceptual model was derived. This conceptual model suggests that the total friction angle at full field scale could be expressed according to the primary part of Patton's (1966) criterion, i.e. total friction angle is the sum of a basic friction angle and a dilation angle. No asperity failure components, s_n, are present at full field scale for hard rocks since the inclination of the asperities involved in the shearing have an inclination lower than required to shear off the asperities at their base.

The model further suggests that the basic friction angle is a constant that mainly depends on the composition of the intact rock and is therefore independent of scale.

Most results presented in the literature points towards the fact that the scale effect originates from the surface roughness. The conceptual model suggests that the main mechanism behind it is that the number and size of the contact points change with scale as a result of roughness. This reasoning, combined with the adhesion theory and the fact that surface roughness could be correlated against a self-affine fractal model, suggests that for rough and perfectly mated joints under a constant normal load, the number of contact points would increase proportional to the area of the sample. As a consequence, no scale effect would be present for these types of joints since the average size of the contact points would not change.

On the other hand, if the joint is rough but unmated, a completely different effect occurs. Under the assumption that different samples in different scales under a constant normal load has undergone a relative shear displacement prior to the shearing which is equal to approximately half of the maximum asperity length that is present on the sample, all samples will have the same number of contact points. As a consequence, the length of the contacting asperities will increase proportional to the increase of the sample length. This occurs since the maximum asperity length present on the sample increase proportional to the increase of the length of the sample. The inclination of these contacting asperities will therefore be reduced with scale, i.e. a "*full*" scale effect will be present.

This suggests that the scale effect is not a mechanism that can be observed for all types of joints. It would also mean that, depending on the degree of matedness, the scale effect could range from no scale effect at all to a "*full*" scale effect. For design purposes, it would therefore be important to distinguish between mated and unmated joints.

Verifying analysis of the conceptual model showed that it can (1) propose an explanation for the measured dilation angle for laboratory samples of perfectly mated, unfilled and rough joints and (2) suggest an explanation for changes in the dilation angle due to an increased scale and different degrees of matedness. However, a complete verification of the model is difficult to perform since it would imply that shear test *in situ* at field size scale have to be performed. However, the results obtained with this conceptual model suggest that the dilation angle at a scale of 10 m might range between 0 to 15^{o} as reported by Patton (1966).

An interesting question is why no back calculated rock slides resulted in higher friction angles, i.e. as those that could be expected for fresh mated joints. A possible answer is that there exists a correlation between aperture and persistence as reported by for example Vermilje and Scholtz (1995). Joints with a small aperture, i.e. mated joints, most likely have a short persistence and could therefore not constitute a large sliding plane in the rock mass. On the other hand, joints with larger aperture, i.e. unmated or partly unmated joints, have a longer persistence and could therefore constitute sliding planes necessary for rock slides to occur. For design purposes, this suggests that it is joints with large aperture that should be looked after when investigations are performed.

In order to study the total friction angle of unfilled and rough joints at different scales, eighteen shear tests were performed. The samples were taken from the rock mass under or near the concrete dam Långbjörn in the northern part of Sweden. The test included seventeen laboratory shear tests and one *in situ* shear test with a sample scale of 700 by 700 mm as recommended by ISRM for *in situ* shear test. The laboratory tests had a sample length between 70 to 250 mm. All tests were performed at a normal stress equal to 0.8 MPa, which was the maximum calculated stress under the concrete dam. The exception was the *in situ* shear test where a normal stress equal to 0.5 MPa was used.

The results from these tests point towards the fact that the basic friction angle is a scale independent property as suggested by, for example, Barton and Choubey (1977). The mean value of the basic friction angle for the coarse grained granite was 36^{o} and the COV≈0.07-0.10. However, the basic friction at peak shear strength for the *in situ* shear test gave a high value on the basic friction angle. Problems with some of the LVDT´s that measured normal displacements resulted in that the obtained basic friction angle became uncertain. Furthermore, two parallel sliding planes existed for one side of the sample which resulted in reduced dilation for that side. It is possible that this affected the calculated dilation angle and thereby also the measured basic friction angle for this test.

The results also showed that the total friction angle, or the dilation, was highest for the smallest samples in drill core scale. It was also observed that the total friction angle observed in the *in situ* test corresponded to a value of 0.7 for the constant of matedness.

An interesting observation was that the samples at 125 mm and 250 mm scale showed lower friction angles than anticipated. The joint surfaces of these samples

were also weathered and pieces of intact rock were lost during the preparation of the samples. The fragmentation of the joints surfaces might also be an effect from blast damages. When the surface was analysed before and after shearing for two of these samples, it was seen that contact points were not located at the steepest asperities facing the shear direction, which is the case for fresh, mated and unweathered joints. Instead, the contact points developed at points of initial contact or where the initial aperture was small. This indicates a more random distribution of the contact points over the surface. In turn, this could imply that it is the average inclination of the asperities, and not the steepest inclination, that govern that dilation angle for weathered joints. However, more tests need to be performed on weathered joints before this could be verified. Nevertheless, it is clear that degree of weathering and matedness, as suggested by Zhao (1997 a,b), has a large influence on the peak shear strength.

Despite the authors attempt to collect samples with uniform conditions for the joints properties at all sample scales, all of the samples in different scales exhibited differences in degree of weathering and infilling material. To draw any firm conclusions from these shear tests regarding the scale effect are therefore not possible. If the scale effect should be investigated in future test series, it is recommended that it is performed on samples where the properties of the joint surface could be better controlled. For example, this might be achieved by using tensile induced fresh joints.

A sliding stability analysis of a monolith at Långbjörn concrete dam was carried out with both deterministic and reliability based methods. The results from this analysis were compared and discussed. From this, it was concluded that the concept with a factor of safety does not result in a uniform level of safety. Furthermore, reliability based methods are preferable in front of the factor of safety since they can incorporate the effect of the uncertainties for each variable together with other types of additional information, such as return periods for different load cases etc., in order to achieve a more uniform level of safety. It is also suggested that future development of sliding stability of concrete dams in Sweden are performed in two steps. In the first step, a more nuanced methodology based on safety factors and an increased use of investigations is suggested. In the second step, it is recommended to start using reliability based methods where target safety indexes partly might be based on back calculated values from existing Swedish dams.

8 SUGGESTIONS FOR FUTURE WORK

During the work with this thesis, the author has gained an increased understanding of the complex mechanisms that underlie the shear strength of rock joints. This is especially true regarding how contact points affect the shear strength. In most cases, when the shear strength of rock joints is estimated, only surface roughness is characterized. However, factors such as initial matedness and relative displacement appear to be important parameters which in most cases are not considered.

The conceptual model described in this thesis suggests that the scale effect is not a mechanism that can be observed for all types of joints. Perfectly mated and unweathered rough joints are suggested to not exhibit any scale effects while rough unmated joints where previous shear displacements have occurred can exhibit a full scale effect, i.e. the number of contact points are in principle constant with increased scale.

Even though it was the author' s intention to study the scale effect of rock joints, the behaviour suggested in the conceptual model has not been completely verified. It is therefore suggested that future work focuses on further verification of the model and into the understanding on how contact points changes during different normal loads, relative shear displacements and different degrees of weathering. By doing so, it is the author's belief that an increased understanding on the scale effect, and the shear strength, of rock joints can be achieved.

If the future work suggested above is shown to agree with the behaviour suggested with the conceptual model, a further development of the model could be done to estimate not only the mean value but also the variance of the friction angle at *in situ* scale. A factor which is important if the reliability of the dams should be determined.

In the past few years, there has been a discussion of the implementation of reliability based methods in geotechnical and dam design. In many aspects, reliability based design is preferable, since it enables to achieve a more uniform level of safety compared to the total safety factor. However, it is not obvious which reliability requirements, i.e. target safety index that should be used. It is recommended that safety indexes for a number of Swedish dams are back calculated. The results from such calculations could be used as guidance in order to attain target safety indexes.

Furthermore, the work in this thesis only considered the sliding in rock joints under the dam. In order to be able to perform complete analyses of the sliding stability, the shear strength in the concrete-rock interface has to be estimated. In many aspects, a question at least as complex as the scale effect of rock joints. In particular, if cohesion should be accounted for or not. Today, methods exist to estimate the shear strength of the concrete-rock interface. However, results by Gustafsson et al. (2008) indicated that even though cohesion might exist,

uncertainties associated with this parameter are so large that it might not be possible to fulfil acceptance requirements for high hazard dams. Another interesting aspect is that the results from the conceptual model suggest that joints with a perfect matedness would have a high friction angle without any scale effects. This would imply that once cohesion is broken, the total friction angle may still be high in the interface. In order to investigate the shear strength in the concrete rock interface, further research is recommended.

9 REFERENCES

Ang. A; Tang, W. (1975). Probability Concepts in Engineering Planning and Design. Volume I, Basic Principles. John Wiley & Sons, Inc. New York.

Amontons (1699). Histoire de l'Academie Royale des Sciences avec les Memoires de Mathematique et de Physique, p. 206.

Archard, J.P., (1957). Elastic Deformations and the Laws of Friction, Proc. Royal Soc., A243, pp. 190-205.

Archard, J.P., (1974). Surface Topography and Tribology. Tribology Int. 7, pp. 213-220.

Bandis, S.C. (1980). Experimental Studies of Scale Effects on Shear Strength, and Deformation of Rock Joints. Doctoral Thesis, Department of Earth Sciences, The University of Leeds.

Bandis, S.C.; Lumsden, A.C.; Barton, N.R., (1981). Experimental studies of scale effects on the shear behaviour of rock joints, Int. J. Rock Mech. and Min. Sci., Vol. 18, No. 1, pp. 1-21.

Barton, N., (1973). A review of a new shear-strength criterion for rock joints. Engineering Geology, Vol. 7, Nr. 4, pp. 287-332.

Barton, N.; Choubey, V., (1977). The shear strength of rock joints in theory and practice. Rock Mechanics, Vol. 10, pp. 1-54.

Barton, N.; Bandis, S.C., (1982). Effect of block size on the shear behaviour of jointed rock, 23rd U.S. Symp. on Rock Mech., pp. 739-760.

Barton, N., (1987). Predicting the behaviour of underground openings in rock. 4th Manuel Rocha Memorial Lecture, Lisbon.

Becker, D.E., (1996). Eighteenth Canadian Geotechnical colloquium: Limit states design for foundations, Part I, An overview of the design process. Can. Geotech. J., Vol. 33, pp. 956-983.

Bellier, J., (1976). The Malpasset dam. Engineering foundation conference on "The evaluation of dam safety", Pacific Grove, CA, pp. 72-136 (First published in TRAVAUX, Paris, July 1967 in French).

Bhasin, R., Høeg K., (1997). Numerical modelling of Block Size Effects and Influence of Joint Properties in Multiply Jointed Rock. Tunneling and Underground Space Technology, Vol 12, No. 3, pp. 407-415.

Borri-Brunetto, M.; Carpinteri, A.; and B. Chiaia, (1999). Scaling phenomena due to fractal contact in concrete and rock. International Journal of Fracture, 95:221-238.

Borri-Brunetto, M.; Carpinteri, A.; and B. Chiaia, (2004). The effect of Scale and Criticality in Rock Slope Stability. Rock Mech. Rock Engng. Vol. 37, No. 2, pp 117-126.

Boverket (1995). BBK 94 - Boverkets handbok om betongkonstruktioner, Band 1, Konstruktion (In Swedish).

Boverket, (2003). Regelsamling för konstruktion, Boverkets konstruktionsregler, BKR, byggnadsverkslagen och byggnadsverksförordningen (In Swedish).

Bowden, F.P.; and D. Tabor, (1950). The Friction and Lubrication of Solids, Part I, Oxford University Press, London.

Bowden, F.P.; and D. Tabor, (1964). The Friction and Lubrication of Solids, Part II, Oxford University Press, London.

Brown, S.R. and Scholz, C.H., (1985). Broad bandwidth study of the topography of natural rock surfaces. J. Geophys. Res. 90, pp. 12575-82.

Canadian Dam Association, (1999), Dam safety guidelines.

Canadian Electricity Association Technologies Inc., CEATI, (1998). Project 9331 G 2002, Sliding Resistance of Concrete Gravity Dams.

Cederström, M., (1995). VASO dammkommittés rapport nr 1, Utrednings- och utvecklingsprojekt med anledning av Flödeskommitténs riktliner, Huvudrapport. ELFORSK, VASO (In Swedish).

Comrel (2008). RCP Consulting Software, version 8.1. Munich.

EN 1990. Eurocode – Basis of structural design

EN 1997-1. Eurocode 7: Geotechnical design – General rules.

Fairhurst, C. (1964). On the validity of the “Brazilian” test for brittle materials, Int. J. Rock Mech. Min. Sci. Vol. 1, pp.535-546.

Fardin, N., (2003). The effect of Scale on the Morphology, Mechanics and Transmissivity of Single Rock Fractures. Ph. D. Thesis, Royal Institute of Technology, Land and Water Resources Engineering, Stockholm, Sweden.

Feng Q, Sjögren P., Stephansson O. and Jing L., (2001). Measuring fracture orientation at exposed rock faces by using a non-reflector total station. Engineering Geology, 59, pp. 133-146.

FERC, The Federal Energy Regulatory Comission, (2002). Engineering guidelines for the evaluation of hydropower projects, Chapter III, Gravity dams.

Fishman, Y.A., (1990). Failure Mechanism and Shear Strength of Joint Wall Asperities. In: Rock Joints, pp. 627-631.

Fuller K.N.G. and Tabor, D., (1975). The effect of Surface Roughness on the Adhesion of Elastic Solids. Proc. of the Royal Society, Vol. A345, pp. 327-342.

Grasselli, G., Egger, P. (2000). 3D Surface Characterization for the prediction of the shear strength of rough joint. Ed. Wittke, W., Eurock 2000, Aachen, Germany, pp. 281-286.

Grasselli, G., (2001) Shear strength of rock joints based on quantified surface description. Doctoral Thesis, EPFL, Lausanne.

Grasselli. G., (2006). Manuel Rocha Medal Recipient, Shear Strength of Rock Joints Based on Quantified surface Description. Rock Mech. Rock Eng. 39(4), 295-314.

Green, R., (1989). Limit states design, some thoughts. Proceedings of the symposium on limit states design in Foundation Engineering. Canadian Geotechnical society – Southern Ontario Section, Toronto, May 26-27, pp. 91-116.

Greenwood, J.A.; Williamson, J.B. (1966). Contact of Nominally Flat Surfaces. Proceedings of the Royal Society of London. Series A, Mathematical and Physical Sciences, Vol. 295, No. 1442, pp. 300-319.

Greenwood J.A.; Tripp, J.H, (1971). The contact of two nominally flat rough surfaces. Proc. Instn. Mech. Engrs. Vol. 185 48/71. pp. 625-633.

Gustafsson, A.; Johansson, F.; Rytters, K.; Stille H. (2008). Dammsäkerhet, Glidstabilitet - Förslag på nya riktlinjer, ELFORSK Rapport 08:59 (In Swedish).

Gustafsson, A.; Johansson, F.; Rytters, K.; Stille H. (2009). Sliding stability of concrete gravity dams founded on rock – Proposal for new Swedish guidelines. ICOLD, Brasilia.

Hasofer, A.M.; Lind, N.C., (1974). An Exact and Invariant First-Order Reliability Format. J. of the Eng. Mech. Div., ASCE, Vol. 100, No. EM 1.

Hencher, S.R.; Richards, L.R. (1989). Laboratory Direct Shear Testing of Rock Discontinuities, Ground Engineering, pp. 24-31.

Hencher, S.R.; Toy, J.P.; Lumsden, A.C., (1993). Scale Dependent Shear Strength of Rock Joints, Conference on Scale Effects in Rock Masses, Ed. Pinto de Cunha, Balkema.

Hoek, E.; Brown, E.T., (1980). Underground excavation in rock, London, Instn Min. Metall. p. 527.

Hoek, E.; Bray, J.W., (1981). Rock Slope Engineering, 3rd ed. London, England, Inst. Min. and Metallurgy. p. 358.

Höeg, K.; Murarka, R.P. (1974). Probabilistic Analysis and Design of a Retaining Wall. Journal of the Geotechnical Engineering Division. Vol. 100, No. GT3, pp. 349-366.

ICOLD, (1993). Rock foundations for dams. Bulletin 88.

ICOLD, (1995). Dam failures statistical analyses. Bulletin 99.

ISRM, (1981). Rock Characterization Testing & Monitoring, ISRM Suggested Mehtods, Pergamon Press Ltd. p. 211.

Jeppsson, J. (2003). Reliability-based assessment procedures for existing concrete structures. Doctoral Thesis. Division of Structural Engineering, Lund Institute of Technology, Lund University. Report TVBK-1026.

John, K.W., (1968). Graphical stability analysis of slopes in jointed rock. ASCE, J. of Soil Mech. Foun. Div. Vol. 94, No. SM2, pp. 497-526.

Johansson, F. (2005). Stability Analyses of Large Structures Founded on Rock – An Introductory Study, Licentiate Thesis in Soil and Rock Mechanics, Royal Institute of Technology, Stockholm, Sweden.

Johnson, K.C., Kendall, K. and Roberts, A.D., (1971). Surface Energy and the Contact of Elastic Solids. Proc. of the Royal Society, Vol. A. 324, pp. 301-313.

Kimura, T., Esaki, T. (1995). A new model for the shear strength of rock joints with irregular surfaces. Ed. Rossmanith, H.-P., Mechnics of jointed and faulted rock. Balkema, Rotterdam, pp. 133-138.

Kulatilake, P.H.S.W., Shou, G., Huang, T.H. and Morgan, R.M., (1995). New peak shear strength Criteria for anisotropic rock joints. Int. J. Rock Mech. Min. Sci. Geomech. Abstr. 32: pp. 673-697.

Kulatilake, P.H.S.W., Um, J. and Pan, G., (1997). Requirement for accurate quantification of self-affine roughness using the roughness-length method. Rock Mech. Rock Eng. 30: pp. 181-206.

Kulatilake, P.H.S.W., and Um, J., (1999). Requirement for accurate quantification of self-affine roughness using the roughness-length method. Int. J. Rock Mech. Min. Sci. Geomech. Abstr. 36: pp. 5-18.

Ladanyi, B., Archambault, G. (1970). Simulation of the shear behaviour of a jointed rock mass, Proceedings of the 11th U.S. Symposium on Rock Mechanics, Vol. 7, pp.105-125.

Lambe, T.W; Whitman, R.V (1969). Soil Mechanics, John Wiley & Sons, p. 553

Lanaro, F., (2001). Geometry, Mechnics and Transmissivity of Rock Fractures. Doctoral Thesis, Division of Engineering Geology, Department of Civil and Environmental Engineering, Royal Institute of Technology, Stockholm, Sweden.

Liu, J.; Feng, X.T.; Ding, X.L., (2003). Stability assessment of the Three Gorges Dam foundation, China, using physical and numerical modelling – Part II: Numerical modelling. Int. J. Rock Mech. Min. Sci., Vol. 40, pp. 633-652.

Logan, J.M.,and Teufel L.W., (1986). The Effect of Normal Stress on the Real Area of Contact During Frictional Sliding on Rocks. Pure & Appl. Geophys. Vol. 124, No. 3, pp. 471-485.

Londe, P.; Vigier, G.; Vormeringer, R., (1969). Stability of Rock Slopes, A Three Dimensional Study. ASCE, J. of Soil Mech. Foun. Div. Vol. 95, No. SM1, pp. 235-262.

Maksimovic, M., (1992). Technical Note, New description of the shear strength for rock joints. Rock Mech. Rock Engng. Vol. 25 No. 4, pp. 275-284

Maksimovic, M., (1996). The Shear Strength Component of a rough Rock Joint. Int. J. Rock Mech. Min. Sci. & Geomech. Abstr., Vol. 33, No. 8, pp. 769-783.

Maliverno, A., (1990). A simple method to estimate the fractal dimension of a self-affine series. Geophys. Res. Lett. 17, pp. 953-956.

Maliverno, A., (1995) Fractals and Ocean Floor Topography; a Review and a Model. Fractals in the Earth Science, Ed. Barton and La Pointe, New York: Plenum Press, pp. 107-130.

Mandelbrot, B.B., (1967). How long is the coast line of Britain? Statistical self-similarity and fractal dimension. Science. 155, pp. 636-638.

Mandelbrot, B.B., (1983). The fractal of nature. New York: W. H. Freeman, p. 468

MathWorks (2007) Matlab, Version 7.4.0.287, Natick Massachusetts, USA.

McMahon, K, (1985) Some practical Considerations for the Estimation of Shear Strength of Joints and Other Discontinuities, Proceedings of the International Symposium on Fundamentals of Rock joints, pp. 475-485.

Melchers, R.E., (1999). Structural Reliability Analysis and Prediction. Second Edition, John Wiley & Sons.

Mortenson, K., (1983). Is Limit State Design a Judgements Killer? Norweigan Geotechnical Institute, Publication Nr. 148.

Myers N.O., (1962). Characterization of Surface Roughness. Wear, 5, pp. 182-189

NBG, Norwegian group of rock mechanics, (2000). Engineering Geology and Rock Engineering, Handbook No. 2. p. 249.

Nicholson, G.A., (1983). Design of gravity dams on rock foundations: Sliding stability assessment by limit equilibrium analysis and selection of shear strength parameters. Geotechnical Laboratory, U.S. Army Corps of Engineers, Waterways Experiment station.

NVE, Norwegian Water Resources and Energy Directorate, (2002), Retningslinje for betongdammer.

Olsson, L., (1986). Användningen av Betametoden i geotekniken. Ph.D. Thesis. Royal Institute of Technology, Stockholm.

Papaliangas, T.T.; Hencher, S.R.; Lumsden, A.C., (1995). A comprehensive peak shear strength criterion for rock joints. 18th Int. Congress on Rock Mechanics, Tokyo, Japan, Volume 1, pp. 359-366.

Papaliangas, T.T. (1996). Shear behaviour of rock discontinuities and soil-rock interfaces. Ph.D. Thesis. The University of Leeds, Department of Earth Sciences, p. 318.

Papaliangas, T.; Lumsden, A.C.; Hencher, S.R., (1996). Prediction of in-situ shear strengths of rock joints, Eurock 96, Torino, Italy.

Patton, F.D., (1966). Multiple modes of shear failure in rock and related material, Ph.D. Thesis, Univ. of Illinois.

Pratt, H.R.; Black, A.D.; Brace, W.F., (1972). The effect of specimen size on the mechanical properties of unjointed diorite. Int. J. Rock Mech. Min. Sci. Vol. 9 pp. 513-529.

Reinius E., (1973). Vattenbyggnad del 3, Dammbyggnader.

Saeb, S. (1990). A variance on the Ladanyi and Archambault´s shear sterngth criterion. In: Rock Joints, Ed. Barton & Stephansson, Loen, Norway.

Saiang, D., Malmgren, L., Nordlund, E., (2005). Laboratory Tests on shotcrete-Rock Joints in Direct Shear, Tension and Compression, Rock Mechanics and Rock Engineering, Vol. 38, No. 4, pp. 275-297.

Seidel J.P.; Haberfield C.M., (2002). A theoretical model for rock joints subjected to constant normal stiffness direct shear. Int. J Rock Mech. Min. Sci. Vol. 39, pp.539-553.

Sfondrini, G. and Sterlacchini, S., (1996). Influence of joint roughness on discontinuity shear strength. Proc. Safety and Environmental Issues on Rock Engineering. Eurock 96, pp. 135-143.

Stesky, R.M. and Hannan S.S., (1987). Growth on Contact Area between Rough Surfaces under Normal Stress. Geophys. Research Letters, Vol. 14, No. 5, pp. 550-553.

Svensk Energi, (2008). Kraftföretagens riktlinjer för dammsäkerhet, RIDAS (In Swedish).

Swahn, G. (1983). Determination of Stiffness and Other Joint Properties from Roughness Measurements. Rock Mechanics and Rock Engineering 16, pp. 19-38

Swahn, G. and Zongqi, S. (1985). Prediction of Shear Behaviour of Joints Using Profiles. Rock Mechanics and Rock Engineering 18, pp. 183-212.

SWECO VBB VIAK, (2002). Långbjörn, Stabilitetsberäkning av betongdammarna (In Swedish, unpublished).

Terzaghi, K. (1925). Erdbaumechanik, Franz Deuticke, Vienna.

Thoft-Christensen, P.; Baker, M.J., (1982). Structural Reliability Theory and Its applications. Springer Verlag, Heidelberg.

Thomas, T.R. (1982) Rough Surfaces. London: Longman.

Tse, R. and Cruden, D.M., (1979). Estimating Joint Roughness Coefficients. Int. J. Rock Mech. Min. Sci. & Geomech. Abstr., Vol. 16, pp. 303-307.

Underwood, L.B., Dixon, N.A., (1976). Dams on rock foundations. Speciality conference on rock engineering and slopes, Boulder, Co., Aug. 1976, Proceedings, Vol. 2.

U.S. Army Corps of Engineers, (1981). Engineering and design, Sliding stability for concrete structures. Technical letter No. 1110-2-256.

Vattenfall (1971). Anteckningar om glidsäkerhet vid betongdammar, Statens vattenfallsverk, Byggnadsteknik, Utvecklings- och kontrollsektionen (In Swedish, unpublished).

Vattenfall (1996). Stabilitetsanvisningar för betongdammar. Vattenfall (In Swedish, unpublished).

VBB Anläggning, (1994). Fördjupad dammsäkerhetsutvärdering av anläggningen vid Långbjörn (In Swedish, unpublished).

VBB Anläggning, (2000a). Långbjörn, Rapport avseende kartering av berg och borrkärnor under betongdammar (In Swedish, unpublished).

VBB Anläggning, (2000b). PM, Skjuvhållfasthet i berggrunden under betongdammarna i Långbjörn bedömd på basis av geologisk ytkartering, 47 kärnborrhål och laboratorieprovning (In Swedish, unpublished).

Vermilye, J.M.; Scholz, C.H. (1995). Relation between vein length and aperture. J. Struc. Geol. 17, pp. 423-434.

Vägverket, (2004). Bro 2004. Publikation 2004:56 (In Swedish).

Wagner, H., (1987). Design and support of underground excavations in highly stressed rock. Proc. 6th ISRM Congr., Montreal.

Westberg, M. (2007). Reliability-based evaluation of concrete dams. Licentiate Thesis. Division of Structural Engineering, Lund Institute of Technology, Lund University. Report TVBK-1033.

Whitman, R.V., (1984). Evaluating calculated risk in geotechnical engineering. J. Geotech. Eng., ASCE, Vol. 110, No. 2, pp. 145-188.

Wyllie, D.C., (1999). Foundations on rock. Second Edition, E & FN SPON.

Yoshinaka, R.; Yoshida, J.; Arai, H.; and Arisaka S., (1993). Scale effects on Shear Strength and Deformability of Rock Joints. Scale Effects in Rock masses93; Proc. 2nd Int. Workshop on Scale Effects in Rock Masses, Balkema, Rotteram, Ed. Pinto de Cunha, pp. 143-149.

Zhao, J. (1997a). Joint surface Matching and shear strength, Part A: Joint Matching Coefficient (JMC). Int. J. Rock Mech. Min. Sci. Vol 34, No. 2, pp. 173-178.

Zhao, J. (1997b). Joint surface Matching and shear strength, Part B: JRC-JMC Shear Strength Criterion. Int. J. Rock Mech. Min. Sci. Vol 34, No. 2, pp. 173-178.

APPENDIX A, RESULTS FROM SHEAR TESTS PERFORMED AT LTU

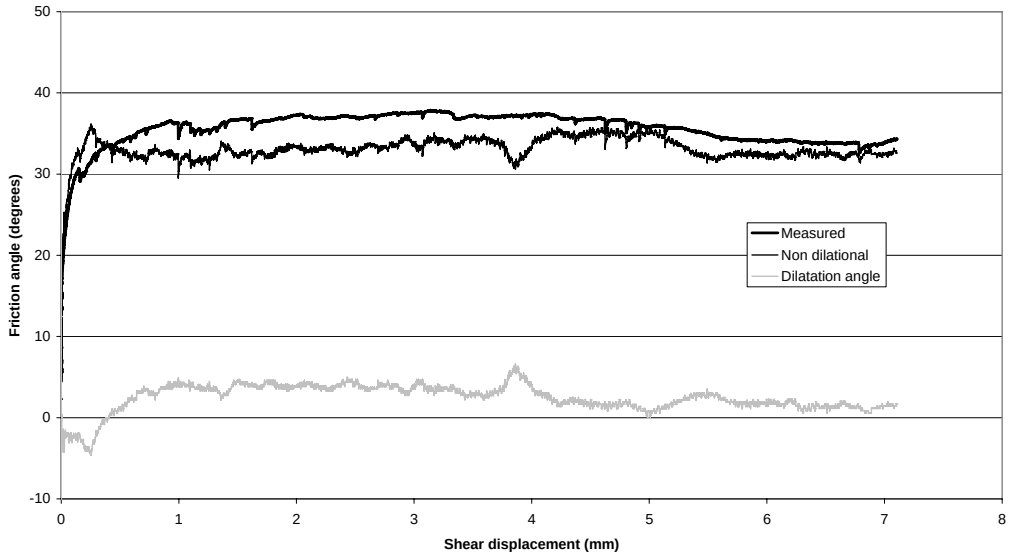

Figure A.1 Measured friction angle and dilation angle, together with non-dilational friction angle for test S1.

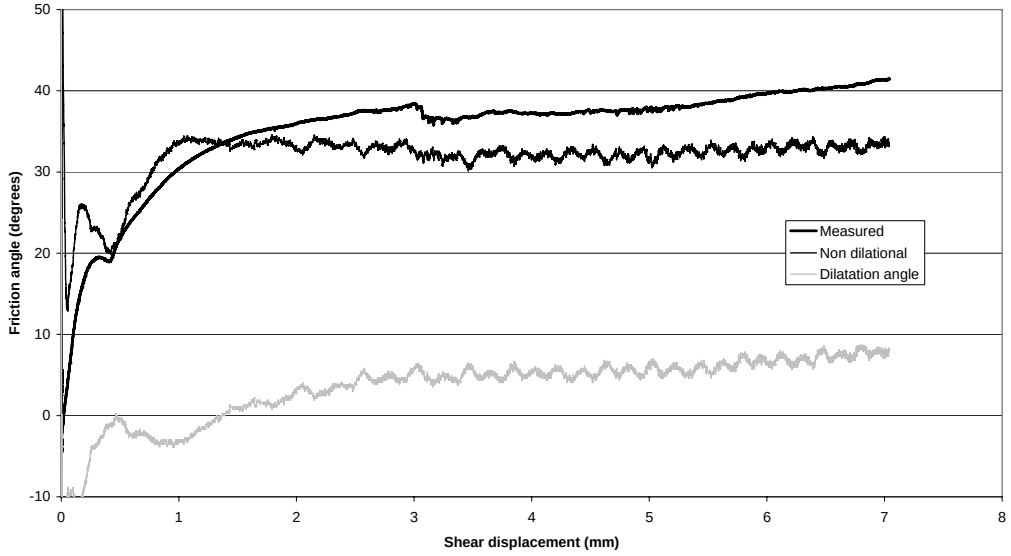

Figure A.2 Measured friction angle and dilation angle, together with non-dilational friction angle for test S2.

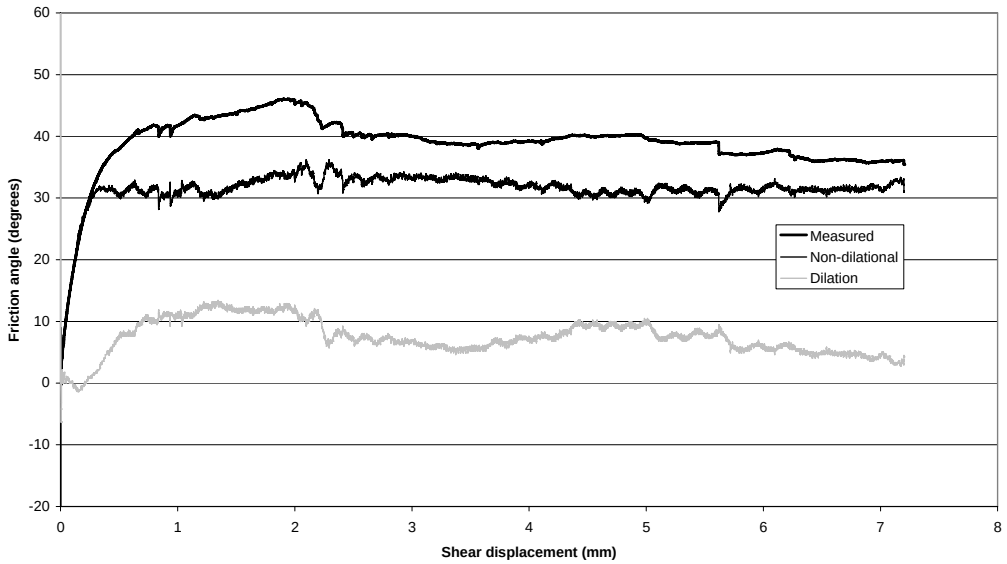

Figure A.3 Measured friction angle and dilation angle, together with non-dilational friction angle for test S3.

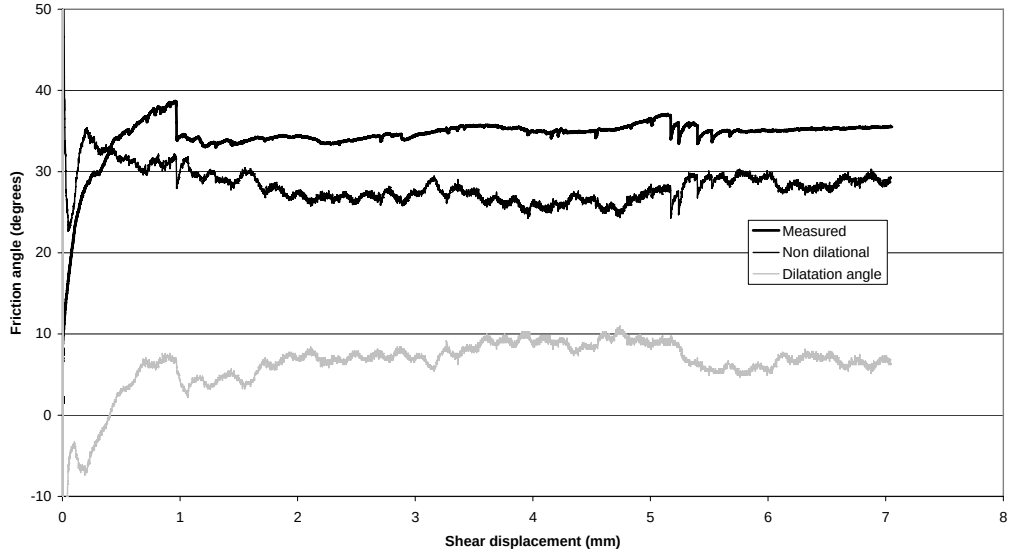

Figure A.4 Measured friction angle and dilation angle, together with non-dilational friction angle for test S4.

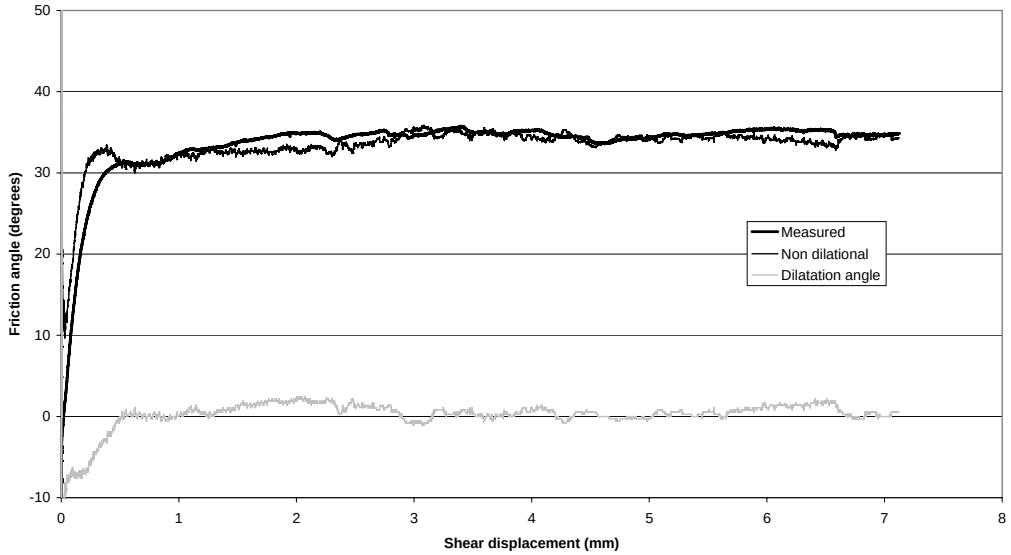

Figure A.5 Measured friction angle and dilation angle, together with non-dilational friction angle for test S5.

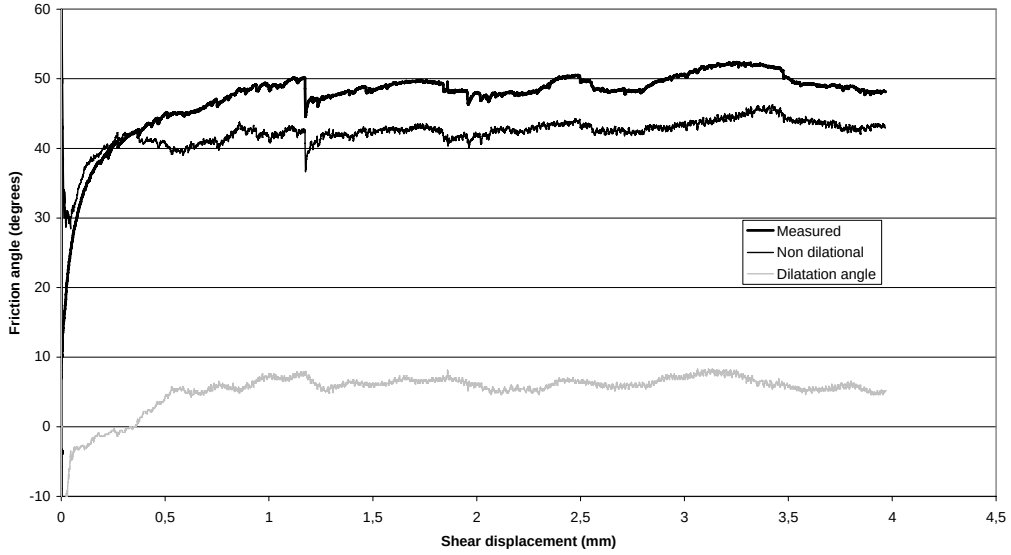

Figure A.6 Measured friction angle and dilation angle, together with non-dilational friction angle for test S6.

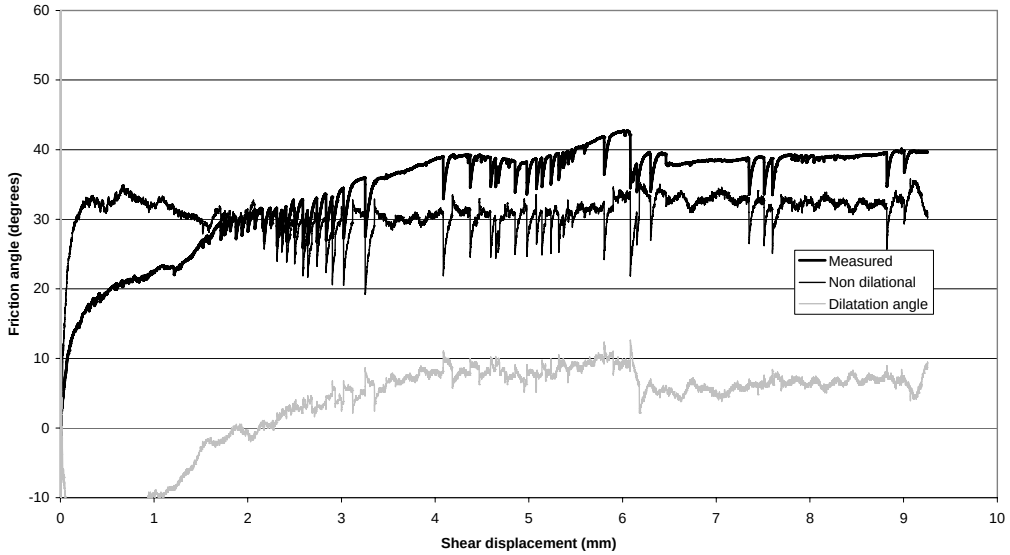

Figure A.7 Measured friction angle and dilation angle, together with non-dilational friction angle for test S8.

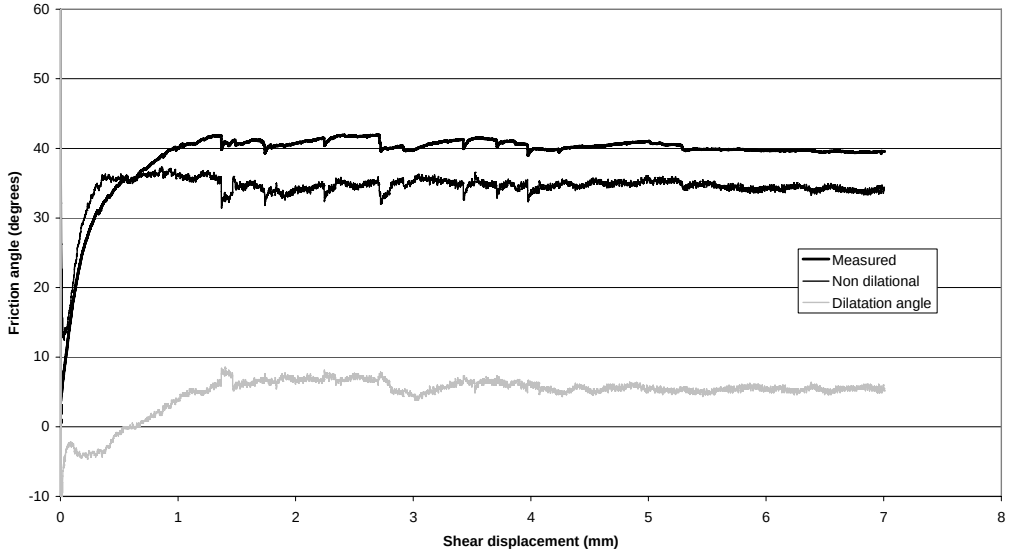

Figure A.8 Measured friction angle and dilation angle, together with non-dilational friction angle for test L3.

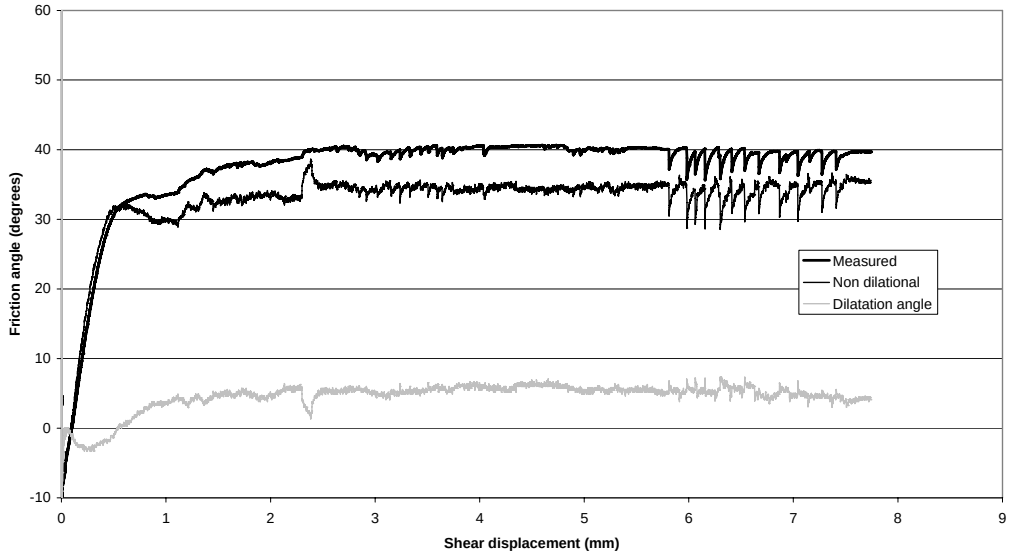

Figure A.9 Measured friction angle and dilation angle, together with non-dilational friction angle for test L4.

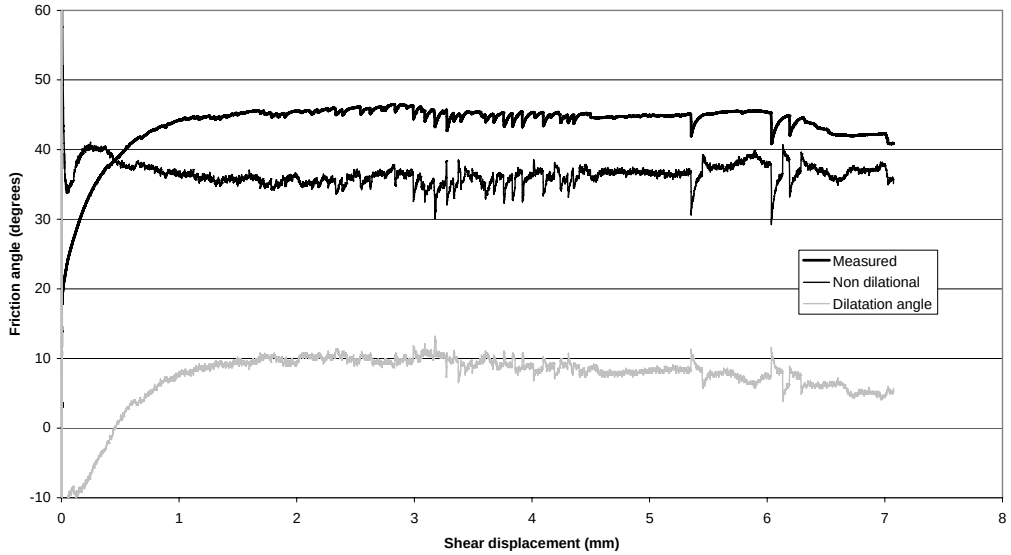

Figure A.10 Measured friction angle and dilation angle, together with non-dilational friction angle for test L6.

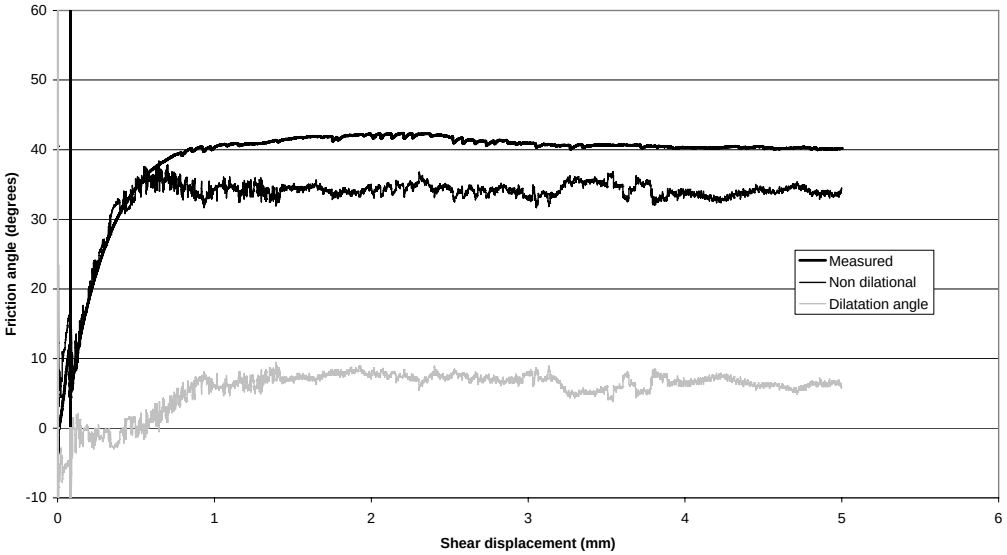

Figure A.11 Measured friction angle and dilation angle, together with non-dilational friction angle for test L7.

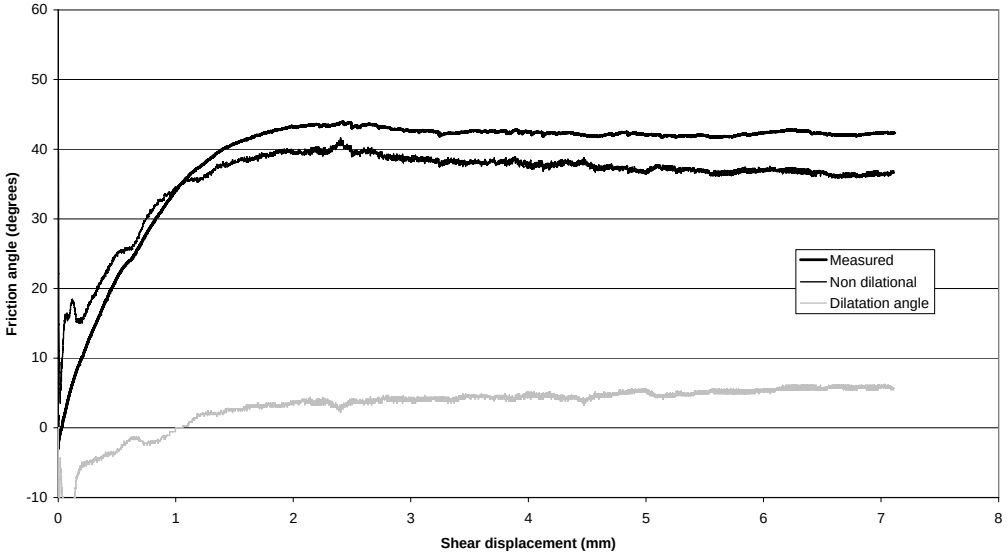

Figure A.12 Measured friction angle and dilation angle, together with non-dilational friction angle for test L8.

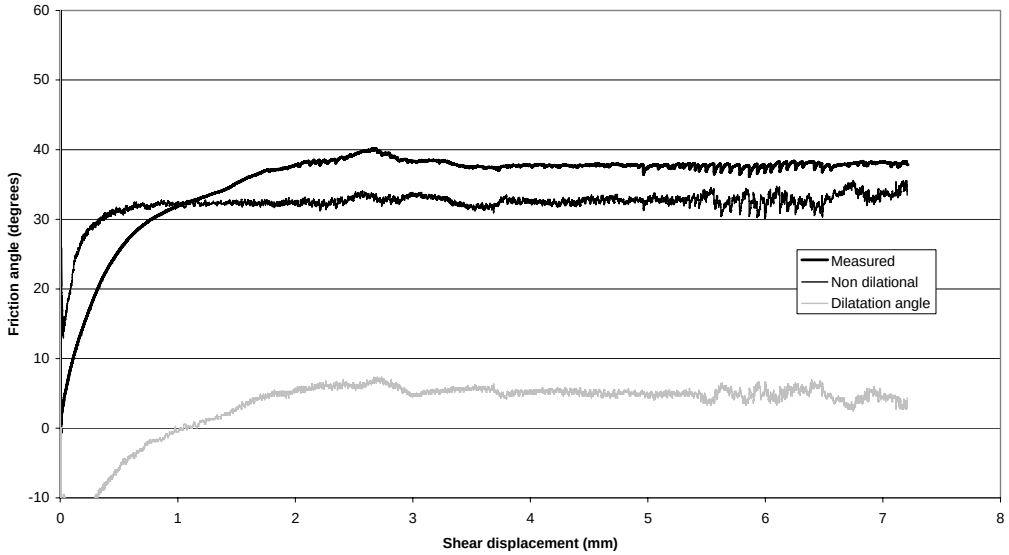

Figure A.13 Measured friction angle and dilation angle, together with non-dilational friction angle for test L9.

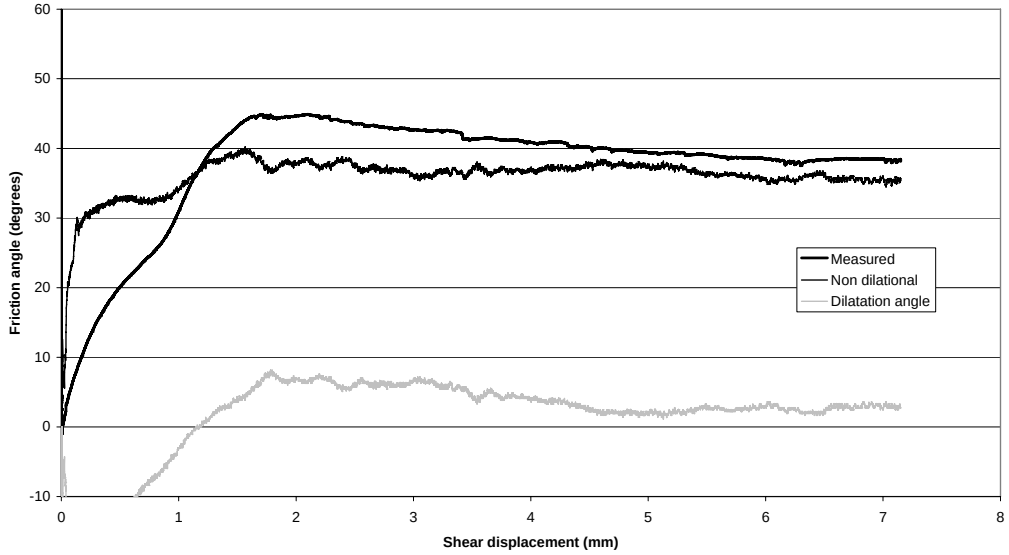

Figure A.14 Measured friction angle and dilation angle, together with non-dilational friction angle for test L10.

APPENDIX B, PHOTOS OF LTU SAMPLES AFTER SHEAR TESTING

Picture B.1a Sample S1 after the shear test (lower part).

Picture B.1b Sample S1 after the shear test (upper part).

Picture B.2a Sample S2 after the shear test (lower part).

Picture B.2b Sample S2 after the shear test (upper part).

Picture B.3a Sample S3 after the shear test (lower part).

Picture B.3b Sample S3 after the shear test (upper part).

Picture B.4a Sample S4 after the shear test (lower part).

Picture B.4b Sample S4 after the shear test (upper part).

Picture B.5a Sample S5 after the shear test (lower part).

Picture B.5b Sample S5 after the shear test (upper part).

Picture B.6a Sample S6 after the shear test (lower part).

Picture B.6b Sample S6 after the shear test (upper part).

Picture B.7a Sample S8 after the shear test (lower part).

Picture B.7b Sample S8 after the shear test (upper part).

Picture B.8a Sample L3 after the shear test (lower part).

Picture B.8b Sample L3 after the shear test (upper part).

Picture B.9a Sample L4 after the shear test (lower part).

Picture B.9b Sample L4 after the shear test (upper part).

Picture B.10a Sample L6 after the shear test (lower part).

Picture B.10b Sample L6 after the shear test (upper part).

Picture B.11a Sample L7 after the shear test (lower part).

Picture B.11b Sample L7 after the shear test (upper part).

Picture B.12a Sample L9 after the shear test (lower part).

Picture B.12b Sample L9 after the shear test (upper part).

Picture B.13a Sample L9 after the shear test (lower part).

Picture B.13b Sample L9 after the shear test (upper part).

Picture B.14a Sample L10 after the shear test (lower part).

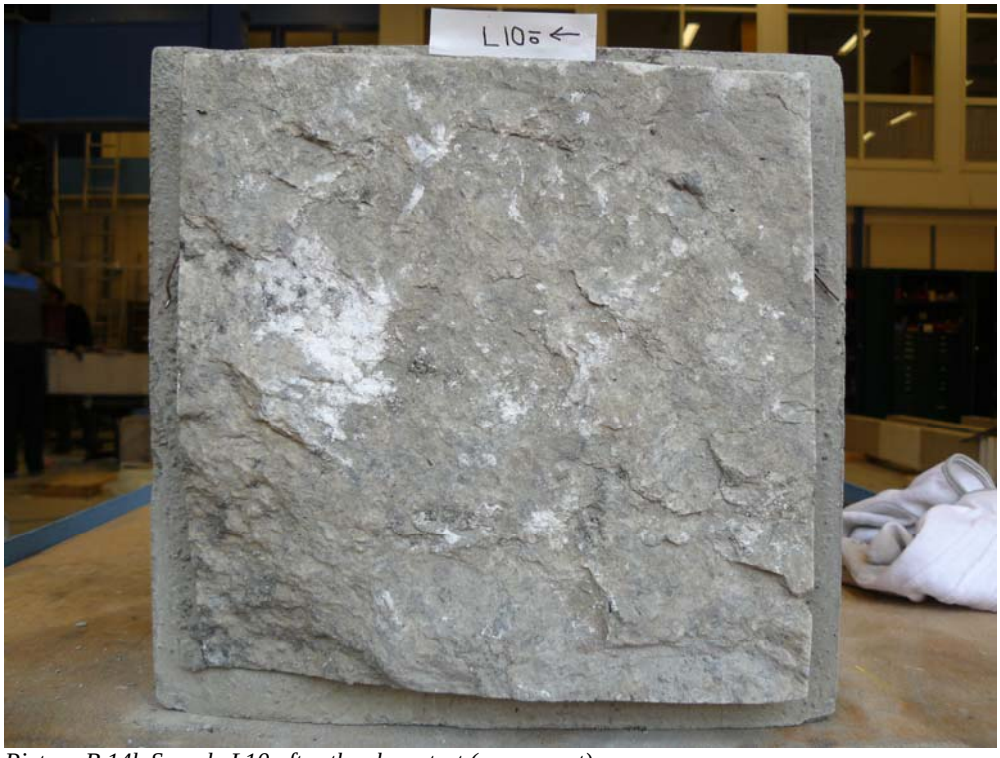

Picture B.14b Sample L10 after the shear test (upper part).

APPENDIX C, ASSUMED NORMAL DISTRIBUTIONS FOR BASIC FRICTION ANGLE

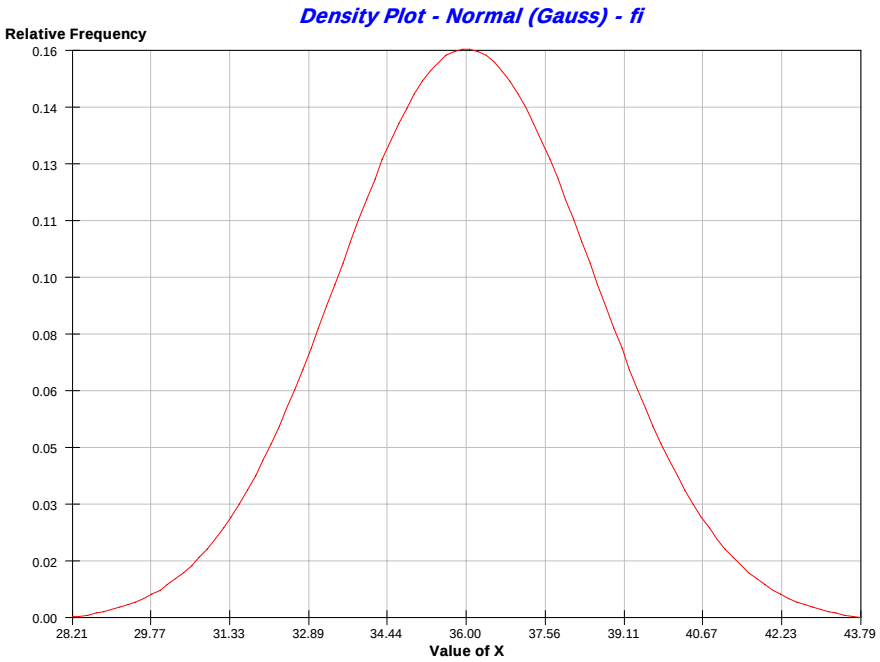

Figure C.1 Basic friction angle, ϕ_b~N(36;2.52)

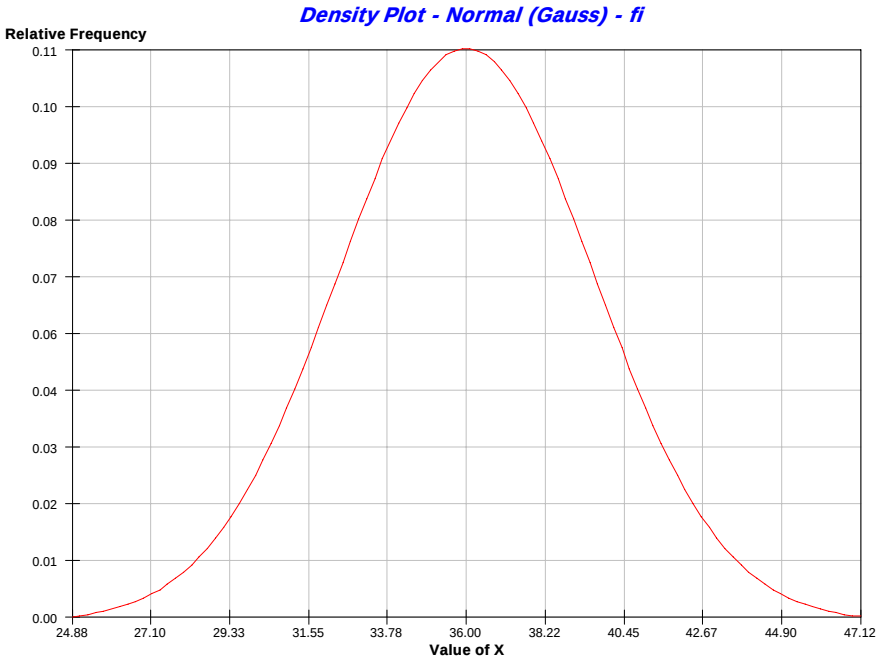

Figure C.2 Basic friction angle, ϕ_b~N(36;3.6)

APPENDIX D, ASSUMED NORMAL DISTRIBUTIONS FOR DILATION ANGLE

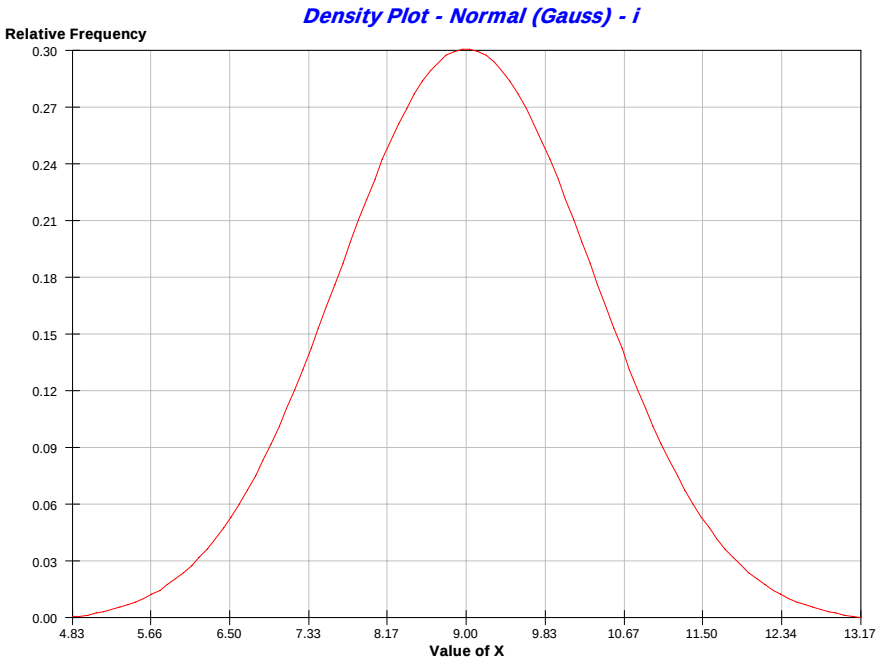

Figure D.1 Dilation angle, i~N(9;1.35)

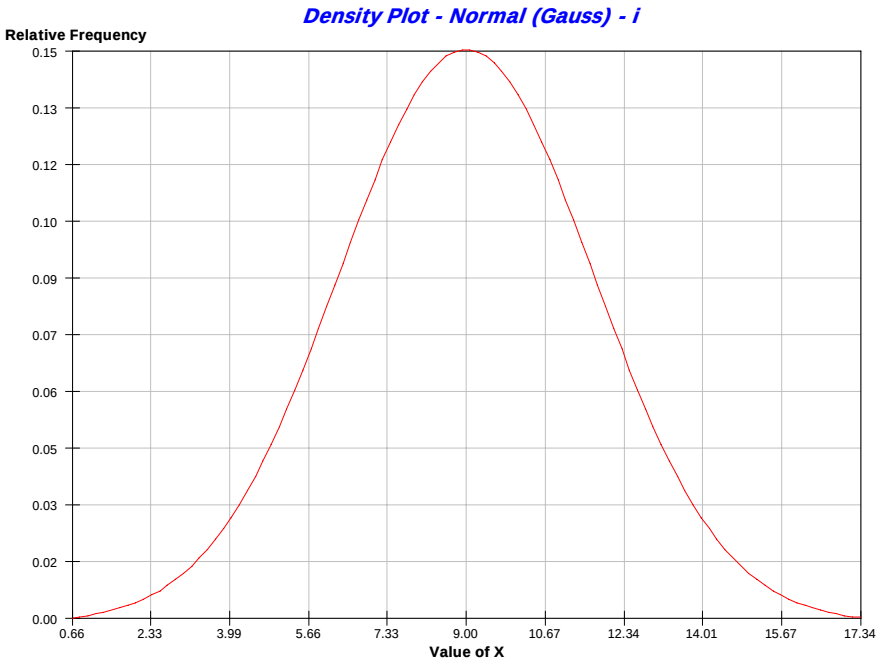

Figure D.2 Dilation angle, i~N(9;2.70)